A Spectral Guide: The Analysis of Solar Irradiance and Soiling Through Spectroradiometry

by

Carmen Lewis

Thesis presented in partial fulfilment of the requirements for the degree of Master of Engineering (E&E) in the Faculty of Engineering at Stellenbosch University

Supervisor: Dr. Johannes M. Strauss

December 2017

Declaration

By submitting this thesis electronically, I declare that the entirety of the work contained therein is my own, original work, that I am the sole author thereof (save to the extent explicitly otherwise stated), that reproduction and publication thereof by Stellenbosch University will not infringe any third party rights and that I have not previously in its entirety or in part submitted it for obtaining any qualification.

Date: December 2017

Abstract

A Spectral Guide: The Analysis of Solar Irradiance and Soiling Through Spectroradiometry

C. Lewis

Department of Electrical and Electronic Engineering,
University of Stellenbosch,
Private Bag X1, Matieland 7602, South Africa.

Thesis: MEng (E&E)

September 2017

The influence of soiling on photovoltaic (PV) modules has been investigated in many research projects before, but this project extended the methods of soiling analyses on photovoltaic (PV) modules through the implementation of spectroradiometry. The objective with the implementation of a spectrometer was to remove the associative characteristics of PV modules within the measurements. Since spectroradiometric measurements are not often used for this application, several measuring and analysis methods are discussed in terms of PV applications. Previous research either failed to consider the module characteristics (such as temperature and manufacturing variances) or spectrometers have not been implemented in the measurement of irradiance and soiling under natural conditions.

An automated measuring system was designed and built to ensure repeatable and accurate measurements of clear-sky irradiance and comparative measurements through glass samples. The combination of these two types of measurements allowed for the determination of relative transmission losses , as a result of the refraction and absorbance by dust particles and glass particles. Furthermore, lab measurements were acquired to indicate that the method used to determine relative transmission losses, was accurate. This project was used to generate a spectral measurement and analysis guide, specifically for the measurement of irradiance and determining the influence of soiling on the transmission of irradiance.

Through relative transmission loss measurements, it was found that clean low-iron float glass (a good approximation for solar glass) induced a transmission loss of $8.6 - 9.2\,\%$. Furthermore, with automated measurements at a fixed angle, the transmission loss was calculated as $9.32\,\%$ to $12.53\,\%$ from clean to minor soiling solar glass samples. Also, an analysis on the shift in transmission within a measurement in the wavelength bands of UV, visible and NIR light was discussed - it was found that the soil and inherent glass particles supressed some photons within the UV and NIR ranges, causing a slight increase in content within the visible range.

Several recommendations regarding the automated system design are supplied. A recommendation in regards to the measurement equipment was that a measuring range greater than

$300 - 1000\,nm$ with good resolution is required for these measurements. This might mean the implementation of a second spectrometer specifically for measuring the NIR range. It was also found that measurements acquired in the direction of the sun location, rather than at a fixed measuring angle, increased the stability and accuracy of measurement, allowing for better approximations of transmission loss as a result of soiling.

Uittreksel

'n Spektrale Gids: Die Analise van Sonenergie en Stofbesoedeling deur Radiometriese Spektrometrie

("A Spectral Guide: The Analysis of Solar Irradiance and Soiling Through Spectroradiometry")

C. Lewis

Departement Eletriese en Elektroniese Ingenieurswese,
Universiteit van Stellenbosch,
Privaatsak X1, Matieland 7602, Suid Afrika.

Tesis: MIng (E&E)

September 2017

Die invloed van stofbesoedeling op fotovoltaïese (FV) panele is al ondersoek deur talle navorsingsprojekte, maar hierdie projek brei uit op die metodes van analise van stofbesoedeling op FV deur die gebruik van radiometriese spektrometrie. Die hoof doel van die gebruik van 'n spektrometer is om die assosiatiewe eienskappe van die FV panele te vermy in die metings. Aangesien spektrometriese metings nie gereeld in die FV veld gebruik word nie, is vele meet en analise metodes bespreek in terme van hierdie FV toepassing. Vorige navorsing het of nie die paneeleienskappe (soos temperature en vervaardigingsverskille) in ag geneem nie, of nie die spektrometermetings voltooi in natuurlik sonstraling en stof omstandigehede nie.

'n Geoutomatiseerde meetopstelling is ontwerp en is gebou om herhaalbare en akkurate metings van sonstraling deur 'n glaspaneel te verseker. Die kombinasie van bloulug en glasmetings laat toe vir die bepaling van relatiewe transmissieverlies, as gevolg van die refraksie en absorbies deur die stof patikels, sowel as die glas partikels. Verder is labratorium-metings bekom om hierdie metode van relatiewe transmissie as akkuraat te bevestig. Hierdie projek was dus gebruik om 'n gids op te stel oor die meet en analise van die sonspektrum, spesifiek vir die bepaling van die sonstraling en om te bepaal wat die invloed van stof is op die transmissie van sonstrale.

Deur hierdie relatiewe transmissie toetse is dit bevind dat skoon "float" glas, met 'n lae yster inhoud (wat 'n goeie benadering vir FV paneel glas is), 'n verlies in transmissie tussen 8.6 % en 9.2 % veroorsaak het. Verder, met geoutomatiseerde toetse, teen 'n vaste meethoek, is dit bepaal dat daar 'n transmissieverlies was van 9.32 % tot 12.53 % vanaf skoon tot lig stowwerige FV glaspanele. 'n Analisie op die skuif in transmissie binne die UV, sigbare en NIR lig golflengte bande onderskeidelik, is ook bespreek, en so is gevind dat stof en selfs partikels inherent in die glas sekere fotone in die UV en NIR bande onderdruk wat dus 'n verhoging in die sigbare ligband veroorsaak.

Verskeie aanbevelings vir die geoutomatiseerde stelsel is bespreek. 'n Aanbeveling in term van die meet gereedskap is dat 'n groter meet band as $300-1000\,nm$ benodig word met goeie

resolusie. Dit kan selfs beteken dat 'n twee spektrometer benodig sal word om spesifiek die NIR band te meet. Dit is ook gevind dat die metings wat in lyn met die son geneem was en nie by 'n vaste meethoek nie, die stabiliteit en akkuraatheid van metings verbeter het wat weer toegelaat het vir 'n beter benadering van transmissieverliese, as gevolg van stofneerslag.

Acknowledgements

My appreciation to the following people:

Dr J.M. Strauss for being an understanding and supportive supervisor, supplying unending knowledge, patience and energy towards this research project and many other.

The technical staff at the Electrical and Electronic Engineering department - Mr J. Arendse, Mr M. Jumat, Mr P. Petzer, Mr A. Swart and Mr W. Van Eeden for the continuous assistance, lending of a helping hand and the brightening of many a stressful day.

Dr Anton du Plessis and Stephan Le Roux from the Central Analytics Facility at Stellenbosch University for their help with transmission tests, use of equipment and sharing of knowledge.

John-Pieter Botha for being the best of help with any task - 3D printing, problem solving to much-needed conversations and laughter; Tashriq Pandy for being a great IT guy and a soundboard to my ideas and musings; Christoff Botha for being a helpful companion.

My parents, Mark and Roezan Lewis for their unending support in all things, from reading first reviews to supplying snacks. Finally, Neil Lamprecht for being a constant companion, providing motivation, laughter and reminding me to slow down sometimes.

Contents

List of Figures

List of Tables

Nomenclature

Constants

$c =$ $2.998 \times 10^{8}\,\mathrm{m{\cdot}s^{-1}}$

$\epsilon_0 =$ $8.8542 \times 10^{-12}\,\mathrm{C^2{\cdot}N^{-1}{\cdot}m^{-2}}$

g $9.81\,\mathrm{m{\cdot}s^{-2}}$

$h =$ $6.626 \times 10^{-34}\,\mathrm{J{\cdot}s}$

$k_B =$ $1.38064852 \times 10^{-23}\,\mathrm{J{\cdot}K^{-1}}$

$\mu_0 =$ $4\pi \times 10^{-7}\mathrm{N{\cdot}s^2{\cdot}C^{-2}}$

$q =$ $1.6021765 \times 10^{-19}\,\mathrm{C} = 1\,\mathrm{eV}$

$R_{earth} =$ $6,353\,\mathrm{km}$

$\gamma =$ $2.89 \times 10^{-3}\,\mathrm{m{\cdot}K}$

$\sigma =$ $5.67 \times 10^{-8}\,\mathrm{W{\cdot}m^{-2}{\cdot}K^{-4}}$

Variables

α	Alititude Angle	$[\,^\circ\,]$
a_c	Acceleration	$[\,\mathrm{m{\cdot}s^{-2}}\,]$
α_a	Angular Acceleration	$[\,\mathrm{rad{\cdot}sec^{-2}}\,]$
a	Effective Molecule Radius	$[\,\mathrm{m}\,]$
A	Area	$[\,\mathrm{m^2}\,]$
β	Surface Tilt Angle	$[\,^\circ\,]$
β_T	Turbidity Coefficient	$[\ ]$
β_{To}	Ångstrom Turbidity Coefficient	$[\ ]$
b	Belt Width	$[\,\mathrm{mm}\,]$
B	Spectral Radiance	$[\,\mathrm{W{\cdot}cm^{-2}{\cdot}sr^{-1}}\,]$
C_P	Calibration Unit	$[\,\mu\mathrm{J{\cdot}count^{-1}}\,]$
δ	Declination Angle	$[\,^\circ\,]$
d	n-the Day of the Year	$[\ ]$

d_b	Bore Hole	$[\,\mathrm{mm}\,]$
$d_{particle}$	Particle Diamter	$[\,\mathrm{m}\,]$
dL_p	Wavelength Spread	$[\,\mathrm{nm}\,]$
D	Earth-Sun Distance	$[\,\mathrm{m}\,]$
D_c	Diffusion Concentration	$[\,\mathrm{m^2{\cdot}s^{-1}}\,]$
D_P	Dark Spectrum	$[\,\mathrm{count}\,]$
ϵ	Electric Permittivity	$[\,\mathrm{C^2{\cdot}N^{-1}{\cdot}m^{-2}}\,]$
η	Efficiency	$[\,\%\,]$
θ_a	Azimuth Angle	$[\,^\circ\,]$
θ_i	Angle of Incidence	$[\,^\circ\,]$
θ_r	Reflectance Angle	$[\,^\circ\,]$
θ_t	Transmission Angle	$[\,^\circ\,]$
θ_z	Solar Zenith Angle	$[\,^\circ\,]$
E	Energy	$[\,\mathrm{J}\,]$
E_g	Band Gap Energy	$[\,\mathrm{eV}\,]$
E_i	Direct Spectral Irradiance	$[\,\mathrm{W{\cdot}m^{-2}}\,]$
E_{oi}	Extraterrestrial Spectral Irradiance	$[\,\mathrm{W{\cdot}m^{-2}}\,]$
E_{photon}	Photon Energy	$[\,\mathrm{eV}\,]$
E_λ	Emissive Power	$[\,\mathrm{W{\cdot}m^{-2}{\cdot}\mu m}\,]$
F_a	Linear Acceleration of Bearing	$[\,\mathrm{N}\,]$
F_ab	Initial Acceleration Force	$[\,\mathrm{N}\,]$
F_ai	Idler Pulley Force	$[\,\mathrm{N}\,]$
F_f	Friction Force	$[\,\mathrm{N}\,]$
F_{fi}	Intrinsic Motion Resistance	$[\,\mathrm{N}\,]$
F_g	Bearing Weight	$[\,\mathrm{N}\,]$
F_w	External Work	$[\,\mathrm{N}\,]$
FF	Fill Factor	$[\ ]$
h_{sea}	Height Above Mean Sea Level	$[\,\mathrm{m}\,]$
H	Power Density	$[\,\mathrm{W{\cdot}m^{-2}}\,]$
I	Solar Irradiance	$[\,\mathrm{W{\cdot}m^{-2}}\,]$
I_i	Incident Flux Density	$[\,\mathrm{W{\cdot}m^{-2}}\,]$
I_{noon}	Solar Irradiance at Solar Noon	$[\,\mathrm{W{\cdot}m^{-2}}\,]$

I_r	Reflected Radiant Flux Density	$[\mathrm{W{\cdot}m^{-2}}]$
I_t	Transmitted Radiant Flux Density	$[\mathrm{W{\cdot}m^{-2}}]$
I_{BH}	Beam Horizontal Radiation	$[\mathrm{W{\cdot}m^{-2}}]$
I_{CHOP}	Choppping Current Threshold	$[\mathrm{A}]$
I_{DH}	Diffuse Horizontal Radiation	$[\mathrm{W{\cdot}m^{-2}}]$
I_G	Global Horizontal Radiation	$[\mathrm{W{\cdot}m^{-2}}]$
I_H	Total Daily Radiation on Horizontal Plane	$[\mathrm{W{\cdot}m^{-2}}]$
I_P	Corrected Irradiance Measurement	$[\mathrm{W{\cdot}m^{-2}}]$
I_{RC}	Reflected Radiation	$[\mathrm{W{\cdot}m^{-2}}]$
I_{SC}	Short-Circuit Current	$[\mathrm{A}]$
I_T	Tilted Total Daily	$[\mathrm{W{\cdot}m^{-2}}]$
I_x	Area Moment in X Direction	$[\mathrm{m^4}]$
I_y	Area Moment in Y Direction	$[\mathrm{m^4}]$
J	Second Polar Moment	$[\mathrm{m^3}]$
J_i	Idler Pulley Inertia	$[\mathrm{kg{\cdot}m^2}]$
k_o	Ozone Absorption Coefficient	$[\mathrm{atm{\cdot}cm^{-1}}]$
K_e	Dielectric Constant	$[\ ]$
K_m	Relative Permeability	$[\ ]$
λ	Wavelength	$[\mathrm{nm}]$
λ_g	Band Gap Wavelength	$[\mathrm{nm}]$
l	Lenght	$[\mathrm{m}]$
μ	Permeability	$[\mathrm{N{\cdot}s^2{\cdot}C^{-2}}]$
μ_r	Dynamic Friction Coefficient	$[\ ]$
m	Reltive Air Mass	$[\ ]$
m_b	Bearing Mass	$[\mathrm{g}]$
m_i	Idler Pulley Mass	$[\mathrm{g}]$
M	Bending Moment	$[\mathrm{N{\cdot}m}]$
ν	Frequency	$[\mathrm{Hz}]$
n	Absolute Index of Refraction	$[\ ]$
n_0	Refractive Index for air at 0.7 µm, $hsea = 0$	$[\ ]$
ψ	Day Angle	$[\mathrm{rad}]$
P	Pressure	$[\mathrm{Pa}]$

P_{MPP}	Maximum Power at STC (Nominal)	[W]
$Power$	Power	[W]
Q	Heat	[J]
QE_λ	External Quantum Efficiency	[ ]
ρ	Ground Reflectance	[ ]
ρ_0	Air Density at $h_{sea} = 0$	[kg·m^{-3}]
ρ_h	Air Density at Height h_{sea}	[kg·m^{-3}]
R	Reflection Ratio	[ ]
RF	Resolution Factor	[ ]
R_b	Ratio of Beam Radiation	[ ]
R_d	Reduction Factor for Direction Dependant Scattering	[ ]
σ_s	Molecule Cross-Section	[m^2]
S	Entropy	[J·K^{-1}]
S_P	Sample Spectrum	[count]
S_t	Stress	[Pa]
SR_λ	Spectral Response	[A·W^{-1}]
τ_a	Aerosol Attenuation Transmittance	[ ]
τ_g	Mixed Gas Absorption Transmittance	[ ]
τ_{oz}	Ozone Absorption Transmittance	[ ]
τ_r	Rayleigh Scattering Transmittance	[ ]
$\tau_{S_{max}}$	Maximum Torsional Stress	[Pa]
τ_w	Wate Vapour Absorption Transmittance	[ ]
t	Time	[s]
t_i	Integration Time	[s]
T	Absolute Temperature	[K]
T_e	Effective Tension	[N]
T_{max}	Maximum Moment	[N·m]
T_t	Transmittance Ratio	[ ]
φ	Latitude	[°]
ϕ	Photon Flux	[photons·s^{-1}·m^{-2}]
v	Velocity	[m·s^{-1}]
V_{OC}	Open-Circuit Voltage	[V]

ω_s	Local Solar Noon Angle	[°]
ω'_s	Sunset Hour Angle	[°]
w	Wavelength Coefficient	[ ]
w_b	Belt Specific Wieight	[N]
W	Work	[J]
W_p	"Wahrscheinlichkeit", Thermodynamic Probability	[ ]
z	Solar Elevation	[°]

Chapter 1

Introduction

1.1 Background

It is common knowledge that various factors influence the yield of a solar module and perhaps the most variable and least known are the environmental factors. These environmental factors include meteorological conditions such as the formation of clouds, atmospheric content and general weather conditions. Furthermore, and the focus of this thesis, is the effect of dust on the solar yield contributed through the environmental soil, landform and vegetation.

The highest direct irradiance is received within the arid to semi-arid areas located 35° north and south of the equator. Off course, harvesting solar energy within these arid areas comprises of its own challenges [1]. By the amount of research available it is therefore anticipated that dust is critical to solar performance, especially in arid and semi-arid environments which is characterized by high variability in rainfall and large quantities of dust carried from surrounding sediments (Aeolian dust).

Studies on the adverse effects of soiling on solar energy have been accomplished in various methods: firstly, comparative studies with photovoltaic modules installed in the field to find a direct correlation between meteorological conditions, exposure period and module output and secondly methods relating to particle distribution to energy loss by simulating the accumulation of dust in a laboratory environment. The difficulty with the comparative studies is separating the associative effects of the specific solar cells, as well as module performance - these studies are thus far investigated by measuring current and output efficiencies [2–4]. The simulation methods [5, 6] have their own disadvantages since simulating varying natural environmental factors such as irradiance, wind, cloud formation and particle distribution are very challenging. Below, the literature repeatedly states that most models for simulating natural factors are only approximations.

Zorrilla-Casanova et al.[7] conducted a soiling analysis using solar modules and claims a mean daily energy loss of 4.4 % per year as an effect to dust, with up to 15 % in losses in summer months without rain. They have also shown that the angle of radiation on the surface with dust present, noticeably affects the losses - this is ascribed to the extinction of radiation beams. Sayyah et al.[1] supplied a summary on daily output power loss due to soiling at solar plants located at places of high solar insolation - this daily loss was up to 1.2 % for Dhaka, Bangladesh. It is known that sandstorms are possibly regular in many of these arid environments - according to Marouani et al.[8], a sand mass of 150 g on a glass surface at a 90° angle reduces the transmission of that surface from 91.3 % to approximately 38.2 % - an affect similar to sandblasting is possible when this sand mass is blown onto the glass. This leads to the increase in surface roughness of the glass which could further ensue

in additional scattering of light from this surface.

With spectral distribution as a key research theme, Qasem et al.[2] recognised that soiling mainly affects lower wavelength bands whereas the transmittance is less effected by wavelengths larger than 600 nm. These conclusions were established through particle size analysis and its impact on spectral transmittance in this literature.

Not only is there a discrepancy in knowledge and techniques of determining the effect of soiling on modules, but more fundamentally a discrepancy in accurate irradiance distributions. A good knowledge of spectral distribution is required to truly understand the effect of soiling on irradiance. Soiling in itself is complicated in a natural environment, determining the effect of soiling on the spectral distribution is more complicated and has not been significantly researched but it is known that soiling is the contribution of environmental factors, such as the location and the dust type predominant in that area, as illustrated in figure 1.1 (adapted from Maghami et al. [9]).

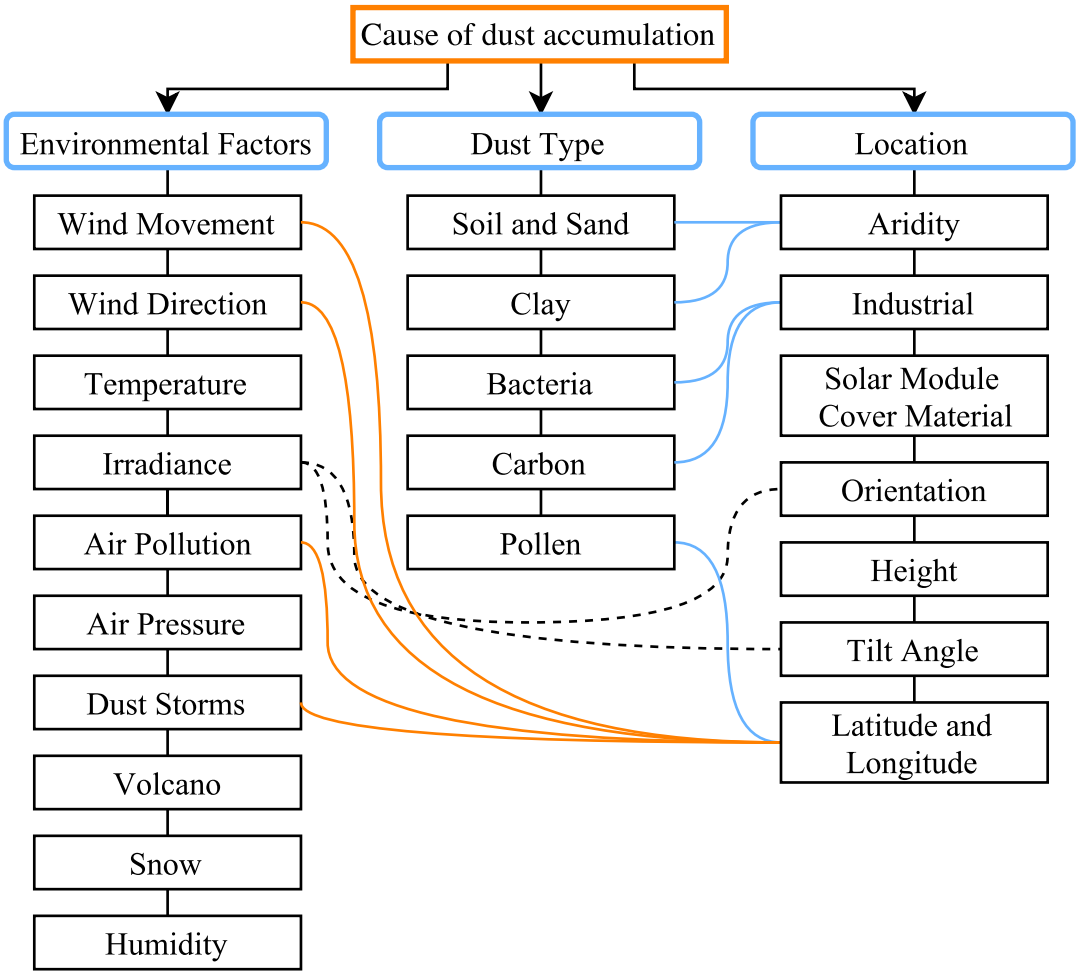

Figure 1.1: Type and cause of dust accumulation on solar modules.

Cornaro and Andeotti [10] had similarly seen the gap in solar irradiance distribution measurements and specifically focused on the Average Photon Energy (APE) index as well as the performance of solar modules in natural conditions. The aim was to implement the APE as a descriptive index for outdoor conditions. The effect of change in season was confirmed through the calculation of the APE - the difference between winter and summer was calculated as approximately 7 % in APE value. Furthermore, an approximate 10 % increase in APE between overcast and clear days were established.

In cities, and to a lesser extend in barely semi-arid environments it might be asked what the true advantage of a complex dust analysis would be, but allowing some extravagant ideas of human settlements on Mars could show the advantage of advanced soiling analysis techniques. It has been determined that a solar array on Mars could degrade within 1 % to 50 % over a mission of merely 30 days [11]. Not only is there considerable dust in the environment that is easily deposited on the modules, but also, a lack of water limits the cleaning of their surfaces.

Rather than merely supplying these values of transmission loss, irradiance and average photon energy as mentioned above, a method of accurately determining these values is required. Setting a precedent of measuring techniques in the photovoltaic industry could expand what is known regarding irradiance and its distribution.

1.2 Motivation and Problem Statement

The usual methods implemented to determine the effect of soiling, as mentioned previously, are wanting in "objectivity" - removing the influence of specific module characteristics and supplying a relation between the environmental conditions of the location and the amount of soiling. Therefore, to circumvent these adverse associative effects influencing other research methods, an analytical approach to determine the transmittance effects due to dust deposition is suggested. This approach comprises solar irradiance measurements through field spectrometry of global irradiance, as well as transmitted irradiance through mounted PV module glass covering samples.

The main objective is to supply a guide to spectral measurements in the PV field, introducing other methods of inspecting irradiance and soiling. Perhaps spectral analysis methods could even lead to quantifiable relations between location, which includes soil type and weather conditions, and transmission losses.

Many observations are made that could perhaps be seen by the reader as unrelated or insignificant but the objectives listed below all relates to the collection of knowledge regarding how spectral distributions and transmission loss are measured, and how these are analysed and quantified.

1.2.1 Research Objectives

Expanding on the objective of creating a collection regarding spectral measurements and analyses, the following questions might be asked:

- How does one measure spectral distribution?
  - How does the spectral measurement instrument response influence the measured distribution?
  - What other instrument factors influence the distribution form?
  - What are the required measurement conditions (e.g. setup, weather) to ensure usable data?
  - What are the limitations to these measurements?
- What does a spectral analysis entail?
  - Which conditional requirements are essential to the usability of a set of data?

  - What analysis methods are available for spectral distributions and specifically relating to solar irradiance?
  - How does the measured distribution compare to total irradiance measured by other equipment?
  - How can spectral distribution data be used to determine transmission loss of glass and soiling?
  - What are the limitations of these spectral analysis methods?

- What is the direct effect of soiling on the amount of radiation transmitted through the glass panel?
  - What are the transmission losses caused solely by the clean glass?
  - How accurately can we measure the transmission losses relating to the clean glass and soiling?

- How can these spectral measurements be improved in terms of accuracy and efficiency?
  - How can the process be automated?
  - How well does an automated system lend itself to measurements with the spectrometer, with little human interference?
  - What is the measuring strategy required to draw sound conclusions regarding the impact of soiling?
  - What, if any, additional measurement conclusion can be drawn through an automated system?
  - How does the automated measurements compare to hand measurements, in accuracy and repeatability?

These questions can be answered through the objectives listed below:

- Collect clear baseline distribution measurements through non- and automated methods.
- Collect measurement samples of the glass, as well as samples that are soiled to some degree.
- Obtain irradiance data measured through other equipment.
- Determine the relation between the distribution data and the obtained irradiance totals.
- Analyse the effect of clean glass on transmission.
- Analyse the effect of soiling or dust on irradiance transmission.

1.2.2 Project Tasks

The objectives set in the previous section can be accomplished by the following tasks:

1. Select and acquire a suitable spectrometer that is compact and field usable.

2. Acquire preliminary measurements that can be used as an instrument learning experience and as non-automated measurement data.

3. Design a XY-plotter that will allow automated measurements at various constant points; also, design the plotter so that a glass plane can be mounted within it. The plotter should be sturdy and rugged enough to withstand varying weather conditions.

4. Implement the spectrometer with the automated plotter so that all parts relating to the system is indeed automated - this includes automated starting times and data written to a database.

5. Acquire automated measurements according to a decided measuring scheme, which should include clear-sky baseline, glass and soiled measurements.

6. Analyse and compare these automated measurements to total irradiance values, as well as the non-automated measurements.

7. Determine the transmission loss by the solar glass as well as some soiling.

The main task is the design, construction and implementation of the XY-plotter. This plotter moves the measuring sensor attached to the spectrometer to multiple points within a frame, supplying comparative baseline measurements (to ensure constant measuring conditions). These baseline measurements are compared to measurement samples that are collected under clean solar glass to determine the transmission loss of the clean glass, and similarly, measurements under soiled glass to determine the additional transmission influence of the particles on the radiation beams.

1.2.3 Hypothesis

According to the research, the following hypotheses can be made:

- Measurements made into the direction of the sun with a large field of view can be estimated as global horizontal irradiance (GHI) whereas measurements with a smaller field of view (if accurately positioned towards the sun) will supply direct normal irradiance (DNI) data.

- Measurements not directed towards the sun but rather at a fixed angle supplies data that are closer to diffuse horizontal irradiance (DHI) but will approximate GHI closer to solar noon.

- Clean solar glass will cause less transmission loss than clean glass of other types.

- Soiling, or dust particles, will either increase or decrease the transmission loss according to the angle of the irradiance beams therefore, soiling transmission loss will not necessarily be constant.

- Automated measurements will increase the accuracy and repeatability of relative transmission loss measurements, making it a useful method of soiling analysis.

1.3 Scope

Following the objectives tasks, the scope and project limitations are discussed. Firstly, the research excludes the relation between an actual solar module and soiling - the emphasis is rather on quantifying soiling influence on irradiance transmission than the soiling influence on the module output and efficiency.

It is anticipated that this project will not necessarily discuss extensive natural soiling since the measuring period will be too short to allow for enough soiling to be described as extensive. Rather, the project will focus on indicating that an analysis of extensive soiling is possible and quite simple with the suggested measuring methods. The focus is to supply a guide to spectral measurements and extending the measurement methods in the PV field.

Although the spectrometer is mostly used to collect radiation measurement in $W{\cdot}m^{-2}{\cdot}nm^{-1}$, it can be used in other modes such as a transmission or colour mode. The transmission mode is applied in a laboratory test to determine the response of the glass with a constant light source but the mode is not applied in the field measurements. The advantage of only using the radiometric mode (or counts to radiation through a calibration) is that while the transmission loss of glass and soiling is determined, the spectral distribution of clear-sky measurements is also investigated, extending the resource pool of solar irradiance measurements.

Although additional total irradiance values from another instrument, such as a pyranometer is used within the analysis, the instrument is not discussed in detail, nor is the data investigated for validity. Rather, the total irradiance values are acquired from trusted sources and it is assumed that the data is indeed valid.

The limitations are extended throughout the project since not all limitations or even scope parameters are completely known as the automated device is first of its kind. Similarly, since no distribution data is readily available some assumptions are made throughout the thesis regarding the validity of the distribution form.

1.4 Thesis Overview

This thesis includes:

- Chapter 2: In this chaper, energy and the spectrum in particle, as well as wave form, is explored. This initial exploration in physics supplies a basis for the connection between soiling analysis and the importance of investigating spectral distribution. Solar irradiance is discussed from extra-terrestrial to terrestrial radiation, how it impinges on surfaces and how it is quantified. Meteorological conditions and their effect on radiation is discussed - clouds, air mass and atmospheric particles all contribute to these affecting conditions.

  Dust particles and their distribution mechanics are briefly discussed, followed by a discussion on photovoltaic modules: module efficiency, their spectral response, the glass covering and the basics of the propagation of light. Finally, spectrometry is introduced which includes some discussion on the optical design and factors to consider when a spectrometer is chosen.

- Chapter 3: The first field experience is introduced in this chapter. This experience was the preliminary introduction to the chosen spectrometer and its particulars. It provided a learning experience for spectral measurements and analysis - several methods were established to ensure that the data used is valid. Daily distribution measurements

were supplied with total irradiance values and errors. The Average Photon Energy indices were calculated to determine the colour content of the measured light. Lastly, the transmission loss as caused by small low-iron float glass samples were calculated through relative transmission measurements.

- Chapter 4: The second preliminary field experience was completed to compare the chosen spectrometer with a second, different spectrometer. This experience also allowed for the investigation of the large solar glass that is an actual solar module covering. Similar to the previous experience, daily distribution measurements are supplied, which includes the Average Photon Energy and relative transmission loss measurements. Additionally, this experience establishes a relation between the measured irradiance and the field of view experienced by the spectrometer.

- Chapter 5: The laboratory experience was a final confirmation of findings before the final automated measurements were acquired. This experience consisted of transmission tests completed with a constant light source, as well as the use of another spectrometer. These transmission tests supplied a spectral response for the low-iron float glass as well as the solar glass pane. Further, the dark spectrum usually required with spectral irradiance measurements were investigated and an approximation for this dark spectrum was established. Similar to the other experiences, relative transmission tests were completed with the low-iron float glass samples - this includes a sample with a dust deposition from the semi-arid environment.

- Chapter 6: In this chapter the automated system and its various relating components are discussed in detail. This discussion includes design choices relating to the drive system such as the motors, pulleys and belts. Design notes were investigated to determine the overall frame and its connected elements. The electronic design is shown through some discussion of its various elements and how it is implemented within the software. The chosen measuring scheme is revealed, as well as the method of controlling the motor to move a specific distance. Finally, the installation is discussed through the assistance of photographs of the actual structure, completed with some design suggestions.

- Chapter 7: This is the final data chapter - conclusions regarding the data accumulated through automated measurements are supplied. This includes in depth analysis of the clear-sky baseline measurements acquired by observing its distribution form and comparing it to acquired total irradiance values. Further, the transmission loss of the large solar glass is analysed for the first time and some soiling measurements is compared to the baseline measurements. As with the preliminary experiences in Chapter 3 and 4, the total irradiance values were compared over multiple days, with the exception that the automated measurement were completed over a much longer period so, multiple days of data were analysed. Similarly, the distribution of irradiance at a specific time is compared over multiple days.

- Chapter 8: Conclusions of the final data from Chapter 7, as well as data from the preliminary experiences are discussed here, supplying an overview of the findings throughout this research and measuring journey. Further, an overview of some important suggestions is supplied and finally what the future holds for the measuring and analysis methods discussed in this thesis.

Chapter 2

Literature Review

2.1 Introduction

The use of spectrometry in the field of engineering compels the engineer to approach the study of solar energy through physics, and even further down to the sub-division of quantum mechanics. This approach supplies an understanding of how the measurement of solar energy; and the use of spectroscopy is unavoidable. Perhaps the most prominent implementation of spectroscopy in the measurement of solar spectral radiance is the Solar Radiation and Climate Experiment (SORCE). This satellite mission is sponsored by NASA (National Aeronautics and Space Administration) since 2003, to supply the Earth Science Enterprise (ESE) with accurate solar spectral radiance data, as well as total solar irradiance data [12].

Perhaps an important technical distinction to point out is the difference between radiation and irradiance. The simple answer is that radiation refers to the process of energy transfer from a specific source - in this case from the sun. Irradiation, a verb, is described as the energy radiated from the source incident on a surface. We could further say that radiation is one process of the release of energy (photons) from the source surface; the other two processes are conduction and convection. Mostly the term irradiation is used for the deliberate exposure of a surface to radiation, as we intentionally expose solar modules to sun radiation - more specifically the word irradiance is used in connection to energy received from the sun. In this discussion the words radiation, irradiation and irradiance are used intermittently to describe the same concept of energy from the sun, unless otherwise stated. Incident solar energy has some basic characteristics that are central to how sunlight and photovoltaic modules interact:

1. the spectral distribution or content of the incident sunlight,
2. the power density of the light,
3. the angle of the incident light on the module and
4. the energy received from the sun throughout a day or year by the module.

The atmosphere also has a significant impact on this interaction between incident sunlight and the modules:

1. reflection, absorption and scattering of light in the atmosphere,
2. a change in spectral distribution of the incident light as reflection, absorption and scattering is strongly wavelength-dependant and

3. variations in the local atmosphere by meteorological conditions and pollution.

This literature study supplies an overview of the nature of particles in accordance to the above points: the motion of the particles and the energy related to these particles - the microscopic physics view of solar energy. Thereafter a macroscopic view is provided with the focus on solar energy: how it is measured and analysed through time. Furthermore, a discussion will ensue regarding the nature of dust particles and their relating mechanics. Finally, an overview of the technologies photovoltaic modules and spectrometers are provided, focusing on the use and design of these technologies.

2.2 Energy and the Spectrum

A continuous spectrum of energy is emitted by the sun - this energy is transported by the electromagnetic mechanism through matter void areas at the speed of light; this mechanism is called radiation. The emitted energy comes from molecules that possess energy due to the orbiting of electrons around a nucleus. The electrons of these molecules absorb and emit energy; a spectrum, or a range of varying wavelengths, originate from variation of the state of these electrons. Considering the basic properties of an atom, we can describe this isolated atom in terms of its quantum, or discrete state. The quantum state and associated energy of an atom can be calculated from quantum mechanics.

2.2.1 The Electromagnetic Spectrum

Electromagnetic radiation is described as the additional energy released spontaneously when an isolated atom moves back into a lower state after it is has been supplied energy in its ground state, as to promote it to an excited state. If the state energies are known, the frequencies of light emitted by the atom can be determined from,

$$E_{photon} = h \cdot \nu, \tag{2.1}$$

which describes the energy carrying the photon, or the quantum of light with a specific frequency or wavelength, with h Planck's constant. The wavelength λ is related to the frequency ν and the speed of light,

$$\lambda = \frac{c}{\nu}, \tag{2.2}$$

with the constant c the speed of light [13].

The above literature has discussed electromagnetic radiation in its more recent discrete particle form rather than quantifying it as a continuous sinusoidal curvature. Both concepts are true - electromagnetic radiation has the inherent properties of waves as well as discrete particles, however they cannot manifest concurrently. A large number of photons will therefore still transport on average an equivalent amount of energy as by an electromagnetic wave. In optics, such as spectrometry the quantum nature is not practical but still supports some basic quantum mechanics concepts which are important to the research.

Combining equation 2.1 and 2.2, it is observed that the energy of the photon is inversely proportional to its wavelength. Simply stated, "blue" light which consists of high energy photons has a shorter wavelength and "red" light consisting of low energy photons has a longer wavelength. The implication is that for the same intensity of light, consisting of only

"blue" or "red" light, fewer photons are required for "blue" light since the content of the energy for each photon is higher.

Therefore, from the properties of the photon and the amount of photon flux (ϕ) for this specific photon incident per second per unit area, the power density [14],

$$H = \phi \times \frac{h \cdot c}{\lambda}. \tag{2.3}$$

2.2.2 Entropy

The sun surface temperature is approximately $5778\,K$ as a result of the energy flow within itself - the radiation spectrum from the sun is therefore similar to that of a $5778\,K$ blackbody. Some deviations are present with this theoretical comparison, most notably by selective absorption.

Blackbody emission is usually described by the Plank function,

$$B(T) = C_1 \int_{\infty}^{\nu} \left[v^3 \left[exp\left(\frac{C_2 \cdot \nu}{T} \right) - 1 \right] \right] d\nu, \tag{2.4}$$

expressed in terms of wavenumber, indicating the dependence of emission on temperature. $B(T)$ is the radiance in $W \cdot cm^{-2} \cdot sr^{-1}$ and C_1, C_2 the first and second radiation constants respectively, $1.909 \times 10^{-12}\,W \cdot cm^{-2} \cdot sr^{-1}$ and $1.438833\,K \cdot cm$ [15].

Considering the more well-known Plank equation for emissive power of a blackbody,

$$E_\lambda = \frac{h \cdot c^2}{\lambda^5 \cdot \left(exp\left(\frac{c \cdot h}{k_B \cdot \lambda \cdot T} \right) - 1 \right)}. \tag{2.5}$$

with k_B the Boltzmann constant equal to $1.38064852 \times 10^{-23} J \cdot K^{-1}$ [16].

Noting that this form of Plank's equation is used considerably in thermodynamics, it is perhaps necessary to discuss entropy and its importance in observing the spectral distribution of energy.

Using Planck's function as supplied in equation 2.5, the spectral curve for a blackbody at any temperature can be calculated for any wavelength range (e.g. as in figure 2.1 $T1 - T4$), except at a temperature of $0\,K$ (division by zero). Figure 2.1 shows the spectral curve of a blackbody at various temperatures with $5778\,K$ being the estimated temperature of the sun surface.

This spectral plot shows the influence of temperature on the spectral radiance amount as well as the distribution, and therefore the peak radiance. This change in location of the peak radiance with change in temperature is described by Wien's displacement law,

$$\lambda_{max} \cdot T = \gamma, \tag{2.6}$$

with γ being Wien's displacement constant [17] in the transcendental equation.

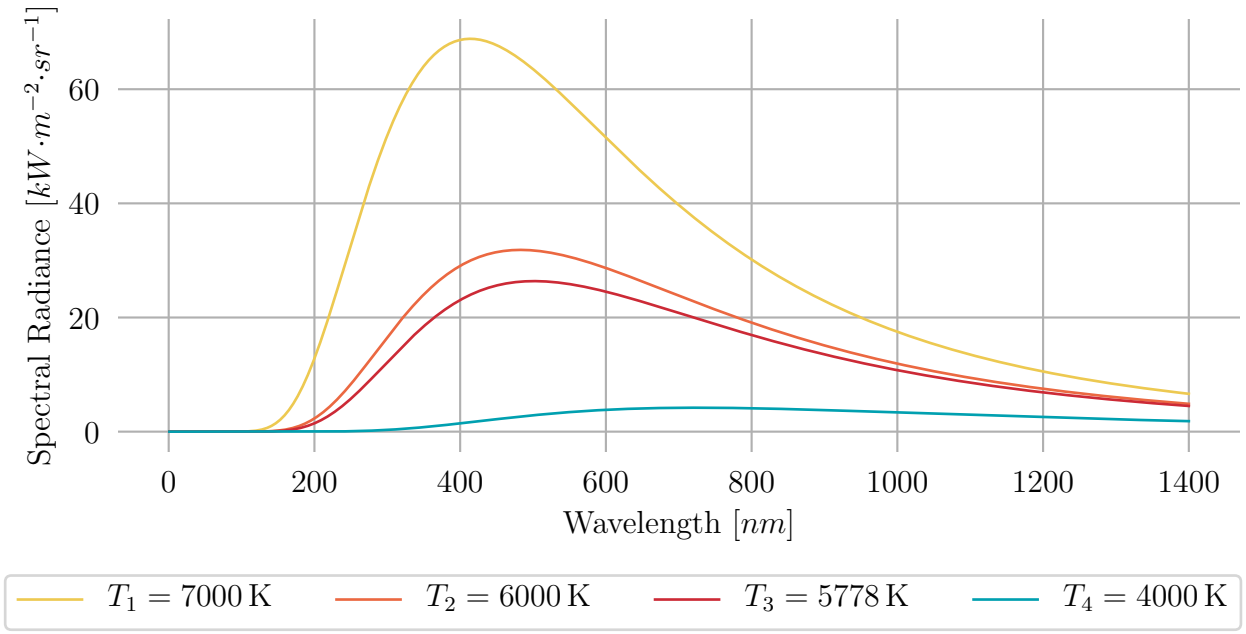

Figure 2.1: The spectral emission of a blackbody at various absolute temperatures.

Also, the power emitted between any two wavelengths can be determined (therefore also the total power emitted) through the Stefan-Boltzmann law of radiation, with σ the Stefan-Boltzman constant,

$$Power = A \cdot \sigma \cdot T^4. \tag{2.7}$$

These stated laws and their encompassing equations are adequate to calculate and interpret wavelengths around the peak in the blackbody distribution calculated through Wien's law. For wavelengths much larger than this λ_{max} in equation 2.6, the Rayleigh-Jeans approximation is required - this approximation is the expansion with a Taylor series of Planck's law. Although these longer wavelengths are not of importance in this research, it is of interest to note that this approximation provides a linear relationship between the surface temperature and spectral radiance, if the emissivity of the surface is known [18].

2.2.3 Boltzmann's Distribution

For chemical processes, and more importantly the flow of heat through radiation, Planck stated that any homogeneous state in a thermodynamic equation should be related to an equally finite number of likely arrangements in which the state can exist. It is known that the behaviour of atoms is probabilistic and that these atoms are at the origin of radiation, as well as absorption. Planck further states that each infinitesimal state change is by nature reversible but an assemblage of these minute reversible changes (processes) inevitably leads to a macro-state which is irreversible [19].

These statements by Planck are a simplified explanation of atom energy states in quantum mechanics theory and Clausius' thermodynamic laws for entropy formulation.

The first law of thermodynamics in differential form is,

$$dE = \delta Q + \delta W, \tag{2.8}$$

also called the "energy conservation law" which is applied to systems in which energy exchange consists of work and heating. Where the change in internal energy is a variable describing the state of the system thermodynamically, the work and heat only characterizes the energy transfers.

δQ (as well as δW) is in fact an inexact differential but by dividing the change in heat with the absolute temperature, and exact differential - the change in thermodynamic entropy dS - is obtained. So simply, the first law of entropy,

$$\frac{\delta Q}{T} = dS. \tag{2.9}$$

Equation 2.9 can further be interpreted by considering that system states are not dependent on path. This can also be interpreted by expanding on the parameters influencing the work such as forces, magnetization, pressure and electric polarization [16].

Following the discussion of Planck on the probabilistic nature of atoms and therefore the states of an atom and the relation to entropy, Boltzmann's equation,

$$S = k_B \cdot ln(W_p), \tag{2.10}$$

indicating the relationship between thermodynamic entropy and the number of possible probable distribution states of the atoms (or molecules) of an isolated system [16].

Boltzmann went further, relating the number of particles in the whole system as well as in each state, to the energy of these states - this is called Boltzmann's Distribution and plays an in important part in spectrometry. This distribution explains the intensity of spectral lines according to molecular mass and temperature. Although these explanations are more suited to the field of physics, it simply emphasises the effect of temperature on the spectral distribution and therefore the measurements accomplished in this research.

2.3 Solar Irradiance

Returning to a macroscopic view on energy and electromagnetic radiation, we consider the sun and the impact of the radiation it emits. Measurements and analysis of the extra-terrestrial solar spectrum have had a significant impact on our understanding of terrestrial solar radiation and the designing of solar technology.

Air mass, commonly referred to as AM only, is described as the atmospheric path length for any zenith angle relative to the above air mass. AM essentially indicates where a specific solar radiation spectrum is measured in reference to the atmosphere and sun. AM1D is or Air Mass 1 Direct refers to a location at sea level with the sun being directly overhead so that radiation passes directly through the air mass. Since extraterrestrial solar radiation does not pass through the atmosphere it is called AM0 [20].

The extra-terrestrial solar spectrum depicted in figure 2.2 (adapted from [20]) is used to determine a model basis for solar spectra since direct beam irradiance at sea level is similar in distribution to that of extra-terrestrial irradiance, with atmospheric absorption the cause of variation between the two spectrums. The solar constant or AM0 spectrum is a spectral integration of the extra-terrestrial solar spectrum over wavelengths from zero to infinity. This solar constant allows the interpretation of solar spectra at other earth-sun distances. It is known that variation in the earth-sun distance causes the irradiation incident to vary up

to approximately 7 % throughout the year; variation in solar activity can cause additional changes up to 1 % [21]. Currently the solar constant is approximated to be $1361\,W{\cdot}m^{-2}$.

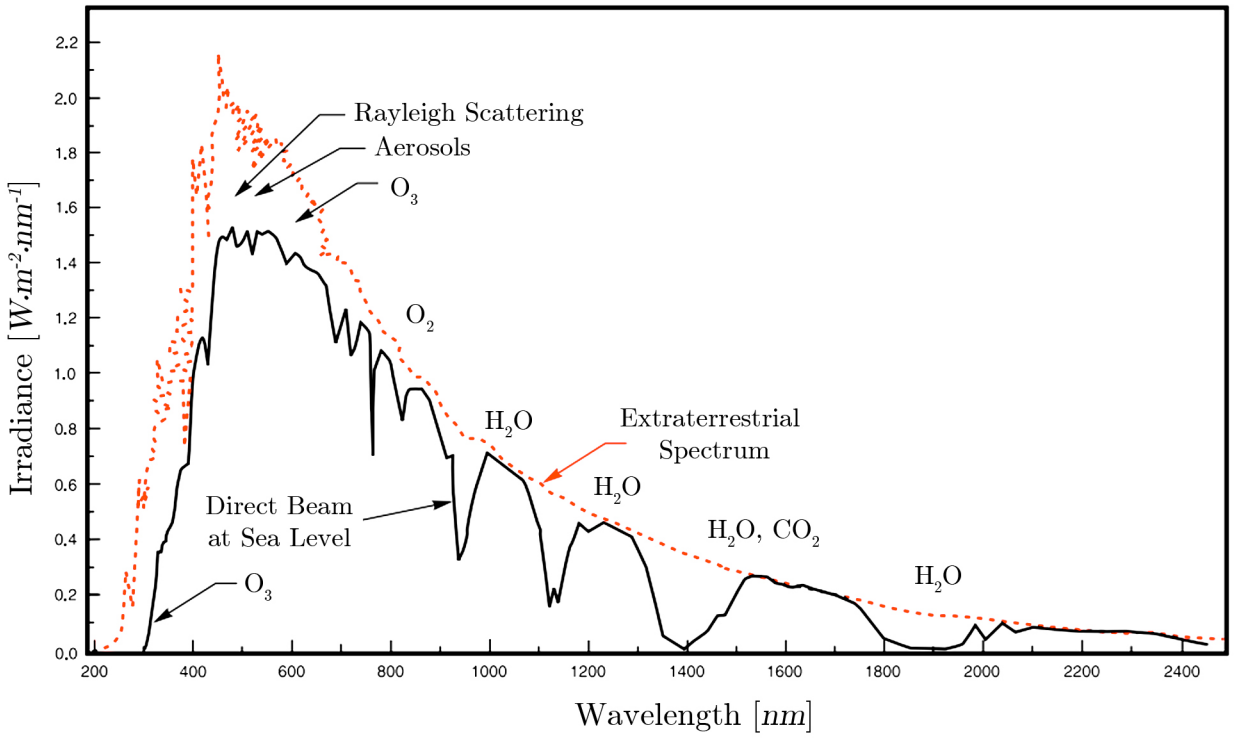

Figure 2.2: Extraterrestrial spectrum and direct radiance with general atmospheric absorption.

2.3.1 Terrestrial Radiation

As solar radiation passes through the atmosphere, the spectrum is inherently modified through absorption and scattering of particles. Wavelengths shorter than $0.19\,\mu m$ are absorbed through oxygen and nitrogen, and some selective absorption of water vapour, carbon dioxide, as well as some oxygen, is present in the near infrared band [20]. This reduces the usable terrestrial spectrum to wavelengths between 0.2 and $2.5\,\mu m$, with waveband regions Ultraviolet (UV), Visible (Vis) and Near Infrared (NIR).

An early theoretical form for direct solar spectral irradiance incident on a surface at ground level at a wavelength $\lambda_i \mu m$,

$$E_i = E_0{\cdot}D{\cdot}\tau_r{\cdot}\tau_{oz}{\cdot}\tau_g{\cdot}\tau_w{\cdot}\tau_a, \tag{2.11}$$

supplying the ground level spectral irradiance by taking into account the extra-terrestrial irradiance E_{oi} at the mean solar distance [22].

Further the integrated quantity of spectral irradiance at a corresponding wavelength,

$$E_\lambda = \sum_{i=1}^{N} E_i \Delta\lambda_i. \tag{2.12}$$

The spectral intervals $\Delta\lambda_i$ used to be supplied in tables before models where computerised. Equation 2.11 is still relevant since it shows the dependency of terrestrial irradiance on τ_r

Rayleigh scattering, τ_{oz} ozone absorption, τ_g absorption by uniformly mixed gas, τ_w water vapour absorption and τ_a aerosol attenuation.

The earth-sun distance factor is supplied from a Fourier series representation of the sun position [23],

$$D = 1.00011 + 0.034221\cos\psi + 0.00128\sin\psi + 0.000719\cos 2\psi + 0.000077\sin 2\psi, \quad (2.13)$$

with the day angle ψ,

$$\psi = \frac{2\pi(d-1)}{365}. \quad (2.14)$$

Moving temporarily from the spectral analysis towards beam analysis: the terrestrial spectrum consists of several components - direct beam radiation (I_B), diffuse radiation (I_D) from surroundings and scattered radiation from the sky. The total radiation flux incident on a horizontal surface is termed the global horizontal radiation. The incident radiation on a tilted surface is the global horizontal radiation with additional radiation from ground reflection, also called the hemispherical radiation [24].

Meteorological data usually supplies total radiation incident on a horizontal plane, so to obtain radiation on a tilted plane a correlation process is required. Quantitatively, the reflected radiation (I_{RC}) on a plane [25],

$$I_{RC} = \rho\cdot(I_{BH} + I_{DH})\cdot\left(\frac{1-\cos\beta}{2}\right), \quad (2.15)$$

where ρ is the ground reflectance, termed the albedo (typically 0.2 for ground or grass), and β the surface tilt angle from the horizontal. Albedo is in effect the relationship between upwelling radiation from the earth's surface and downwelling radiation directed toward the earth's surface. Therefore, if the surface is horizontal, β equals zero, equation 2.15 equals zero.

A more complex equation is supplied by Badescu for the monthly average daily total radiation. Equation 2.16 takes into account the ratio (R_b) of beam radiation incident to the tilted surface in respect to that of the horizontal plane. The tilted total daily radiation [24],

$$I_T = I_{BH}\cdot R_b + I_{DH}\cdot\left(\frac{1+\cos\beta}{2}\right) + H\cdot\rho\cdot\left(\frac{1-\cos\beta}{2}\right), \quad (2.16)$$

with I_H the total daily radiation incident on a horizontal plane. The ratio R_b for a surface located in the southern hemisphere, inclined towards the equator [26],

$$R_b = \frac{\cos(\varphi+\beta)\cos\delta\sin\omega_s' + \omega_s'\sin(\varphi+\beta)\sin\delta}{\cos\varphi\cos\delta\sin\omega_s + \omega_s\sin\varphi\sin\delta}, \quad (2.17)$$

where the sunset hour angle,

$$\omega_s' = min\{\arccos(-\tan\varphi\tan\delta), \arccos(-\tan(\varphi+\beta)\tan\delta)\}, \quad (2.18)$$

with φ the latitude, ω_s the hour angle from solar noon ($15°/hour$) and the declination angle [27],

$$\delta = 23.455 \cdot \sin\left(\frac{(284+d)}{365} \times 2\pi\right), \tag{2.19}$$

with n the n-th day of the year. Also, the angle of incidence,

$$\cos\theta_i = \sin\delta\cos\beta + \sin\delta\cos\psi\sin\beta\cos\theta_a + \cos\delta\cos\psi\cos\beta\omega_s - \cos\delta\sin\psi\sin\beta\cos\theta_a\cos\omega_s - \cos\delta\sin\beta\sin\theta_a\sin\omega_s, \tag{2.20}$$

with θ_a the azimuth angle. A relation for the hour angle, as supplied by Cooper [27],

$$\sin\omega_s = \frac{-\cos\alpha\sin\theta_a}{\cos\delta} = \frac{\sin\alpha - \sin\delta\sin\varphi}{\cos\delta\cos\varphi}, \tag{2.21}$$

with α the altitude angle rewritten as,

$$\sin\alpha = \sin\delta\sin\varphi + \cos\delta\cos\omega_s\cos\varphi. \tag{2.22}$$

The altitude and azimuth of the sun varies throughout the day, producing a varying angle of incidence of the collimated beam radiation on a surface, either horizontal or tilted. The solar zenith angle (θ_z) is equal to the direct solar incident angle upon a horizontal surface, which is the complement of the solar elevation (altitude). Therefore, the global horizontal radiation (I_G) according to Lambert's cosine law[24],

$$I_G = I_{BH}\cdot\cos\theta_z + I_{DH} = I_{BH}\cdot\sin\alpha + I_{DH}. \tag{2.23}$$

Equation 2.24 is adapted for a tilted surface,

$$I_G = I_{BH}\cdot\cos\theta_i + R_d\cdot I_{DH} + I_{RC}, \tag{2.24}$$

with θ_i the angle of incidence on the normal of the tilted surface and R_d an estimated reduction factor for direction dependant scattering. This reduction factor is an estimated ratio determined through multiple models in literature [26].

Irradiance is defined as the power, or radiant flux, received by a surface per unit area in $W\cdot m^{-2}$, also called insolation. To determine the spectral response of the glass samples and the dust deposit the spectral irradiance is investigated - defined as the irradiance on a surface per wavelength in $W\cdot m^{-2}\cdot nm^{-1}$. Specifically, with irradiance measurements, it is important to ensure that absolute irradiance is measured which results in accurate distribution and magnitude measurements of the spectrum.

A simple half sine model can be used to calculate clear-day solar irradiance, especially to predict solar irradiance under these conditions [28],

$$I = I_{noon}\cdot\sin\left[\frac{180\cdot(t - t_{sunrise})}{t_{sunset} - tsunrise}\right], \tag{2.25}$$

in degrees, with t the time in hours of a 24 hour-clock.

Determining the exact sun location is important in any solar application - it is even more essential when the spectral distribution of solar irradiance is measured, as in this research.

2.3.2 Solar Radiation Measurement

Traditionally in PV research, solar irradiance transmission through the atmosphere is measured either by a pyrheliometer for direct radiation measurements, or a pyranometer for diffuse and global radiation measurements [29]. These measurements supply the power density for a defined area - the amount of irradiation in $W{\cdot}m^{-2}$ but to determine the spectral content of this incident light requires a spectrometer. Predominantly, spectrometry is applied to the analyses of absorption, reflectance and transmission [30]. These measurements are well suited to laboratory studies but field solar spectral measurements are observed in oceanography [31], atmospheric studies [32] and other fields of biology, physics and chemistry [33].

Spectrometry is very applicable to PV research since the cells are responsive to a specific spectrum range. This responsiveness is characterised by the transport in material, thickness of the cell and band gap [34]. Spectrometry for solar irradiation can further be classified as spectroradiometry since it is the measurement of radiant power impinging on a surface per unit area in the UV, VIS and NIR wavelength range.

Some methods and metrics do exist to apply conventional measured solar data to allow more detailed information regarding the solar conditions. One popular used metric to indicate the spectral quality and distribution of irradiance is the Average Photon Energy (APE) in electron-Volts (eV) [35],

$$APE = \frac{\int_b^a E(\lambda)d\lambda}{q\int_b^a \phi(\lambda)d\lambda}. \tag{2.26}$$

This APE allows for spectral characterisation that is device independent and is simply the integrated broadband irradiance (E) divided by the integrated photon flux density (ϕ). A standard value for APE with AM 1.5, obtained from the total spectrum range of $0.35 - 1.05\,\mu m$, is calculated as $1.88eV$. If the total solar spectrum ($0.28 - 4.00\,\mu m$) is used in obtaining the APE value, it is equal to a lower $1.60\,eV$. A higher value is obtained for the smaller spectrum range since a greater amount of energy is contributed from these specific ranges, the VIS and NIR ranges [36].

This APE parameter varies as the type of light varies, which consequentially varies with atmospheric composition, i.e. the time of day, year and atmospheric constituents. APE therefore quantitatively indicates the atmospheric attenuators and influencers as discussed previously. The APE could also be described as the measure of blueness of a spectrum and so it could be expected that a higher APE value would be beneficial to PV devices that have a higher bandgap and therefore absorb more in the blue spectrum section. Also, since materials with a lower bandgap have a broader spectral response, they would not be as sensitive to the spectrum [34].

2.4 Meteorological Sky Conditions

According to Berger [37] there is a definite difference between mostly cloudy and overcast - all organizations worldwide have weather definitions for both sky states. From this we assume that cloudy conditions refer to the sky being covered with at least 50 % of clouds. Mostly cloudy is specified as the being covered with $80 - 90\,\%$ cloud coverage. Overcast is when the sky is almost completely covered with clouds - a dull looking, grey sky. This definition of overcast still does not technically specify how we could differ between an overcast and mostly cloudy sky. A meteorologist [38] describes a mostly cloudy sky as one in which the

clouds are outweighing the sunlight but there are occasional shifts in the clouds in which blue sky could be seen. It is said that the individual clouds, or cloud elements are clearly discernible and has definition. Now in contrast, an overcast sky is defined as a grey cloud layer that is uniform and widespread; it could also be said to be featureless. So even though to most these two concepts are assumed to be the same the contrasting description given above supplies a helpful distinction to describe environmental measuring conditions more appropriately.

2.4.1 Atmospheric Attenuation

Cloud coverage has a complex effect on solar irradiance but this is also not the singular cause for atmospheric attenuation. Multiple factors, as discussed below, influence how solar irradiance is attenuated in the earth's atmosphere.

2.4.1.1 Clouds

The absorption by clouds can directly be described through the amount of water vapour present in the atmosphere. Similar to extra-terrestrial absorption, absorption by specific elements in the earth's atmosphere affects specific wavelength bands more than others. Water vapour absorption is mostly located at the wavelength bands of $724\,nm$, $824\,nm$, $937\,nm$ and $1120\,nm$, with liquid water absorption beyond. It should also be noted, that although clouds can cause absorption it can also cause irradiance enhancement from multiple reflections from the clouds themselves as well as the enhanced reflectivity of the earth's surface. Enhancement of irradiance caused by cloud coverage has been shown to increase certain areas, or bands, within the spectrum; usually the increase is seen predominantly in the UV and VIS regions [39].

This enhancement of irradiance could specifically be advantageous to photovoltaic cells with good response in these enhanced areas in the spectrum and increases the complexity of determining the standard output references for photovoltaic devices. The effect of clouds on solar irradiance transmission is complex but it is suggested that clouds act as a neutral-density filter up to $0.72\,\mu m$, and beyond absorbs radiation in selective bands [39]. When acting as a neutral-density filter it modifies the intensity of all wavelengths equally. It is also known that clouds inevitably degrades the signal to noise ratio of the spectrometer since it significantly attenuates irradiance - this is typically observed in wavelengths longer than $1.1\,\mu m$ [30].

The reduction of extra-terrestrial solar irradiance by the atmosphere is approximately 30 % on very clear days and up to 90 % on very cloudy days [40]. It has been suggested by Nann et al.[39] that spectral normalization for cloudy sky conditions is possible, specifically by reducing the bulk attenuation. Spectral normalization,

$$I_{ref}(\lambda) = \frac{measurement(\lambda)}{clear - skysimulation(\lambda) \cdot N360}, \tag{2.27}$$

with a reference value of $630\,nm$,

$$N360 = \frac{measurement(630\,nm)}{clear - skysimulation(630\,nm)}. \tag{2.28}$$

This reference value was assumed since at this wavelength the spectrum is not influenced by water vapour absorption, also the scattering by particles are less predominant than in shorter wavelengths.

2.4.1.2 Air Mass

The effect of atmospheric absorption is substantial and therefore the solar zenith angle is a critical parameter. The air column density increases as the zenith angle increases from the vertical - therefore the water vapour increases. At a large zenith angle, for example at 9 AM, the amount of water vapour in the path of radiation is still significant and might increase variability and distortion in the spectrum measurements [30].

In other words, air mass (AM) has a noteworthy influence on spectral variation. This spectral variation is also noted throughout the year because of the Earth's elliptical trajectory. In winter months, the solar radiation path to the ground is increased, or rather the AM is increased, and a range increase in the higher wavelengths is observed (also called a red shift) [10]. Similarly, it can be expected that the observed spectrum will be more red in mornings and bluer in the afternoon.

Returning to equation 2.11, the effect of ozone absorption on ground surface spectral irradiance can be described by the transmittance function,

$$\tau_{oz} = exp(-k_o(\lambda) \cdot l \cdot m), \tag{2.29}$$

takeing into account variation in latitude as well as the seasonal variation by the absorption coefficient k and the normalized amount of ozone in the vertical column l.

Next the critical parameter air mass can be calculated. The relative optical air mass [41],

$$m(z) = \frac{m_{abs}(z)}{m_{abs}(90°)}, \tag{2.30}$$

with z the solar elevation and the absolute air mass,

$$m_{abs}(z) = \rho_0 \int_0^\infty \left(\frac{\rho}{\rho_0}\right) \left(1 - \left[1 + 2\delta_0 \left(1 - \frac{\rho}{\rho_0}\right)\right] \times \left[\frac{\cos z}{(1 + h_{sea}/R_{earth})}\right]^2\right). \tag{2.31}$$

The optical parameter $\delta_0 = n_0 - 1$, with n_0 the refractive index of air at $0.7\,\mu m$ and a height of zero, which is not a mechanical quantity.

A further approximation for air mass is also supplied by Kasten [41],

$$AM = \frac{1}{\cos\theta_z + 0.50572(96.07995 - \theta_z)^{-1.6364}}, \tag{2.32}$$

in terms of θ_z, the zenith angle in degrees, where $AM = 37.92$ at sunset ($\theta_z = 90°$). The AM is calculated in equation 2.32 by a reducing ratio of the local air pressure to standard atmospheric pressure at sea level. Since the elevation angle z can merely be described as $90° - \theta_z$, Hankin supplies a simplified equation to estimate the air mass [42],

$$AM = \frac{1}{\sin z}. \tag{2.33}$$

The simplification to equation 2.33 is useful when observing table 2.1 [43]. This table shows the association between a decreased solar elevation angle and the increase in atmospheric absorption and Rayleigh scattering. Further, it can be noted that a range of values is supplied for Mie scattering - this value is strongly dependant on location and the number of air-borne particles subsequently involved.

Table 2.1: The dependancy of irradiance on the elevation angle and the relating percentage losses.

z	AM	Absorption	Rayleigh	Mie	Overall
90°	1.00	8.7 %	9.4 %	0 - 25.6 %	17.3 - 38.5 %
60°	1.15	9.2 %	10.5 %	0.7 - 29.5 %	19.4 - 42.8 %
30°	2.00	11.2 %	16.3 %	4.1 - 44.9 %	28.8 - 59.1 %
10°	5.76	16.2 %	31.9 %	15.4 - 74.3 %	51.8 - 85.4 %
5°	11.50	19.5 %	42.5 %	24.6 - 86.5 %	65.1 - 93.8 %

More information regarding Rayleigh and Mie scattering is supplied in the paragraphs to follow. Noting again, the overall reduction cannot exactly be predicted since local weather conditions will further ensure a greater reduction in irradiance.

2.4.1.3 Atmospheric Particles

A secondary form of attenuation is found in the atmosphere that scatters and absorbs solar radiation; this attenuation is by the atmospheric aerosol content. The aerosol content comprises of fine particles either in solid or liquid form which is either natural (e.g. fog) or artificial particles (e.g. dust). The distribution of these particles as well as their composition, shape and size influence the transmission.

Fundamentally the effect of aerosol extinction cannot be quantified because of its complex nature but the power law function for aerosol attenuation is usually considered,

$$\tau_a = exp\left(-\beta_T \cdot \lambda^{-w} \cdot m\right), \tag{2.34}$$

with the constant w the wavelength coefficient and β_T the turbidity coefficient. Looking at Mie theory regarding the extinction of particles and the dependency of extinction by wavelengths, some discrepancies have been found in experimental research and the wavelength coefficient is used to account for these discrepancies. Usually the constant value selected is $0.8 \leq w \leq 2$.

The turbidity coefficient, relating to the haziness of the atmosphere is described in terms of Ångstrom's turbidity coefficient [22],

$$\beta_T = \beta_{T0} \cdot 0.5^{w-1.3}, \tag{2.35}$$

at an optical thickness $\lambda = 0.5\,\mu m$.

Without going into too much detail further, the turbidity of the atmosphere will vary continuously either because of natural incidents or by artificial means, which increases over time through an increase in pollution. The average value used for turbidity varies in literature since measurement conditions and selections vary significantly.

Perhaps the most important conclusion to be drawn from atmospheric attenuation research is that its complexity lends itself to the use of empirical models rather than quantitative models and even more importantly that atmospheric attenuation by particles does have an effect on solar irradiance, more specifically the spectral content of the solar irradiance.

2.4.2 Rayleigh Scattering

The atmospheric scattering, or Rayleigh scattering, defines the interaction between particles smaller than the radiation wavelength they react with; Rayleigh scattering is a more specific discussion on atmospheric attenuation by particles. The effect produced by the interaction of light and these small particles is explained through the constant phase of the radiation across the entire particle [18]. Interaction of larger particles, such as aerosols, leads to Mie scattering as well as absorptive extinction. The portion of light that either reaches earth or reflects into space is defined by the balance between these two scattering processes mentioned above [34].

For equation 2.11, the spectral irradiance, the Rayleigh scattering transmittance function is,

$$\tau_r = exp\left(-0.008735{\cdot}\lambda^{-4.08}{\cdot}m{\cdot}\frac{P}{P_0}\right). \tag{2.36}$$

Further, in summary, for Rayleigh scattering the cross-section of a molecule is supplied by Rees [18],

$$\sigma_s = \frac{128{\cdot}\pi^5{\cdot}a^6}{3{\cdot}\lambda^4}, \tag{2.37}$$

taking into account the effective molecule radius a, approximated as a conducting sphere.

In effect, any scattering of light by particles smaller than the wavelength itself is defined as Rayleigh scattering and is therefore not exclusive to atmospheric scattering. The light scattered by Rayleigh scattering is predominantly blue light, especially Rayleigh scattering in the atmosphere since blue light has a similar wavelength range to that of the particles - this is often called the λ^{-4} dependence. This scattered blue light in affect to Rayleigh scattering has no specific scattered direction and is therefore called diffuse light.

Rayleigh scattering can be described through equations to determine dissipated power and polarizability but extends beyond the scope of this research. From the discussion above it can be assumed that Rayleigh scattering can also be expected under clear-sky conditions since atmospheric particles are always present.

2.4.3 Fraunhofer lines

As mentioned previously, the solar spectrum distribution is characterized significantly by selective absorption and reflection. Ozone absorbs significantly at wavelengths shorter than $400\,nm$ [30], whereas water vapour has absorption bands in NIR and SWIR, with the first absorption band at approximately $1360\,nm$, which falls outside the range of interest for this research.

Spectral lines allow the characterization of atomic components within a light source and since the sun is to an extent a well-studied light source, most absorption (or spectral) lines can be noted already. Table 2.2 lists the elemental absorption per wavelength as characterized by

Fraunhofer. Absorption mostly occurs in the sun photosphere, with the exception of symbols A, B, a, y and Z which indicates the absorption of O^2 in the earth atmosphere [44].

Table 2.2: Fraunhofer lines at respective wavelengths.

Symbol	Element	$\lambda[nm]$	Symbol	Element	$\lambda[nm]$
y	O_2	898.8	c	Fe	495.8
Z	O_2	822.7	F	H_β	486.1
A	O_2	759.4	d	Fe	466.8
B	O_2	656.7	e	Fe	438.355
C	H_α	656.3	G'	H_ψ	434.0
a	O_2	627.7	G	Fe	430.8
D_1	Na	589.6	G	Ca	430.8
D_2	Na	589.0	h	H_δ	410.2
D_3	He	587.6	H	Ca^+	396.8
E_2	Fe	527.0	K	Ca^+	393.4
b_1	Mg	518.4	L	Fe	382.0
b_2	Mg	517.3	N	Fe	358.0
b_3	Fe	516.9	P	Ti^+	336.1
b_4	Fe	516.8	T	Fe	302.1
b_5	Mg	516.7	t	Ni	299.4

The absorption and Fraunhofer lines are used to characterize spectral measurements - the varying peaks and valleys in an irradiance spectral distribution can be ascribed to some form of absorbance rather than a measurement error. The Fraunhofer is applied in the measurement section of this research.

2.5 Dust

The quality of air surrounding us is aggravated by natural and increasingly, human processes. Unsurprisingly the effect of dust deposition is more critical in arid environments where geological corrosion causes an increase in airborne soil. Both organic and inorganic dust are known to settle on surfaces when the wind settles, and could be airborne again with an increase in wind speeds. Settled dust particles could adhere to a surface due to humidity, dew and other forms of vapour creating formations of dirt layers on the surface in question. The amount and size of these deposited particles therefore not only depend on the environment in which it is located but also how the environment influences particle adhesion to surfaces. This would mean that the tilt angle of the surface as well as the characteristics of the surface material in conjunction to the environmental factors would influence the degree of particle adhesion. The deposition of particles is often referred to as a "soiling" effect [1].

2.5.1 Particle Characterisation

Since dust includes a broad range of inorganic and organic contaminations several properties of the particles are relevant: size and shape, its charge distribution and surface energy, the composition of the dust layer as well as its biological characteristics. Deposited particles on modules interfere with spectral transmission by mitigating and scattering irradiance possibly decreasing the beam intensity - this is called extinction [45]. The scattering of radiation by particles is defined by the ratio between the particle diameter and the incident wavelength,

$$\alpha_{scatter} = \frac{\pi \cdot d_{particle}}{\lambda}. \tag{2.38}$$

From this ratio in equation 2.38 it can be inferred that if the particle is significantly larger than the wavelength, the scattering will not be affected by variation in the wavelength [45]. So, it could be said that very large particles cause wavelength independent scattering and absorption - this is called non-selective absorption [18].

Dust is often used as a common term for particles with a diameter smaller than $500\,\mu m$. It has been found that the deposition of finer dust, versus coarser particles, has a greater adverse effect on module performance. Finer particles have the tendency to distribute more uniformly, whereas larger particles leave voids where light can still pass through but the light passing through these beneficial voids is inconsistent and an effect similar to that of partial shading is possible [46].

2.5.2 Distribution Mechanics

In discussing the accumulation of particles on a surface it is perhaps necessary to first exclude the influence of the meteorological conditions and focus on how the adhesion mechanics relates to the circumstances which determines the amount and type of particle accumulation on the surface.

Firstly, the scenario where the surface - or more specifically the glass covering of the PV module - has a tilt angle of 0° and is therefore faces directly upwards. The adhesion mechanic primarily responsible for dust deposition in this scenario is gravitational settling. Secondly, a scenario where the surface is at a vertical position, with a tilt angle then of 90°, the deposition of particles on the surface will be caused by diffusion. These scenarios, and all tilt angles in between, can simply be described by the movement of aerosol particles. Unlike gas molecules which rebound with surface interaction, aerosol particles adhere to a certain degree.

It is assumed that under stable meteorological conditions - slight to no wind and little moisture - this surface at a tilt angle of 0° will experience the highest rate of dust deposition. This is assumed since larger particles will settle on the surface. According to Hinds [47] the cumulative deposited particles (per unit area of the surface),

$$N(t) = 2 \cdot N_0 \cdot \left(\frac{D_c \cdot t}{\pi}\right)^{0.5}, \tag{2.39}$$

per a duration of time. Equation 2.39 assumes that the particles will maintain its initial uniform concentration, but it still supplies a functional prediction of the number of particles depositing on a surface. The diffusion coefficient,

$$D_c = \frac{k_B \cdot T \cdot C_c}{3 \cdot \pi \cdot \eta \cdot d_{particle}}, \tag{2.40}$$

showing that particle size is the most describing factor of particle or aerosol behaviour. Equation 2.40 also takes into account Boltzmann's constant k_B, the environment temperature T, the Cunningham correction factor C_c to account for non-continuum characteristics and the viscosity η of the environment. It is important to note that the Cunningham correction factor also relies on the particle diameter. The relation between particle size and diffusion or settling on a horizontal surface is described in table 2.3, from equations 2.39 and 2.40 [47].

Table 2.3: The cumulative deposition density on a horizontal surface under standard conditions in a time of 100 s.

Diameter [μm]	**Diffusion** [number·m^{-2}]	**Settling** [number·m^{-2}]	**Ratio** Diffusion/Settling
0.001	2.6×10^4	0.68	3.8×10^4
0.01	2.6×10^3	6.9	380
0.1	3.0×10^2	88	3.4
1.0	59	3500	1.7×10^{-2}
10	17	3.1×10^5	5.5×10^{-5}
100	5.5	2.5×10^7	2.2×10^{-7}

The summarising table supplied above is only for use under controlled conditions but since deposition becomes more complicated when the environment is turbulent and variant, the ratio still supplies some knowledge to how particle diameter influences the deposition method.

Even though turbulence (wind) in the environment is challenging to quantify, it is known that the wind can remove some particles from the surface - even more so if the wind speed is relatively high and the surface has a high tilt angle [1]. Since the effect of the adhesion of the particles to the surface is a factor of the particle diameter, removal of the particles by wind becomes less probable - the removal force is less than the adhesion force.

Since the adhesion of particles are determined by the settling mechanism as well as the surface particulars, one would like to conclude that textured cover glasses would increase the adhesion between the particles and the glass cover, but Piliougine et al.[48] has shown that it has in fact no influence and would therefore respond to particle adhesion, similar to adhesion on non-textured glass. The particulars of textured and patterned glass surfaces are discussed in the following sections.

2.6 Photovoltaic Modules

Photovoltaics, as well as concentrated solar thermal technologies, have some type of glass included in the construction - either to protect or to induce absorption or reflection, as in the case of thermal reflectors and concentrators. In thin-film modules the glass is the substrate to which the photovoltaic material is attached - whereas in the crystalline silicone technologies the glass merely serves as protection for the solar cells of the module. Throughout this research the focus is primarily on the glass coverings used in these crystalline silicon modules.

2.6.1 Efficiency

Crystalline solar cells consist of two silicon layers - the sun facing layer is doped negatively with phosphorus while the back layer is doped positively with boron. Sun light falling on the cell leads to the separation of charge carries which if connected to any load, will supply current through the cell metal contacts to the load. These metal contacts are applied to both sides of the solar cell, often causing shading within the cell array, contributing to 3 % loss in incident energy converted. The recombination of electrons and holes contributes another 8.5 % loss. Another 20 % loss is ascribed to the potential gradient in concentration in the depletion region where the electrons combine with the holes. Adding these aforementioned losses with the ohmic losses, 32 % losses are already revealed. Further, high photon

energy in the short-wave spectral band contributes 30 %, and low photon energy in the long-waveband another 22 %. This leaves only 16 % of useable converted electrical energy [43]. Naturally, these are only approximations and could differ for varying circumstances, modules and manufacturers.

Although the solar spectrum constitutes of wavelengths $0.2-2.5\,\mu m$, the longer wavelengths are limited by the band gap of the cell material and the short waves are limited by material absorption [49]. These limitations by the cell material can be ascribed to the energy of the photon: if the photon's energy is less than that of the band-gap energy (E_g) the photon cannot be absorbed by the cell material but merely transmitted, or if the photon's energy is more than that of E_g it can excitate another electron-hole pair, or a carrier-carrier pair which will scatter the electrons - this is called the Shockley-Queisser Efficiency Limit and is attributed to the aforementioned 22 % and 30 % loss in the solar cells [21].Therefore the wavelength range under investigation is limited to $0.3-1.1\,\mu m$, where reasonable resolution is required.

The solar module and even the system connections, such as converters and cables, all further contribute to overall losses. The system losses can only be approximated, but the cell and module losses at Standard Test Rate Condition, as stated in the next section, can be calculated. The efficiency of a cell or module is based on the amount of radiation from sun that can be converted to electrical power output. Therefore, the efficiency [43],

$$\eta = \frac{P_{MPP}}{A{\cdot}I} = \frac{FF{\cdot}V_{OC}{\cdot}I_{SC}}{A{\cdot}I}. \tag{2.41}$$

The area, A in equation 2.41 can either refer to the area of the cell (to calculate the cell efficiency) or the area of the module (to calculate the module efficiency). P_{MPP} is the maximum power at the maximum power point at standard conditions. This power can be calculated from the fill factor (FF), that describes a quality standard of the solar cell; this value is usually $0.5-0.85$. The open-circuit voltage, V_{OC}, is the measured voltage when the solar cell is not connected to a load; the short-circuit current, I_{SC}, is the measured current that the solar cell will provide when the two connections are directly joined.

Further, a nominal efficiency can be calculated for a cell or module, to calculate the efficiency of that specific cell or module under specific temperature and irradiance conditions. Under the standard conditions of the module, the efficiency approximation will be supplied, also called the nominal efficiency,

$$\eta_n = \eta_{STC} = \frac{P_{MPP(STC)}}{A{\cdot}1000[W{\cdot}m^{-2}]}. \tag{2.42}$$

Lastly, the efficiency at a specific irradiance and temperature is,

$$\eta = \eta_n - \Delta\eta. \tag{2.43}$$

The equations above are standard ways of monitoring the efficiency of modules and solar plants - monitoring the open-circuit voltage and short-circuit current supplies knowledge to how the module is faring under varying conditions, since the module will in fact rarely operate under standard conditions.

2.6.2 Spectral Response

Sellers and consumers of PV modules sell and buy modules in accordance to energy units - so in effect the rated output power of the module determines its price. The estimated performance of the module is also supplied in the form of a ratio called the Performance Ratio: the ratio of the theoretical energy generation considering the power rating to the actual energy yield. The module's efficiency significantly depends on the conditions under which it is evaluated in operation and because of this dependency standardisation was required. Standard Test Conditions (STC) provides the standardisation for the efficiencies of cell and modules.

The STC is merely a guideline and only simulates the conditions under which modules will operate. Table 2.4 states the conditions and their values at STC, as well as the rarity of actual operating conditions being similar to that of STC [34].

Table 2.4: Discrepancy between true outdoor conditions and STC.

Condition	Percentage (Time Satisfied)
Module Temperature $(25 \pm 2)°C$	8.8 %
Irradiance $(1000 \pm 50) W \cdot m^{-2}$	2.9 %
Spectrum $(AM1.5G \pm 0.1) eV$	1.2 %
Temperature AND Irradiance	0.1 %
Temperature AND Irradiance AND Spectrum	0.0 %

Combining the idea that the operating conditions have a significant influence over the response of the module, and Planck's equation as discussed in section 2.2.2, spectral response is,

$$SR_\lambda = \frac{q \cdot \lambda}{h \cdot c} \times QE_\lambda. \tag{2.44}$$

The external quantum efficiency (QE_λ) is the probability of a photon, of a specific wavelengths, being converted to supply an electron to the cell [34]. Therefore, it can be said that the spectral response is determined from the characteristics of the cell; the thickness of the cell, the band gap and the transport in cell material influences the likelihood of a photon supplying an electron.

In essence, the band gap energy is the minimum required for an electron to break away within a semiconductor. The band gap energy of silicon is determined as $1.12\,eV$ [50]. The energy required for these electrons to break away in a silicon solar cell, is supplied by the sun, therefore from equation 2.1 and 2.2, the band gap energy corresponds to the wavelength of the energy band,

$$E_g = \frac{h \cdot c}{\lambda_g}. \tag{2.45}$$

Observing the photon energy plot, figure 2.3 - at approximately $1.1\,\mu m$ the photon energy is $1.12\,eV$ and therefore it can be said that all photons with a wavelength less than $1.1\,\mu m$, will have enough energy to excite an electron within the silicon material.

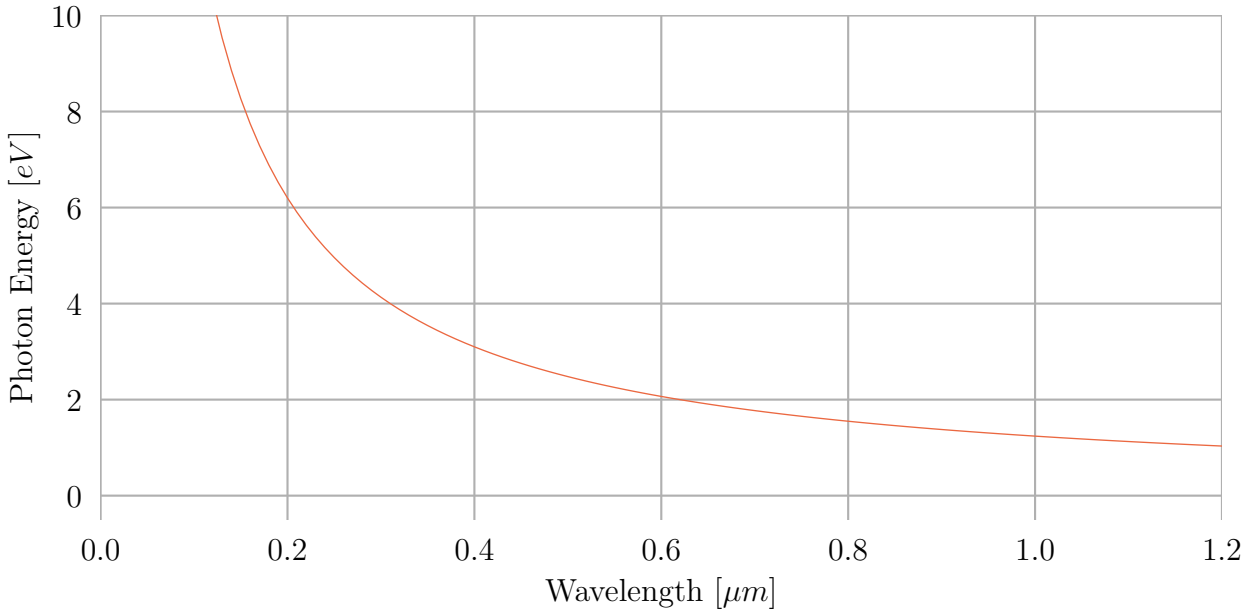

Figure 2.3: Photon energy plot from Planck's equation.

Several methods of determining the spectral response and quantum efficiency of solar cells are available. The spectral response of mono-crystalline silicon (mono-c-Si), ploy-crystalline (poly-c-Si) and amorphous silicon (a-Si) is shown in figure 2.4. The mono-c-Si cell was measured by a photovoltaic calibration laboratory and the amorphous and poly-crystalline cells were measured through the use of polychromatic filters by [51].

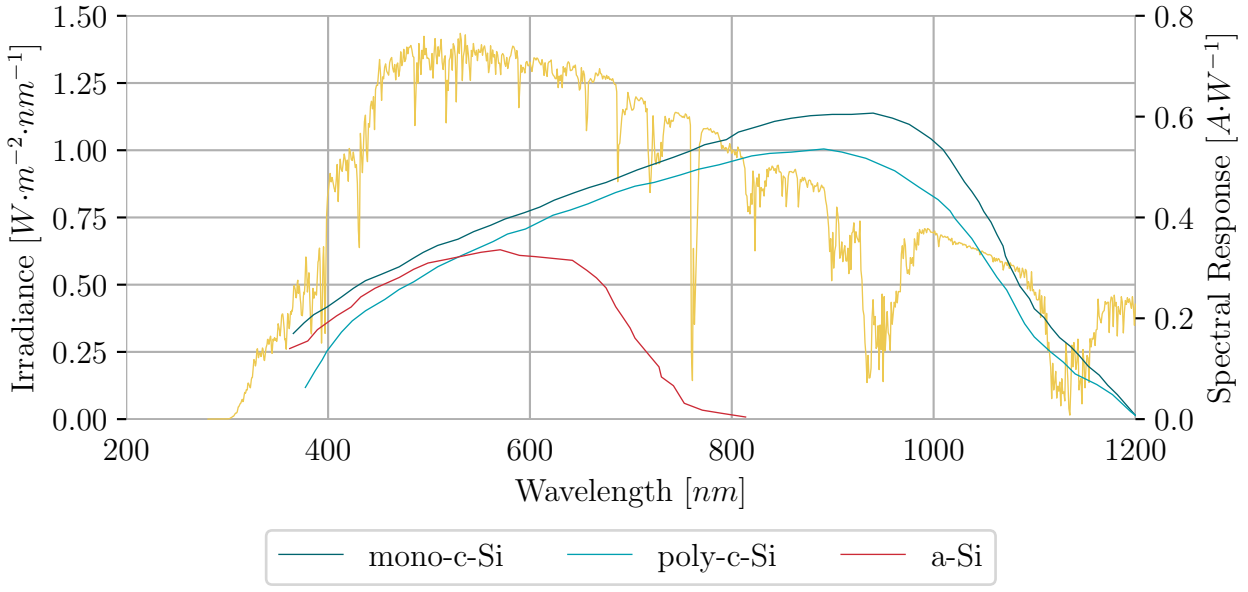

Figure 2.4: AM1.5 reference spectrum and the spectral response of three different silicon solar cells.

It should be noted that newer generation photovoltaic technologies, such as the amorphous silicon cells, have a narrower response to the irradiance incident on them, as seen in figure 2.4, the amorphous crystalline cells. This observation gives some evidence to the increasing importance of spectral measurement in the photovoltaic field. Also, from the analysis of

spectral response of photovoltaic modules and the market available measuring equipment, the wavelength range under investigation is limited to $0.3 - 1.1\,\mu m$, where reasonable resolution is required.

2.6.3 Solar Glass

Mono- and polycrystalline cells are encapsulated between a sheet of glass and an EVA (Ethyl Vinyl Acetate) layer. This encapsulation process ensures that the electrical connections in between the solar cells are protected from corrosive progressions as a result of water or dust particles; it also ensures isolation of the cell string. The top layer of encapsulation of crystalline modules is often called solar glass.

Typically, clear glass with low-iron oxide (FeO) content is used for solar applications. According to the solar glass patent [52], glass categorized as low-iron float glass has consistent high visible, high infrared, as well as, high total solar transmission throughout the glass sample. The glass composition is made through the float process to ensure that FeO is low in the formed glass as to ensure the previously mentioned characteristics. The solar glass can be either patterned or not patterned, even though it changes how light is transported through the material. The result from patterning the surface of the glass is that the incident light is diffracted; continuing to the semi-conductor material at angles to increase the path length. These patterned surface may have a surface roughness of approximately $0.1 - 1.5\,\mu m$, between crests and valleys [52]. The float process produces glass of a uniform thickness and a flat surface; we can assume that its surface roughness will be less than $1.5\,\mu m$, since this is the maximum surface roughness for patterned glass.

To increase the performance, both glass types might also include anti-reflective coatings. For additional coatings, roughness range is $0.16 - 2.5\,\mu m$, depending on the cover, process and the impurities of the substrate. Either an anti-reflective coating or patterning is often implemented to improve module performance, by reducing reflection losses. Texturing the glass not only allows for longer optical transmission paths but also allows for light trapping which is particularly effective for non-textured solar cells. For textured high-efficiency solar cells, eliminating reflection with a coating is more effective.

Adding a patterned surface or an anti-reflective coating to the solar glass seems like a straightforward solution to increase the efficiency of the module without changing the inherent character of the solar cells; one should ask how these additions to the surface will influence the adhesion of dust particles.

The patent for one textured surface design by Blieske et al.[53] supplies a solution: retaining a smooth surface on the light receiving side to minimise dust adhesion, but increasing the optical path by adding a rough etching in the shape of pyramids or cones at the cell side of the glass covering. Many other texture designs are available - some more efficient in repelling dust adhesion that other. However, recently researchers have started incorporating natural designs into these textures - using plant epidermal cell replicas to create omnidirectional light collecting surfaces from glass plates, with a broad spectral range [54].

To describe the properties of the glass in terms of the laws of reflection and refraction, it should be shown that glass is in fact optically smooth. From equation 2.50 and a wavelength range of $0.1 - 1.1\,\mu m$, table 2.5 summarises the expected range of roughness. From this it is concluded that the same glass sample can be considered as either optically smooth, or not, according to the wavelength and the angle of the incident light.

Table 2.5: Range of roughness at a specific wavelength and incident light angle.

Angle [°]	**Roughness** [μm]	
	$0.3\,\mu m$	$1.1\,\mu m$
45	0.053	0.194
85	0.430	1.578
89	2.149	7.879

If the light beam is always incident on the surface at an angle of 90° on a glass sample that is either patterned or non-patterned, we can assume that the sample is optically smooth from equation 2.50. Although we assume an incident angle of 90°, it is recognised that this will rarely be the case for natural occurrences of radiation.

The optical properties of glass - reflection, absorption and transmission - is not constant but subjective to the thickness of the sample, the surface conditions, the angle of incident light, temperature, as well as the spectral distribution of the radiation. Even though these parameters modify the optical properties, they do not change the frequency of the radiation.

2.6.4 Propagation of Light

Glass is a commonly used solid dielectric and the response of this dielectric nature of the material to an electromagnetic field is important in discussing scattering, absorption, dispersion and reflection. Before light propagation can be examined, the nature of the dielectric material, in this case glass, should be considered.

An explanation is: the heterogeneity of an obstacle, which an electromagnetic wave is incident on, determines the characteristics of scattering (and absorption) of that wave. In this case the obstacle is considered to be the particles of which the glass is comprised. The electric charges inherent to this obstacle are set into motion by an electric field when it is illuminated by the electromagnetic wave [55].

Considering Maxwell's equations, without going into first principles of isotropic dielectrics in a free space, the absolute index of refraction is,

$$n = \frac{c}{v} = \sqrt{\frac{\epsilon\mu}{\epsilon_0\mu_0}}, \tag{2.46}$$

simply supplying a ratio between the speed of an electromagnetic wave in vacuum, to the nature of the matter; this is further expanded by considering the permittivity ϵ and permeability μ of the matter. The permittivity of free space is $\epsilon_0 = 8.8542 \times 10^{-12}\,C^2{\cdot}N^{-1}{\cdot}m^{-2}$ and the permeability of free space is $\mu_0 = 4\,\pi \times 10^{-7} N{\cdot}s^2{\cdot}C^{-2}$ [56]. For this research, it is enough to only recognise that the permittivity is an indication of the electrical behaviour of the matter and the permeability describes the response of the matter to a magnetic field.

Furthermore, the characteristic nature of matter can be simplified by the use of the dielectric constant,

$$K_e = \frac{\epsilon}{\epsilon_0}, \tag{2.47}$$

and the relative permeability,

$$K_m = \frac{\mu}{\mu_0}. \tag{2.48}$$

Equation 2.46 can therefore be simplified to Maxwell's relation,

$$n = \sqrt{K_e}, \tag{2.49}$$

since most materials, and specifically glass is only weakly magnetic and therefore $K_m = 1$. K_e is strongly wavelength dependant since it supplies an indication of the speed of light through the matter and therefore the refraction index n will also be wavelength dependant. This dependency of wavelength is called dispersion. The special case where $n = 1$, propagation transpires in free-space.

Dispersion in itself can be explained through the atomic nature of material, which is not crucial to this research. However, it is important to note that dispersion is strongly related to the ability of matter to absorb certain electromagnetic wavelengths - these are the characteristics that determine the visual appearance of matter.

The interaction between an electromagnetic wave and a surface can be attributed to:

- the diffuse reflection by uneven surfaces,
- the diffraction of light by edges, gratings and slits,
- the specular refraction and reflection

of optically smooth surfaces [55].

2.6.4.1 Scattering and Absorption

An atom in the matter can respond to the incident light in essentially one of two ways depending on the frequency (or wavelength) of the particle. The particle nature of electromagnetic waves supplies an idea to when an atom (or particle) will absorb light - if the photon energy of the light is equal to the energy of the state of the atom in the matter; it could be said that it will absorb the light. If the energy does not match, the atom in the matter will scatter the light, transporting an equal amount of energy as the initial incident light, in some direction [56].

Bohren and Huffman [55] state that the fundamental issue with investigating the effect of dust on scattering and absorption of light is in fact characterising the behaviour of a single light particle, since a collection of particles cause no more analytical difficulties that a singular particle. Multiple particles in a "collection" are coupled electromagnetically so that the external field will excite every particle, followed by scattering of the resultant field in reaction to all other particles. So, to assume single scattering of particles, it is required to state that the number of particles within the collection is small, they are separated by the appropriate distance between particles and that the scattered field is smaller than the external field.

With these exceptions for the assumption of single scattering it can be said that clouds cannot scatter light according to this model but can rather only be explained by multiple scattering, which is more trying to state analytically. Further, it can be said that glass and dust particles will scatter light according to the single scattering model [55].

Another explanation for the scattering phenomena is that it can be categorised according to the size and shape of the object scattering the light particles. Generally, scattering phenomena is anisotropic - being dependant on direction; this is true for glass surfaces and its substrates.

2.6.4.2 Reflection and Refraction

Modelling refraction and reflection for optically smooth surfaces are simple and would therefore be an advantageous method of analysis for the clean glass samples. An important assumption made in this model is that glass is indeed optically smooth, as discussed previously. Since no surface is absolutely smooth, an approximation criterion was developed and so a surface is deemed optically smooth when,

$$d_{surface} < \frac{\lambda}{8\cos\theta}, \tag{2.50}$$

with $d_{surface}$ the surface roughness measured from a reference plane, λ the wavelength of the incident light and θ the angle of incidence [57].

If the glass sample can be considered optically smooth, the reflected and refracted light directions are defined by the law of specular reflection and refraction, as well as Snell's law [55].

Considering an electromagnetic wave on a surface (AD), figure 2.5 with an incident angle θ_i, a reflection angle θ_r and a transmission angle θ_t, it is seen that

$$\frac{\sin\theta_i}{\overline{BD}} = \frac{\sin\theta_r}{\overline{AC}} = \frac{\sin\theta_r}{\overline{AE}} = \frac{1}{\overline{AD}} \tag{2.51}$$

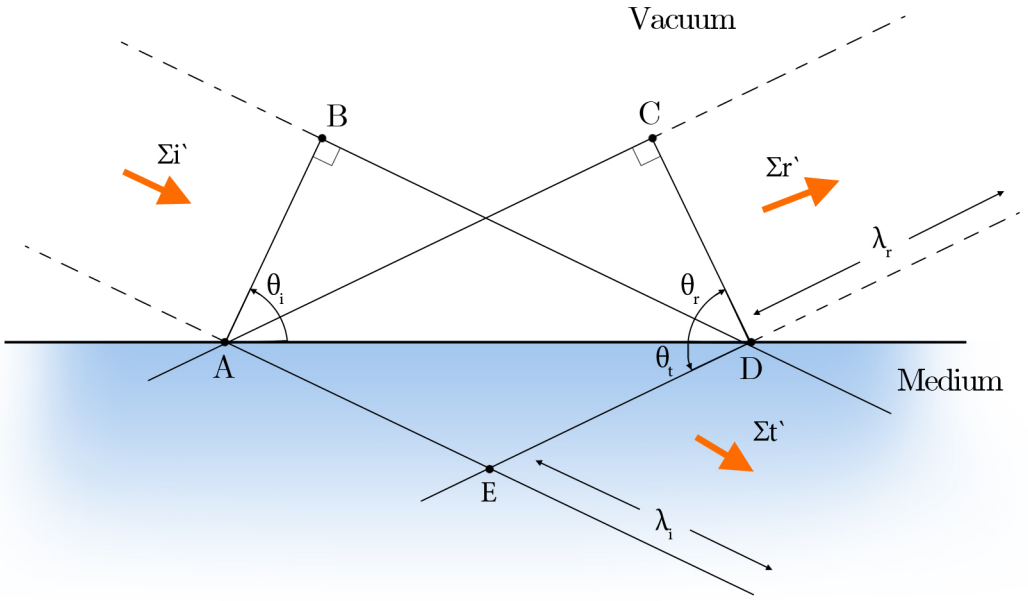

Figure 2.5: The law of reflection, indicating the incident, reflected and transmitted waves.

Since it is assumed that the material through which the wave passes respond linearly, Huygens's principle on the behaviour of wavelengths is used to relate the speed of light to its

angle. Stating that the material or medium is linear, simply conditions that the propagation of a wave transported through the medium can be modelled through a linear differential equation quite accurately. In summary, Hugens' principle,

$$\frac{\sin\theta_i}{v_i} = \frac{\sin\theta_r}{v_i} = \frac{\sin\theta_t}{v_t}. \tag{2.52}$$

So we see that the angle of incidence and reflection,

$$\theta_i = \theta_r, \tag{2.53}$$

which is known as the law of reflection [56]. Therefore, the law of specular reflection simply states that light at a certain angle (to the normal) incident on a polished smooth surfaces will reflect the light at the same angle to the normal. This reflection is usually applied to mirrors, or highly reflective surfaces, but transparent glass also specularly reflects some of the incident light beams.

From equation 2.52, Hugens' principle,

$$\frac{\sin\theta_i}{\sin\theta_t} = \frac{v_i}{v_t}, \tag{2.54}$$

and since $\frac{v_i}{v_t} = \frac{n_t}{n_i}$, the law of refraction can be deduced as,

$$n_i \cdot \sin\theta_i = n_t \cdot \sin\theta_t. \tag{2.55}$$

More frequently these relations above are called Snell's law, which considers the geometry of the angle rather than relating it first to the speed at which light passes through the matter. Snell's law also states the following assumptions: the surface is clean and uniform glass and the refractive index of the air on both sides of the glass sample is equal. Considering then an optically smooth surface, the process is more specifically identified as specular reflection. Then for surfaces that are rough to the extent that the irregularities are larger than the wavelength incident on it, the reflection is called diffuse reflection, as shown in figure 2.6.

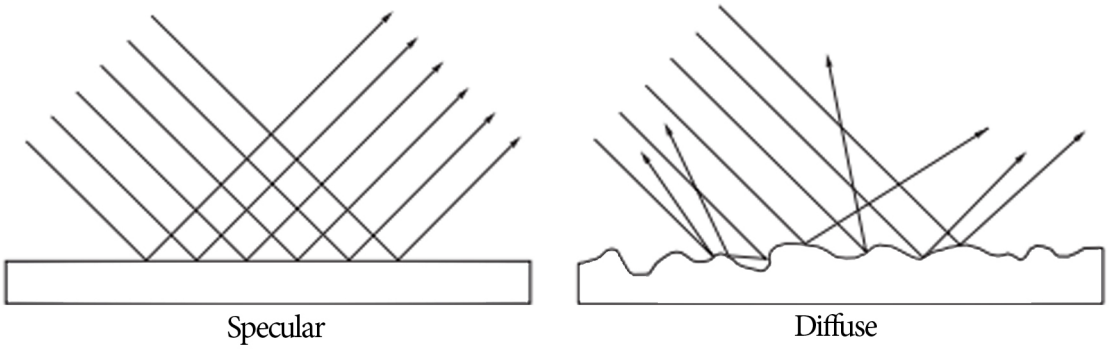

Figure 2.6: Specular and diffuse reflection.

Usually optical smooth surfaces are assumed to be refracting media that is perfectly homogenous, when it is in fact only statistically homogenous. In general, refractive analyses, the assumption is an inconsequential approximation but the reflectance and absorbance of

small particles stem from the fact that material is only statistically homogenous. It is also true that the density fluctuation of molecules in a sample of an optically dense medium propagates scattering of incident light [55].

So far, this research has covered the laws of reflection and refraction without considering the flux densities of the electromagnetic waves. A secondary, more complex approach, confirms the previous laws by considering the electromagnetic theory of light.

From this electromagnetic theory approach and the law of reflection, the Fresnel equations supplies a reflection ratio,

$$R = \frac{I_r \cos\theta_r}{I_i \cos\theta_i} = \frac{I_r}{I_i}, \tag{2.56}$$

that describes the ratio of reflected flux density to the incident flux density. The reflection ratio can also be related back to the refractive index of the matter in which the light is being transported, if there is little to no absorption [56]. Therefore, the reflectance ratio,

$$R = R_{\parallel} = R_{\perp} = (\frac{n_t - n_i}{n_t + n_i})^2. \tag{2.57}$$

2.6.4.3 Transmittance

Transmittance is more complicated than reflection since the speed of energy incident and transmitted is not equal, also, the area of the incident and transmitted beam on a planar surface are not equal; therefore, the flow of energy per unit area differs. Similarly to equation 2.56, a transmittance ratio of defined by the Fresnel equations [56],

$$T_t = \frac{I_t \cos\theta_t}{I_i \cos\theta_i}. \tag{2.58}$$

Also,

$$T_t = T_{\parallel} = T_{\perp} = \frac{4n_t n_i}{(n_t + n_i)^2}. \tag{2.59}$$

Therefore, it can be concluded from 2.59 that 4 % of light normally incident on an air-glass edge will be reflected - either reflected internally ($n_i > n_t$) or reflected externally back ($n_i < n_t$). The first scenario $n_i > n_t$, is called internal reflection and is characterised by the critical angle θ_c. If the incident angle of the light is equal to this critical angle, $\theta_t = 90°$ it simply means that all the incident energy is reflected back into the medium. For a glass-air edge, the critical angle is approximately 42° [56]. The law of conservation of energy does however show that the internally reflected light would move forwards and backwards within the medium until it is reflected through the edge into the initial source medium.

Theoretically this could be extremely advantageous to solar applications since less radiation would be reflected into the atmosphere from the surface of a module. Unfortunately, solar radiation is much more complex than light being transported in one specific beam at a specific angle.

2.7 Spectrometry

As mentioned previously, spectrometry or spectroradiometry has found more specific attention from the fields of science and chemistry. As short-term prediction for solar energy becomes of more importance, more detailed data and prediciton is required and hence new ways of collecting data are required. As technologies evolve, laboratory equipment evolves into more robust equipment which can be applied to the field of engineering.

Specifically, with advancements in optical technologies, a great improvement in size and price of these technologies have become prevalent. As a result, the miniature spectrometer has become commercially available with field work in mind.

2.7.1 Optical Design

A spectrometer collects light to break it down into its spectral components which are then interpreted by an array detector (also called a spectrograph) - similar to the functioning of larger bench spectrometers. The main difference between the miniature and bench spectrometer is this device that separates the beam into wavelength components, the bench spectrometer's device is rather called a monochromator since it has moving parts, unlike the miniature spectrometers spectrograph. The most common design used for these miniature field spectrometers is the uncrossed Czerny-Turner spectrograph design as seen in figure 2.7 (adapted from [58]).

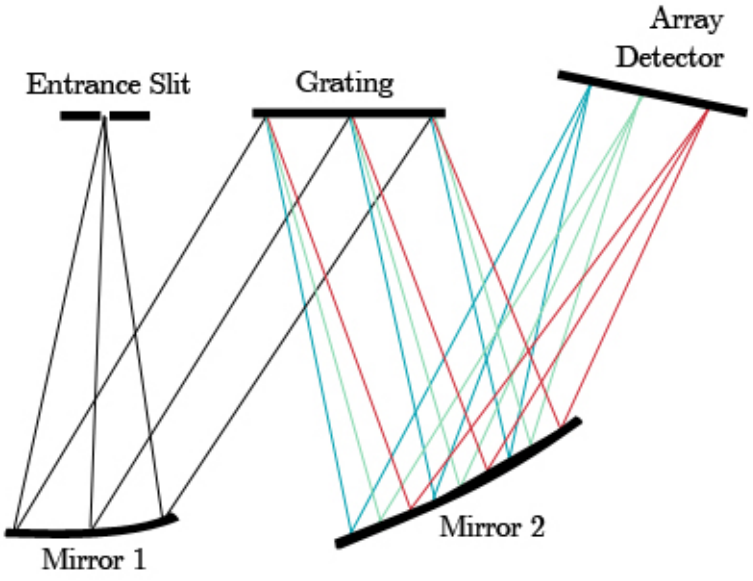

Figure 2.7: Miniture spectrometer optical design, uncrossed Czerny-Turner.

Light is transported through a fibre optic to the entrance slit where it is reflected by a concave mirror onto a grating; light is dispersed by the grating with varying angles onto a second concave mirror which again reflects it onto the detector.

2.7.1.1 Slit

In effect, the size of the narrow aperture or slit determines the number of photons entering the spectrometer. Simply stated, the slit size is the width in millimeter of the entrance of

the spectrograph.

With most miniature spectrometers, the manufacturer supplies multiple slit size options. The spectrometer performance is somewhat reliant on the slit size - as the slit size decreases, the resolution increases but the signal strength decreases. The main purpose of the slit is therefore the control of the spectral resolution of the spectrograph, the resolution describing the spectrograph's ability to distinguish between adjacent wavelengths. Also, the slit size limits the wavelength range with reasonable resolution [59]. Therefore, the wavelength range,

$$\delta\lambda = \frac{RF \times \Delta\lambda \times W_s}{n \times W_p i}, \tag{2.60}$$

with $\delta\lambda$ the spectral resolution and RF a resolution factor. Four important factors influence this resolution: the wavelength range ($\Delta\lambda$), the width of the slit (W_s), the detector pixel elements (n) and the width of the pixel ($W_p i$).

2.7.1.2 Diffraction Grating

The diffraction grating determines the wavelength range and, in part, the resolution of the spectrometer - as the number of grating lines increase, the resolution increase; the disadvantage is that the wavelength range decreases. The traditional grating used in Czerny-Turner design is a flat ruled grating; a second variation on this design is a holographic concave grating that incorporates both mirrors as well as the flat grating [60].

The traditional ruled grating is a reflective coated substrate with parallel etched grooves on the surface to disperse light. The manufacturing process makes this grating the least expensive of the designs available, but is prone to more errors because of surface imperfections and groove placement errors; this could cause an abundance of stray light. The second, holographic grating is manufactured by applying UV beams to an optical glass sample to induce a sinusoidal shaped refractive index in the glass. This allows for a more uniform response but with a lower efficiency.

The groove density or frequency determines the amount of dispersion possible and therefore the wavelength range of the spectrometer. By increasing the wavelength range of the spectrometer, the spectral resolution will decrease - this could therefore limit the density of the grooves for longer wavelength applications.

The diffraction grating is described by two angles:

- the dispersion angle, as discussed above,
- the blaze angle or the facet angle of the groove itself.

Usually the second descriptive factor cannot be chosen when a spectrometer is selected but it is rather at an angle chosen to alleviate the weaker part of the spectral range of the spectrometer to improve the signal to noise ratio [60].

2.7.1.3 Array Detector

The light beam photons incident on the array detector is converted into electrons which are digitised. In effect, the spectrometer measures the number of raw counts for each pixel in the array from the CCD (Charge Coupled Device) before it is corrected for instrumentation sensitivity or processed for specific units. This raw count measurement is called scope mode and supplies the response function of the specific instrument. This response is called the

instrument response function (IRF). Every optic forming part of the instrument, such as the fibre, lens, grating, mirror, filter and detector contribute to the IRF and therefore calibration against a standard is imperative [61].

Multiple types of detectors exist, even in these small spectrometers, but the important factor is the type of semiconductor material used to produce the detector. The bandgap energy of this spectrometer determines the upper limit to the wavelength that the spectrometer can detect.

2.7.2 Absolute Irradiance

Absolute irradiance is a common term in spectrometry when measuring irradiance. Absolute irradiance supplies a solar irradiance spectrum that is accurate in shape (or distribution) as well as magnitude. Every spectrometer has an IRF characterised by its unique wavelength dependant response and therefore, calibration is an important process, as mentioned previously. The calibration reduces inherent instrument measurement errors; this also allows the processing of these raw counts measured by the spectrometer.

Calibration values are usually supplied by the manufacturer of the spectrometer; this process supplies the energy response of each pixel in the CCD, supplied in $\mu J{\cdot}count^{-1}$. Irradiance measurements in $\mu W{\cdot}cm^{-2}$ are possible by considering the size of the sampling area and the integration time of the measurement.

In general, the corrected irradiance measurement is supplied by Ocean Optics [61] for any miniature spectrometer,

$$I_P = C_P \times (\frac{S_P - D_P}{t_i{\cdot}A{\cdot}dL_P}), \tag{2.61}$$

where C_P is the calibration unit, S_P the sample measurement (the count measurement), D_P the dark spectrum, dL_P the wavelength range, A the receptor collection area and t_i the integration time.

Correcting count values to absolute irradiance does limit the sampling optics that can be used to acquire measurement samples. The sampling optics that can be used includes: bare fibre, cosine corrector and an integrating sphere - the most common sampling optics. This absolute irradiance spectrum (a spectroradiometric measurement) can further be processed into radiometric measurements by integrating over wavelength bands to describe total power.

2.7.3 Spectrometer Selection

In selecting spectrometry instrumentation, several specifications were analysed to compare the utility of the spectrometers. These specifications are as supplied by a spectroscopy company, Ocean Optics [61].

1. **Wavelength Range**: The wavelength range of a spectrometer is vastly dependant on the intended application since spectrometers are designed to capture and process light successfully only in a certain wavelength range. This range is determined by the spectrometer detector range, as well as the diffraction grating, as mentioned previously.

2. **Dynamic Range**: The dynamic range of a spectrometer refers to a measurement of the instrument performance without taking into consideration how the instrument is used. This range is determined by dividing the maximum detectable signal by the

minimum detectable signal. The maximum signal is typically seen at saturation - saturation occurs when the incident light exceeds the number of electrons that each detector pixel can store successfully. The minimum signal refers to a signal with an average equal to the baseline noise, which is the summation of readout, dark and electronic noise of the instrument.

3. **Optical Resolution**: Optical resolution is the principal characteristic of precision in an instrument in spectrometry. This is a specification seen in various imaging and measuring systems to describe the ability of the instrument to resolve detail in that which is imaged or measured. The resolution of a spectrometry system depends on the combination of grating density and diameter of the slit and fibre.

4. **Signal to Noise Ratio (SNR)**: SNR is a measure of how accurately the spectrometer can measure specific light levels. Usually this value is the maximum, determined at saturation. This ratio can also be described as the intensity of the signal divided by that of the noise, at a particular signal level.

5. **Sensitivity**: Sensitivity is the relation, or response, of light input to the spectral output - the detector sensitivity is measured as the current per incident radiometric power.

6. **Stray Light**: Although the spectrometer slit is usually directed in the path of the light, some unintentional light may fall on a part of the detector, disrupting the accuracy of the output. This source of disturbance might be from the projected source, or from another source.

7. **Thermal Stability**: Temperature variation causes a drift of peaks in the spectral response, ensuing in inaccurate measurements. The thermal stability measure is usually a temperature range where minimal thermal contraction and expansion of the spectrometer optics are present. Thermal stability is an important factor when field spectrometry is undertaken. Usually thermal stability is maintained by applying a thermoelectric cooling technique inside of the spectrometer casing. This is not often seen in smaller field spectrometers but rather a solution for larger laboratory spectrometers.

2.7.4 Collimated Response

Since radiation beams are composed of multiple beams which might reflect from other surfaces, local and environmental, random scattering and reflection of light in the measurement process should be limited, if not eliminated. Receptors can be attached to the measuring end of the fibre optic, reducing the field of view (FOV) from which it collects light to a specific angle from as small as 5° to as large as 180°. This receptor is simply an optical diffuser that restricts light beams entering the measuring probe, as seen in figure 2.8, from [61]. Further, to restrict the light entering the probe, the characterisation of the light can be changed from diffused to collimated, by physically extending the edge of the receptor. By making this adjustment only parallel light, or collimated light, can enter the probe.

According to Ocean Optics [61], a measuring sample's spot diameter can be estimated as 0.5 of the distance between the measuring element and the measuring plane, the measuring plane in this project is perceived as the glass; unfortunately this approximation only hold's for FOVs of 25°. The cosine corrector allows for a 180° FOV; it has a Lambertian response: the amount of light is dependent on the angle of incidence on the corrector. For the measurements in this project, it is best if the corrector is as close as possible to the measuring plane.

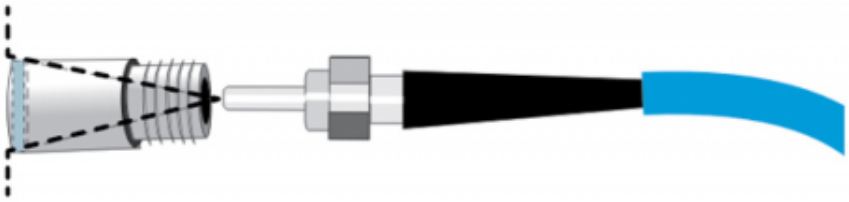

Figure 2.8: 180° FOV cosine receptor extending the edge of the receptor.

Examining apertures in any optics supplies a better understanding of the measuring sample that is observed. The amount of light or energy seen by the detector will essentially be directly relational to the area of the entrance slit. It is also known that if any losses are neglected, the irradiance or flux density observed by the detector is inversely relational to the "image" area - in the sense of a camera. The aperture is basically the entrance area of the optical element; therefore, the aperture is,

$$ApertureArea = \pi \left(\frac{D}{2}\right)^2 = \pi \left(\frac{f}{2N}\right)^2, \tag{2.62}$$

with f the focal length and D the aperture or entrance opening diameter.

Also, the second part of equation 2.62 is true since the f-number,

$$N = \frac{f}{D}. \tag{2.63}$$

Equation 2.63 is called the f-number - the relation between the focal length and aperture; a smaller f-number indicates that more light is able to reach the detector or "image" plane [56].In the case of measuring objects that are infinitely far away, such as sunlight, a second equation is prominent - the working f-number,

$$N_w \approx \frac{1}{2NA_i} \approx \left(1 + \frac{|m|}{P}\right) \times N, \tag{2.64}$$

with NA_i the numerical aperture, P the pupil magnification (usually approximated as one) - to accommodate for lenses of symmetry, $|m|$ the magnification absolute value for a specific distance between the object and measuring element and N the uncorrected f-number as in equation 2.63. These equations allow for approximating the measuring spot size of the spectrometer.

In the section on the propagation of light, the term free space was used - this relates to the environment in which light beams are measured, or another explanation is, how light beams are measured according to their environment. Free space optics refer to the collection of "open" beams on a surface; free space measurements comprise of many variables since the direct environment in which the measurements are completed, is not completely known. To restrict the amount of these variables in the system, free space measurements are best implemented when the spectrometer receptor and other component, such as the glass, are fixed within a structure so that their location within the system is known.

Understanding the influence of FOV and the response of any receptor, is important in spectral measurements of solar irradiance. As shown previously, solar irradiance consists of

multiple components and when spectral measurements are conducted it should be understood which components are in fact measured and which is excluded. Naturally, one should then assume that if a fixed measurement system (the receptor not directed towards the sun) is implemented, that a smaller FOV will receive less light than a larger FOV - or one could say that a smaller FOV is more suited for applications where it is accurately directed towards the light source. A larger FOV is more diverse and allows the measurement of direct, as well as, circumsolar irradiance.

Chapter 3

Preliminary Field Experience I

3.1 Instrumentation Specifications

Preliminary measurements were acquired with a non-permanent setup to test the spectrometer and determine if this instrumentation, and the measuring process, delivers valid information. It is expected that these preliminary measurements will be less accurate than the measurements planned with an automated system; the automated system will reduce human error and increase reproducibility of the measurements. Still, the preliminary measurements set a good basis for analysis and improvement of the measuring process.

This first preliminary field experience was completed in Stellenbosch, July 2016 - these measurements were particularly reliant on the environmental conditions and therefore data was collected on certain days only.

As previously mentioned, spectrometry provides an insight to the spectral distribution of radiation - specifically the direct beam radiation when it is directed toward the sun location. In a broader sense, it can be implied that the spectrometer measuring irradiance is an improvement of the pyranometer and how direct irradiance is measured. Not only does the spectrometer supply more information regarding the measurement.

Several spectrometers were considered for this application; these are listed in table 3.1. All mentioned specifications and their relevant values were determined from the datasheets of the various instruments.

The datasheet of the Flame series states a wavelength range of $190 - 1100\,nm$ but through the grating selection available, the spectrometer cannot optimally function in the total range specified. The most suitable grating supplies a wavelength range of $400 - 700\,nm$, with merely an approximate $30\,\%$ efficiency in the range of $530 - 1100\,nm$.

The StellarNet spectrometers have a significant larger SNR than the other spectrometers - this greater ratio indicates higher signal intensity and less noise transmission, theoretically. Further, the Black-Comet with its increased wavelength range, as well as the ULS2048x64 from AvaSpec, is too large for the intended application.

Table 3.1: Spectrometer specifications, with "?" not supplied by manufacturers.

Spec.	Ocean Optics		StellarNet			AvaSpec
	Flame-S	Flame-T	Black Comet	Blue Wave	Silver Nova	ULS2048 x64
Dynamic Range	1300 : 1			2000 : 1		?
Resolution [*bits*]	?		$1.3-8$	$0.8-6$	$0.75-8$	$1.4-21.3$
SNR	250 : 1	300 : 1		1000 : 1		450 : 1
Stray Light	$< 0.1\,\%$		$< 0.2\,\%$	$< 0.1\,\%$	$< 0.15\,\%$	$< 0.4\,\%$
Wavelength [*nm*]	$190-1100$		$220-1100$	$300-1100$	$190-1100$	$300-1160$
Thermal Stability	$0-50°$		?	?	?	?
Mass [*g*]	265	?	400	?	?	855
Dimensions [*mm*]	89.1×63.3×31.9		69×100×150	25×75×125	60×17×15.5	175×110×44

3.1.1 Instrumentation

In response to the literature study on spectrometer instrumentation, a $f/4$ Czerny-Turner spectrometer, called the Miniature BLUE-Wave spectrometer, from StellarNet Inc. has been selected, figure 3.1. The instrument has a $600\,g/mm$ ruled grating, 2048-pixel CCD detector, 16-bit digitizer and a range of approximately $300-1100nm$. A slit size of $25\,\mu m$ was chosen for reasonable resolution of $1.0\,bit$ without compromising the signal strength. The CCD detector is not cooled but a software temperature regulation function is available to use.

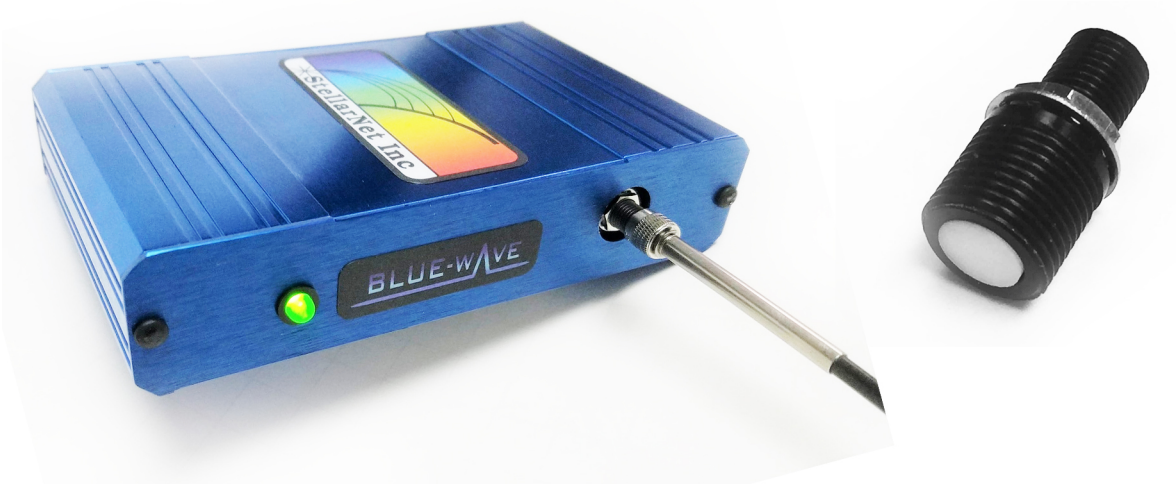

Figure 3.1: The BLUE-Wave spectrometer and a UV-Vis-NIR cosine receptor, both by StellarNet Inc.

Further, a $600\,\mu m$ diameter armoured and solarisation resistant fibre optic cable, with an UV-Vis-NIR cosine receptor will be attached to the spectrometer. From chapter 2, the focal

length and aperture of the fibre,

$$ApertureArea = \pi \left(\frac{D}{2}\right)^2 = \pi \left(\frac{0.6}{2}\right)^2 = 0.283\,mm. \tag{3.1}$$

It is known that the f- number of the detector is $f/4$, therefore the focal length of the fibre optic,

$$f = N \times D = 4 \times 0.6 = 2.4\,mm. \tag{3.2}$$

Similarly, it is known that the cosine receptor has a $1/4\,inch$ diameter, approximately $6.35\,mm$ therefore, the $ApertureArea = 31.669\,mm$ and $f = 25.4\,mm$.

3.1.2 Calibration

The BLUE-Wave spectrometer was calibrated by StellarNet Inc. according to NIST traceable irradiance measurements for absolute intensity for wavelengths larger than $200\,nm$.

3.1.2.1 Laboratory Calibration

The National Institute of Standards and Technology (NIST) calibrate various instruments specifically for laboratory use, to ensure data that is accurate and instrumentation that is reliable. A wavelength calibration is required to validate any spectrum measured - this calibration corrects for any spectral response received from the CCD detector. The calibration required, consists of multiple partial spectra from a fixed source, such as a krypton lamp. The same process is used to capture a calibration for reference relative irradiance spectra [62]. The spectrum supplied in figure 3.2 is a radiometric calibration supplied by StellarNet. The calibration is observed singularly since it has a strong response form - this might influence the measured spectra.

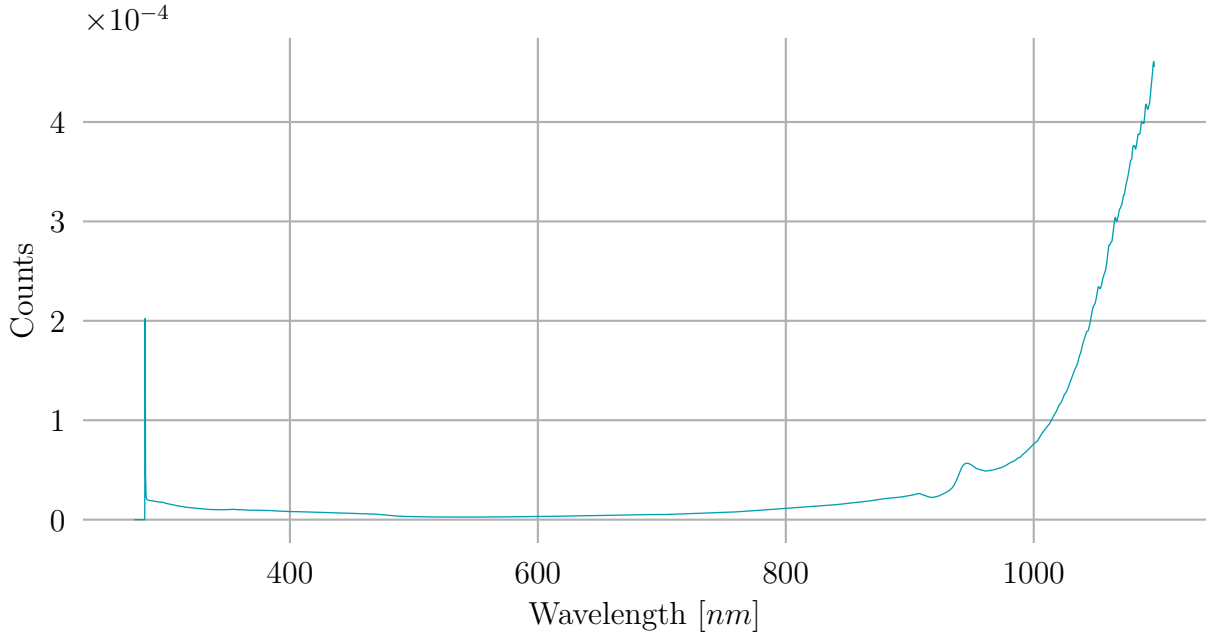

Figure 3.2: Calibration distribution supplied by the manufacturer of the BLUE-Wave spectrometer.

3.1.2.2 Dark Spectrum Calibration

The dark spectrum is the background signal that is expected from the instrumentation when no light is present; this is required to correct offsets. The outliers in the noise profile of the instrumentation could cause variation in the measurement of a sample - these outliers are called a hot pixel. In effect, these hot pixels have a higher dark current than the average pixel. These hot pixels are stored in the dark spectrum to correct the profile.

The dark spectrum does not necessarily stay constant. Temperature variation can cause the background signal to have an offset; this is called baseline drift [61]. The dark spectrum is specifically used to correct for fixed noise, as well as shot noise in the instrumentation, whereas dark noise refers to the offset created by the semiconductor of the CCD itself. Dark noise is vastly dependant on temperature since it refers to the variation in thermally produced electron-hole pairs formed within the CCD detector. Dark noise is independent of the generated signal and the rate at which these electrons are generated at a specific temperature - this is called the dark current. Dark noise creates an interesting response in the detector: as the instrument temperature increases, dark noise will increase but the offset created by the detector could decrease and therefore cancel the baseline drift of the instrument.

So, temperature variation causes a change in dark noise but also changes the photon response. This response, called Photo Response Non-Uniformity (PRNU), describes the intensity variations between adjoining pixels and is the main cause of pattern noise observed in a measured spectrum. This non-uniformity can also be caused by long integration times. Since a dark spectrum roots from pattern noise compensation, it could be assumed that the dark spectrum required will also change with a variation in temperature, as well as with a change in integration time.

Still, thermoelectric cooling used for thermal stability in larger laboratory spectrometers does not specifically address PRNU but rather only the increase in dark noise. Often, noise other than dark noise can be controlled by using spectral averaging and naturally, by controlling the instrument temperature externally.

In effect, a temperature controlled device is most desirable; a simple solution such as the Peltier cooling effect could be an advantageous addition to the spectrometer. Even with controlled temperature, it is in good order to acquire a dark spectrum before any radiation measurement is completed, as well as when a measurement specification, such as integration time, changes in radiometric measuring function. In a hand-measurement setup this is easily accomplished by mechanically closing the opening slit or receptor completely and saving this acquired dark spectrum. In an automated system, this is accomplished only with additional mechanical and electronic parts to create a type of shutter. A second alternative is to acquire a single dark spectrum and digitally supply this to the spectrometer before a sample measurement is acquired. Off course, this second method does not take temperature compensation into account.

The manufacturer of the BLUE-Wave spectrometer suggests the subtraction from a spectrum of approximately $1500 - 2000$ counts per wavelength to account for the dark spectrum, if the measurement is completed in scope mode and a physical dark spectrum cannot be acquired.

3.1.3 Measurement Parameters

The spectrometer software has several parameters the user can set to determine how data is captured. Perhaps the most important parameter is the integration time, a time-value between 1 and $65535\,ms$. The integration time determines the amount of time a pixel will

be illuminated by the light source, controlled by an electronic shutter. Integration time is usually optimized before a measurement or measurement set is captured to prevent saturation of the spectrometer; this optimisation includes maximising the SNR and the output from the detector.

The second important parameter is the number of scans to average; in effect, the number of spectra to average before capturing the output. The averaging increase smoothing in the Y-axis since the SNR is increased by the square root of the number of scans being averaged. A higher averaging with greater intensity and shorter integration time improves the data quality. Further smoothing is applied via various smoothing controls: Pixel Boxcar, Savitzky Golay, Display Persistence and Average Dark Baseline. Pixel Boxcar has four smoothing levels, each relating to the number of adjacent pixels used for the moving average. Savitzky Golay also consists of four smoothing levels according to a least-square technique introduced by Golay in 1946 [63]. Display Persistence is generally used for smoothing digital outputs according to exponential smoothing. Lastly, Average Dark Baseline adapts the baseline level by computing the dark average.

3.1.4 Measurement Accuracy and Precision

Errors in measurement are predominantly caused by the inconsistency between the unknown measured sample and the calibration - this forms part of the first rule of radiometric measurements. This makes measurements more difficult in the case of this project since the measurement conditions will only differ vastly from the calibration conditions but will also vary continuously. Malacara [64] stated, in 1988, the following losses to account for to ensure accuracy and precision for radiometric measurements:

1. Regarding radiant power - it should be uniformly distributed in respect to the angle and area on the surface it will be incident on. If the radiant power falls within the centre of the dynamic range of the instrument and measured irradiance is similar to the calibrated irradiance, the then additional uncertainty is approximately 0.1 to 0.5 %.

2. If the above conditions are not met, additional uncertainties should be accounted for - variation in direction, position and responsivity is 1 %; variation in wavelength and calibration errors are 3 %; nonlinearities within the instrument and the dynamic range 0.5 %.

3. Uncorrected temperature variations of the instrument accounts for another $0 - 10$ % loss, specifically when the instrument is not thermoelectrically cooled.

4. A calibration becomes less accurate as the instrument deteriorates over time, this time interval can account for up to 1 % in losses.

Although these aforementioned losses were stated in 1988, the types of losses to account for today has not changed significantly. According to Malacara, the predominant errors will occur in the shorter wavelength band where the radiation is less and the longer wavelength band where radiation is predominantly scattered. Some strategy is required to ensure that measurements are accurate and precise - precision is easily obtained through repeated measurements. Accuracy of measurements can only be determined through additional data.

One proposed method to determine the accuracy of the acquired data is to compare the measured spectral irradiance data to a reference spectrum as well as the momentary data acquired by a pyrheliometer. Since the spectrometer measures a distribution of energy over

a wavelength band, numerical analysis is required to calculate a total irradiance value at a specific moment in time that can be compared to the value acquired by the pyrheliometer. The numerical analysis required is numerical integration and Simpson's rule is implemented since the wavelengths are equally spaced. Simpsons's approximation [65],

$$\int_a^b f(x)dx \approx \frac{b-a}{6} \cdot \left[f(a) + 4f\left(\frac{a+b}{2}\right) + f(b) \right]. \tag{3.3}$$

3.2 Design Setup

The preliminary measurements were collected by designing a simple system that would allow for the spectrometer probe to be directed towards the sun when a measurement is taken. A three-plate and shaft component was designed to house the measuring probe (in the middle plate) as well as a small low-iron float glass sample (on the top plate). This glass and probe holder was attached to a camera tripod with a rotating ball head, allowing the holder to be moved throughout a wide angle without moving the setup.

The holder component is also used for determining if the sun is approximately incident with a 90° angle on the glass and probe. The top two plates were clamped together and a small hole was drilled through both - these are called alignment holes, similar to that used to setup a pyrheliometer. The alignment holes are explained through the sketches in figure 3.3 - the first image shows light falling perpendicular to the top plate, allowing the light beam to pass through both plates, showing a light spot on the bottom plate. The second image show light passing through the first hole at an angle, which means the beam cannot pass through the second hole and therefore no light spot will show on the bottom plate.

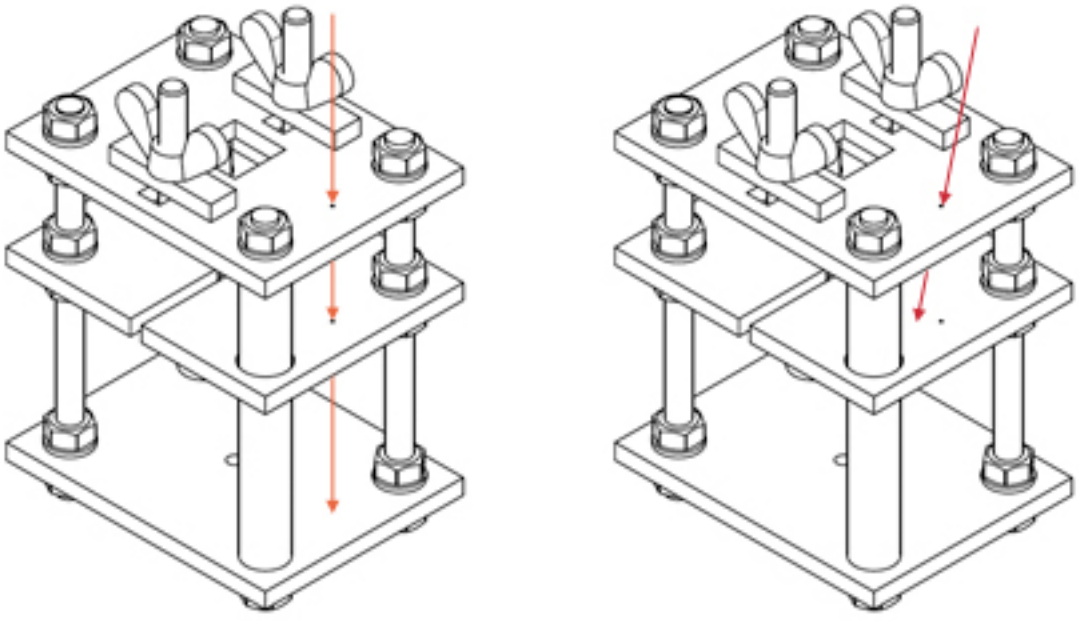

Figure 3.3: Preliminary measurements design sketch, showing alignment holes and how light beams might travel through these holes if the angle is correct.

Before each measurement set (every $10-20$ minutes), the tripod ball head was rotated until a sun spot is visible on the bottom plate. The more light beams are passing through these holes onto the bottom plate, the brighter the spot becomes, confirming that a high content of light beams are indeed falling parallel to the measuring probe. This method to determine the measuring position has the disadvantage that it cannot be used when the sky is overcast or very cloudy. The three-plate component is shown in figure 3.4.

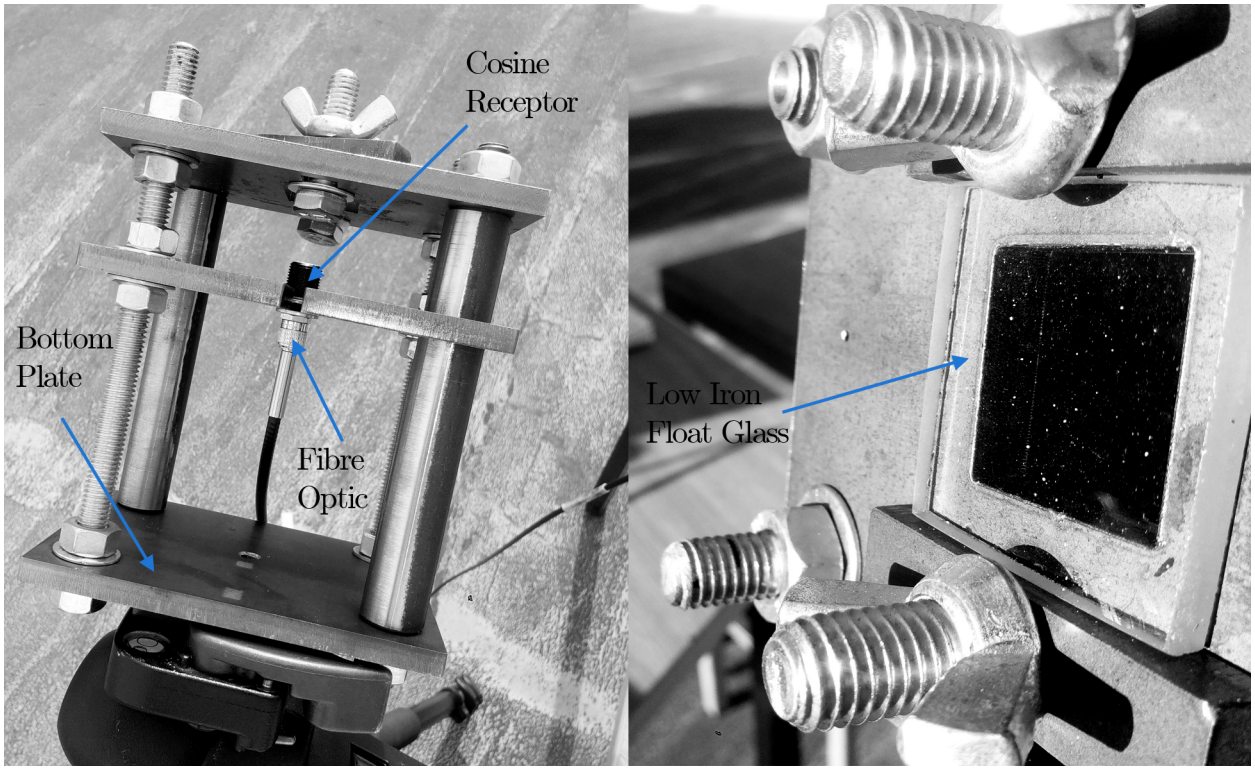

Figure 3.4: Preliminary measurements photos - these photos show the three-plate and shaft component as well as the fibre optic and cosine receptor. The second photo shows the low-iron float glass and how it is attached to the setup.

3.3 Interpreting Data

The software (SpectraWiz) supplied by the spectrometer manufacturer, StellarNet, has multiple functions. For these measurements, multiple modes and settings were tested. Using the software for Windows, there is the advantage that radiation measurements can be acquired since the program completes calibration to determine these radiation values from pixels. Measuring in the radiometric mode, spectrum data is collected in a .IRR file which is similar to a text file - plotting this data is straightforward since the file supplies the radiation value at its measured wavelength at a fixed chosen step of $0.5\,nm$. The second mode in SpectraWiz is the scope mode; this mode supplies the pixel or count value measured by the spectromter with its according wavelength also at a fixed step position. The file extension is .SSM. An irradiance plot, however, can be calculated from the count values measured through implementing 3.4 at every wavelength step. Therefore, the irradiance,

$$I = (counts - darkcounts) \times calibration \times \left(\frac{calibrationtime}{counttime} \right), \tag{3.4}$$

with counts in this equation referring to the measured count values in scope mode; dark counts refer to the black spectrum captured. Calibration refers to the calibrated values supplied by StellarNet, and therefore calibration time refers to the integration time of the calibration file, which is a fixed value of 300 ms. Count time similarly refers to the integration time of the measurement.

However, to calculate the radiation values from these measured count values is more challenging than expected since the wavelength step of the calibration is not only dissimilar to that of the measurement, the wavelength step is also not constant. This means the method of interpolation is required to determine data points from the measurement to determine it at the wavelength steps of the calibration. The discreet set of data points known could either be the calibration or the measured data. Since it is chosen to always measure in wavelength steps of 0.5, it would be easiest to interpolate the calibration file to this 0.5 step. The measured range of wavelength was $278 - 1124.5\,nm$.

Figure 3.5 supplies a comparison in measurement and an idea to the accuracy of the conversion from count to irradiance. Table 3.2 summarises the totals and differences for each wavelength band of interest. Even though these two measurements differ quite vastly in the NIR wavelength band, they only differ with 0.57% in the visible wavelength band.

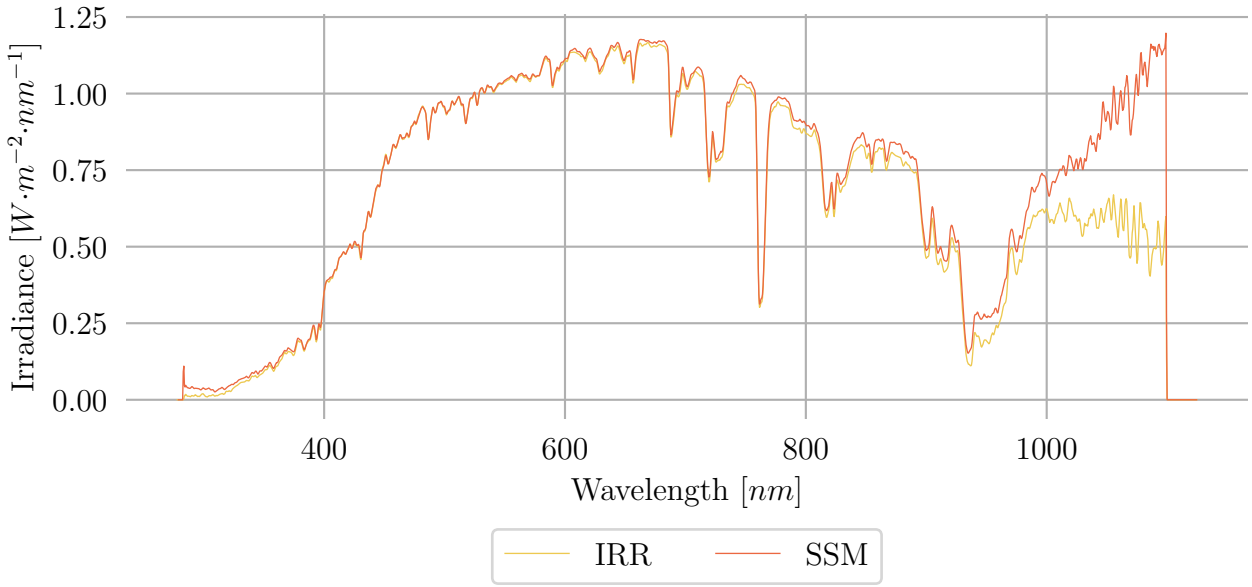

Figure 3.5: A comparison graph of a radiometric measurement (.IRR) and the calculated irradiance from a count measurement (.SSM).

Table 3.2: Range of roughness at a specific wavelength and incident light angle.

	IRR Irradiance	**SSM Irradiance**	**Difference**
Total	556.758	604.535	8.58 %
UV $(10 - 400\,nm)$	10.637	12.299	15.63 %
Visible $(400 - 700\,nm)$	283.403	285.403	0.57 %
NIR $(700 - 1200\,nm)$	261.663	306.185	17.02 %

Measuring the raw count values through a Linux system running a Python script, supplies 2047 comma-separated single integer values. These count values represent the number of photons measured by the spectrometer as well as wavelength. The position (i) of the pixel within the string can be converted to the wavelength as supplied by StellarNet,

$$\lambda = \left(C_4 \cdot \frac{i^3}{8}\right) + \left(C_2 \cdot \frac{i^2}{4}\right) + \left(C_1 \cdot \frac{i}{2}\right) + C_3, \tag{3.5}$$

where C_1 to C_4 refer to coefficients of the spectrometer, also supplied within the calibration file.

3.4 Stable Conditions

If we consider the measurements taken in July 2016, which were hand measurements taken directed towards the sun position, it is clear that the measurement process was extremely reliant on the sky-condition. Differentiating between sky conditions was even more important than merely stating if it was cloudy, mostly cloudy or overcast. Even if it had been only cloudy, with approximately 50 % cloud coverage, the measurement could have been taken at the exact moment when a cloud passed by, or not. Even in less cloud coverage, there is a chance that a cloud could move in front of the position of the sun. Through multiple measurements within a short period of time, it could perhaps be determined when cloud coverage influenced the measurements.

Under clear-sky conditions main features can be identified in the measured spectra as by Hill et al.[66]:

1. Topographical structures varying with wavelength, mainly ascribed to oxygen and water vapour absorption bands and Fraunhofer lines.
2. A trend of smooth decreasing intensity in increasing wavelengths. This feature manifests from:
    a) Planck's Law and the varying solar intensity of a blackbody at 5800 K.
    b) The instrumentation which is more responsive to visible than NIR light.
    c) The Rayleigh scattering of light which is strongly wavelength dependant.

After the research discussion on meteorological conditions it can be realised that these conditions are challenging to describe quantitatively and therefore predicting the effects on spectral radiation measurements seemingly impossible. Although this research aims to support prediction of these effects through real-time measurements, some limitations to the conditions under which measurements are completed, should be discussed.

With the first and second preliminary measurements, as well as the final automated measurements, the sky-conditions influence the stability of the measurements - increased water vapour in the atmosphere could cause measurements to fluctuate extremely from one measurement to the next, only a few seconds apart. So, to assure that most environmental variability is excluded in the core measurements, measurements were not completed on days when it was overcast or predominantly cloudy - this only applies to the preliminary measurements.

For valid measurements and conclusions on a specific measurement set, the environmental conditions should be stable over the measurement time of the set. Since the preliminary

measurements were taken predominantly in winter months, some variability was expected due to an increase in water vapour presence in the air. Direct beam measurements without any obstruction such as a glass sample, is considered the baseline measurement.

The response of the spectrometer is established against the ASTM G173-03 reference spectra as supplied by NREL [67]. This reference spectra characterises terrestrial solar irradiance under vary specific atmospheric conditions relating to temperature, pressure aerosol density, air mass ($1.5AM$), total column water vapour and the surface spectral reflectivity.

Figure 3.6 presents the reference spectra and the measured irradiance at a specific time (10:00) on four different clear days in July 2016 - where the $AM1.5$ refers to the reference direct and circumsolar irradiance; the direct normal irradiance with nearly parallel beams, excluding scattered and ground reflection radiation and spectral irradiance with a $\pm 2.5°$ field of view. The measured spectra conform to the same characterisation as the reference spectrum with the exception of the larger field of view of 180°. These data points were measured with an integration time of $35\,ms$ and software temperature compensation turned on; also, the averaging method was set to average dark baseline.

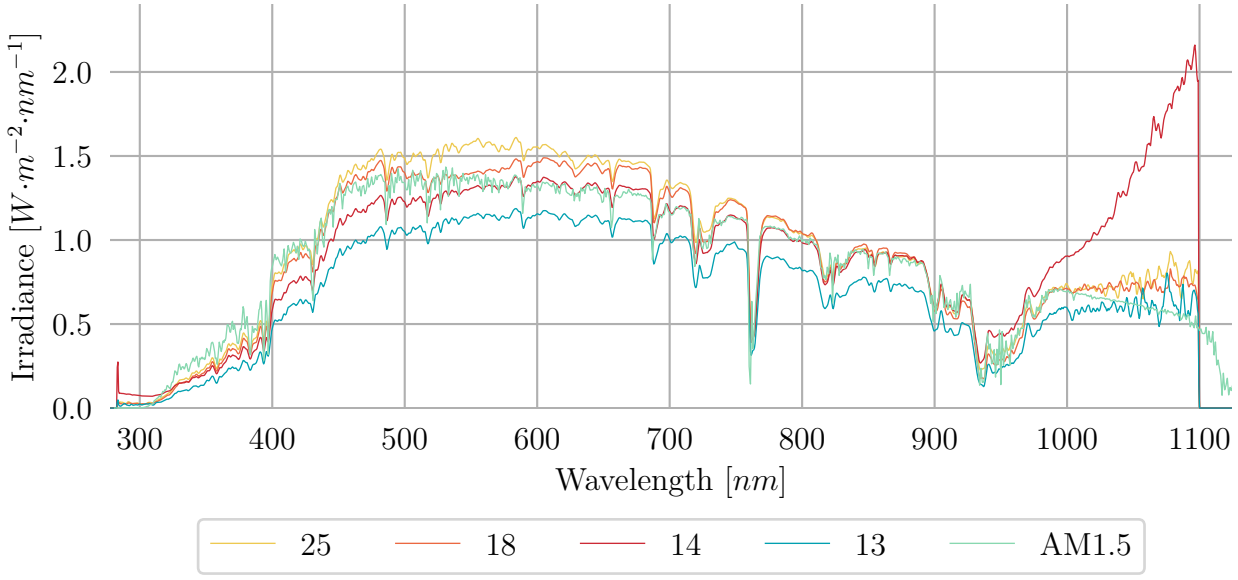

Figure 3.6: AM1.5 reference spectra with measurements on various days at 10:00, to conform the measurement spectra distribution.

Plotting these various spectra together allow for several observations and discrepancies:

1. The response on all four days in the upper band ($> 1000\,nm$) are dissimilar to the reference spectrum and quite sporadic; a slight decrease in irradiance is expected.
2. Exceptionally high values are noted on 14 July in the upper spectrum band, $1000 - 1100\,nm$.
3. An unexpected dip in the visible region is seen on July 18.
4. A similar response to the reference spectrum is observed on July 13 and 25; the total irradiance values are lower or higher but with similar shapes except for the upper band.

The first major discrepancy can be noted against to the calibration supplied in figure 3.2, it is noted that in this discrepancy region, the form is very similar; the discrepancy would therefore be attributed to the sensitivity and noise of the spectrometer. Further communications with the suppliers of the spectrometer confirmed that this discrepancy often arise with the sensitivity of the temperature compensation setting, as well as the average dark baseline. An unexpected dip in the visible region can usually either be attributed to some saturation of the measurement or an environmental phenomenon which reduces irradiance mostly in the visible region; the second explanation being quite uncommon.

From these initial measurements, it was concluded that a standard for stable conditions is required to compare soiling measurements with direct irradiance measurements, since irradiance could vary substantially over short periods of time.

It was decided that conditions will be considered stable when,

1. The measurement is a baseline measurement, i.e. measured without any obstruction such as shadows, glass, etc.

2. The measurement has an approximate response similar to that of the reference spectrum as in figure 3.6.

3. Two baseline measurements within 1 minute differ less than 5 % in value.

Peaks and valleys are assumed in the measured spectra since intensity varies over the spectrum but to further confirm the instrumentation is operating as expected, topographical markers in the spectra is investigated, as seen in figure 3.7. The measured spectra are baseline measurements on a clear-sky day between 09:00 and 10:20 (18 July). As expected, three main absorption bands of water vapour and oxygen are present (indicated by the red dotted lines), 720, 820 and 940 nm as described by Hill et al.[66]. Furthermore, the major extra-terrestrial Fraunhofer lines are indicated (yellow dotted lines) as described before. As mentioned, the waveband 1000 nm and upwards do not behave as expected and therefore few conclusions can be drawn of this region.

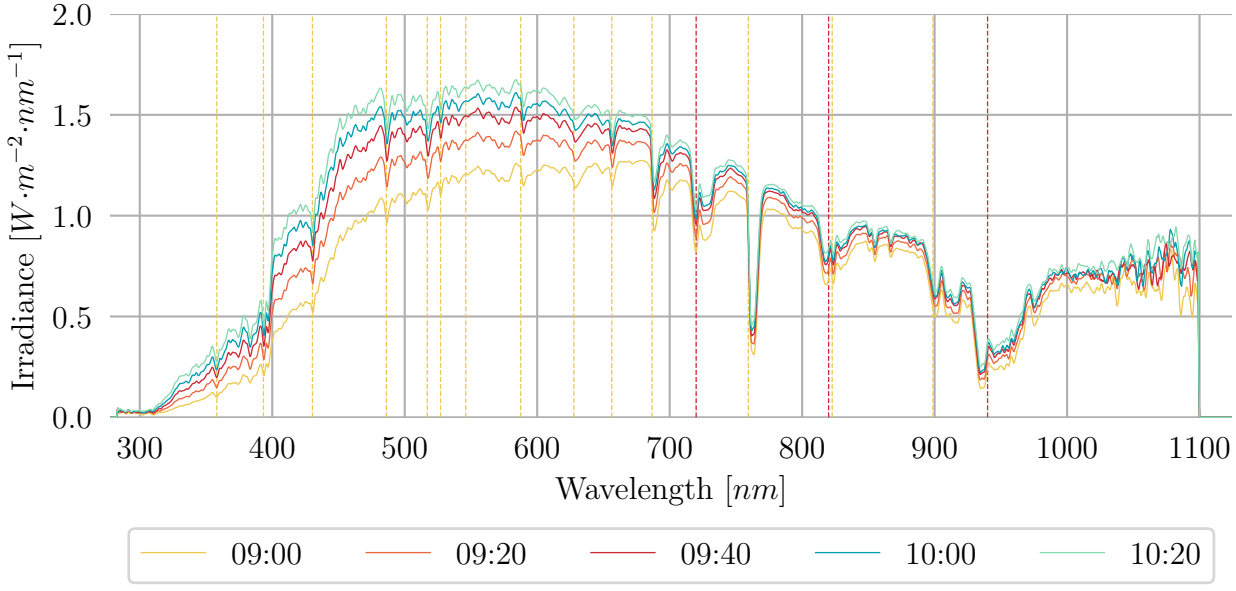

Figure 3.7: Measurements acquired within one day (18 July) with main absorption and Fraunhofer lines.

These stable condition considerations are further investigated throughout the measurement process; as these considerations are not fixed rules but rather an interpretive manner to ensure that measurements are consistent and that data can be interpreted in a reliable manner.

Mostly within the first field experience, a measurement set is labelled with the time it is approximately measured on although each measurement set consists of two baseline measurements, $2-4$ glass measurements and finally another two baseline measurements.

3.5 Daily Measurement

As explained previously, confirming stable conditions is imperative for every measurement set, even if the sets are only 10 minutes from each other. Figure 3.8 is a diagrammatical procedure initially applied to analyse the data and to ensure that every set on every day is similarly investigated.

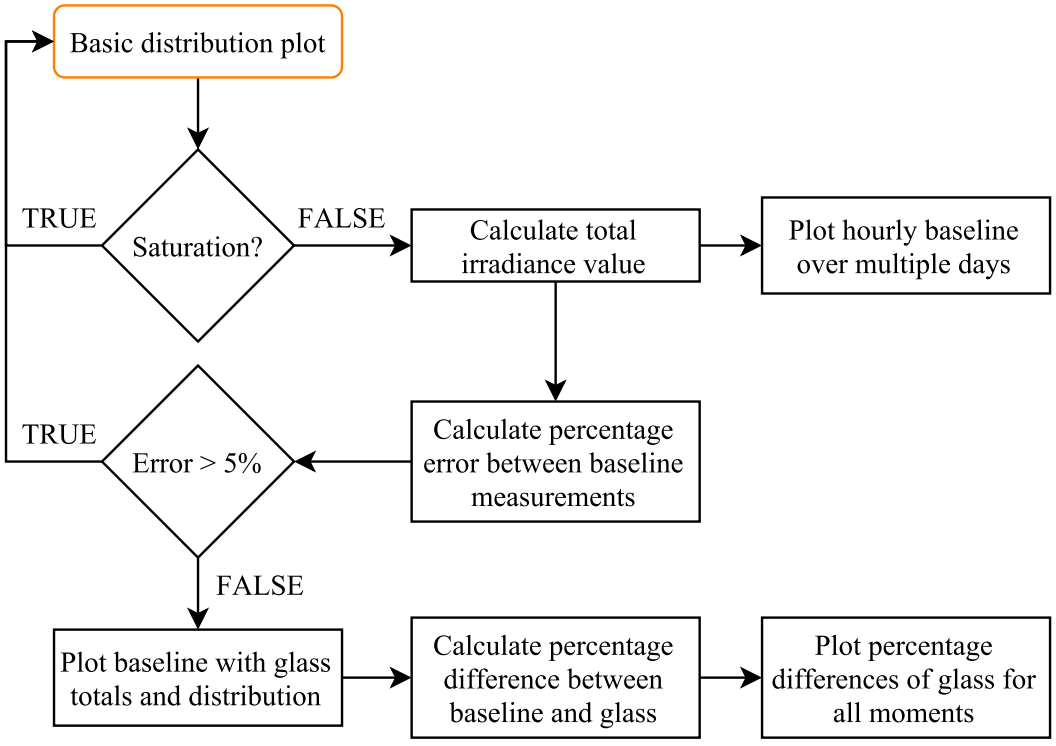

Figure 3.8: Diagrammatical procedure for considering preliminary measurements sets.

Every measurement set is unique in what is observed within the measurements; to draw a conclusion between the sets, each set's markers should be known - observing the distribution of a set is therefore the first step in analysis.

3.5.1 Distribution

Firstly, sky measurements or baseline measurements are investigated - determining which days and time sets satisfy the baseline conditions, and does the spectral distribution exhibit what is expected. Comparing figures 3.9 and 3.10 is an example of why data should be analysed in all forms available - the first graph exhibits the phenomena of saturation, the second is more correct in distribution.

The first day of the preliminary measurements, 12 July:

1. Less than 10 % of the sky consisted of transitory cloud formations - enough sun was available throughout the day to successfully use the alignment holes described before.
2. An integration time of 300 ms was used.
3. Several indicators are observed:
   a) A singular significant hollow in all measurements in the approximate wavelength band $400 - 800\,nm$.
   b) Minimal noise in the longer wavelength band, $1000 - 1100\,nm$.

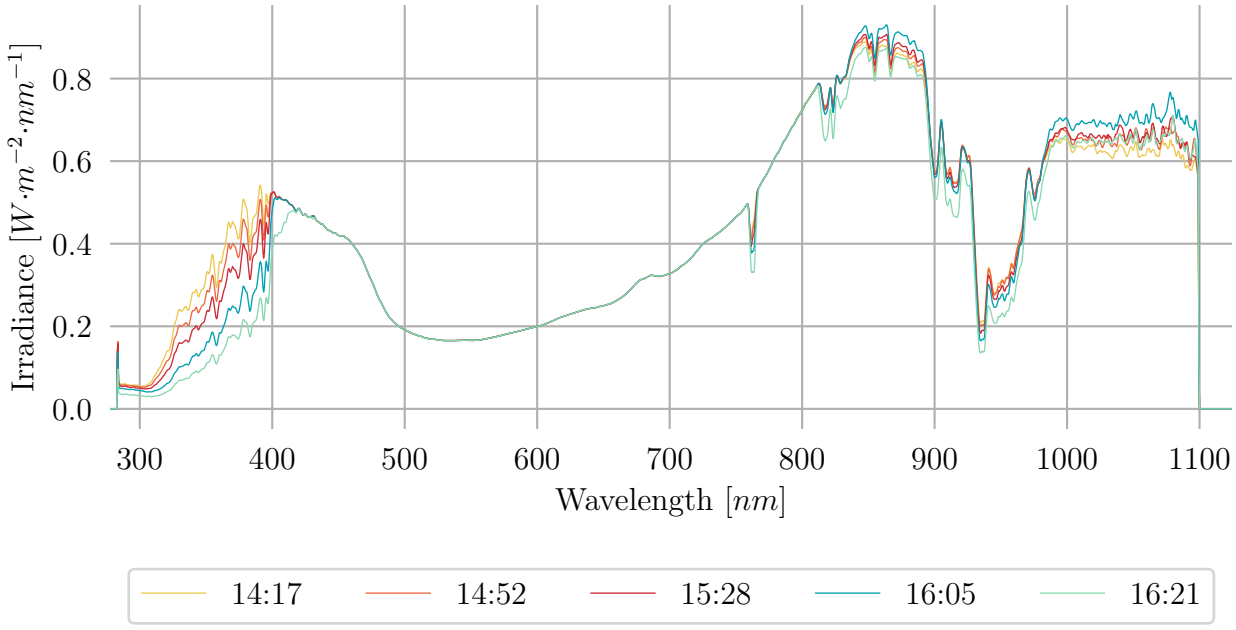

Figure 3.9: Baseline measurements on 12 July in the radiometric function in SpectraWiz - with integration time of 300 ms.

The indicators mentioned above have the same source of origin - the length of integration time. The longer the integration time, the less noise is observed, specifically in the short wavelength band $270 - 300\,nm$ as well as in the long wavelength band $1000 - 1100\,nm$. Although the longer integration time is advantageous in these bands, measurements are easily saturated within the visible wavelength band for integration times longer than approximately 40 ms. Saturation occurs when the detector cannot store the large number of electrons exposed to it, within the visible wavelength band and therefore supress these highest irradiance values.

Observing the second day, 13 July, figure 3.10:

1. Measurements are limited to before approximately 12:00 since the morning became progressively cloudy and measurements became unattainable.
2. The integration time was reduced to 35 ms.

3. At face value, 13 July indicates a distribution similar to the $AM1.5$ reference spectrum observed before but some discreet indicators are observed:

   a) Additional noise at $1000 - 1100\,nm$.

   b) A small decrease at $500 - 600\,nm$, especially at times when the total irradiance is higher.

   c) A total decrease in irradiance from 12:29 onwards.

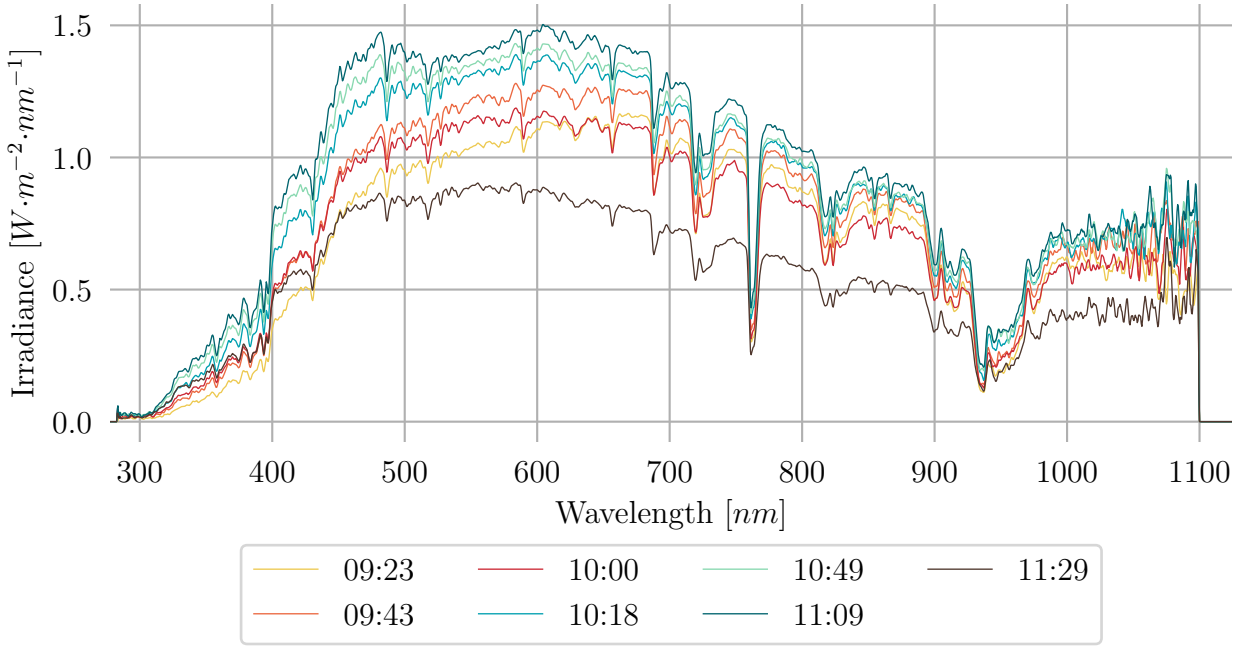

Figure 3.10: Baseline measurements on 13 July in the radiometric function in SpectraWiz - the integration time of $35\,ms$.

The first observation of 13 July confirms the statement that shorter integration times is more susceptible to noise; the second leans itself towards saturation, especially since where a maximum irradiance value should be, a hollow is observed - even though the software does not indicate saturation. The total decrease is expected since it became progressively "darker" towards noon.

Unlike the previous two days discussed 14 July, figure 3.11, consisted of measurements through most of the day since it was clear throughout; the integration time was $35\,ms$.

On 14 July the following is observed:

1. As expected, the spectra increase from morning until a maximum at approximately 13:00 and decreases throughout the afternoon.

2. At 10:00, similar distribution indicators are seen in before in 3.6 - an increasing trend in the longer wavelength band and a outlier peak before $300\,nm$.

Similarly, on 18 July clear conditions prevailed throughout the measuring period, figure 3.12; the integration time was $35\,ms$ until 12:00, where after it was further reduced to $20\,ms$. Now,

the hollows or valleys observed on the previous days can indeed be ascribed to saturation, even though the software did not indicate this phenomenon.

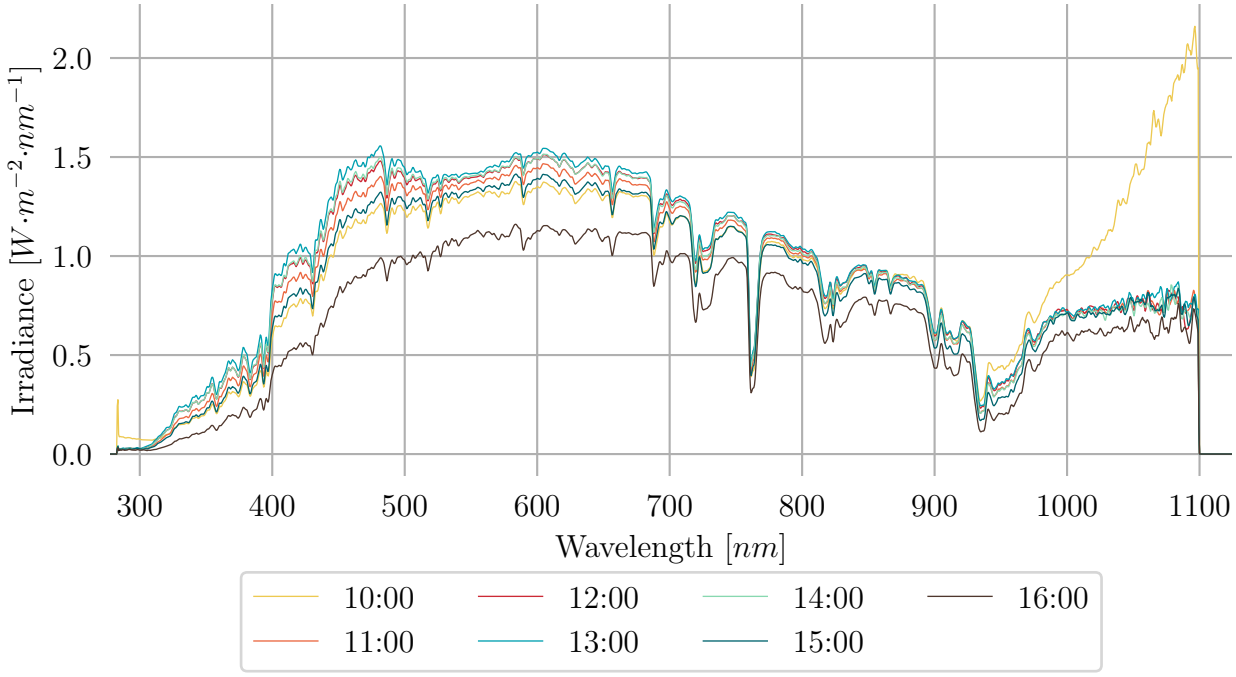

Figure 3.11: Baseline measurements on 14 July 2016.

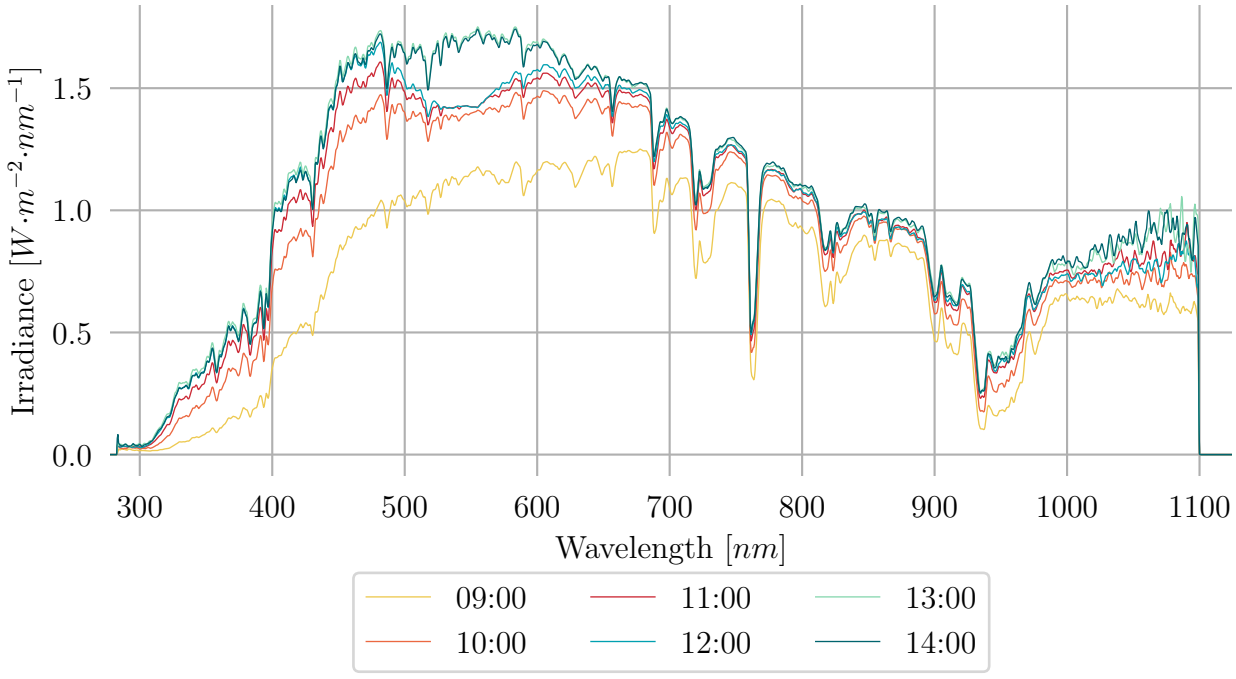

Figure 3.12: Baseline measurements on 18 July 2016.

13:00 and 14:00 on 18 July are good reference measurements since it indicates a response very similar to the reference spectra; even though the long wavelength band is riddled with

noise and indicates a rising trend, it is not too large a variance to impact the analysis to follow.

3.5.2 Total Baseline Irradiance and Error

Even though the stable conditions with a tolerance of 5 % have been selected, the validity of this condition has not been established. The three days which conformed to the initial condition on distribution was analysed further: the total irradiance is calculated, the average error between the total irradiance within the measurement set, as well as, the total irradiance as measured through a SAURAN station located within the area of the measurement setup. The data and station details are located at SAURAN [68].

The total irradiance data used from SAURAN is DHI (Diffuse Horizontal Irradiance) measurements in $W{\cdot}m^{-2}$ by a Kipp & Zonen pyranometer on a SOLYS tracker. The data captured is minute-averaged, therefore figures 3.13 to 3.15 shows a plot of the SAURAN data at the specified time with two minutes before and a minute after. Although the spectrometer data plotted is measured within one minute; the additional data from SAURAN was added to show the variability within the pyranometer measurements against the variability in the spectrometer data.

Figure 3.13 indicates the error within the measured set which consisted of four baseline measurements; the initial increase in cloud cover mentioned previously is now confirmed more easily by viewing the total irradiance from the spectrometer - this is also confirmed by the SAURAN GHI.

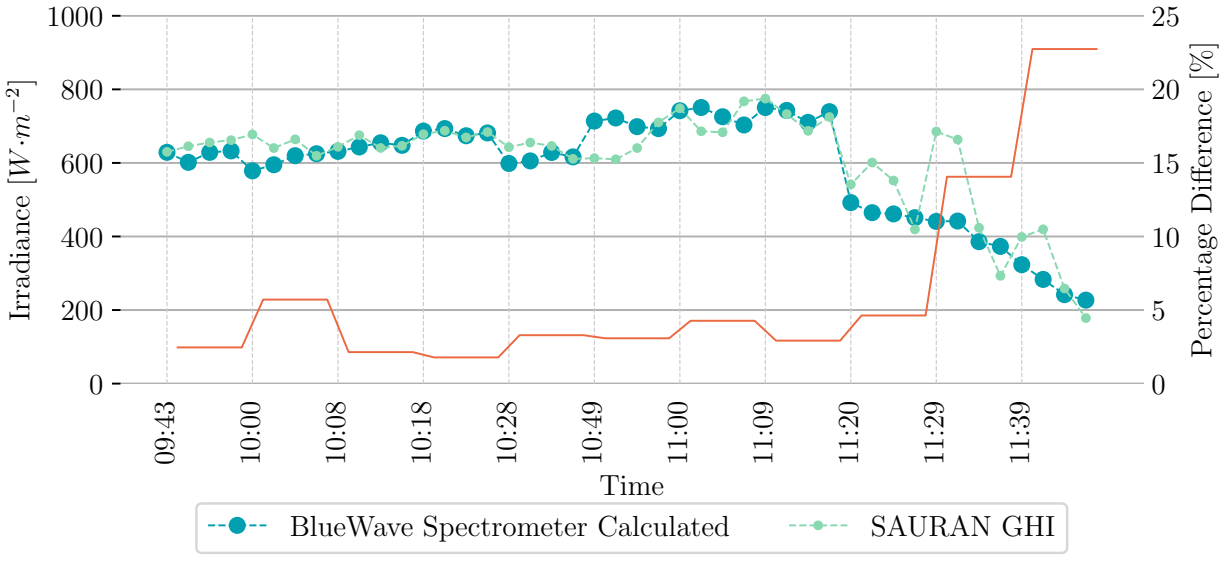

Figure 3.13: Four total irradiance baseline measurements within a set with the percentage error between the first and last baseline measurement within the set on 13 July 2016.

From figures 3.13 and 3.14 some direct relation might be said between the variability of the BlueWave measurements and the difference between the BlueWave and SAURAN measurements: as the variability within the set increases, the more the BlueWave and SAURAN points differ. Therefore, it could again be said that a measurement set with a variance between its baseline measurements is more than 5 % could not be accepted as a valid measurement set.

Since clear conditions prevailed on 14 July, both the measured BlueWave irradiance totals and the SAURAN GHI are quite constant, as observed in figure 3.14. Furthermore, from 10:00 on, the error in the baseline measurement sets is less than 1 % throughout the day. Interestingly, the difference between the measured points and the SAURAN data is approximately 4 % − 8.88 % over this period of small variance in the baseline measurements.

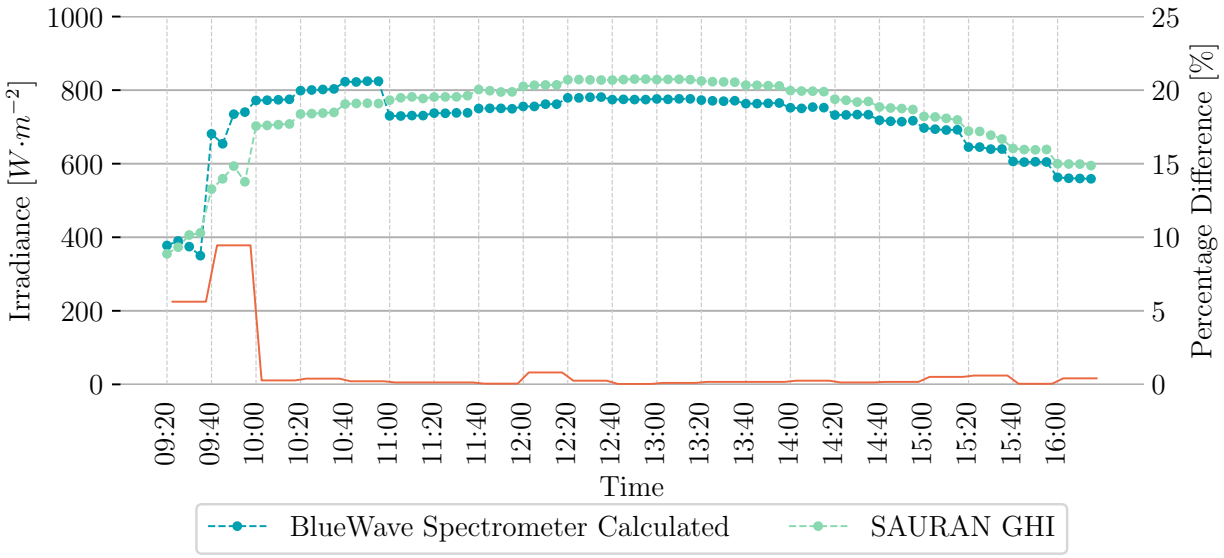

Figure 3.14: Four total irradiance baseline measurements within a set with the percentage error between the first and last baseline measurement within the set on 14 July 2016.

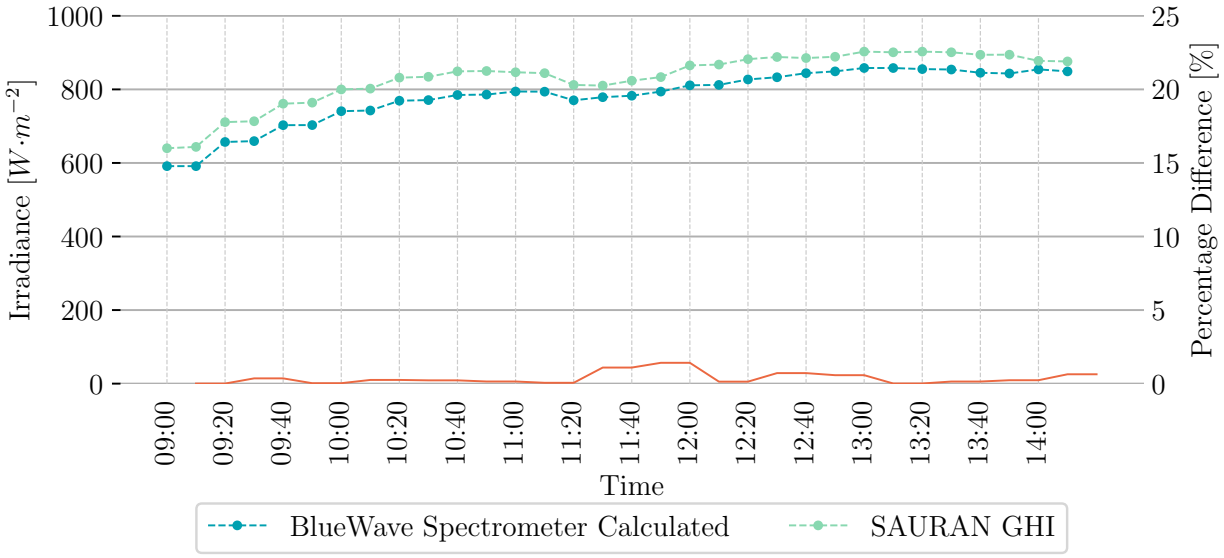

Figure 3.15: Two irradiance baseline measurements within a set with the percentage error between the baseline measurements within the set on 18 July 2016.

Similarly, a constant difference is observed between the two major data sets in figure 3.15 - an offset of approximately 3 % − 7.6 %; still, only an offset range can be supplied rather than a quantitative single offset between the two sets. So, although it looks as if the offset is constant an example is supplied: at 09:00 the difference in the set is a meagre 0.005 % and the difference between the two sets are calculated as 7.61 % but then at 13:30 with a

set difference of 0.009 %, the major difference is 4.93 %. With more clear days, the relation could perhaps have been extended to declare an offset expected at certain times of the day.

Most importantly, the stable condition requirement has been confirmed as a valid analysis of the accuracy of the measured data. Although the SAURAN GHI was seen to be relatively close to what was measured, this might not be the case for the final automated system since it would not measure directly into the sun, but now it is shown that the spectrometer does supply valid measurements.

Lastly regarding error analysis, the distribution of error, i.e. the error at every wavelength point is shown in figure 3.16.

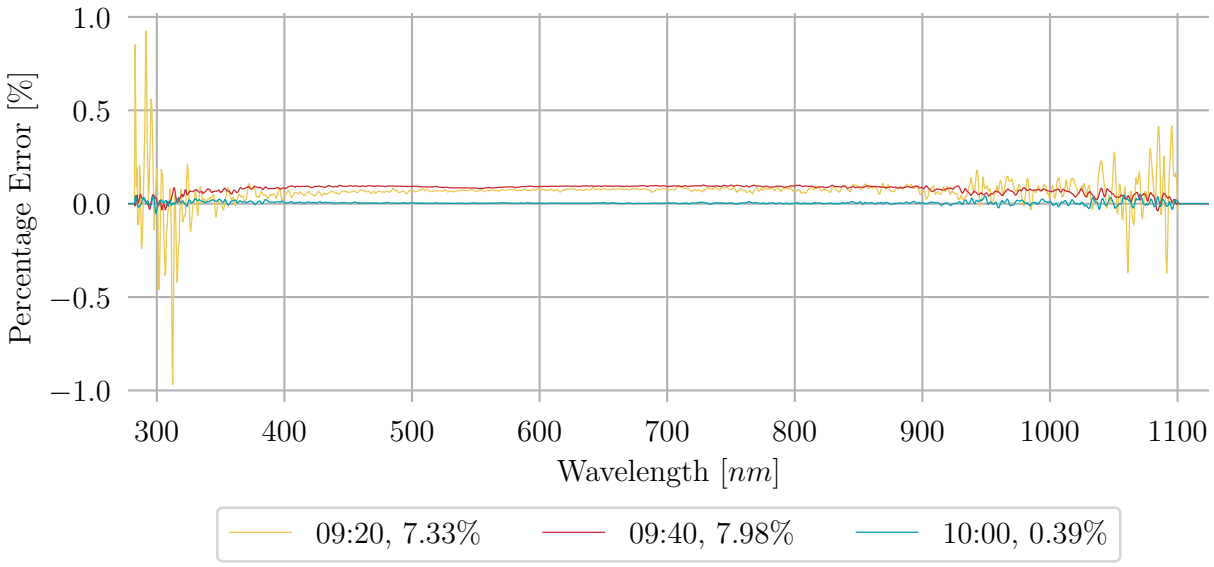

Figure 3.16: The error distribution between a first and last measurement within a set, from three different sets on 14 July 2016.

Initially, it does not seem that figure 3.16 indicates much, but it does show a discrepancy of note: it is expected that two measurement sets within a short period of time would should show a similar error distribution if the total error is similar in value. It can be seen in figure 3.16, that this is not the case, even though 09:20 and 09:40 have a total error difference of only 0.75 %; the first shows a multitude of random outliers (noise) in the usual areas of noise, in the lower and upper wavelength range. Still, the other two error graphs show very little noise in these areas. These observations are important to note when analysing the final data from the automated system.

3.5.3 APE

Previously, the method to determine the spectral quality of light was briefly discussed - the APE. Although it was only briefly discussed, the APE is a straightforward indication of light contents and how it might change over time. The APE was calculated from equation 2.26. Figure 3.17 is the APE of the three days analysed previously. Although the datasets are not complete the expected trend is still discernible. Since the APE is a measure of blueness of the spectrum it is expected that the APE value will be higher in the afternoon and lower in the morning - this is seen in the APE plot, with lower values in the morning and late afternoon.

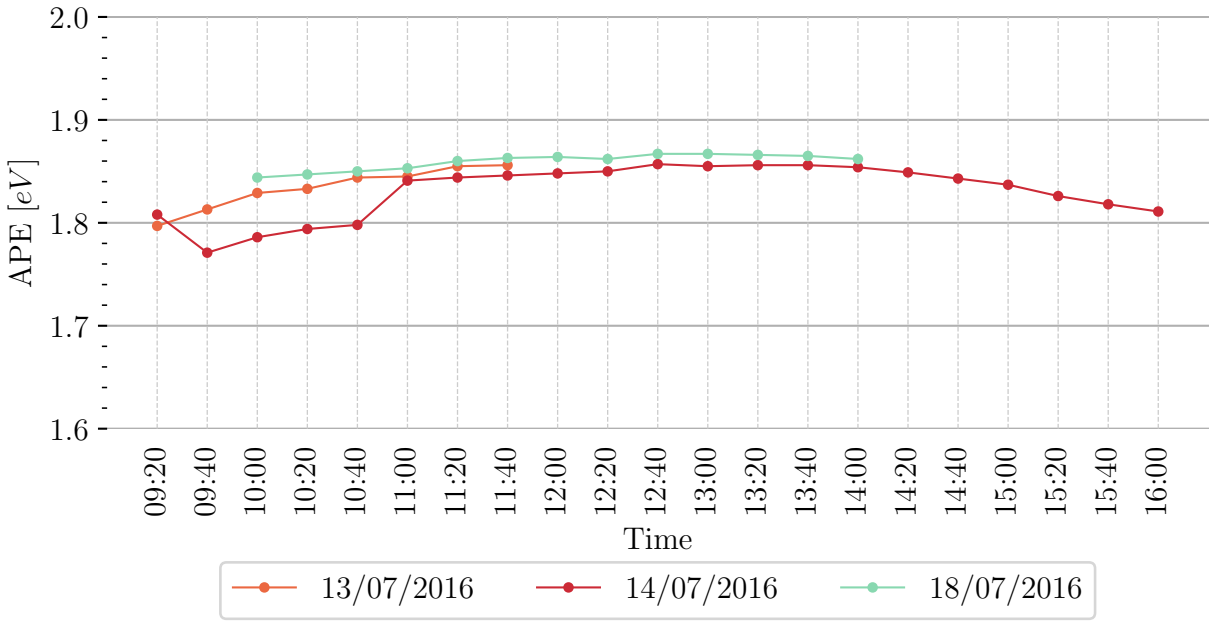

Figure 3.17: Calculated average photon energy (APE) on several days in July.

The APE in this figure is calculated for $350 - 1050\,nm$. As mentioned previously, for this wavelength range with AM1.5 a standard APE value of $1.88\,eV$ is expected. The highest APE calculated in these three days were $1.867\,eV$ - over a longer period of time this might show the norm for winter months, where monthly variation could indicate seasonal changes.

For interest sake, the percentage of each colour of light within each measurement was calculated, figure 3.18. Although the curves are slight, the relation between the blueness of the spectrum and the APE can be observed: The times when the APE was higher, the blue content in figure 3.18 shows a slight increasing trend whereas the red content is showing a decreasing trend.

The foremost purpose of observing the APE and colour content is to indicate to how much information a single spectrum measurement can supply. Although there are many considerations when measuring spectral data, it shows the importance of these types of measurements in the PV field and therefore broadens the understanding of how sunlight interacts with the solar cells and how this could be monitored.

3.5.4 Conclusion

Although little useable data was acquired through this preliminary experience, it has shown some key factors in the measuring process:

1. An initial distribution analysis and comparison with the standard spectrum is critical to ensure only unsaturated, correct data is used.
2. A stable condition assessment is required to ensure that condition is not to variant to ensure for good measurements.
3. A 5 % stable condition requirement is an adequate initial error limit for the assessment according to the variance seen in reference data.
4. The colour content or spectral quality of the spectra can be calculated.

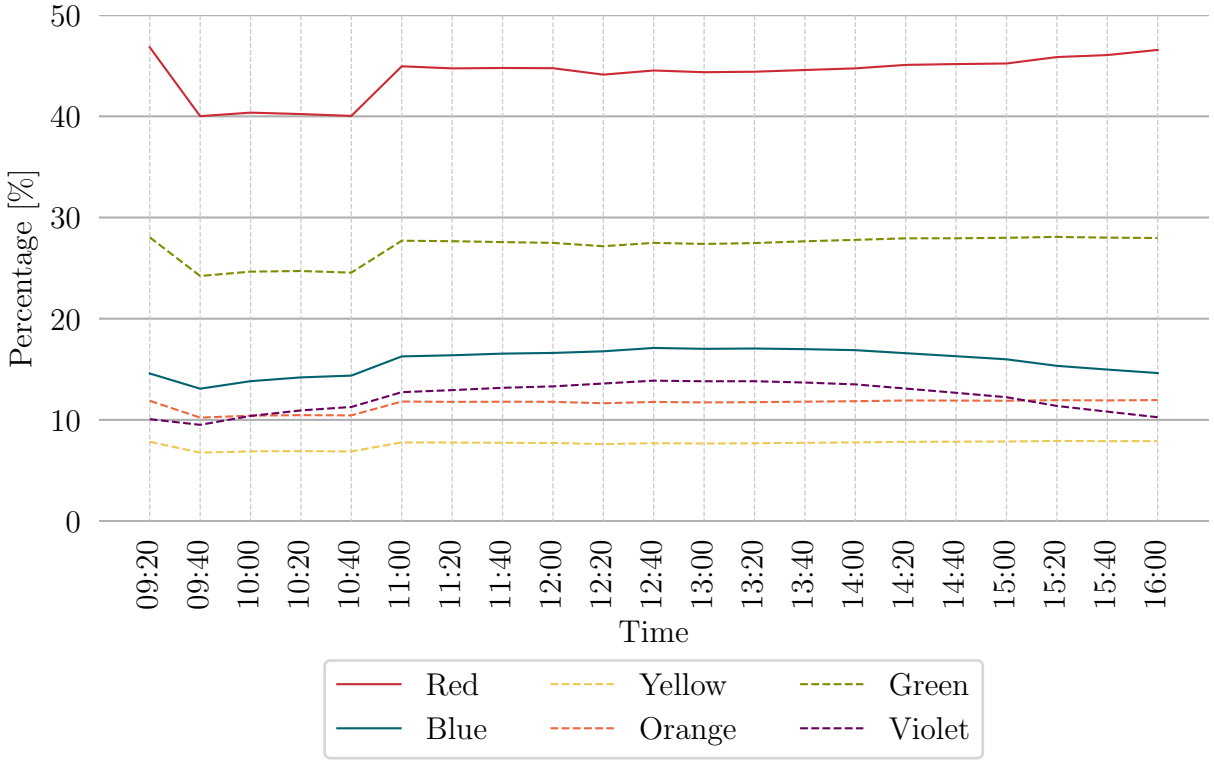

Figure 3.18: Colour content of visible light within a measurement per 20 minutes.

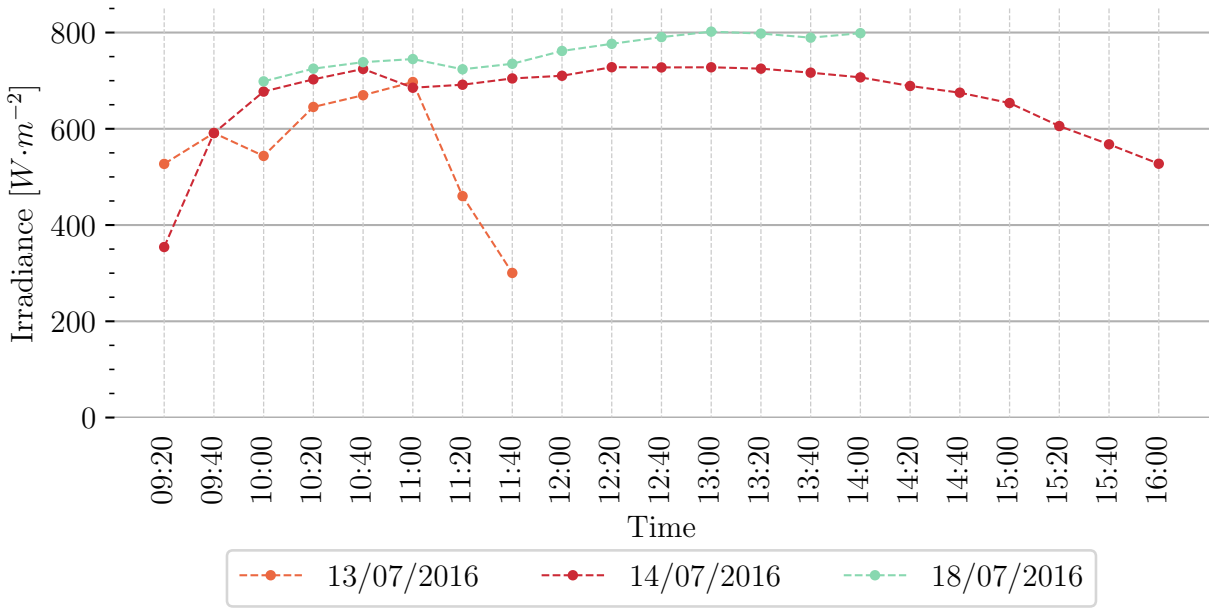

Figure 3.19: Total calculated irradiance over three days in July.

Figure 3.19 is additional to complete this section on baseline measurements. Most markers and observation have already been discussed regarding these graphs. In their totality they do however show how quickly the measurements will vary when cloud coverage is present. Especially since most of the measurements within this project was completed within winter months, the data sets will undergo multiple stages of sifting before presenting them; without critical selection, the data can very easily seem overwhelming and unusable.

This preliminary experience created an opportunity to explore the spectrometer and its capabilities, as well as spectral analysis in all its forms. These, and more, techniques was used further to analyse the following preliminary experience as well as the final automated tests.

3.6 Glass Transmission

As mentioned previously, the optical properties of glass are not constant and it is therefore anticipated that the clean glass samples will have some influence on the measured direct beam irradiance. The glass is classified as clean when it is wiped for any visible particles but has not been buffed or polished to remove minor scratches and fine imperceptible particles.

The glass samples used are un-tempered $4\,mm$ low-iron float glass. To determine the effect of the clean glass on the measured irradiance, the spectrometer receptor is directed towards the sun and 6 samples are taken in a 1-minute time span - firstly two samples without glass, two with glass and again two samples without. This method ensures that the conditions are indeed stable over the measurement, as indicated before, and the true effect of the clean glass sample can be determined.

Although the 5 % stable condition requirement is a good initial condition, it would mean that the transmission loss of the glass can only be determined within a 5 % error margin. Further, to determine the transmission loss of the glass averages are used, which could also incorporate some loss in the calculation. Table 3.3 shows an example of the calculation process applied to each measurement set.

Table 3.3: Calculation of errors and glass transmission loss for a measurement set.

10:10	Total Irr.	Errors	Base Error	Glass Mean	Rel. Error	Base Mean	Rel. Error	Diff.	Spec. Diff.
B1	788.485	0.049					0.212		7.891
B2	788.103						0.2607		7.8466
G1	726.547	0.079	0.450	737.278	0.066	790.163		8.087	
G2	725.981				0.039				
B3	792.016	0.004					0.264		8.302
B4	792.047						0.238		8.305

The first column shows each measurement within the set; "B" is for the baseline measurement and "G" for the glass measurement and the order in which it is displayed is the order of measurement - B1 is always the first measurement and B4 always the last within the set. The second column, Total Irr.(irradiance) displays the calculated total irradiance through integration in $W{\cdot}m^{-2}$. The third column is the error between B1, B2 and G1, G2 and B3, B4 as a percentage. The next column is the baseline error between B1 and B4. The glass mean is the average total irradiance value as calculated from G1 and G2, with the following column the error between this average value and the original total value. Similarly, the Base Mean is the average value between all four baseline measurements with the following column the error between this average and the original value. Next is the final difference or loss calculated between the glass and baseline measurement. The last column is simply the transmission loss without taking the average baseline value into account - this supplies an overview of the effect of using an average value.

The process explained above was applied to all measurement sets on 14 July - the sets with no difference $> 1\,\%$ is shown in figure 3.20.

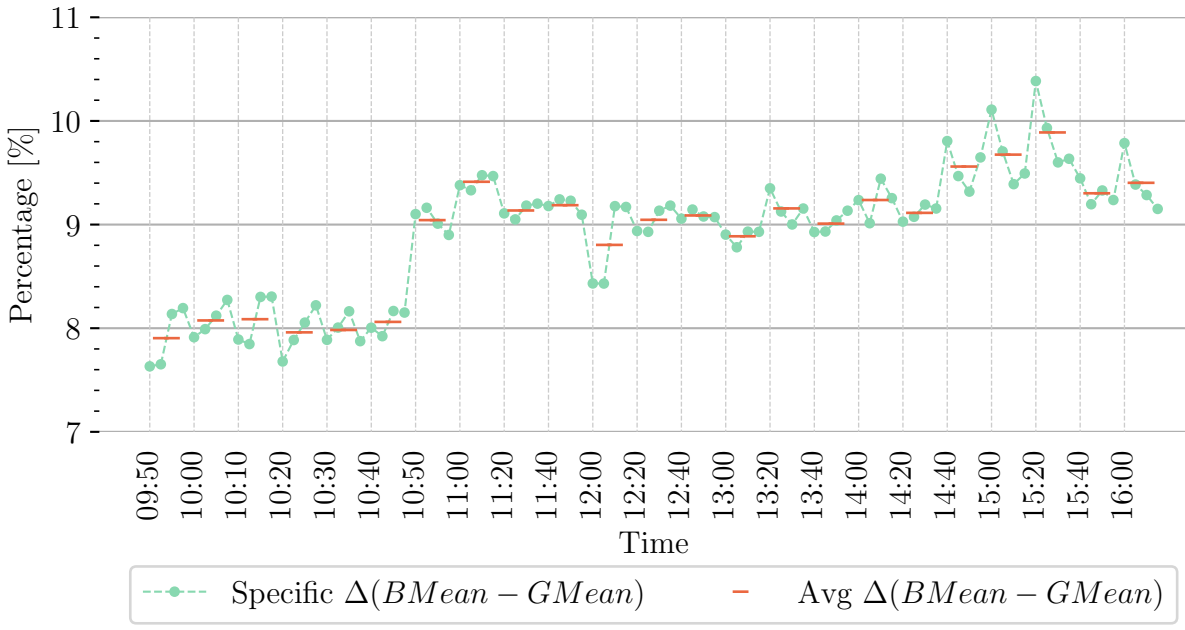

Figure 3.20: Summarising graph of errors and glass transmission loss on 14 July.

Even with the differences being smaller than $1\,\%$, the specific differences variated up to $0.496\,\%$ from the average difference calculated. The smallest difference was calculated as approximately $0.001\,\%$, with a calculated difference between baseline and glass $9.236\,\%$ - this was calculated at 14:00 on 14 July. This is the approximated transmission loss for the solar glass, calculated with direct transmission on 14 July 2016.

Further, as in figure 3.21, on 18 July the minimum difference between the specific difference and the average difference, as previously, is calculated as $0.004\,\%$, with the calculated difference being $9.125\,\%$. This only differs with $0.111\,\%$ from the previous calculated difference of $9.236\,\%$.

On 18 July, the measurement set was extended to include two measurements of a slightly soiled low-iron float glass sample. The idea with these measurements were not to quantify the amount of dust on the glass but rather only to show that quantifying soiling on glass is possible with this method of analysis. The glass sample was simply left outside in a horizontal position for approximately two weeks at the location of the final measurement setup. This resulted in minor dust particles that are visible - the soiling was less than anticipated since rain was present for approximately three days within the two-week period. The glass was specifically left in a horizontal position to increase the soiling process.

The soiled-glass measurements are not anticipated to be consistent - according to theory, the particles could absorb, reflect and diffuse the light beams in a multitude of ways that would influence the amount of light passing through the glass sample. This could theoretically cause a variant soiled-glass measurement; this is observed in figure 3.21 at 10:20. At this time period the difference error was only $0.102\,\%$, still it differs with approximately $3\,\%$ of the other soiled glass measurements. The measurement mentioned before (13:00) with the smallest error of $0.004\,\%$ indicates an increase of transmission loss by soiling with $0.988\,\%$.

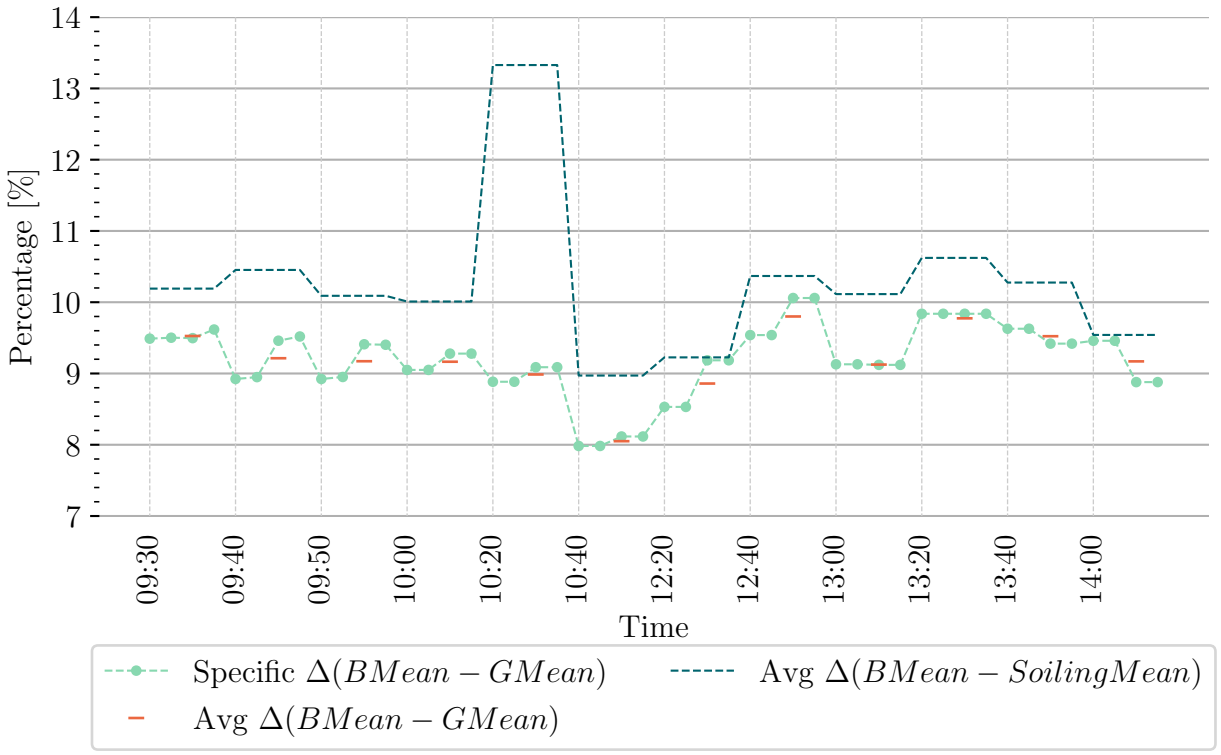

Figure 3.21: Summarising graph of errors, glass transmission loss and soiling loss on 18 July.

Returning to the analysis of the clean glass sample: since the analysis of spectral distribution is the main objective of this project, it is also important to observe the distribution of irradiance measured through the glass sample. Perhaps the simplest method to analyse the spectral distribution is to multiply each 0.5 nm wavelength step of the baseline measurement with the a glass transmission response graph. This response graph is shown and discussed in Chapter 5, to follow. Since the errors were the smallest at 14:00 on 14 July, the first baseline measurement (B1) from this specific measurement set was used to calculate a theoretical glass impact, plotted in figure 3.22.

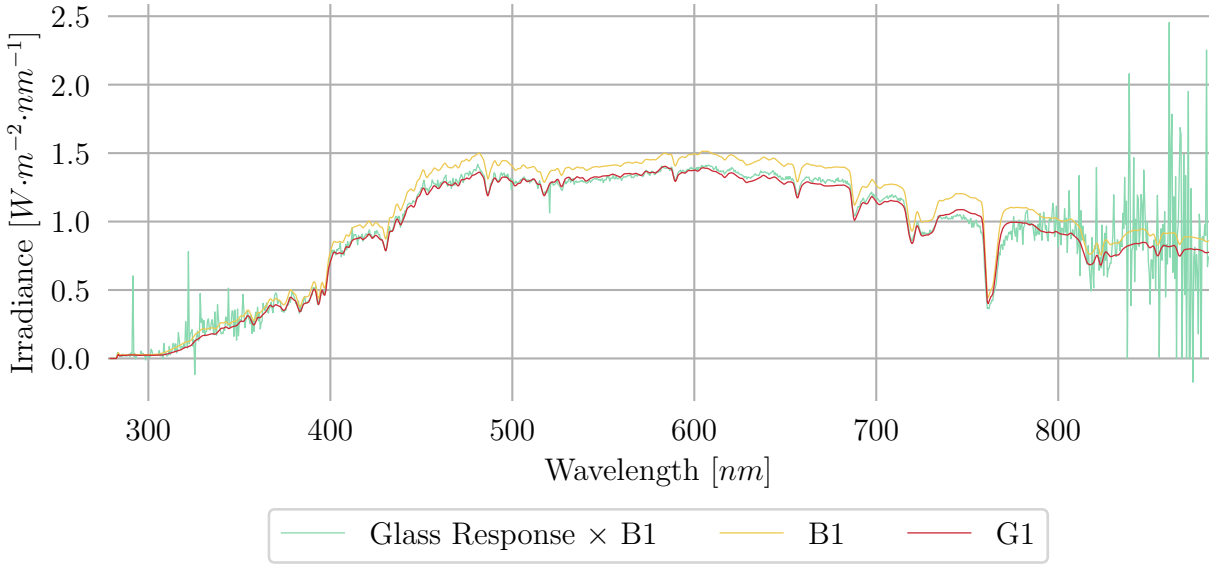

Figure 3.22: B1 and G1 measurement sample with a calculated glass response.

The graph simply spans from 278 to 882.5 nm since the glass response distribution only spans for this wavelength band. The noise observed is also discussed in the next chapter but it can be observed that approximately 350 nm and 770 nm - in this specified range the theoretical glass transmission is very similar to the actual measured glass transmission. The maximum error is calculated as approximately 0.1 %.

In conclusion to the first preliminary experience: although few measurement sets were collected and even fewer usable, some important observations were made in regard to spectral analysis. Further, within a set the clean glass transmission loss were approximated to 9.236 % with seemingly insignificant soiling contributed to another approximate 0.988 % loss.

These techniques and methods is applied further to measurement sets collected in various setups, to validate their use again and to perhaps extend the analysis methods.

Chapter 4

Preliminary Field Experience II

4.1 Instrumentation and Setup

A second preliminary experience with non-automated relative transmission loss measurements were completed on Kalkbult in the Northern Cape of South Africa, mid October 2016. Kalkbult is a good example of semi-arid conditions where fine dust particles are prevalent, paired with little rain fall and strong wind gusts. These measurements were similar in their purpose to determine the relative transmission loss, but differed to the previous experience since the measurements were at a fixed angle of 30° - the angle of the fixed glass plane. Considering this, the measurements will vary more since the receptor was not directed towards the sun location.

Arid environments can only unquestionably be described through aridity, since in most other aspects they are quite diverse. The aridity is described through the amount of rainfall and temperature prevalent in these environments. Since the precipitation in Kalkbult is approximately $300 - 400\,mm$ annual, it is characterised as a semi-arid environment.

The worth of this experience was the addition of a second spectrometer from Spectral Evolution, this supplied two sets of data measured simultaneously with differing equipment. This addition of a second spectrometer allows for the comparison of the instrumentation as well as confirming the results collected by either of the spectrometers. A comparison of technical specifications of the two used spectrometers is supplied in table 4.1. Similar to the BlueWave spectrometer, the PSR-1100F is also factory-calibrated according to a NIST-traceable source for irradiance.

Table 4.1: BlueWave and Spectral Evolution spectrometer technical specification comparison.

Specification	**BlueWave StellerNet**	**PSR-1100F Spectral Evolution**
Detector	$2048\,pixels$	$512\,pixels$
Digitiser	$16 - bit$	$16 - bit$
Range	$278 - 1100\,nm$	$320 - 1100\,nm$
Slit Size	$25\,\mu m$	$50\,\mu m$
Resolution	$1.0\,nm$	$\leq 3.2\,nm$
Integration Time	$1 - 6500\,ms$	$8 - 2000\,ms$

As mentioned, the glass was mounted at 30° in a fixed frame - the frame was designed to hold

approximately 200 low-iron float glass samples, the samples used in the previous example, as well as two large solar glass panes, as seen in figure 4.1. The large solar glass pane used is similar to the pane used for the final measurements and is a 3 mm thick full-size PV module glass covering supplied by First Solar.

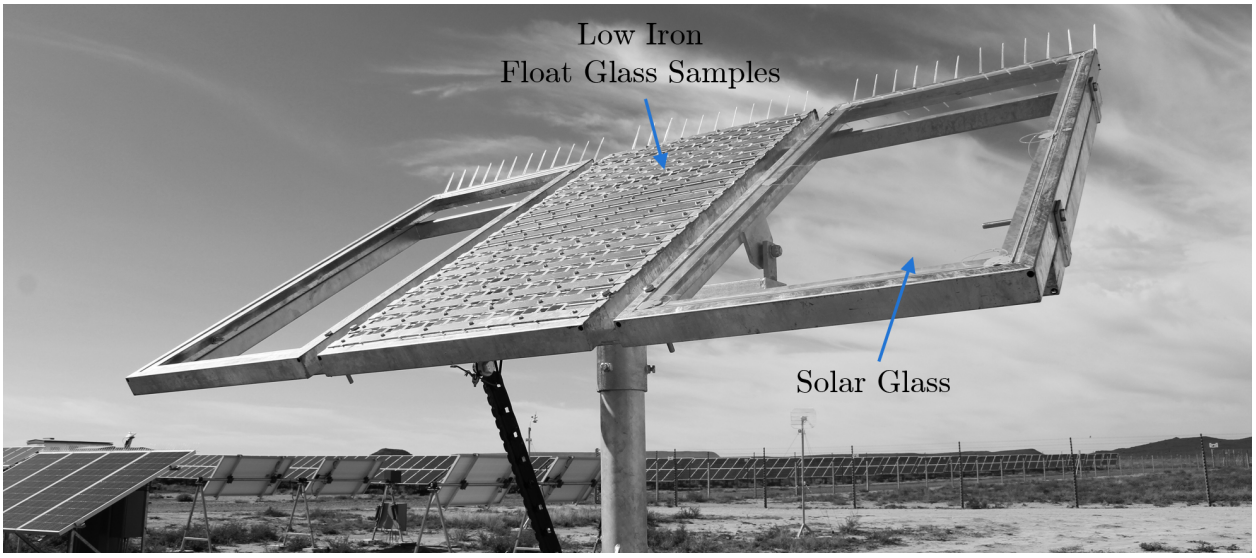

Figure 4.1: Glass frame setup for low-iron float glass samples and a solar glass pane.

A drawback of the glass frame is that it is quite reflective, also the frame casts shadows over the measuring area late afternoon. The middle pane with the low-iron float glass samples was designed so that the glass samples could be removed without interfering with the soiling process of any other glass sample. The measurement locations for each type of measurement were kept as constant as possible to ensure that similar type of reflections and shadows will occur, so as to measure the true circumstances.

4.2 Results

Although the main idea with this preliminary experience was relative transmission measurements, some insight to the following is also supplied through this experience:

1. How FOV influences the measurements and how it corroborates what was assumed previously.
2. How the daily baseline measurements will differ from the baseline measurements acquired with positioning towards the sun position.
3. How the APE or colour might differ because of this fixed measuring angle.
4. If the small glass test could be repeated, to show similar results to the first experience.
5. The transmission loss of the large solar glass.

Where possible, the analysis method was kept similar to that of the first experience to ensure repeatability and ensuring ease in comparing the various experiences.

4.2.1 Field of View

Another advantage of the addition of the PSR spectrometer is its various attachable receptors: 5°, 25° and 180° FOV receptors. So, although the BlueWave only has a 180° FOV receptor and it was assumed that this was the best FOV to use for the application, figure 4.2 confirms that the 180° FOV is indeed the most suitable angle to use.

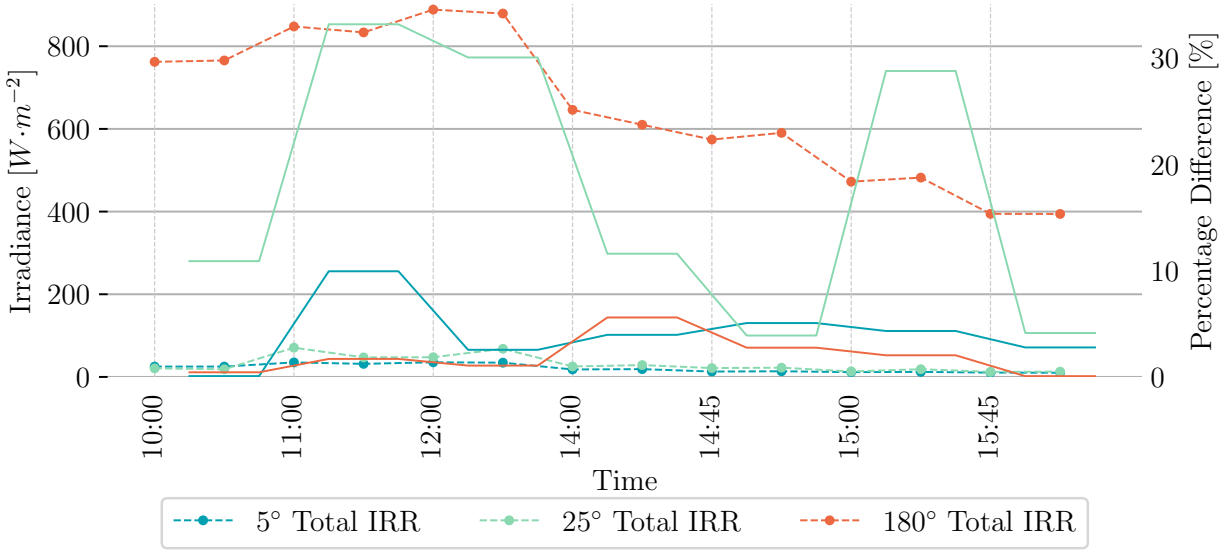

Figure 4.2: Three measurement sets with various FOV as measured by the Spectral Evolution PSR-1100F spectrometer; solid lines represent percentage difference.

A 180° FOV is most suitable since it is the only, of the three tested, that supplies a total irradiance anything similar to the expected GHI (Global Horizontal Irradiance) - this is later confirmed in figure 4.7. As seen in figure 4.2, the 180° FOV supplies total irradiance values almost 10 times the irradiance the other two FOV's supply, simply because the 180° FOV measures, in effect, a larger "area" of light. The 5° or 25° FOV would have been more suitable if the receptor were directed towards the sun location, as in the previous experience. It can also be seen in the figure 4.2 that the 180° FOV supplies more stable baseline measurements than the other FOVs; the 25° FOV supplies particularly variant measurements. Further, only data with the 180° FOV is used for analysis.

4.2.2 Daily Measurement

Similar to the process followed in the first field experience, the distribution and stable conditions are established for both spectrometers. First, baseline measurements between the two spectrometers are compared - in figure 4.3 the spectral data is plotted for the minimum wavelength range of the PSR-1100F. Several observations are required; although the response seem similar, some discrepancies is noted, especially for the BlueWave spectrometer: Firstly, the BlueWave shows some saturation again in the band of $500 - 600\,nm$ and shows an increasing trend in $1000 - 1000\,nm$ - both these discrepancies have been discussed in the first preliminary experience. Secondly, the BlueWave measured higher total irradiance values than the PSR, approximately $14.8\,\%$ higher. In figure 4.4 it is observed that that the difference is between 0.5 and $-0.5\,W \cdot m^{-2} \cdot nm^{-1}$ - the two spectrometer measurements are closest in response in $800 - 900\,nm$.

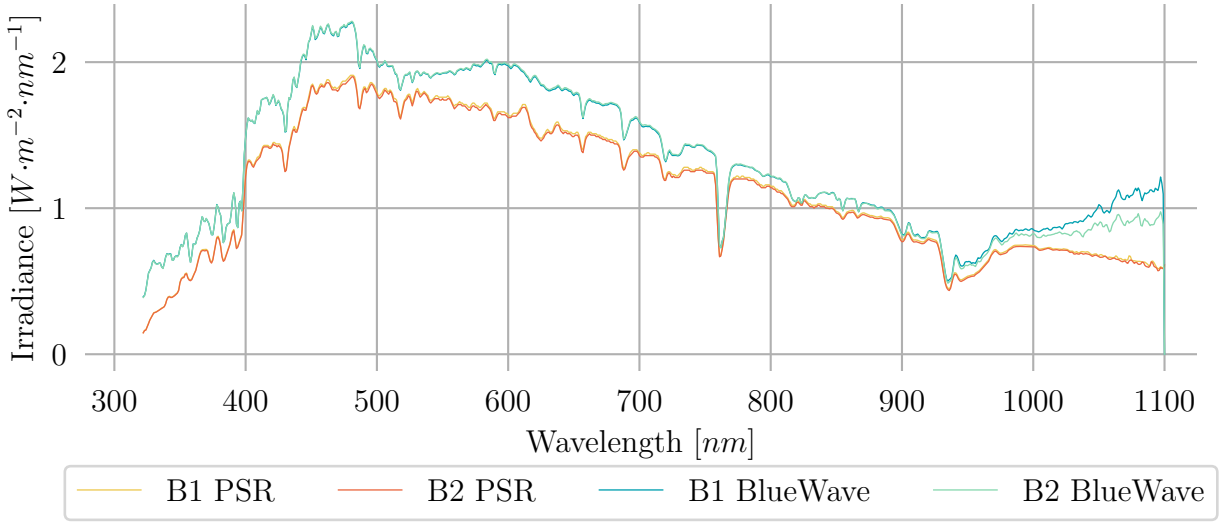

Figure 4.3: Two baseline measurements acquired per spectrometer on 17 October 2016 at 11:50 with 180° FOV.

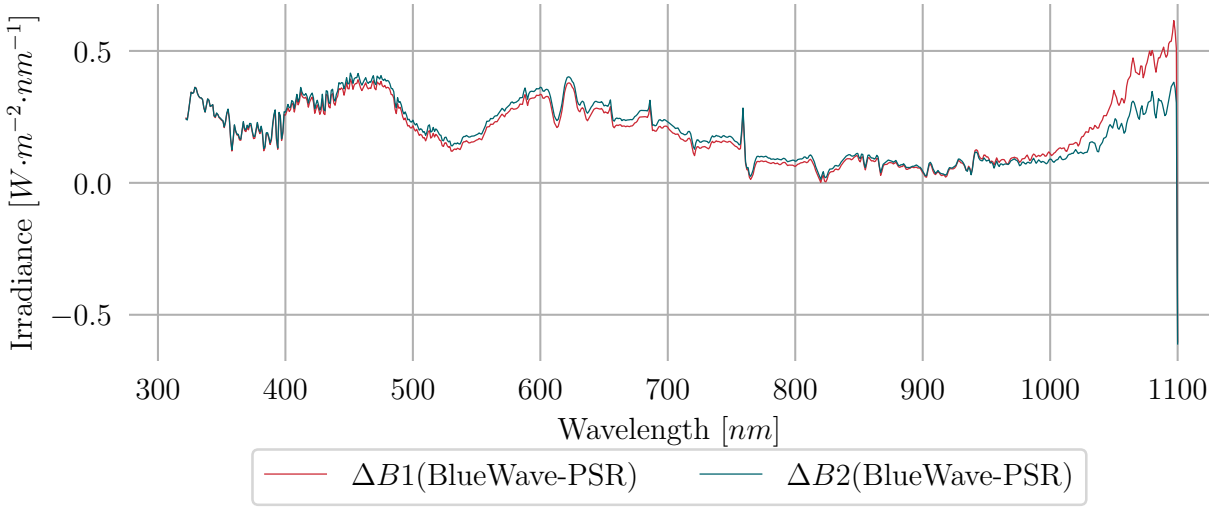

Figure 4.4: Calculated difference between the spectrometer measurements on 17 October 2016 at 11:50 with 180° FOV.

Although the two spectrometer measurements differ quite significantly in value, their data can be used separately since the distribution in each is constant throughout the measurements. Consequently, the data of each spectrometer is presented separately.

The total baseline irradiance values, as well as the baseline errors are presented in figure 4.5 and 4.6. From the BlueWave measurements it can be seen that three sets do not conform to the stable condition requirement and only four sets have an error less than 1 %. The irradiance values measured are significantly higher than measured before - in the first experience no irradiance values exceeded $900\,W \cdot m^{-2}$ but an increase in irradiance values are expected since this second location is closer to the equator and therefore higher irradiance values are prevalent.

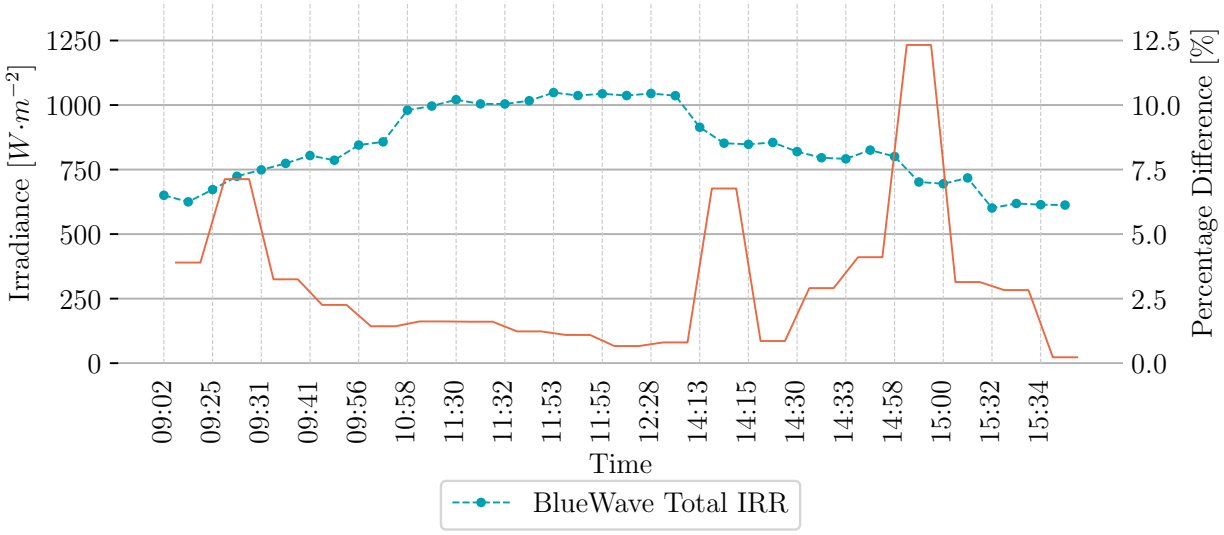

Figure 4.5: Calculated totals and errors with the BlueWave spectrometer measurements on 17 October 2016 with 180° FOV.

Considering the measurements acquired with the PSR, the total irradiance values measured has a minimum value lower than measured in the first experience - this is possible since the measurement was not in the direction of the sun position. Now these contradictory statements do not allow for the confirmation if either the PSR or BlueWave has measured total irradiance values closer to the true GHI value.

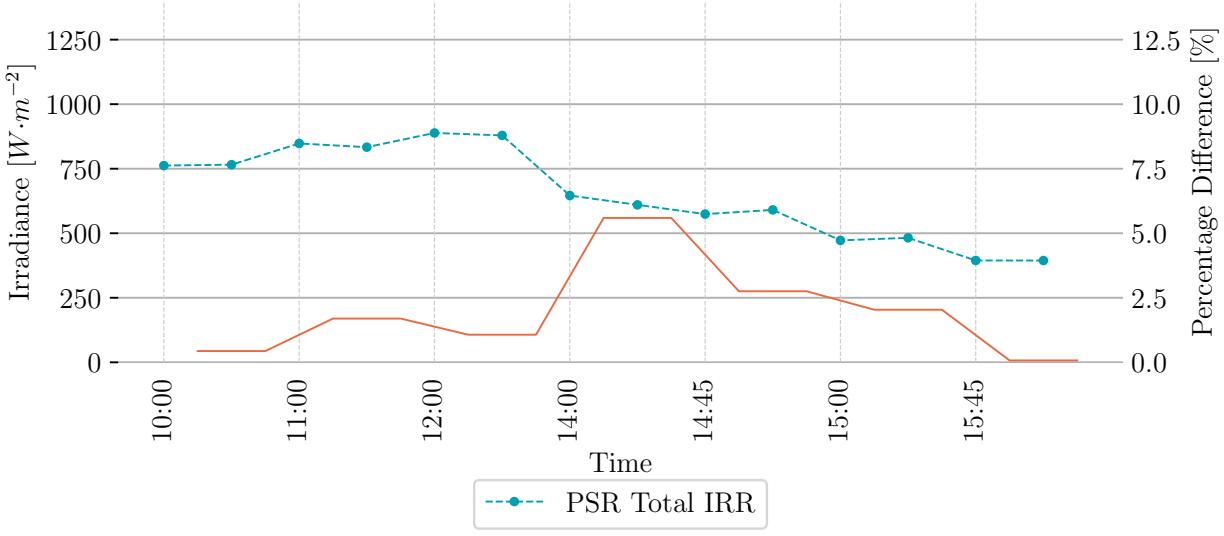

Figure 4.6: Calculated totals and errors with the PSR-1100F spectrometer measurements on 17 October 2016 with 180° FOV.

Unfortunately, no GHI values for the experience period was located to confirm which spectrometer total irradiance values are more accurate, but as an approximation GHI values of October 2014 was used from GeoSun Africa [69]. Figure 4.7 presents a period in October 2014, similar to the experience period in 2016; the first day presented was variant with the next two clear. As 17 October 2016 was a clear day, 17 and 18 October 2014 can be perceived as a good approximation for this day in 2016. Observing the data from 2014, the

values correlates better with the measurements of the BlueWave spectrometer than that of the PSR.

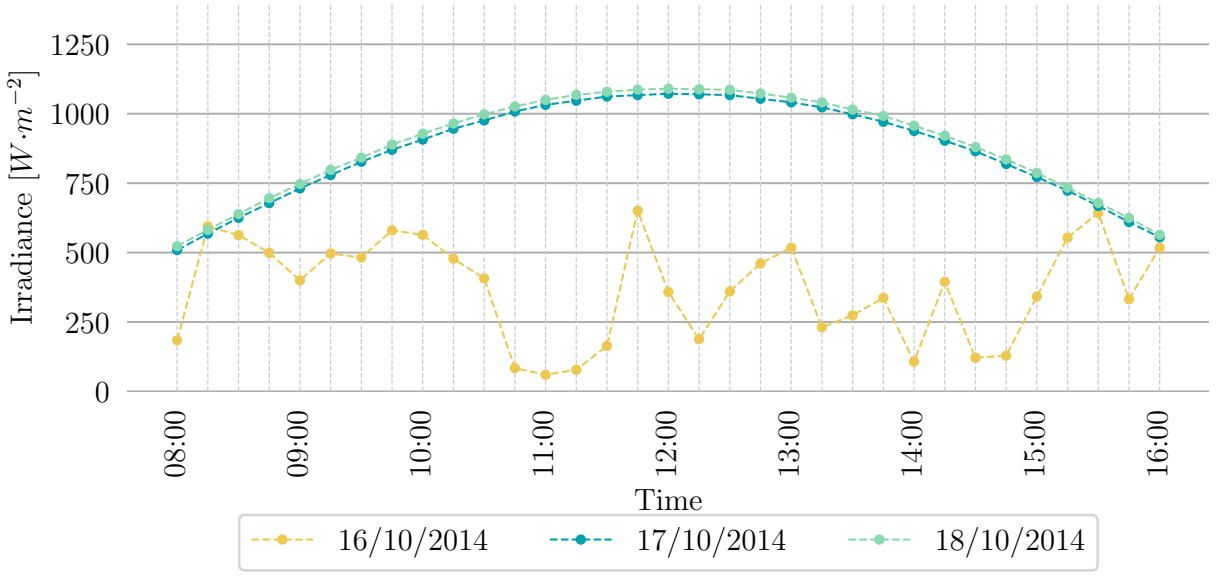

Figure 4.7: Global Horizontal Irradiance by GeoSun on three days in October 2014.

Even though the PSR measured lower irradiance values, within its own measurements some correlations can still be confirmed, supplying additional relative transmission data. Since the measurements were acquired through a constant angle of 30° from the ground plane, it is expected that additional variance will be observed. Figure 4.8 indicates this variance where difference in baseline measurement decreases towards solar noon - similarly it will increase from noon to evening. Previously, the noise regions of the spectrometer was indicated, this also shows in the calculated difference where the difference is quite constant in approximately $400 - 900\,nm$, with a singular valley in $500 - 600\,nm$ as a result of saturation.

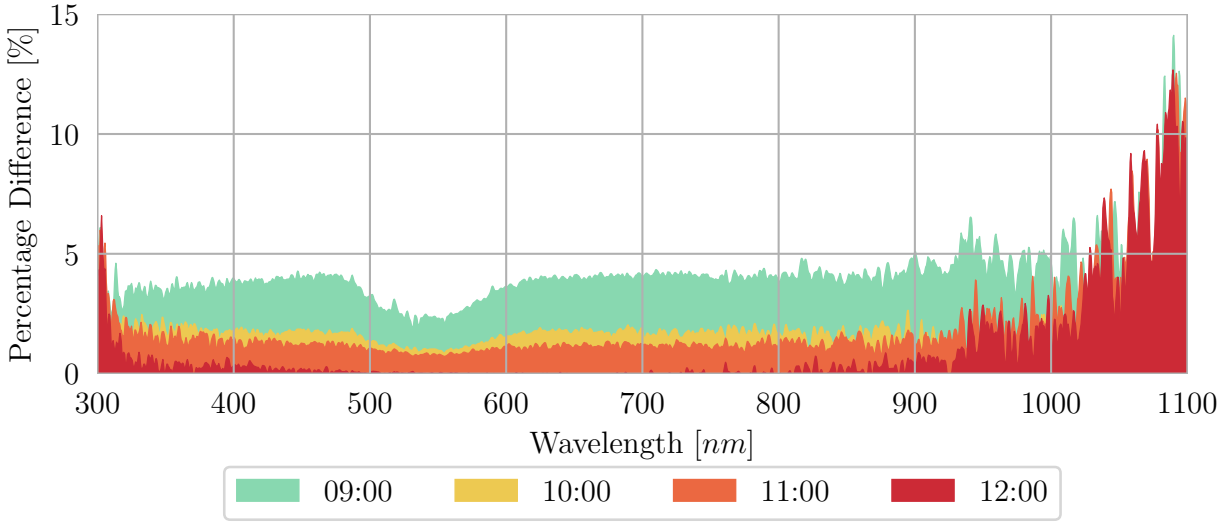

Figure 4.8: Percentage difference in baseline measurements across the spectrum, calculated from the BlueWave data.

Furthermore, observing then the calculated APE for both the PSR and BlueWave data in figure 4.9, the APE for the BlueWave spectrometer is naturally higher since the irradiance values were higher. The maximum APE calculated from the BlueWave data is 1.91 eV, where the standard value is 1.88 eV as mentioned previously. Still, this higher APE is probable since the location is closer to the equator than Stellenbosch.

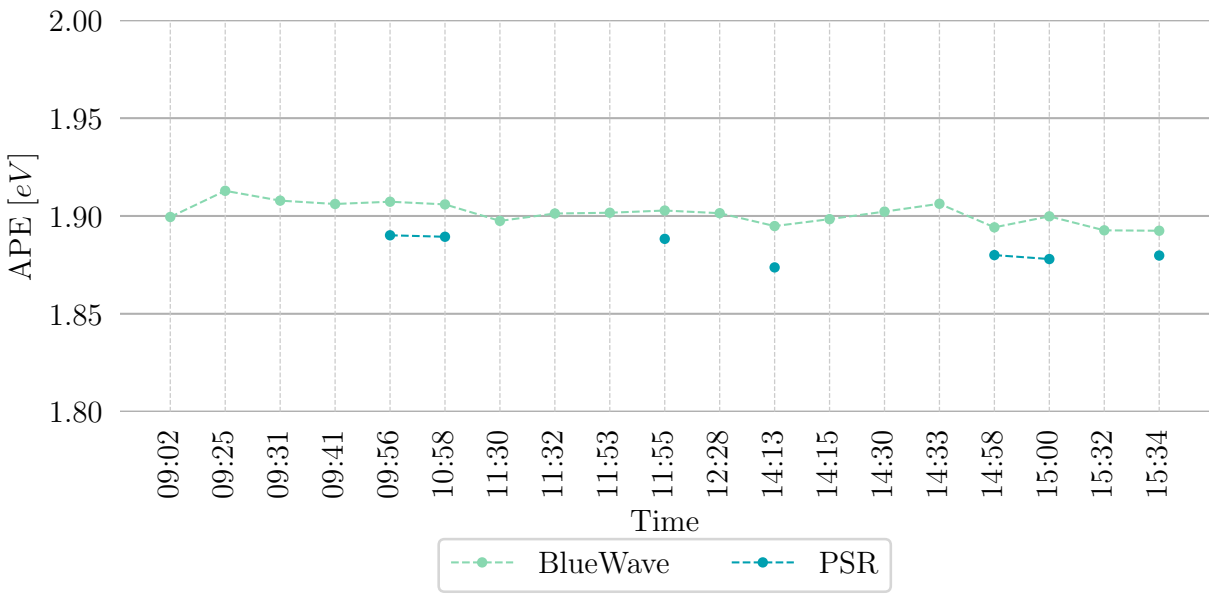

Figure 4.9: Calculated average photon energy on 17 October 2016 with both the BlueWave and PSR spectrometers.

Stable conditions and realistic total irradiance values have now been confirmed for the measurement in this experience. Next, these datasets are implemented in the relative transmission loss method to determine the contributing effect of the low-iron float glass, solar glass and some soiling. The process followed with these measurements are similar to the relative transmission loss of the previous experience.

4.2.3 Glass and Soiling Transmission

The clean low-iron float glass samples were only tested with the BlueWave spectrometer. Figure 4.10 is a summary of the specific and average relative transmission loss total calculated of the sets where the baseline irradiance measurements conform to the stable condition requirement, so the error is less than 5 %. The graph also indicates the two sets where the specific errors within the set where less than 1 %. These two average values for relative transmission loss of the samples was calculated as 8.722 % and 8.166 %, individually. Looking back at the first preliminary experience, the transmission loss of those samples were calculated as between approximatly 9.125 % and 9.236 % - less than 1 % higher than calculated within this experience. Considering that this second experience measured relative transmission loss with a fixed angle and the varying sun position, this is still a successful approximation. Similar the to the calculated small glass distribution figure in the previous chapter, a response was calculated with the laboratory transmission distribution, again the results were similar.

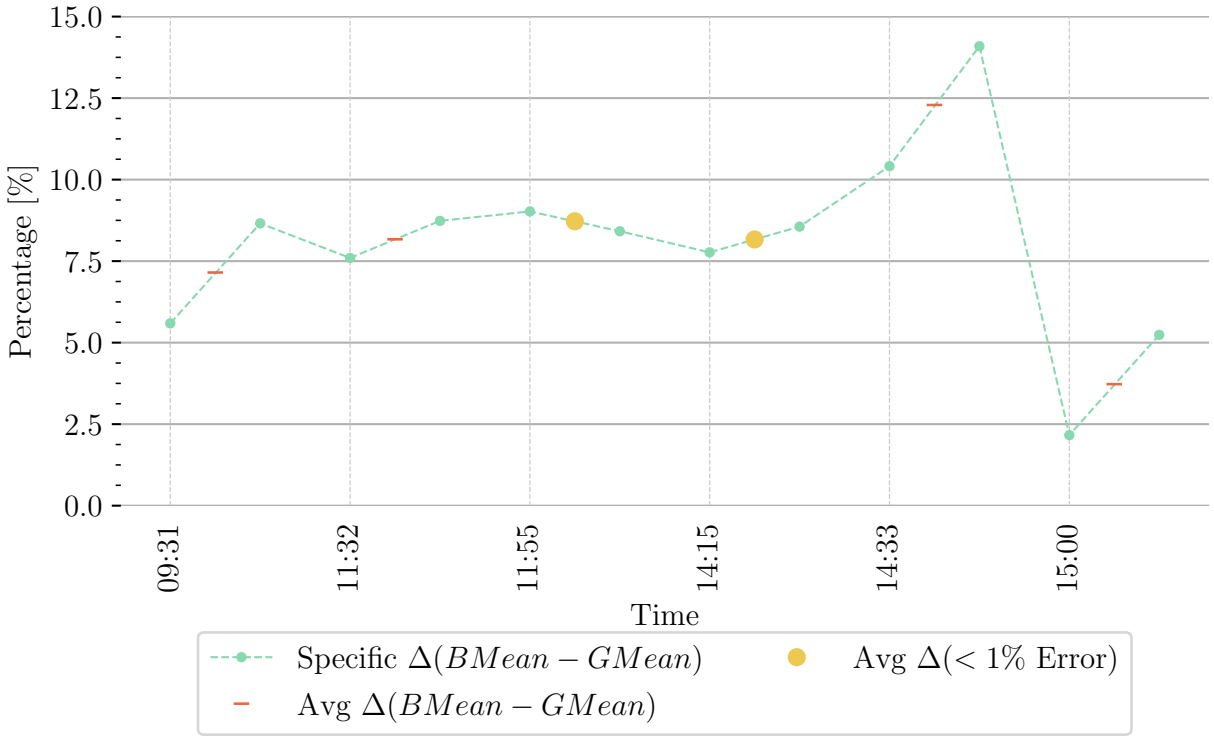

Figure 4.10: Selected calculated relative transmission loss of low-iron float glass samples with the BlueWave.

Next the large glass, for both the PSR and BlueWave spectrometers, are analysed. Unfortunately, the experience was too short to acquire extensive soiling measurements still, half of the solar glass sample was cleaned before the measurements. The soiling half can be described as spots of a water-dust combination leaving visible but faint particles - the contribution of strong wind gusts and a few scattered rain drops over three days.

Figure 4.11 at first glance indicates that a test at a constant angle, not directed towards the sun position, does indeed cause additional variation. 14:13 as well as 14:58 had baseline errors larger than 5 % and only 12:28 had all errors smaller than 1 %, this simply means that less constant data is available to analyse. The figure also indicates the two measurements with the lowest errors: 12:28 and 11:53 (with errors just over 1 %) still, even though their errors only differ slightly, their calculated average difference between the baseline and glass measurements differ with 3.052 %. Furthermore, it is expected that the solar glass will have a smaller effect on transmission loss than the low-iron float glass samples, therefore a conclusive value for the relative transmission loss of the solar glass cannot be supplied through these relative measurements from the BlueWave spectrometer.

Between approximately 11:09 and 15:17, the percentage difference calculated through the PSR and BlueWave data are quite similar, indicating that the wildly varying transmission loss is not caused by the instrumentation but rather the measuring circumstances. The PSR's measurements with errors all less than 1 % however, are located at other positions: 10:20 and 15:45 but the difference between their calculated transmission loss percentages vary even more than that of the BlueWave measurements. Separately, the transmission loss of the glass were calculated as 9.31 % and 1.9694 % as seen in figure 4.12 - this could be since the angle of the sun has a significant effect on the transmission of the glass although this cannot be confirmed as yet.

Still, it is reasonable to expect that the soiling might increase (increased absorbance) or decrease (increase deflection) the transmission with a change in angle in light. Perhaps not as obvious in figure 4.11 is that some average soiling transmission loss values were actually less than that of the clean glass, indicating perhaps that the soil particles aided the transport of light beams through the solar glass - this is more obvious in figure 4.12 where the soiling sample's transmission loss is approximately 2 % lower than that of the clean sample with an error smaller than 1 %.

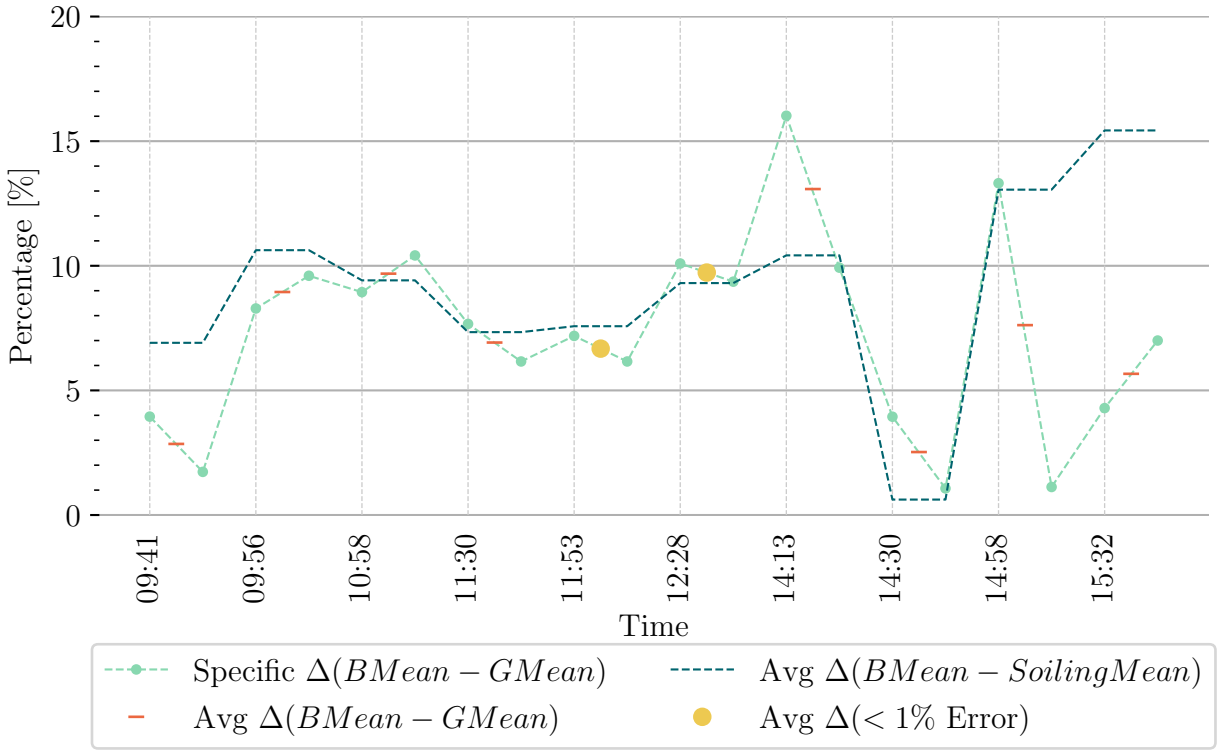

Figure 4.11: Calculated relative transmission loss of solar glass and soiling loss with the BlueWave.

The spectral transmission curve of the solar glass (as in the previous preliminary experience) were multiplied with the average baseline measurement and compared to the measured glass distribution in figure 4.13. Unlike the distribution comparison in the first experience which had a maximum error of 0.1 % in the constant specified range, the solar glass response has a total difference between the measured and calculated of approximately 4.7 % with both the PSR and BlueWave measurements. This larger error is not only limited to the solar glass, the distribution of the low-iron float glass showed a 2 % difference between the calculated and measured.

In conclusion: the second preliminary experience had additional variance within the measurements, as a result of the fixed measuring angle, but since the final automated system will also consist of a fixed measuring angle, it was important to investigate the effect of a fixed angle versus a moving angle. In addition, the measuring setup was not ideal and this caused additional variation within the measuring environment - additional ground and frame reflections were prevalent. Also, even though few glass and soiling measurements were available within this experience, it was shown that relative transmission loss measurements are possible within the field.

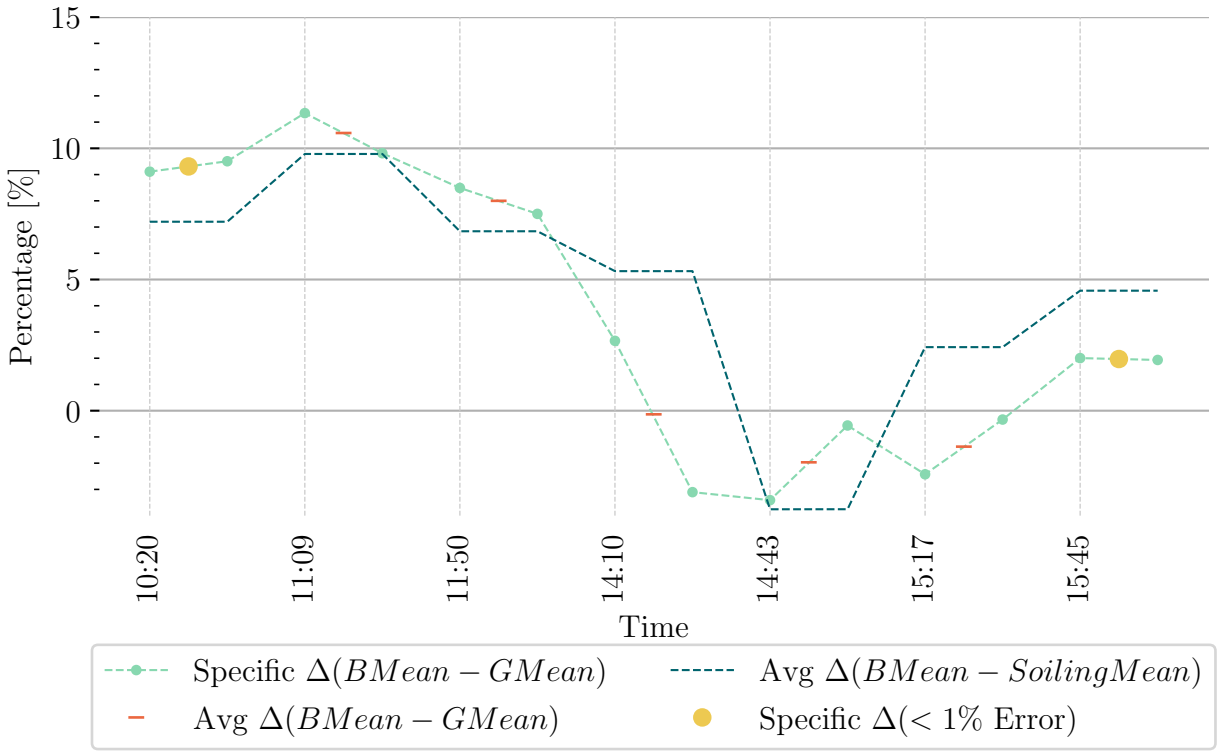

Figure 4.12: Calculated relative transmission loss of solar glass and soiling loss with the PSR-1100F.

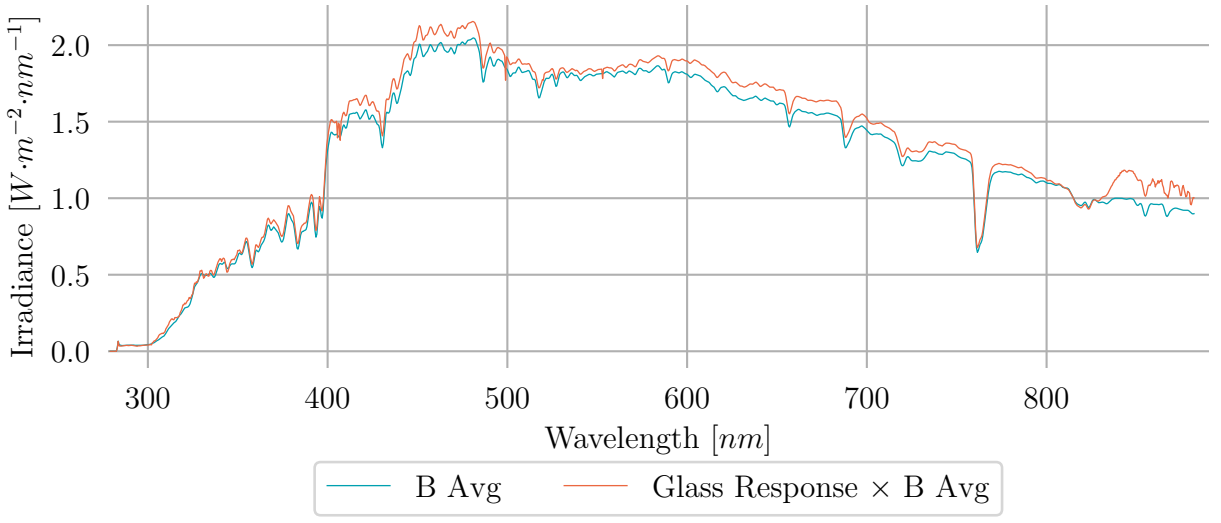

Figure 4.13: Baseline average at 12:28 (error $< 1\,\%$) with the calculated glass response from a sample distribution curve with the BlueWave.

Chapter 5

Laboratory Experience

5.1 Transmission Test

After the two preliminary measurement events in the field, it was realised that the spectrometer response could perhaps be better understood through measurements in a controlled environment with a constant light source.

The first of the laboratory tests were completed by Dr Anton du Plessis from Stellenbosch University's Central Analytics Facility (CAF). The USB2000 Ocean Optics spectrometer was used for this transmission test; its technical specifications are listed in table 5.1. The resolution can be determined from the grating and slit size of the spectrometer - these values are unknown. Fortunately, this spectrometer was only used for measuring transmission, as explained below.

Table 5.1: USB2000 Ocean Optics spectrometer technical specifications.

Ocean Optics	**USB2000**
Detector	CCD, 1×2048 pixels
Wavelength Range	$150 - 800nm$
Integration Times	$3 - 3000ms$
Dynamic Range	$2{\times}10^8$
SNR	250 : 1
Stray Light	$< 0.5\,\%$ at $600\,nm$; $< 0.1\,\%$ at $435\,nm$

Rather than determining the transmission from reference measurements, as in the previous field tests, the transmission function of the spectrometer was used, supplying a percentage transmission per wavelength. This test was completed without a fibre optic connection, but rather the glass was place directly against the slit opening of the spectrometer.

Rather than try to simulate solar irradiance in a laboratory setup, a constant light source was used, a Halogen light source (HL-2000-FHSA) from Ocean Optics. This same light source was used for all laboratory tests further discussed. The light source specifications are supplied in table 5.2.

Table 5.2: Halogen light source HL-2000-FHSA specifications.

Ocean Optics	**HL-2000-FHSA**
Source	Long Lifetime Tungsten Halogen
Wavelength Range	$360 - 2400\,nm$
Colour Temperature	$2960\,K$
Stability	$0.5\,\%$

Figure 5.1 displays a 100% transmission baseline - this allows for the determination of the wavelength range where little to no noise is experienced from the instrument. This wavelength range is approximately $480 - 850\,nm$.

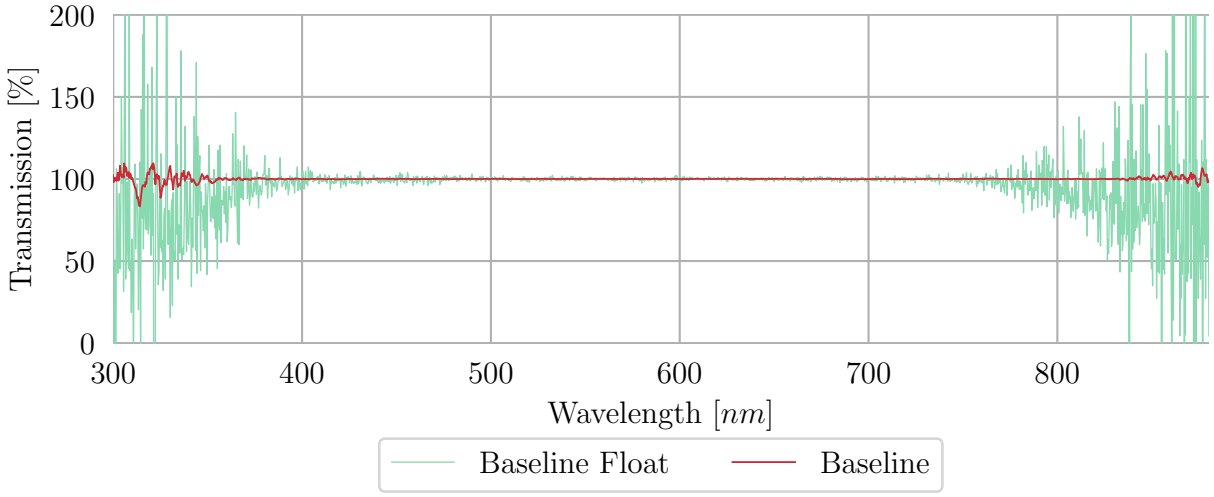

Figure 5.1: Laboratory transmission baseline measurements at two different measurement occasions.

The transmission data of three types of glass were supplied, data for: $4\,mm$ low-iron float glass sample, $5\,mm$ "lab" glass and finally $3\,mm$ solar glass - the solar glass is the glass sheet that will be used in the final measurements. The float glass sample tests were completed on a different occasion, with the same equipment but as light measurements are extremely reliant on environmental conditions, even in a laboratory setup, a baseline is required.

Figure 5.1 shows as expected; the two different measurement occasions have varying responses, even though the setup was similar. The "Baseline Float" is the baseline measured before the transmission of the float glass sample was measured - the other baseline was captured before the measurement of the solar and lab sample. Furthermore, figure 5.2 supplies a detailed response for the baseline transmission, where the float baseline is riddled with noise whereas the second baseline is quite linear and smooth.

The noise on the baseline could be ascribed to external light influencers, or the increased temperature of the Halogen light source. Even though these baselines are dissimilar, it is useful when observing figure 5.3. The great variation observed in the transmission plot for the float glass can be ascribed to external factors rather than mistakenly ascribing it to the glass sample's response.

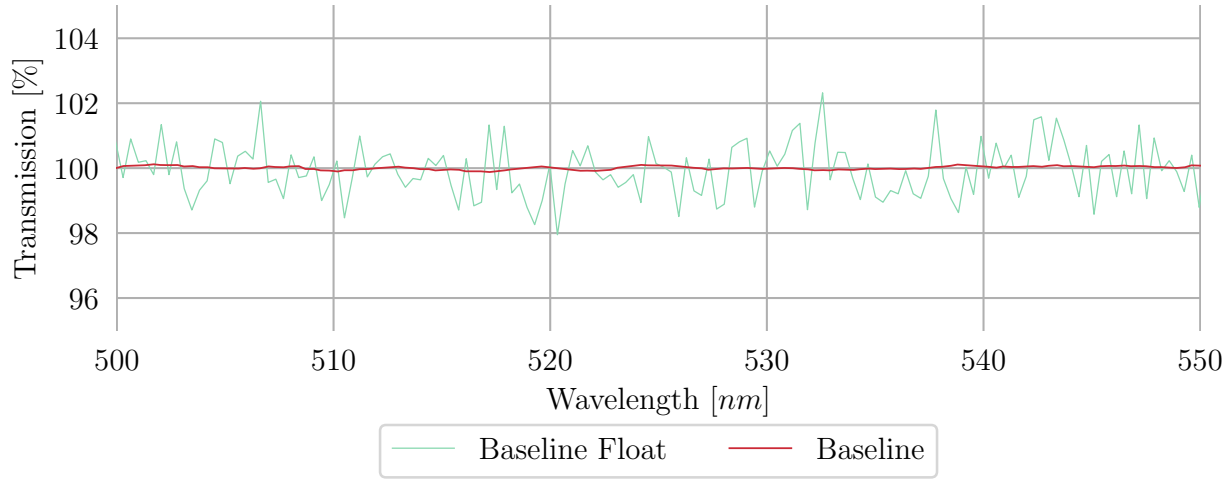

Figure 5.2: Laboratory transmission baseline measurements at two different measurement occasions, detailed.

The float glass response shown in figure 5.3 was used in Chapter 3 to compare the measured transmission of the float glass and the theoretical transmission.

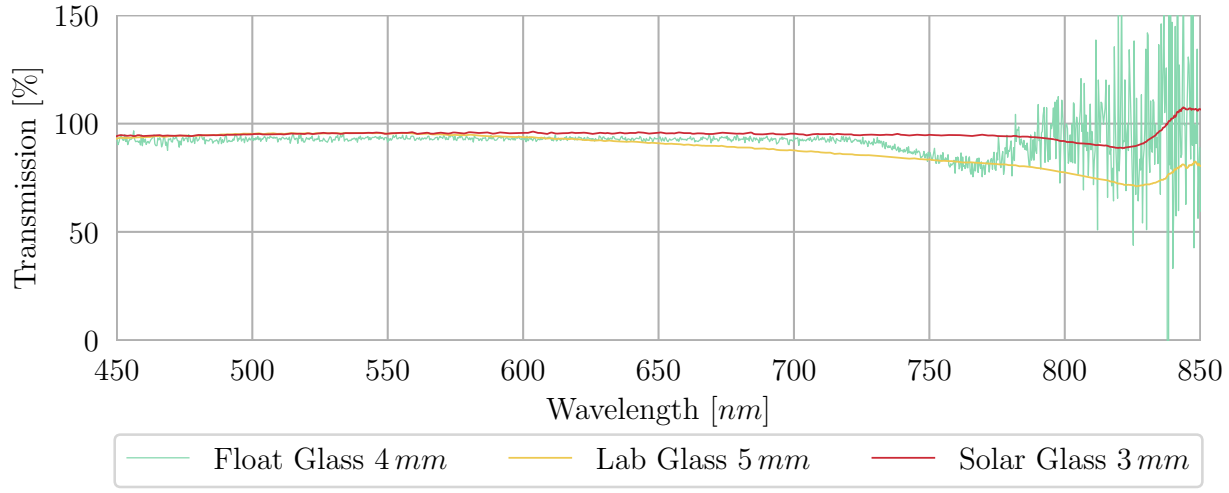

Figure 5.3: Laboratory transmission measurements for three various glass samples.

Still, it can be said that all three samples show a similar response in the lower wavelength bands, with a constant value of approximately $93 - 95\,\%$ transmission. The solar glass response relates into less transmission loss than the other two samples - as expected. The lab glass has a similar response, but with more losses, cause by impurities and the manufacturing process of the glass. The response of the float glass used in the preliminary experiments has a dissimilar response and this is taken into account when the data is discussed.

5.2 Dark spectrum Acquisition

The necessity for a dark spectrum as part of the calibration for radiation measurements, was discussed previously. It was assumed that the external optical fibre extensions, as well as the receptor separately, could contribute to the baseline noise seen by the spectrometer.

These dark spectrum measurements were completed by measuring the counts seen by the instrument, by mechanically closing any of the receptor end points completely - this ensures that little environmental light contributes to the measurement.

Theoretically, it can be assumed that the dark spectrum would consist of zero pixels but practically it can be seen to vary between $1500 - 2000\,counts$ consistently over the measuring range of the spectrometer, as illustrated in figure 5.4. Measurements 1 to 3 were acquired with an integration time of $25\,ms$, whereas measurement 4 were acquired with $1000\,ms$. The outliers are only observed in measurement 4 with the longer integration time. Repeatedly and increased integration time ensued in some outliers, as seen at $500\,nm$ in figure 5.4.

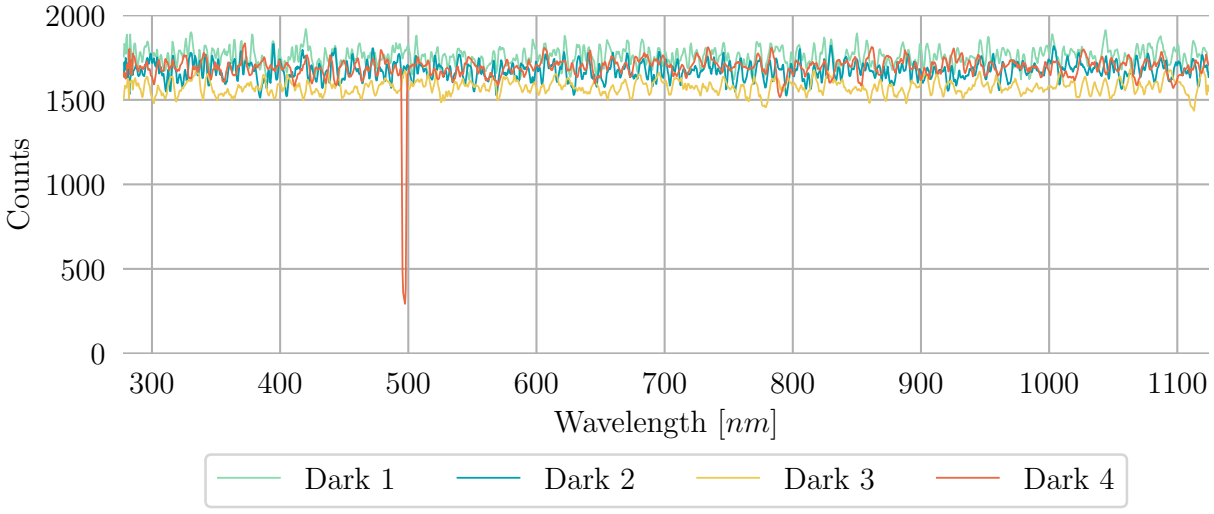

Figure 5.4: Laboratory dark spectrum measurements with noise detail.

The peak observed in figure 5.4 Dark 4 was originally peaking upwards, and reversed when the black spectrum was captured. Therefore, it was observed that the dark spectrum directly compensated for the irregularity in the spectrometer response. Thermal noise is particularly critical in the NIR wavelength band since the photons are of low energy. This is seen in figure 5.5. Higher response is observed in the approximate wavelengths of $800 - 1100\,nm$.

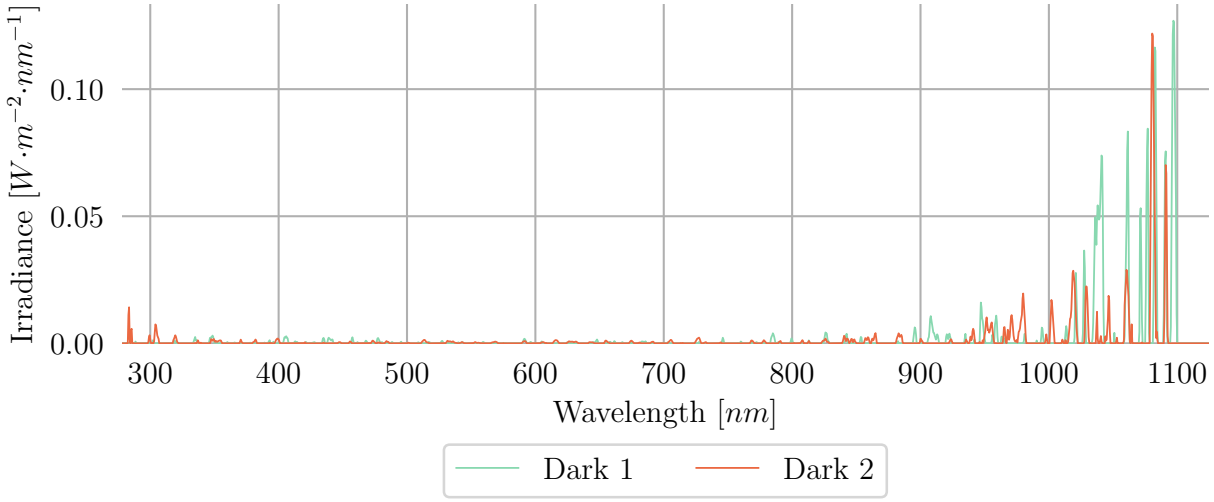

Figure 5.5: Radiometric dark spectra acquired with the BlueWave spectrometer.

The dark spectrum samples plotted were measured directly after one another under the same circumstances and exact spectral processing, still it is seen to variate within the particular distribution. It should also be noted that the dark spectra were measured with the spectrometer in approximate controlled temperature of 25° - so even though the instrumentation was not operating above the average operating temperature, some noise was still present.

This response distribution is seen to be similar to the calibration distribution shown in figure 3.2 since the noise is superimposed with the calibration file when measurements are completed in the radiometric application function. Under similar controlled circumstances, with relative constant temperature, several samples were acquired consisting of an irradiance measurement before the dark spectrum was acquired and a measurement after (figure 5.6).

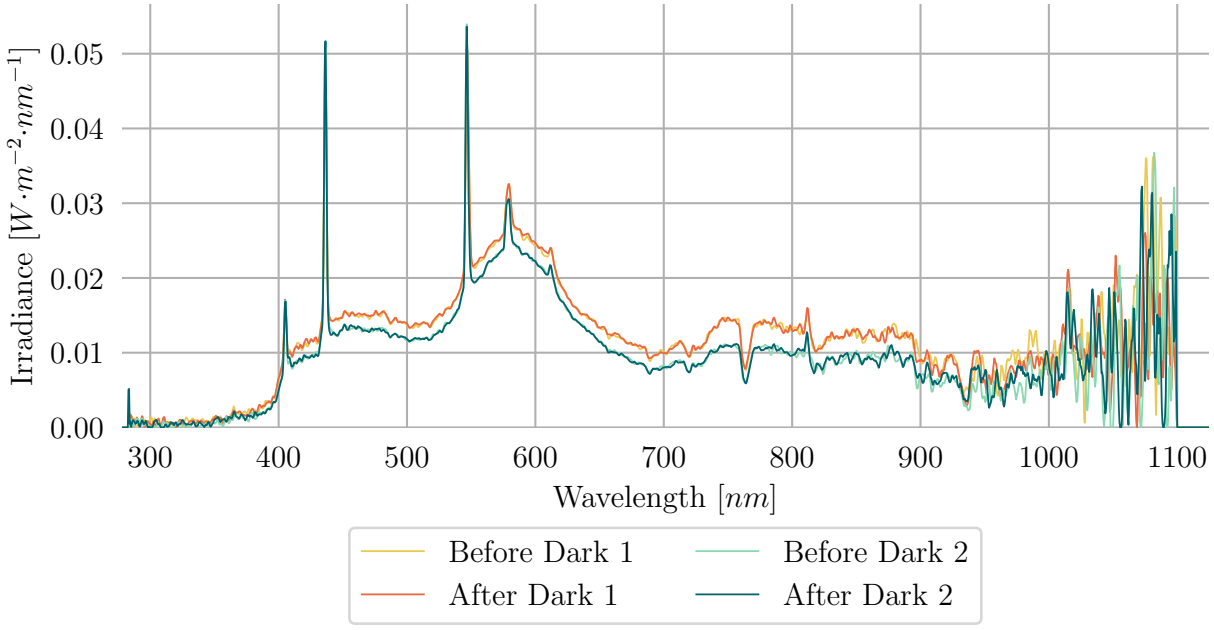

Figure 5.6: Before and after dark spectrum acquisition samples with BlueWave spectrometer.

Both measurement sets are seen to only variate slightly between the measurement acquired before and after the spectrum in the stable wavelength region. Only one measurement set from the overall sample varied noticeably. This variation is so slight in general that under natural conditions it will not be noticeable between all the other external influences.

Similar results were found for the measurement in Scope Mode, where the y-axis is the number of counts, or pixels, measured. Even from these figures above some question remains to the need for a black spectrum, especially in natural environmental conditions.

According to the help section of the SpectraWiz software, black spectrum acquisition becomes significant when the integration time is longer than 250 ms in scope mode. They state that it is not specifically required but it will remove any constants applied by the detector structure. The addition of a black spectrum is predominantly important when measurements are completed in radiometric mode but it could be helpful when system parameters are changed to ensure that pixel non-uniformity is eliminated.

In summary of the dark spectrum acquisition: with acquiring the dark spectrum it is confirmed that the suggested $1500 - 2000\,counts$ by StellarNet is a valid approximation of the dark spectrum. This approximation is applied to the automated system measurements.

5.3 Relative Transmission Loss

The relative transmission loss test has a similar purpose to the preliminary field experiences, as well as, the transmission test previously. First, it was confirmed that the distance between the point light source and the entrance to the measuring point - either the spectrometer itself, fibre optic or the cosine receptor - does not influence the distribution of energy as much as it changes the amount of energy perceived by the spectrometer.

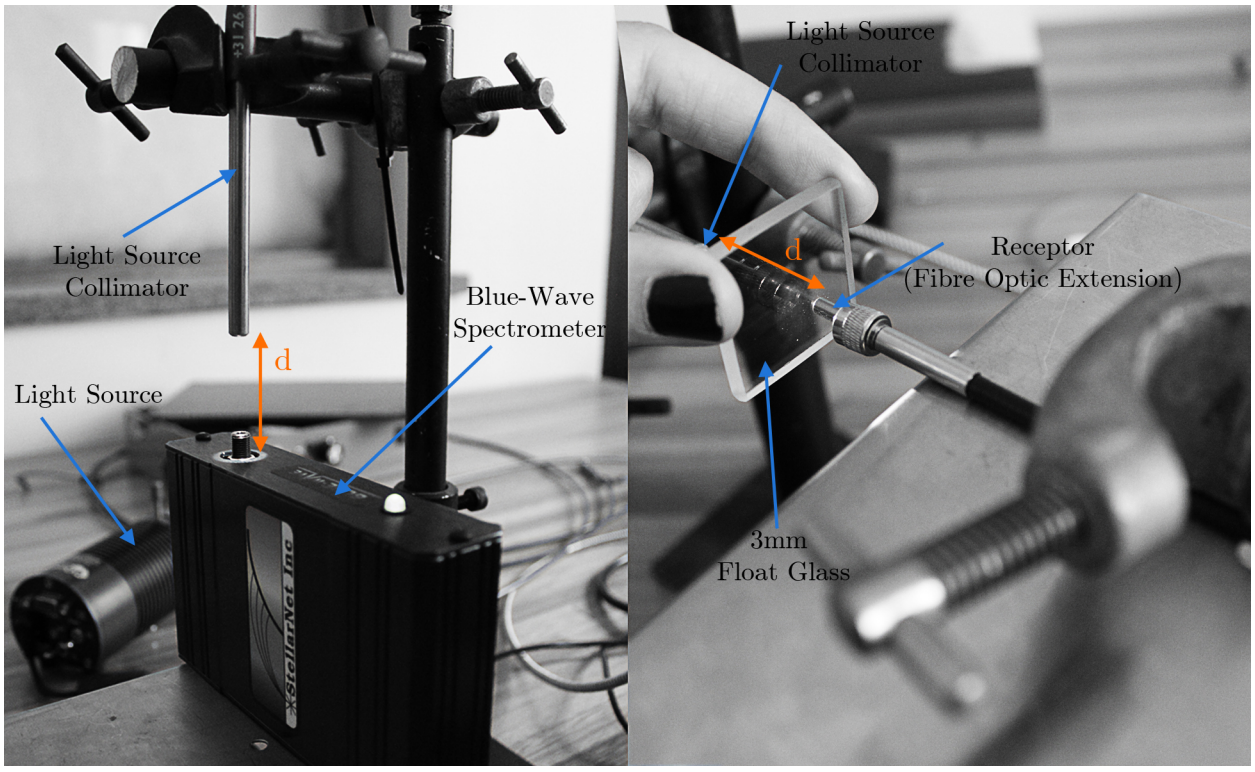

Figure 5.7: (a) Vertical and (b) horizontal experimentally setup.

The laboratory measurements are further displayed in *counts*, since the irradiance plot is more suitable to solar radiation measurements rather than a constant light source.

Firstly, considering a measurement of the constant light source without the fibre, as seen in figure 5.7(a), at a distance d of either $10\,mm$, $30\,mm$ or $50\,mm$. Even though the light source seemed to be directed directly into the measuring slit, a significant amount of light was not perceived, as seen in 5.8.

According to these observations, the laboratory relative transmission loss test was completed with the fibre optic. The measurements were conducted with two different measuring setups: firstly the light and the spectrometer measuring point was placed vertically in line, similar to the setup seen in figure 5.7(a). Secondly, the measurement was horizontal, as seen in figure 5.7(b). Plotting the horizontal baseline constant light source measurements within a figure showed that the measurements were not consistent. Therefore, only the vertical data was used for the relative transmission loss calculations.

The great variability in measurements at the same distance and the low intensity is mostly ascribed to the physical profile of the spectrometer slit. Figure 5.9 shows the difference in profile between the fibre optic cable and that of the slit opening on the spectrometer casing. Most of the light does not reach the slit opening but is rather either diffracted or reflected away by the screw thread casing or the light is trapped within the cylindrical shape of the

attachment. This theory is confirmed by figure 5.10; the measured intensity has a constant distribution between the different distance when a fibre optic extension is used.

In essence, the point light source originating area is larger than that of either the two measuring holes; the main difference is that the spectrometer casing requires the light beams to be forced within a "tube", therefore the traveling distance of the light is much further to the measuring hole than in the case of the fibre optic. Further, the spectrometer casing's "tube" is made of black plastic which absorbs the light whereas the fibre optic is reflective.

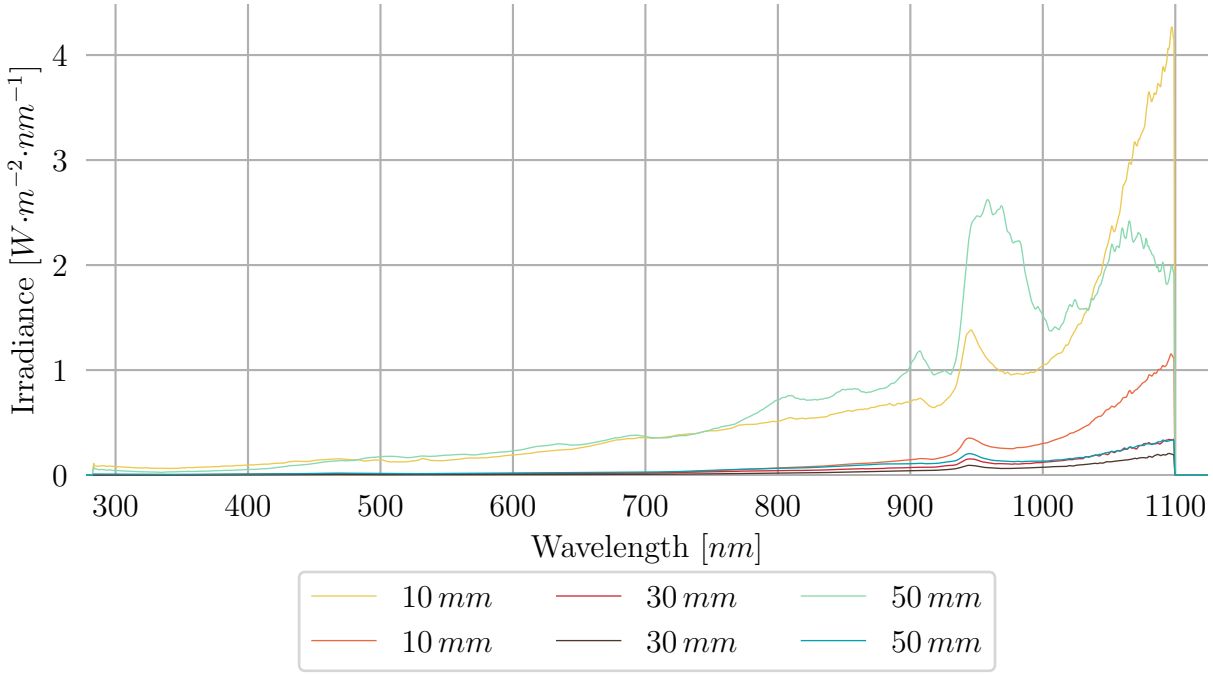

Figure 5.8: Constant light source measurements without any fibre optic, at various distances between the source and measuring point.

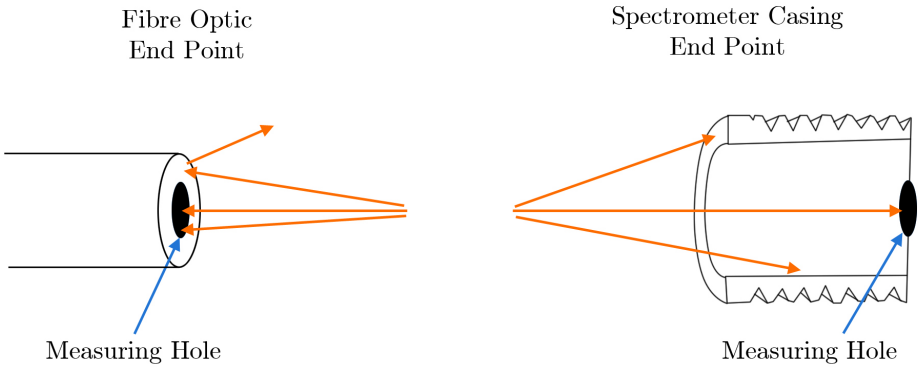

Figure 5.9: A graphical representation of the fibre optic end point versus the spectrometer casing and the location of the measuring hole.

Figure 5.11 is three measurement sets with $d = 30\,mm$. Still, the first measurement set's baseline measurement was more than the following two sets; it was calculated that the first and second measurement set's baselines differed with 10.282 %.

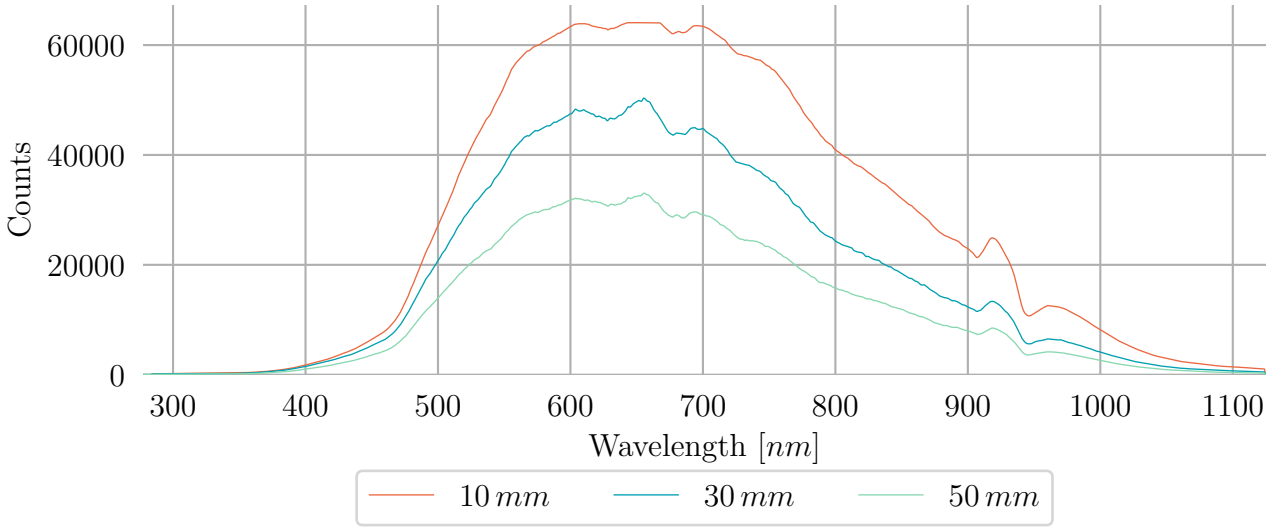

Figure 5.10: Constant light source measurements with an optic fibre extension, at various distances between the source and measuring point.

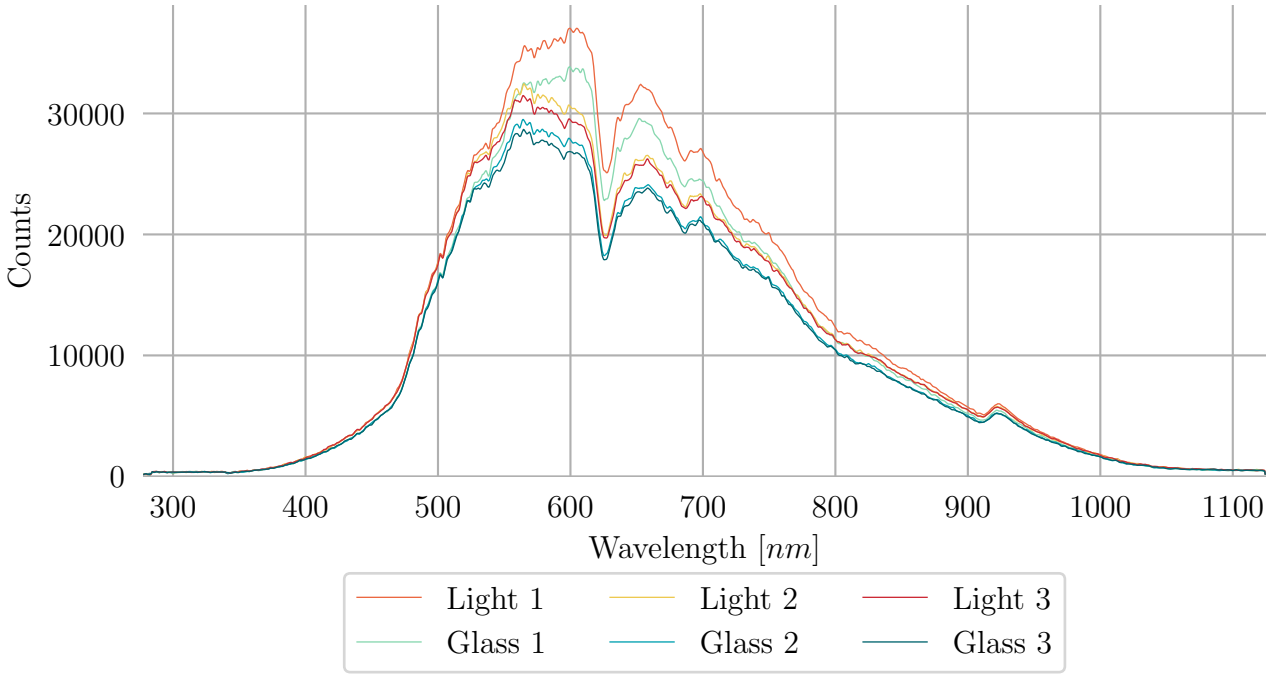

Figure 5.11: Three measurement sets, each consisting of a baseline and glass measurement with a constant light source..

The second and third (figure 5.11 differed with only 1.391 % still, all three measurement sets showed a difference between baseline and glass measurement of $8.6 - 8.8\,\%$. This calculated transmission loss is less than 1 % smaller than what was calculated in Chapter 3, with the preliminary experience measurements.

Furthermore, a simulated soiling test was completed - this entailed the deposition of fine dust particles on the float glass sample, as seen in figure 5.12. Although the amount of dust particles deposited on the glass is unknown, it could supply an awareness of the impact of soiling.

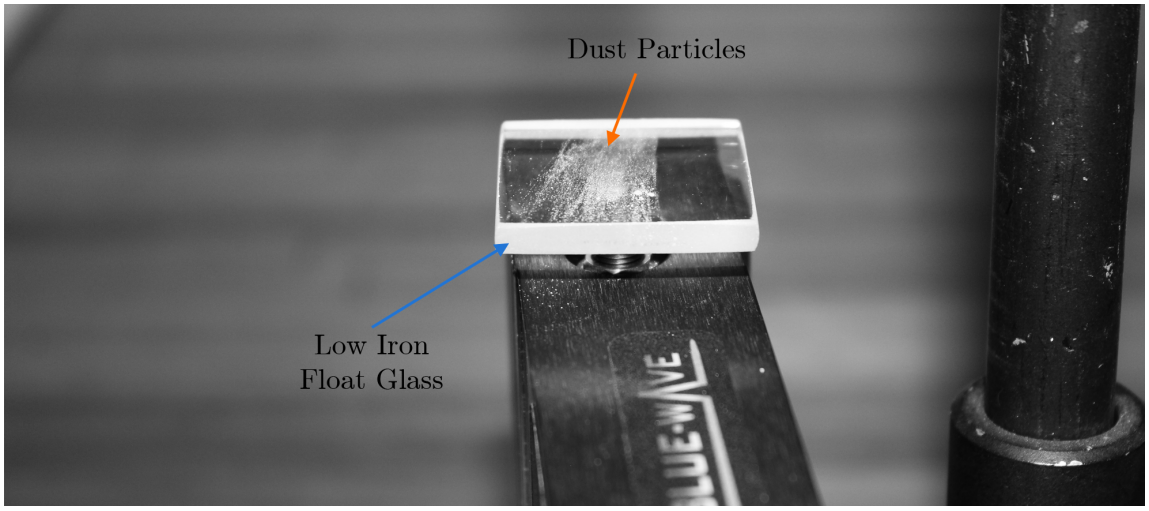

Figure 5.12: Laboratory manual dust deposition on a low-iron float glass sample.

Although only one baseline measurement per set is shown in figure 5.13, each set consisted of two - the difference in baseline measurements for the first set was calculated as 0.171 % and the second, 0.622 %, both therefore falling under stable conditions. The glass transmission loss for the first set was calculated as 9.065 %, falling in the range of the previously measured relative transmission loss tests and the dust was calculated to cause an additional 16.909 % loss. Similarly, the second set the glass transmission loss was 8.326 % with the dust an additional 20.996 % loss.

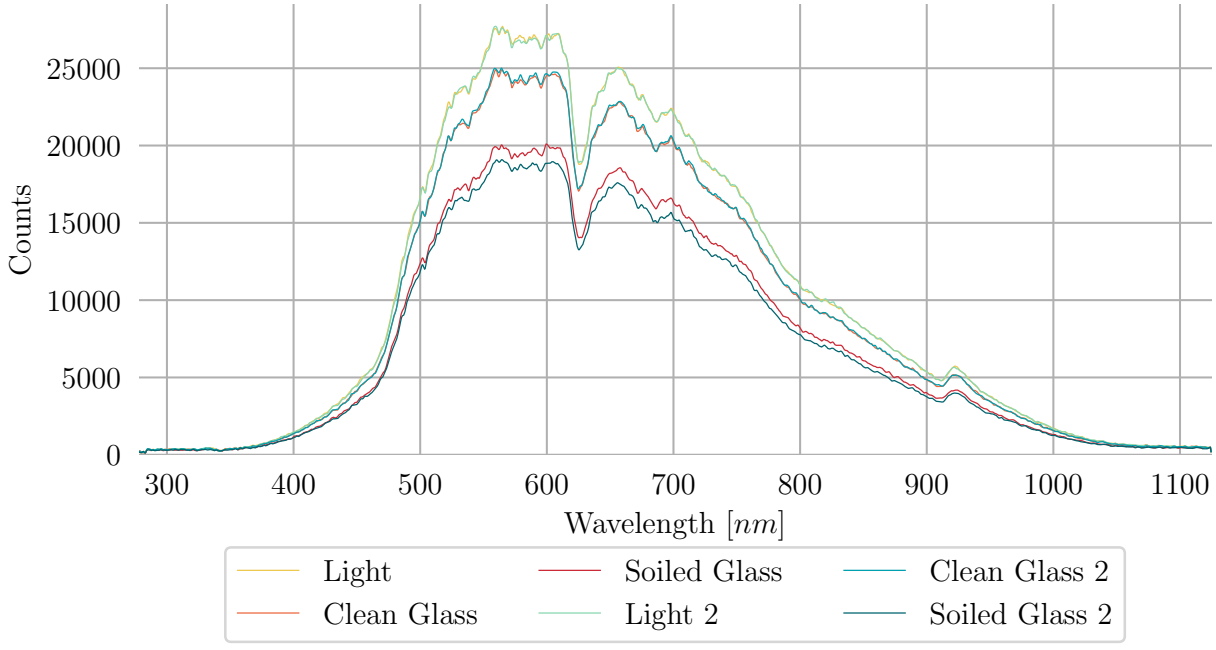

Figure 5.13: Two measurement sets, each consisting of a baseline, glass and soiled glass measurement with a constant light source.

A relative transmission test, similar to the previous with the small glass, was attempted with the large solar glass - unfortunately its size made it challenging and constant results were not established. Still, the relative transmission loss in the laboratory experience showed similar results to that found in the first experience in Chapter 3. One advantage of this laboratory experience is the addition of a controlled soiling test - an idea of the impact of dust was supplied by a simple test with the deposition of small dust particles on the float glass.

The tests completed within this laboratory experience indicate that even within a relatively controlled environment, many variances are possible within the measuring setup. Not only should one therefore consider the environmental conditions, but also the way in which the spectrometer is used. The few observations made within this chapter leads to the conclusion that a laboratory test is critical when new equipment is used - even though it does not supply conclusive data, it does supply knowledge in regard to the equipment.

Chapter 6

Automated System

6.1 Introduction

Several design ideas were considered; design ideas from CNC machines, printers and 3D printers were incorporated. What made this design especially challenging is the required size and secondly, it is required to be placed outside in harsh conditions - these requirements therefore increase the required quality and cost of the components. It is important to remember that the system designed is a first prototype and therefore exceedingly expensive components were not acquired, but rather components that suit the requirements, if only barely.

In this chapter, all of the elements of the automated system design, as well as, installation are discussed. First, the drive of the automated system is discussed - this includes how the motors and pulleys are selected. Further, the electronic design is discussed and how the electronic elements fit together; an overview of the software is also supplied. Finally, a section is dedicated to the installation of the automated system, as well as, what worked well in the design and which elements need to be revised.

6.2 Drive

The first detail investigated for the drive design, is whether a stepper or DC motor will be more suitable for the application. DC motors are very efficient and can sustain high torque at a high speed; the dynamic response is good and it delivers a smooth motion profile. Stepper motors on the other hand are very reliable with sustainable torque at lower speeds - more suitable to the design applications. Stepper motors have the advantage of open-loop control and therefore no feedback is required to control the motor, therefore the stepper motors were the decided type of motor for this project. Some questions were considered with the choosing of the specific stepper motors required:

1. How will the motor and load connect to each other?
2. What is the speed and acceleration required of these motors?
3. What torque capacity is required to move the connecting loads?
4. What is the required accuracy of the system?

Two motors are required - one for each of the axis of the frame. The x-axis is the width of the frame and so has a smaller load to carry over a shorter distance, than is required of

the y-axis. The x-axis will only move the receptor-end connected to the fibre optic. Many variables exist in this system since the requirements are somewhat flexible, since this is a first prototype it is more important to determine the limitations of the system through an iterative process.

The second component of the drive train, is the linear mechanical actuators - converting the rotational motion from the motor into linear motion. The options considered are belt drives and ball screw actuators. Some considerations for choosing an applicable actuator type are the required stroke distance and the required load capacity - a long traveling distance is required in the y-axis while the load capacity is somewhat smaller. To ease installation and maintenance it is decided to keep both the x- and y-axis actuators similar. From the aforementioned considerations, a belt driven train is chosen. Ball screw actuators are more applicable to high load capacities and higher thrust force, whereas belt drives are very suitable to long traveling distances at higher speeds. Figure 6.1 (adapted from [70]) supplies a sketch of a linear position, similar to the design of the X- and Y-Axis.

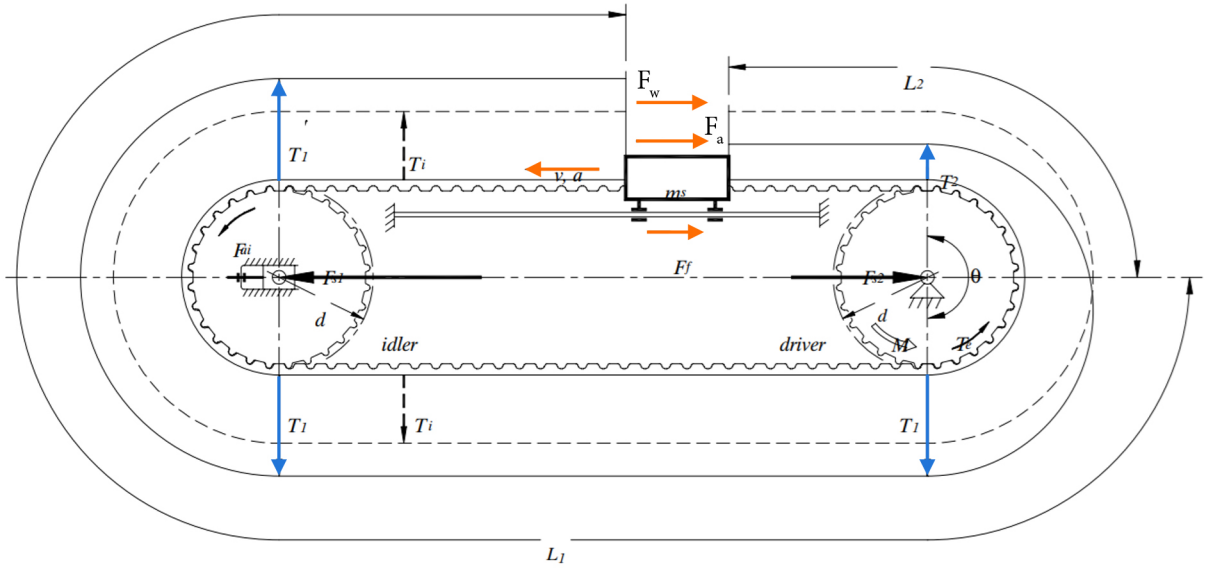

Figure 6.1: Drive pulley and belt system force diagram.

In this linear position, the bearing is where the main load will act. Therefore, the effective tension will be calculated at the bearing is,

$$T_e = F_a + F_f + F_w + F_g + F_{ab} + F_{ai} = T_1 - T_2, \tag{6.1}$$

with T_1 and T_2 the tight side and slack side tensions. The acceleration force of the bearing (F_a) is merely the mass of the bearing (m_b) and the linear acceleration (a_c),

$$F_a = m_b \times a_c. \tag{6.2}$$

The frictional force of the bearing on the axis (or rather, axle), taking into account the dynamic friction coefficient of the bearing μ_r, the resistance of motion that is load independent (F_{fi}), the acceleration of gravity (g) and the angle of the bearing (β),

$$F_f = \mu_r \times m_b \times g \times \cos\beta + F_{fi}. \tag{6.3}$$

The weight of the bearing,

$$F_g = m_b \times g \times \sin\beta, \tag{6.4}$$

and the initial acceleration of the belt,

$$F_{ab} = \frac{w_b \times l \times b}{g} \times a_c, \tag{6.5}$$

where l is the belt length,b the belt width and w_b the specific weight of the belt. Finally, the idler pulley force F_{ai},

$$F_{ai} = \frac{2 \times J_i \times \alpha_a}{d} = \frac{m_i}{2} = \left(1 + \frac{d_b^2}{d^2}\right) \times a_c, \tag{6.6}$$

with the idler pulley inertia is J_i, m_i the idler pulley mass, α_a the angular acceleration and d_b the idler pulley bore hole. In effect, the maximum tension within the belt can therefore be calculated by simply knowing a few parameters of the chosen pulley and bearing. Since the acceleration of the mass will not be exceedingly large, these calculations are shown to explain which components of the drive system influence the design choices.

Simply stated, the torque required of the motor will increase as the load increases. Since some factors of the belt and pulleys was not known at this stage the torque required by each motor was estimated. The chosen x-axis motor is a stepper motor with a body similar to that of the Nema 17. The motor for the y-axis is also a stepper motor but with a larger holding torque and body similar to the Nema 23 - the motors are manufactured by Wantai and their specifications are listed in table 6.1

Table 6.1: Selected motor specifications by Wantai Motors.

Body Model	**Nema 17**	**Nema 23**
Model	$42BYGHW609$	$57BYGH627$
Deg/Step	1.8	1.8
Rated Current $[A]$	1.7	3.0
Rated Voltage $[V]$	3.4	3.0
Holding Torque $[g{\cdot}cm]$	4000	19000
Detent Torque $[g{\cdot}cm]$	220	680
Motor Weight $[kg]$	0.26	1

With the chosen motors and belts, accompanying pulleys are selected.

Basic pulley theory shows that the amount of steps the stepper motor is required to turn circulalry to move $1\,mm$ linearly,

$$steps\_per\_mm = \frac{motor\_steps\_per\_rev \times driver\_microstep}{belt\_pitch \times pulley\_teeth}. \tag{6.7}$$

The amount of steps for a full revolution of the stepper motor is calculated from the degrees per step specified by the moto manufacturer - this is usually either 0.9° or 1.8°, with $0.9°/step$ supplying double the precision. Since a full revolution is 360°, the number of steps in a full revolution is,

$$motor\_steps\_per\_rev = 360°/0.9° = 400\, steps/turn. \tag{6.8}$$

Similarly, 1.8° is 200 $steps/turn$. The driver-microstep in equation 6.7 refers to the microstep mode, discussed later in the Software section. All these elements are more related to the belt, driver and motor - perhaps the most important element that is chosen is the amount of pulley teeth. From equation 6.7 it is observed that resolution decreases with an increase in the amount of pulley teeth but the speed also decreases. This simply means that 20 pulley teeth will turn slower, twice the speed of 36 teeth, but the error will be larger with 20 teeth.

The second selection in regard to a pulley, is the pulley diameter; it is known that torque is the radius of a pulley turning multiplied with the force supplied to the pulley for rotation therefore, the larger the pulley diameter the more torque is required to turn the pulley. Accuracy is one of the main concerns, therefore 36 teeth pulleys are selected - the increased torque required is not problematic since the motors deliver more torque than required.

The belt length required for each axis, for equal pulleys on each side,

$$L_{belt} = 2{\times}C + \pi{\times}d, \tag{6.9}$$

with C the centre distance and d the pulley diameter.

6.3 Frame

The frame of the automated system was envisioned as the platform which would hold all the elements of the system together and would also serve as the interface between the system and the stand - or in a later time, the double-axis tracker. The frame would be constructed of square tubing - a large $50{\times}50\, mm$ square tubing is selected. This ensures that the frame would not bend under the weight of the drive components and the glass, but also supplies a larger surface for the attachment of the drive components, as seen in figure 6.2.

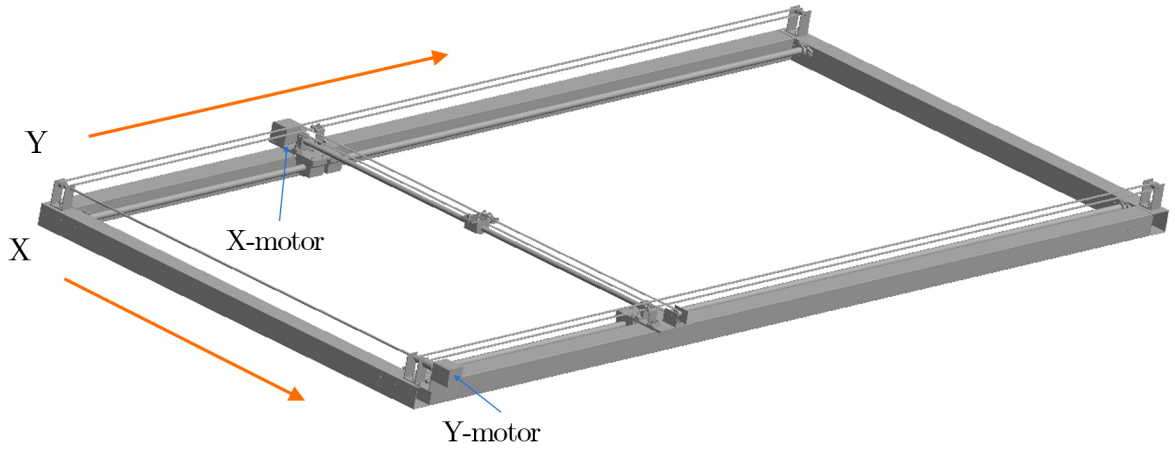

Figure 6.2: XY-plotter semi-final design completed in Autodesk Inventor.

Each element of the design was created on Autodesk Inventor - these elements were constrained together to supply a clear image of what the design entails. Unfortunately, as the design evolved, certain elements were not updated, but the drawing list supplied in appendix A.2 does supply a general idea of the level of detail of the design.

The design transformed from this basis into an idea how each axis would look - a simplified drawing of figure 6.2, which was one of the semi-final designs. With this basic sketch, several important design notes were compiled:

1. The frame size is required to be larger than the glass so that baseline measurements could be acquired.
2. What would the diameter and therefore the selected bend radius be on the shafts that would carry the bearings?
3. How will the second Y-axis drive be driven, a second motor or a torque transmitting shaft?
4. What will the bend radius on this torque transmitting shaft be?
5. The motors should be placed on opposite sides of the frame as to balance the total weight.
6. Could a solenoid be incorporated as a shutter for the spectrometer receptor?
7. What material could the shafts be made of to ensure little wear and rust, within a reasonable price range?
8. What material and manufacturing process is required and available for the elements connecting the pulleys to the bearings?
9. How will the belts be hold in position?

With the basic design formulated and created on Inventor, an iterative stress and load analysis were required - the intent was not to analyse every point but focus on the important factors such as the bending moments on the shafts. The mass of the elements connected to the x-axis were approximated:

Table 6.2: Apprxomate weight for various elements attached to the x-axis.

Amount	**Element**	**Mass [kg]**
4	AS 1110 M5×10	0.003
1	Receptor Holder	0.02
2	AS 1237 6	0.001
1	X-belt Fitting	0.028
1	X-belt Clamp	0.018
2	ANSI M5×0.8	0.002
2	AS 1237 5	0.00
2	AS 1110 M5×12	0.003
4	AS 1110 M3×8	0.001
1	Bearing	0.092
1	Shaft $\phi 12, L = 1014$	0.89
	Total (without Shaft)	0.186

Figure 6.3 supplies a free body diagram of the X-axis shaft, with the end points as well as the bearing imagined as point loads rather than distributed load intensities. Although the y and x components that support the bearings are called shafts, they do not rotate and therefore do not transmit power - this should in fact be called an axle, which merely support the pulleys and bearings. Since these components are axles they can be analysed as static beams.

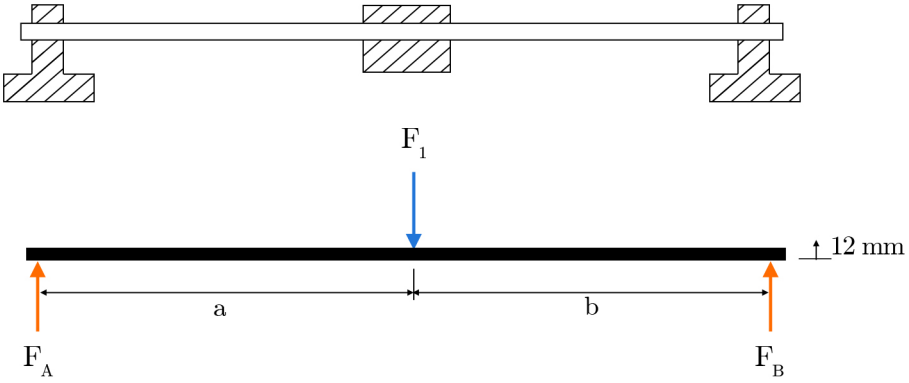

Figure 6.3: Free body diagram of the X-axis shaft, bearing and end points.

The force at an end-point of the shaft is calculated through the moment created by the point load of the bearing,

$$F_A = \frac{F_1 \times a}{a + b}. \tag{6.10}$$

Naturally, the weight of the bearing and its attached components would be most prominent when the distance between it and the end points are at a maximum, which in this case would be in the centre of the shaft. Further, the maximum torsional stress $\tau_{S_{max}}$,

$$\tau_{S_{max}} = \frac{F_A}{(\pi d^2)/4}. \tag{6.11}$$

with d the shaft diameter. Similarly, the stress, or material yield, of the shaft can also be calculated. The area moment (I) of a slender rod is supplied by Shigley [71] as,

$$I_x = I_y = \frac{1}{4}\pi r^4. \tag{6.12}$$

So, the stress is calculated by,

$$S_t = \frac{M \times y}{I} = \frac{mgy \times y}{I}. \tag{6.13}$$

with M the bending moment and y the y-axis distance to the point of force. With the equation listed above, it is simply compared to the yield stress of the shaft material - this is the stress at which the shaft material will permanently deform.

A second approach was also implemented - the maximum moment is calculated through the polar moment of inertia of the shaft - in this manner the maximum deflection of the shaft can also be calculated. The maximum moment,

$$T_{max} = \tau_{max} \times \frac{J}{R}. \tag{6.14}$$

with J the second polar moment and R the radius of moment. Incorporating the equation for the polar moment of a solid shaft, it is simply said the diameter is,

$$D = 1.72 \left(\frac{T_{max}}{\tau_{max}} \right)^{1/3}. \tag{6.15}$$

Similarly, the weight of the Y-axis components was calculated and implemented to approximate a good diameter for the shafts. Finally, the shafts selected are manufactured form carbon steel (yield strength 370 MPa); the X-axis has a diameter of 12 mm and the Y-axis shafts 16 mm.

6.4 Electronic Design

The centre of the electronics is a Raspberry Pi B+ connected to a breakout board via 20×2 headers. As seen in figure 6.4, the breakout board is in turn connected to stepper motor boards via 4×2 headers to voltage regulating boards.

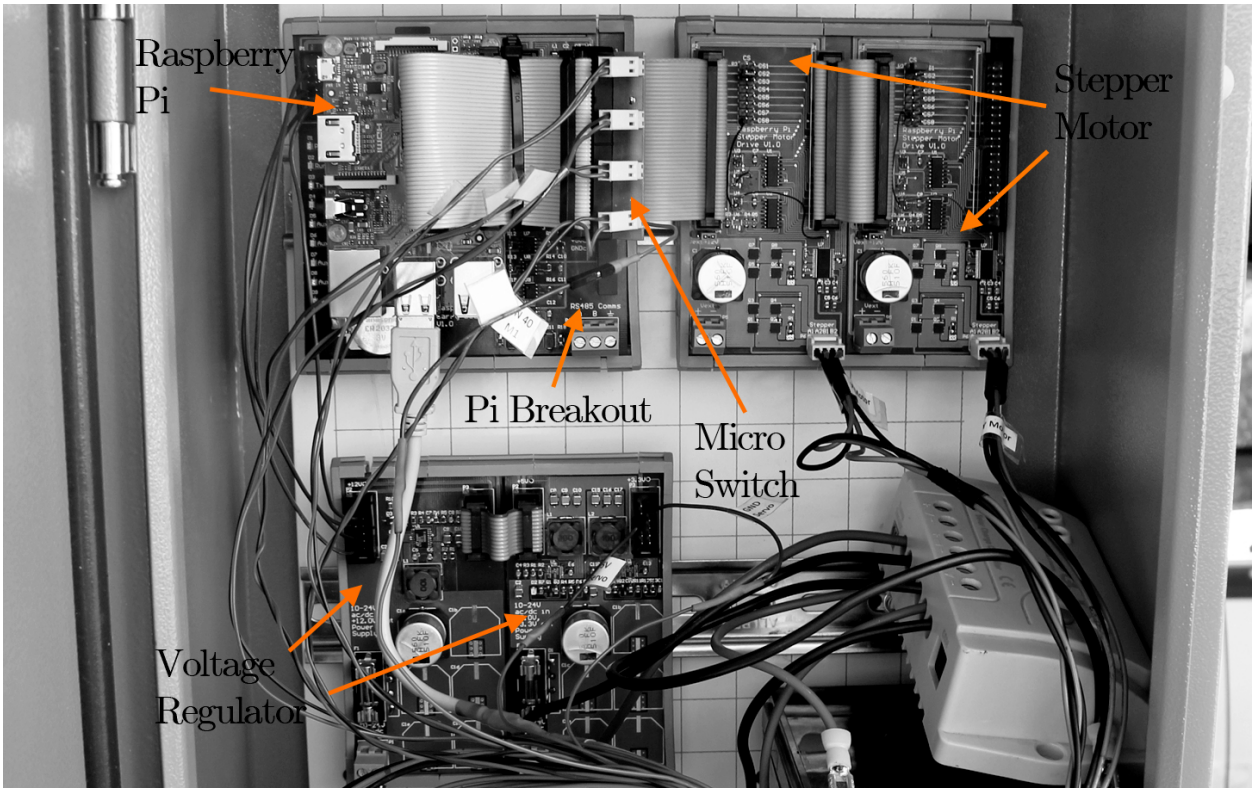

Figure 6.4: Final electronic hardware installation.

6.4.1 Raspberry Pi

The main reason for selecting the Raspberry Pi as the main control is the accessibility of it, as well as the ease in which communication types can be implemented. Also, the Pi supplies the spectrometer with power via the USB port. The Raspberry Pi running Raspbian, an operating system based on Debian, can run Python scripts with ease - this is how pins can be set and used for the various tasks required. The Pi is powered by the voltage regulating boards, these supply voltage regulating boards regulates $10 - 24\,V$ to $12\,V$, $5\,V$ and $3.3\,V$; the Pi requires $5\,V$.

The Raspberry Pi has several GPIO (General Purpose Input/Ouput) pins - some pins are dedicated, but many pins are available for general input/output use. All of the pins are reflected on the Pi Breakout Board as well.

6.4.2 Pi Breakout Board

The Pi breakout board allows for the interfacing of the Raspberry Pi with all the other necessary components of the system. The dedicated GPIO pins mentioned before are two SPI (Serial Peripheral Interface), TX and RX for RS 485 communication, a hardware PWM0 pin to supply to the stepper motors, several CSs as well as GPIO micro switch pins. Figure 6.5 supplies the schematic that indicates which pins are in use.

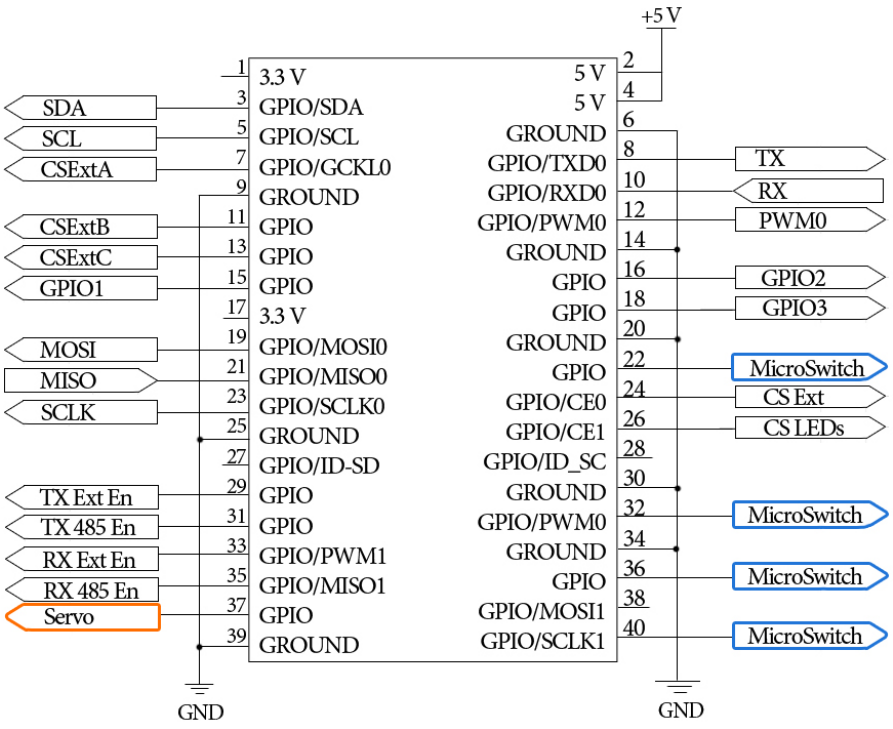

Figure 6.5: Raspberry Pi I/O pin layout.

CS Ext, and CS Ext A,B and C extend into eight CS through a shift register; two of these eight CSs are dedicated to each of the stepper motors. Further CS LEDS supplies access to eight of nine LEDS that can be switched on or off on the breakout board.

After the initial implementation of all electronic and mechanical hardware, as well as the software, the need for external micro switches were observed. A micro switch is an electrical actuator which requires little force to trigger. These micro switches are usually SPDT switches - single-pole, double throw; the switch consists of three terminals - C (Common), NC (Normally Closed) and NO (Normally Open).

The electrical circuit for each switch is shown in figure 6.6; the header from the Raspberry Pi was extended by reflecting all pins on the Micro Switch board which was created at the University with a PC Board CNC machine.

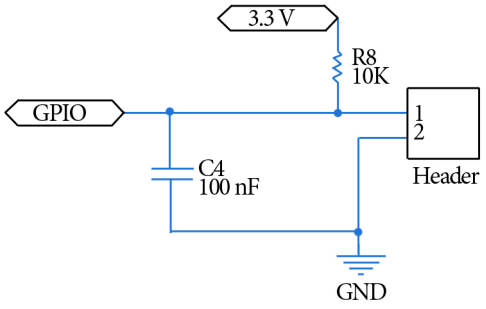

Figure 6.6: Electrical circuitry for a singular switch.

An additional miniature servo motor was also attached at a later time to GPIO pin 37, $5\,V$ and ground. The servo motor is used in a type of shutter to protect the spectrometer cosine receptor from water. The shutter parts were 3D printed; the servo turns a gear that turns a linear gear, that moves a thin plastic square over the cosine receptor. Figure 6.7 is a photo of the final shutter open and closed.

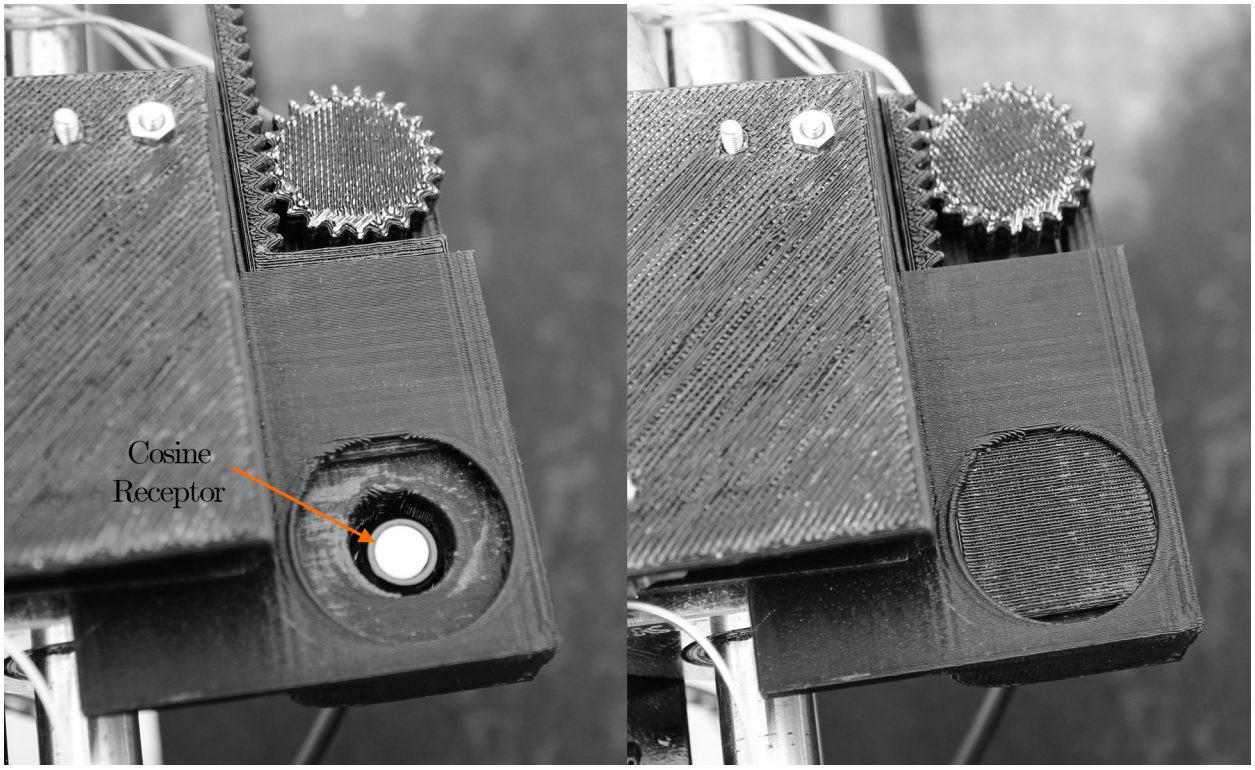

Figure 6.7: Open and closed 3D printed shutter containing the cosine receptor.

6.4.3 Stepper Motor Board

The heart of the stepper motor board is the DRV8711 IC from Texas Instruments. The gate driver scheme determines how current is switched between the motor windings, how power is dissipated within the scheme and what losses are prominent. The following questions assist in the selection of a fitting driver:

1. Is the stepper motor Unipolar or Bipolar?
2. What is the motor specifications?
    a) What is the maximum current that the motor windings can manage without overheating - what is the amps per phase of the stepper?
    b) What is the resistance per phase of the motor?
    c) what is the motor voltage?
3. What is the driver specifications?
    a) What is the maximum voltage that can be supplied by the driver to the motor?
    b) What is the maximum continuous current that can be supplied by the driver?
4. Is a specific power-switching topology required, and which - IGBT vs. MOSFET?

The stepper motors, such as the Nema motors chosen for this design, are 2-phase bipolar motors that consists of two groups of coils - these types of motors require two full H-bridges to reverse the current in the phases. The switching in all bipolar motors are similar to the waveforms seen in figure 6.8. Each group coils consist of a signal and the signal inverse - the A terminal is always inverted for A', similarly B and B'.

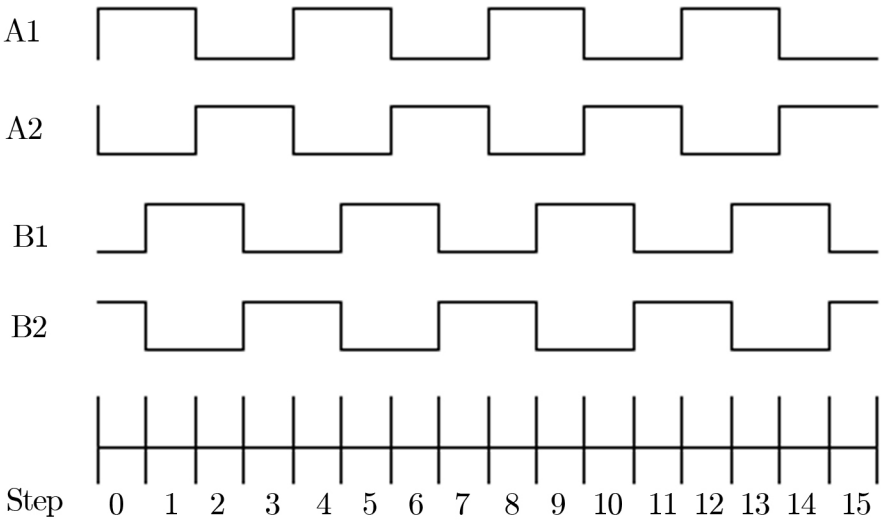

Figure 6.8: Bipolar stepper motor driver waveform.

The motor specifications are known, whereas the driver specifications and selection is dependent on availability and ease of implementation. The DRV8711 IC is not a simple gate driver but the basics remain the same - an external PWM (Pulse Width Modulation) is

required and MOSFETs are required for the switching of the current. The MOSFETs allow for faster switching than IGBTs, and therefore less switching losses. The other advantage of the MOSFET implementation is that it consumes little gate power in an ON state even though more power is required to turn the phases on and off - the ON state consuming little power will decrease the heat dissipated within the driver.

The implementation of the driver is mainly through the software, discussed later in this chapter.

6.5 Software

Although the Raspberry Pi supplies a method of control over the hardware, some form of data management is required. Originally, the spectrometer software supplied by StellarNet for Linux stores the string of pixel values in the JSON (JavaScript Object Notion) format. Although JSON is said to be a simple human-readable format that is easily parsed and generated by machines, it is only recently incorporated within Raspbian, and more specifically MySQL. MySQL is a database management system that is open-source and readily used on Raspbian - the latest stable version does not as of yet officially support the JSON format (June 2017).

Also, the StellarNet software allows for the writing of the string to the terminal - although this is advantageous to the original use of the spectrometer, in an automated system data handling should occur without human interference. Therefore, the original source code was modified writing each data point to a string and the total string written to the MySQL database.

The connection between scripts and interfaces is illustrated in figure 6.9.

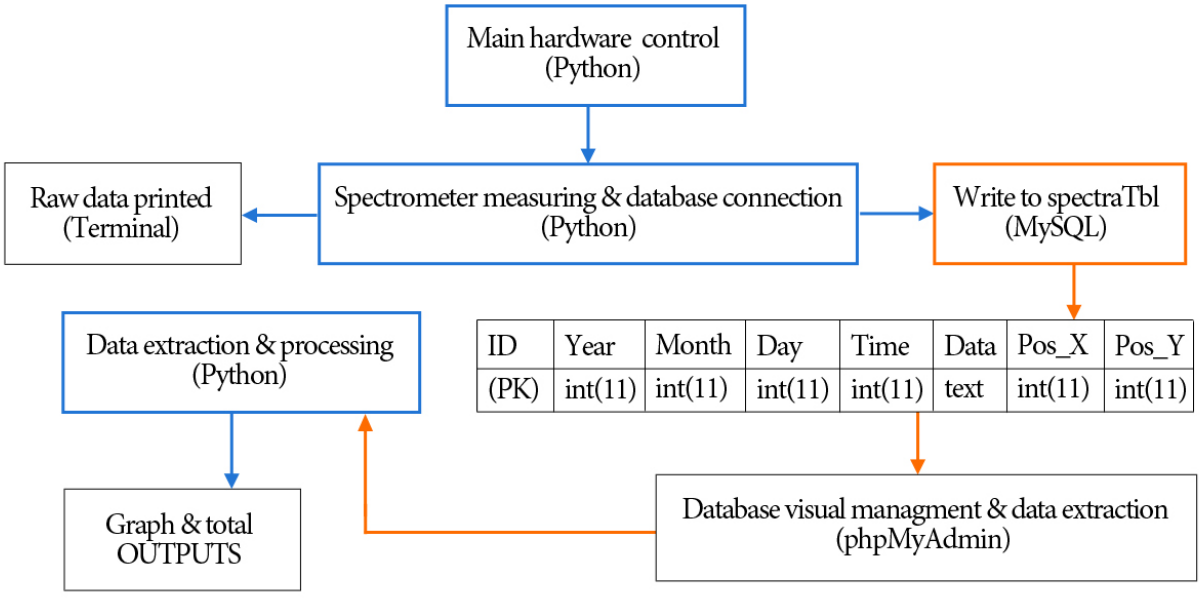

Figure 6.9: Script and interfacing of control and data management.

6.5.1 Stepper Motor Driver

Stepper motor control is achieved by the use of a DRV8711 IC from Texas Instruments [72]. This stepper control IC allows for high performance control of a bipolar stepper motor by

driving external N-Channel MOSFETs. The DRV8711 contains two H-bridge pre-drivers - an externally supplied hardware PWM signal regulates the current through the motor windings by switching the H-bridges. The rise of current through the motor windings is at a rate dependant on the DC voltage supplied externally to the driver, the inherent inductance of the windings as well as the back EMF. The bridges disable the current for a certain amount of time (set in the OFF register) when the current rises to the value of the chopping current threshold. The chopping current threshold,

$$I_{CHOP} = \frac{275 \times TORQUE}{256 \times ISGAIN \times R_{ISENSE}}. \tag{6.16}$$

In equation 6.16, $TORQUE$ refers to the setting in the TORQUE register with a hex value from 0×00 to $0\times FF$. $ISGAIN$ is set in the CTRL register and determines the amount of gain in the internal qualifiers. The voltage is compared over a current sense resistor R_{ISENSE} - a value of $68m\phi$ was selected for this resistor value.

In effect, the current through the windings are regulated in a sinusoidal approach to ensure a smooth current profile. Further, smooth stepper motor motion is achieved by the addition of micro stepping, current decay and adaptive blanking time.

The integrated micro stepping indexer in the DRC8711 allows for modes from full step to $\frac{1}{256}$ step, set in the CTRL register. Full step mode states that the motor will step the full step angle as indicated by its datasheet - this is usually an angle of either 0.9° or 1.8°. Similarly, any other mode indicates the fraction of this basic motor step angle to be completed, naturally increasing the smoothness of motion and increasing the resolution. Micro stepping also improves vibration and noise of the stepper motor.

When the chopping current is reached, the current is required to reroute within the driver. The H-bridge has several modes to specify how this decay current should be regulated: fast decay specifies that the state of the H-bridge reverse so that the opposite FETs within turns on to reroute the current; slow decay specifies that the current should be recirculated between the low-side FETs within the bridge. The DRV8711 also allows for mixed decay modes.

As mentioned previously, open-loop control is predominantly implemented with stepper motors. The DRV8711 overcomes this disadvantage by monitoring the back-EMF to report on a stall state. Several other protection circuits are implemented within the driver, this includes: overcurrent protection (OCP), pre-driver fault, thermal shutdown (TSD) and under-voltage lockout (UVLO). These protection devices set a bit in the STATUS register when the fault is registered within the driver.

Device operation is programmed through serial communication, SPI (Serial Peripheral Interface). The SPI transaction is always simultaneously on the MISO and MOSI lines; the transfer mode is mode 0 - the clock idle state is 0, the data captured on the rising edge and the data is sampled on the first clock edge. The SPI communication is enabled through a package called Spidev, which consists of Python bindings for the Linux kernel SPI driver. Spidev can be found via the Python Package Index [73].

The $16-bit$ serial data consists of a read/write bit, three address bits and twelve data bits. The data sequence is big-endian, with the MSB (Most Significant Bit) the first bit. the first bit will always indicate a read state if the bit is 1 and a write state if 0. The next three bits indicate the register to which should written, or read; this is hex 0×00 for the CTRL register until 0×07 for the STATUS register. All the registers are fully described within the DRV8711 [72].

6.5.2 Measuring Scheme

The experience gained throughout the preliminary experiences, the optic theory and basic logic, the necessity of a measuring plan or scheme was comprehended. Although only one measuring scheme was implemented it is certainly not the only possible way of completing a measurement set. Figure 6.10 is a diagrammatical way of indicating the 15 measuring points decided on; the sensor moves according to the arrows to each measuring point in numerical order, before acquiring a measurement. After all fifteen measurements, the sensor moves back to the home position indicated.

Also, visible on the figure is that points 1, 5, 6, 10, 11 and 15 are clear baseline measurements. The layout of the measuring scheme is planned so that the first and last measurements in the set are baseline measurements. Further, the baseline measurements are acquired on both sides of the glass to ensure that a shadow possibly thrown by the frame or edge of the glass does not supply false information regarding the measurement set. For similar reasons, all measurements are in line - this supplies a reasonable overview of the measurements.

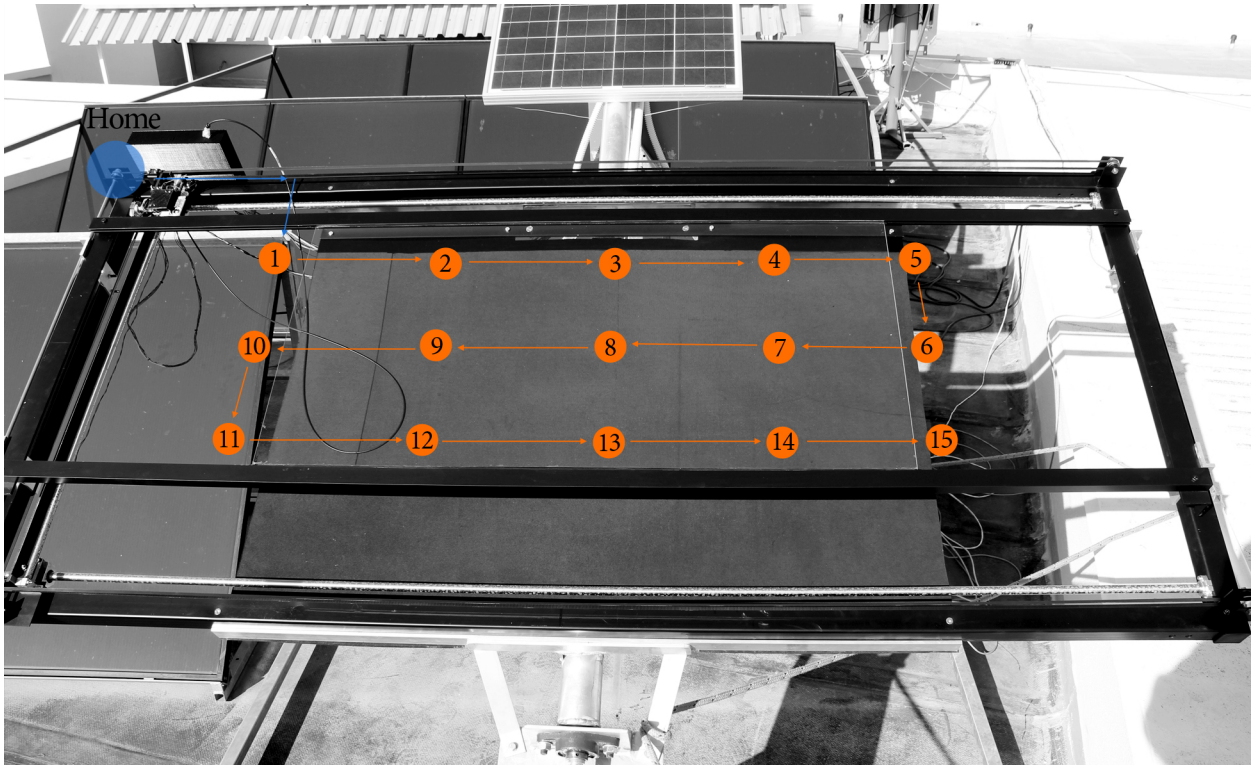

Figure 6.10: The home position, as well as the 15 measuring points.

Naturally, more measuring points would be advantageous to represent the glass plane increasingly with accuracy, but since the measurement period will not be extended enough to acquire true natural soiling, fewer measuring points are adequate for this project. Therefore, although the measuring plane of the receptor was calculated as approximately 31 mm, the soiling on the glass is approximated since the total area of the glass plane are not measured through the 9 glass measurements in the set.

Another measuring detail that has not been discussed in the software section is how the stepper motor control was implemented to move to a specific point. Ideally, one would like to specify the number of steps a stepper motor should take to reach a specific point, unfortunately that is not how the control could be implemented. Rather, the stepper motor

is essentially moving an x-number of steps to reach a specific point but how the instruction is supplied differs.

Combining first principles and the pulley theory as in equation 6.7, the following was reasoned: the velocity v and the angular velocity ω is related to linear distance λ, time t and frequency f. So velocity,

$$v = \frac{\lambda}{t} = \lambda \times f, \tag{6.17}$$

since $f = \frac{1}{t}$.

Further, the angular velocity,

$$\omega = \frac{2\pi}{t} = 2\pi f. \tag{6.18}$$

For angular velocity it is also true that,

$$\omega = \frac{v}{r}, \tag{6.19}$$

with r the pulley radius. Since the velocity is kept constant the linear length of one pulley rotation is calculated by combining equations 6.17 to 6.19. So that simplifies the linear distance,

$$\lambda = 2\pi r, \tag{6.20}$$

for 1 revolution. For the pulley with diameter $23\,mm$ used, one revolution equals linear movement of $72.257\,mm$. Further, the step mode is incorporated to calculate the time a specific amount of steps will require,

$$t = \#steps \times \frac{stepmode}{f}. \tag{6.21}$$

Since it is known that the stepper motor requires 200 steps to complete a full revolution, it is calcualted that $72.257\,mm$ linear distance equates to 200 steps, it is also known the how long each step requires at a specific frequency and step mode - the time for a specific linear distance is therefore easily calculated.

In essence, the required time to move a certain linear distance is calculated (as above), the hardware PWM is switched on and a delay is activated equal in length to the time calculated. With the delay finished, the PWM is simply switched off again. Naturally, this means that the processor is doing nothing but waiting for the delay time to be over - this limits the processing power of this system. One element where this method was quite disadvantageous is the interrupt handling of the micro switches on the Pi. If the interrupt was applied to the start of the script to execute whenever the switch is triggered, the script will wait as if the total distance is moved - this can cause the processor to infinitely pause although none of the motors are turning.

To circumvent the problem the distance that should be moved, if it the exact distance to move is not exactly known, is divided into short distances and repeatedly executed until the switch is triggered. The homing function specifically requires the motor to move a certain

distance, without necessarily knowing what that distance is; figure 6.11 is the flow chart for the Home() function.

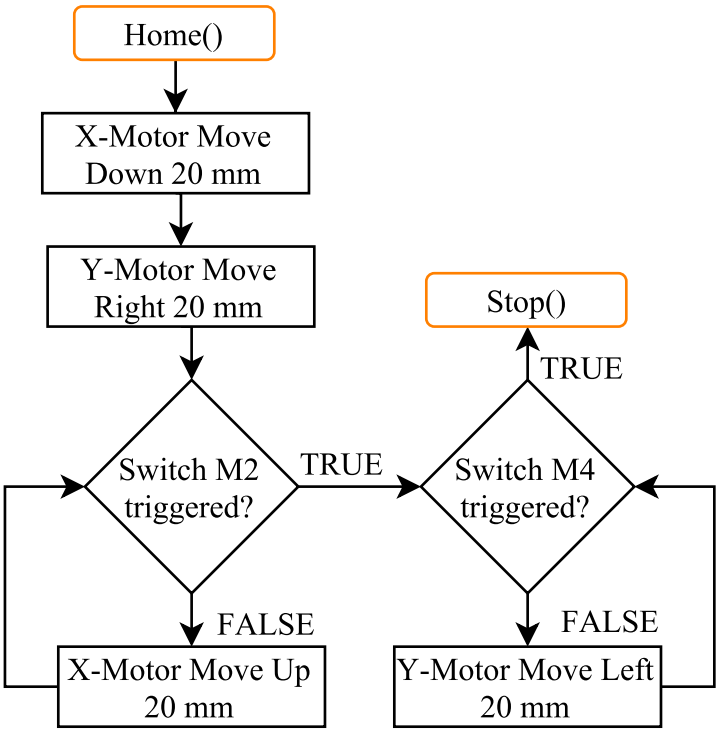

Figure 6.11: Homing function flow chart.

Further in the flow diagram, two initial instructions are given - each motor should move $20\,mm$ in the opposite direction of movement (as specified within the while loop). These additional movement in the seemingly wrong direction is to ensure that when the Home() function is called and the sensor is perhaps already at the home position (and the switches already triggered) that the processor is not continually held up by the interrupts.

6.6 Installation

The design originated from the basic requirements: a XY-plotter that would allow for the measurement of the spectrum on various points. As the design came together in a physical structure, several additional ideas and requirements came forward.

One of the last additions to elevate the project as a free-standing automated system was the addition of a solar power source. Since the voltage regulating boards allowed for a wide range of voltage input and the total electronic system drew little current, it was easily powered by a $50\,W$ solar panel connected through a charge controller to a $12\,V\,12\,Ah$ lead acid battery. The solar module is mounted above the plotter as seen in figure 6.12; the charge controller and battery are stored within the electronic box behind the structure.

The electronic hardware discussed earlier, is also located in this IP65 rated metal electronic box as seen in figure 6.13. The wires from the box is run through wire protecting tubing to the top centre of the plotter - the wires are further loose to ensure mobility of the wires when the plotter moves.

6.6.1 Final Installation Details

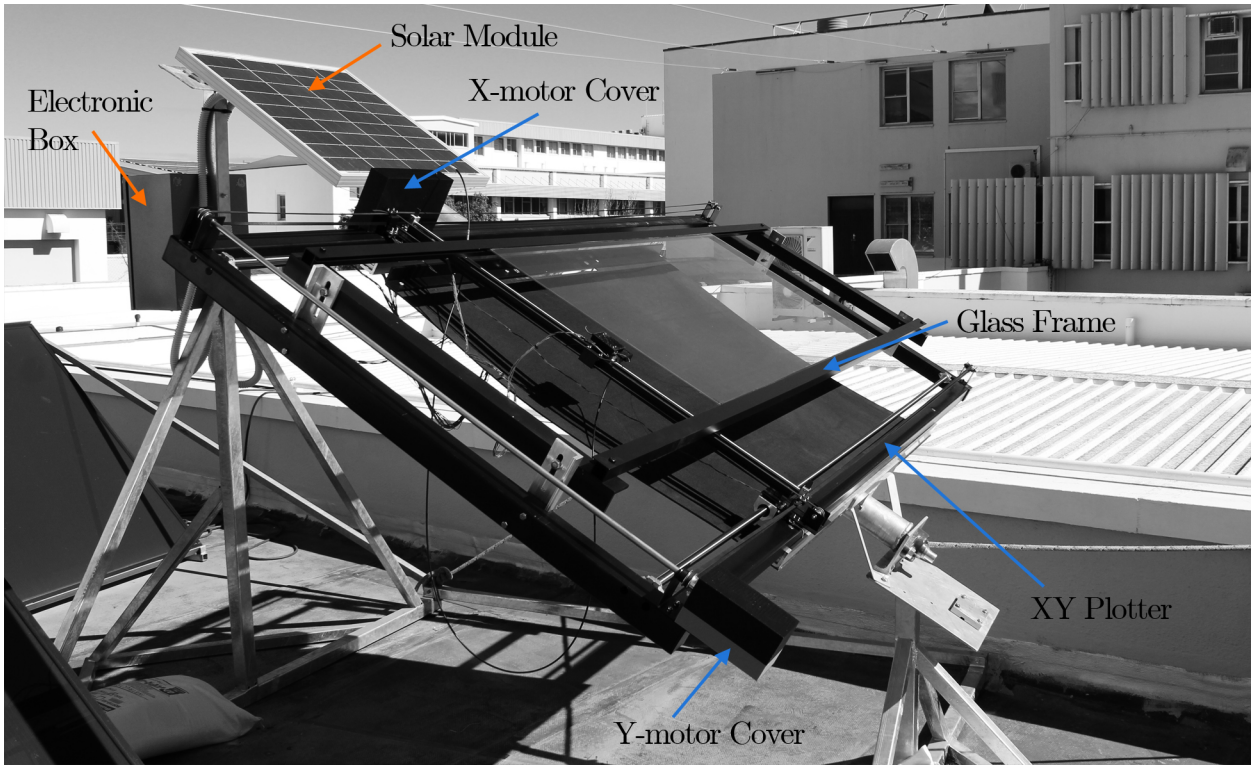

Figure 6.12: Total installation of the XY plotter structure with the glass in a frame, the electronic box and the final setup location.

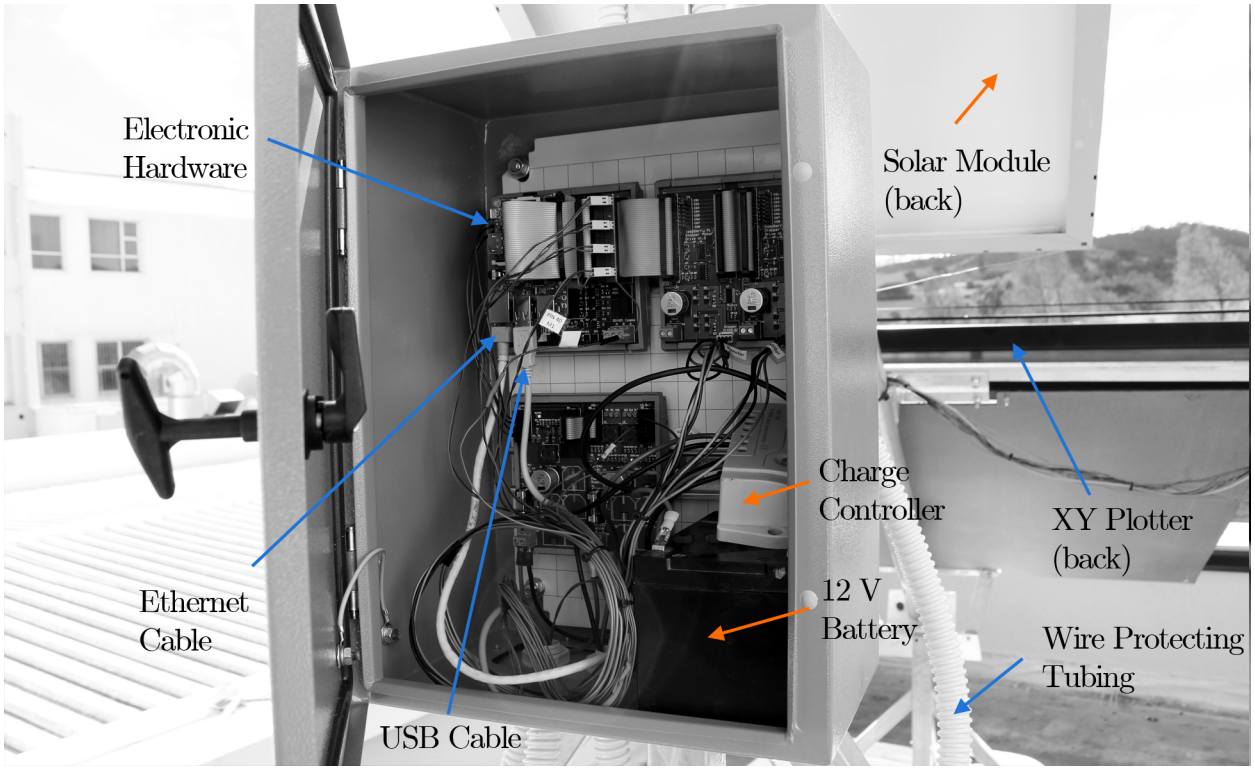

Figure 6.13: Total installation of electronics and the solar power supply.

In figure 6.14 a 3D printed cover is shown - this cover was additionally printed to protect the motor and spectrometer. The X-belt is threaded through the casing since the pulley is located within the enclosure. Similarly, the fibre optic is threaded through a circular hole at the top of the enclosure, but since the hole is located where rain and dust can easily enter, and additional rubber grommet was fitted to the hole around the fibre optic.

The belt clamp in both the X- and Y-axis was designed to simply hold the two ends of the belt together - this is a simple design where a top plate is forced close to the clamp through four bolts and nuts, keeping the belt ends together. After the micro switches were installed, it was perceived that the latches had nowhere to trigger against properly therefore, a small metal plate was attached to both ends of the shaft holders on the X-axis. There is a micro switch located on the opposite side of the bearing that cannot be seen in figure 6.14.

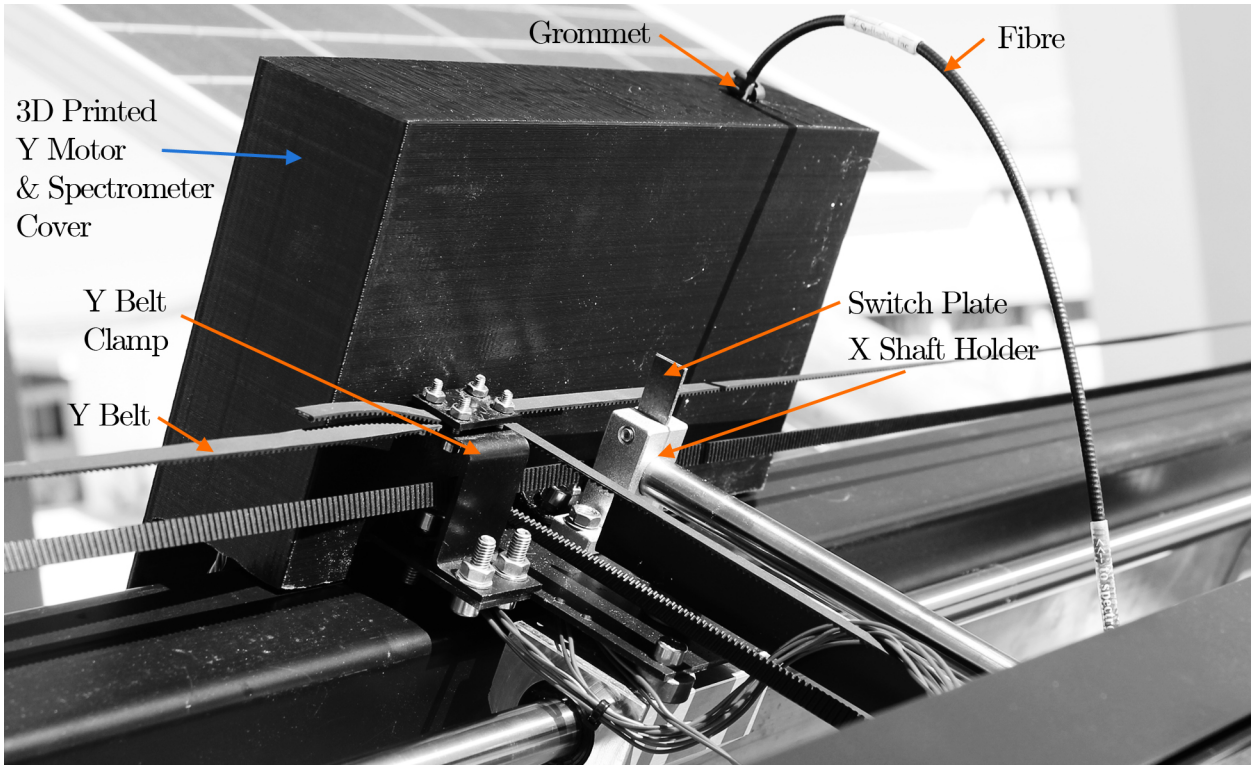

Figure 6.14: Final Y axis installation with a 3D printed cover over the spectrometer and X axis motor.

Perhaps the most complicated part of the hardware design was fitting all the necessary elements of the X-axis. Figure 6.15 shows the details of the bearing located on the X-axis. Originally this configuration only included the belt clamp and a singular plate to hold the sensor, later the 3D printed shutter was included and the micro switches on each side of this bearing. The micro switch terminals and wire connection were very exposed, therefore the terminals were covered with silicone and a switch cover was printed that merely fits over the existing switch bolts.

From the first use of the plotter serious twisting of the X-bearing was observed - the force of the belt pulled the receptor holder, which as a result twisted around the shaft. The addition of the stabiliser or guide rail solved this issue but with the addition of the weight of the shutter, servo motor as well as the pull of the fibre ensued into twisting in the opposite direction of the guide rail. Lastly, the 3D printed stabiliser clip was added to the arrangement

- the clip is a simple design that also fits on the existing clamp bolts, with the bottom sliding over the guide rail.

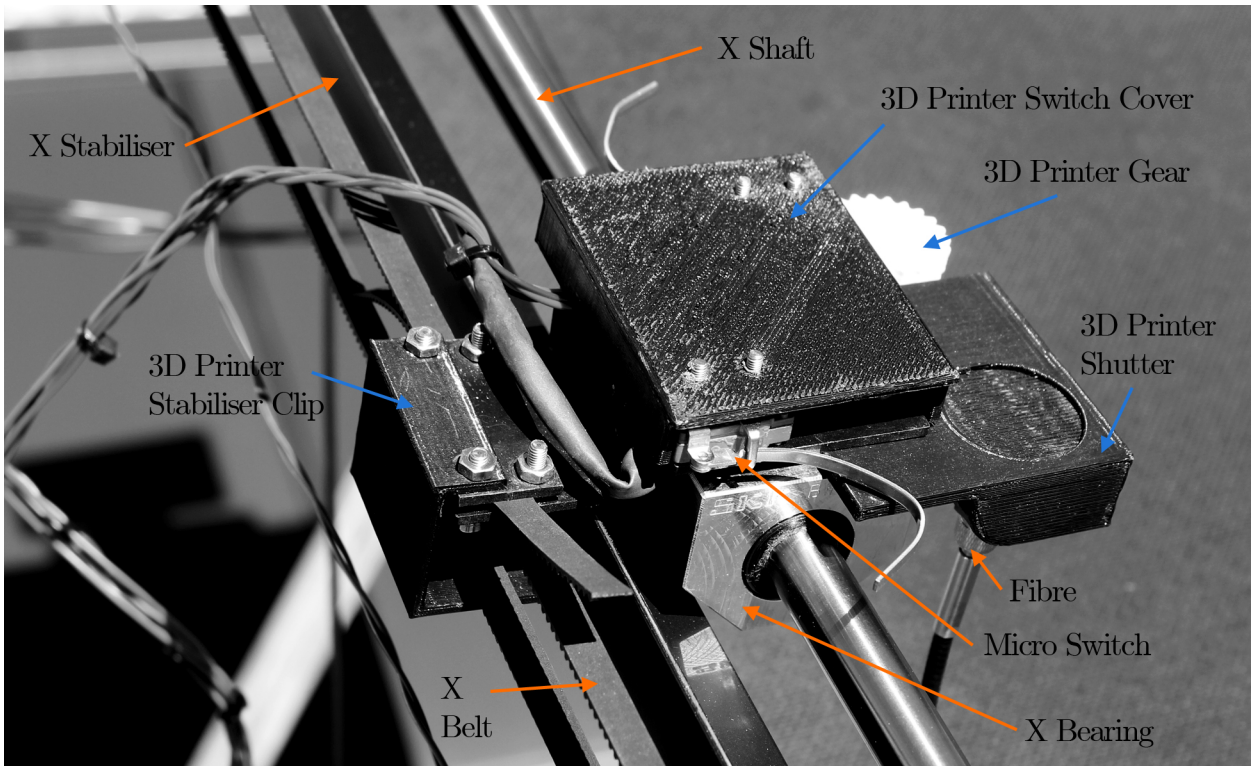

Figure 6.15: Final X shaft and bearing installation with 3D printed parts.

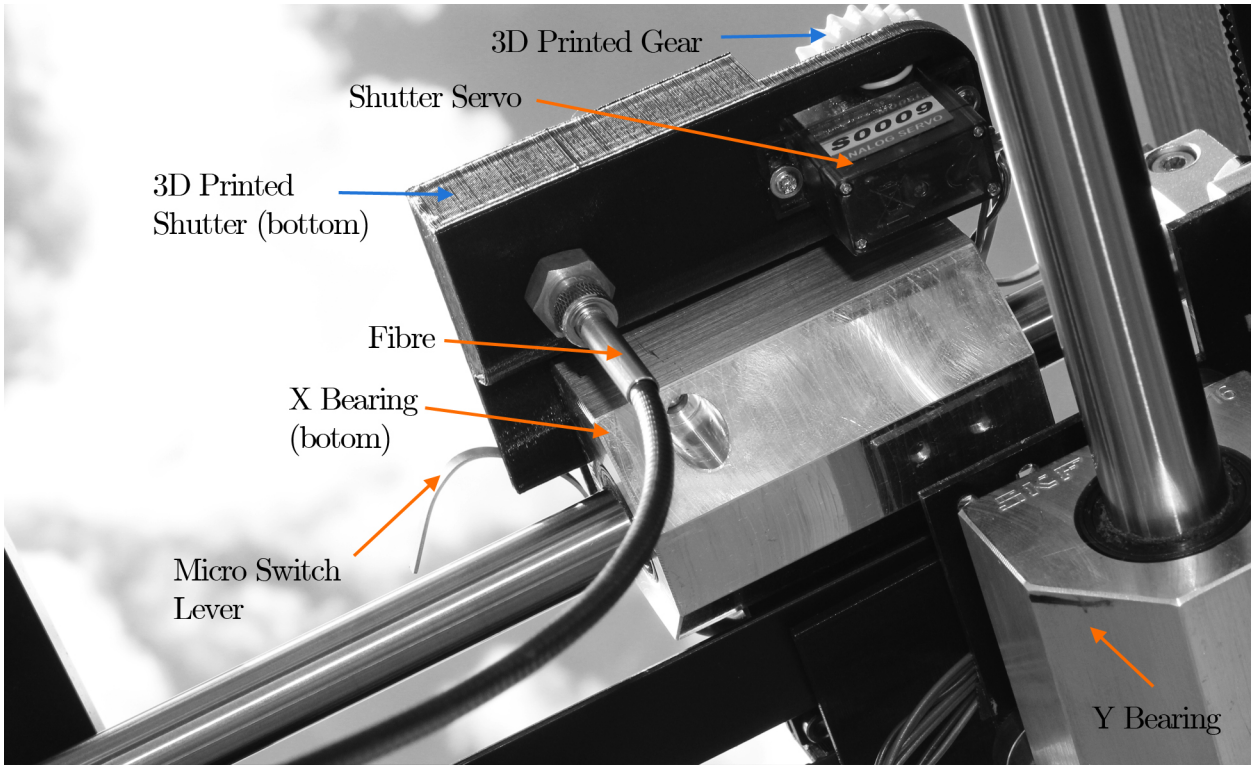

Figure 6.16: Final X shaft and bearing installation with 3D printed parts, a bottom view as to indicate servo motor of the shutter.

The underside of the X-bearing can be observed in figure 6.16 - this simply indicates how the servo motor is attached and how it drives the gear and therefore the shutter. The fibre end point screws on the cosine receptor which is located within the printed shutter; a nut keeps the cosine receptor from moving within the shutter holder.

In figure 6.17 it can be observed that the belts are threaded through each other as to ensure that the belts are as low as possible. Even with this adaption, the Y-pulleys were placed higher than originally intended, as to clear the X-belt. The concept of the configuration which is attached to the Y-bearing on each side of the plotter is a basic flat plate which holds the pulley, shaft and clamp elements. Spacers were used to lift the plate high enough to clear the frame of the plotter, since the shafts were located within the space of the frame. This clearance allowed for the addition of a micro switch underneath the bearing plate, removing it from the direct impact of water and dust.

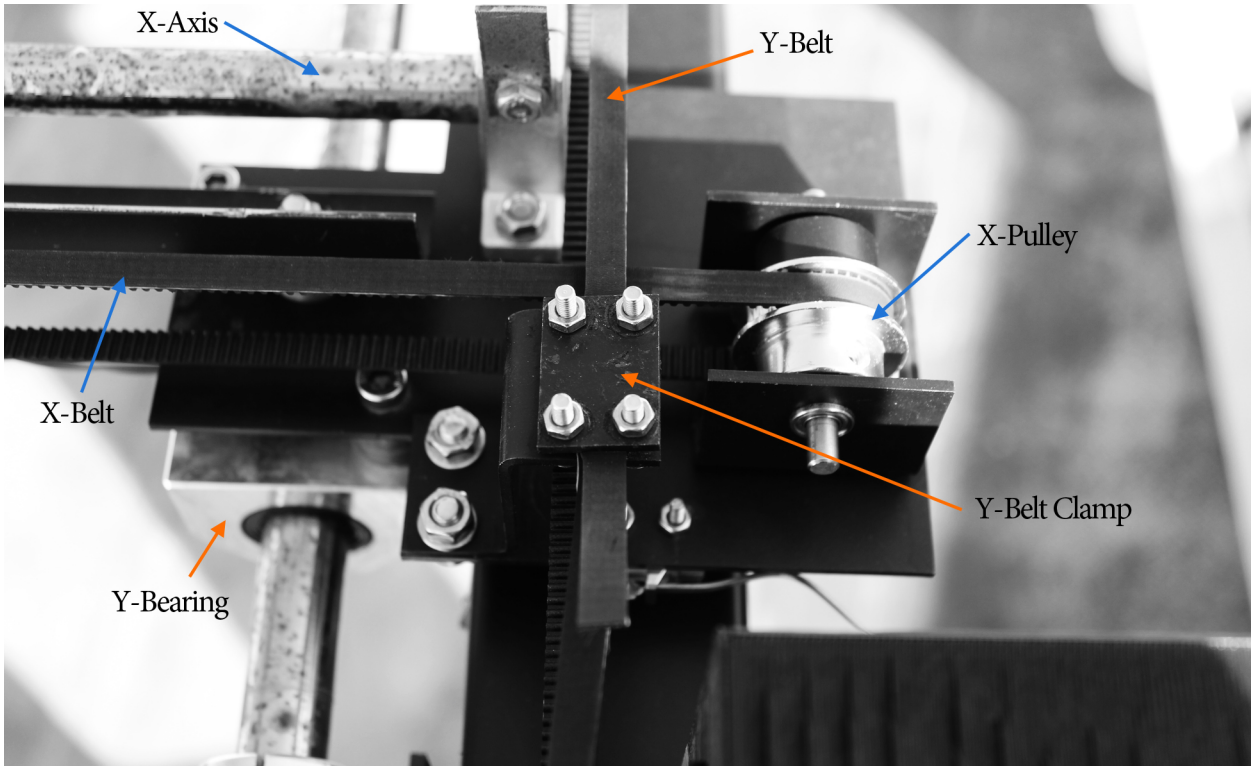

Figure 6.17: X-axis pulley and belt clamp attachment.

The plotter was finally fixed to an existing structure, with an angle of 30° facing true north atop a three story building. The location of structure is as such that it only receives environmental shading after 16 : 00 - even in the morning, no shading is possible by any structural element located around the plotter. There are some reflective elements in the vicinity - especially a white roof located to the right of the plotter. Fortunately, this can be considered within the data analysis since the measurement scheme allows for measuring points on the opposite side where possible reflection form the roof cannot influence the measurement.

6.6.2 Mechanical Accuracy and Precision

The accuracy and precision of the plotter movement can only be estimated through observation and repetition. One method applied to determine the precision was to place markers on the glass where the sensor is expected to stop - the movement cycle was executed multiple

times to observe how close the sensor stops after x-amount of cycles at each designated point. From this method of observation it was determined that the sensor stops in both Y- and X-axis in the approximation of 10 mm, in all directions, from the designated point. Figure 6.18 supplies a graphical representation of this observation.

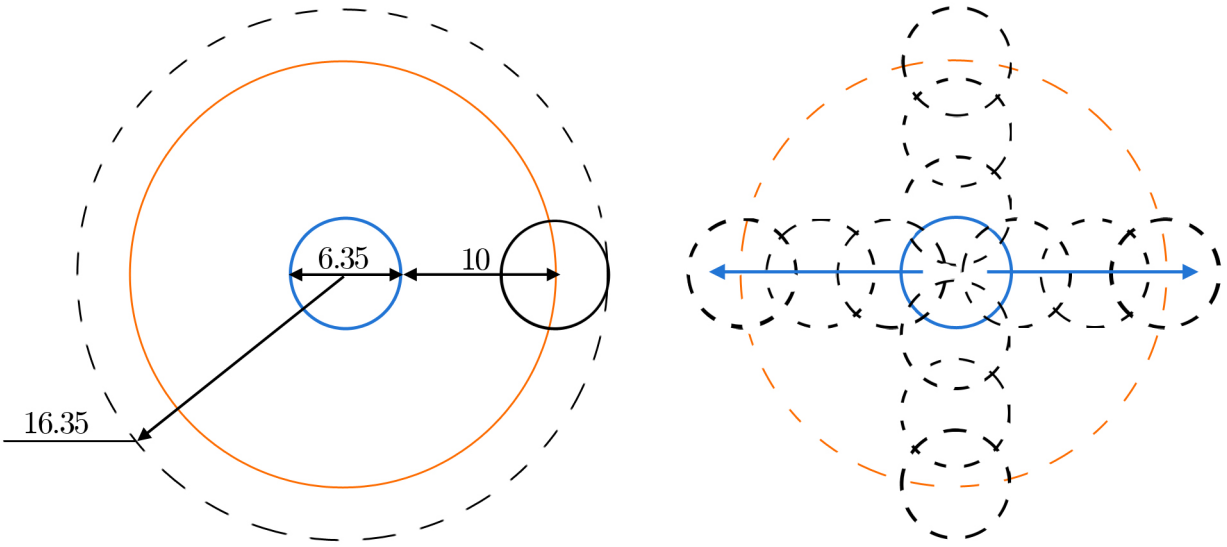

Figure 6.18: Accuracy and precision test result of the plotter movement, indicating the viewing circle and possible locations.

Previously, through optical theory, the "viewing" area could be calculated which was 31.67 mm^2 for the cosine receptor with a diameter of 6.35 mm. To calculate the possible area in which the measurement can be located is described through the accuracy and precision test figure. With the displacement error of 10 mm taken into account, the total possible area in which the measurement could be located is 839.82 mm^2 - perhaps a distorting view of the accuracy since the sensor can actually only be 10 mm out to the left or right, or up or down, as seem in the second diagram in figure 6.18.

Several factors could contribute to this linear displacement error - most probable in such constant errors:

1. The belt tension, especially over long belt lengths.
2. Inaccurate starting position.
3. Control method - the specified number of steps or time the motor should move.

Belt tension is extremely important when discussing displacement errors since the relationship between belt tension and the linear displacement forces, in equations 6.1 to 6.6, has already been established. Especially with the Y-axis belt being a considerable length, belt tension could play a role in the errors observed. Unfortunately, there is no direct way to determine the effect of belt tension on accuracy and precision - perhaps the easiest solution is to ensure the belt tension is good and this can be accomplished by the addition of a spring between the belt clamp and belt end.

Off course, if the position point is reliant on relative position an inaccurate starting position will cause the point to not stop at the expected position. This plotter does rely somewhat on relative positioning since there is no way of verifying what the actual position of sensor

is and since some trouble was experienced with the interrupt handling on the Raspberry Pi, it is reasonable to assume that an inaccurate starting position can cause the errors, or at least contribute towards it. An interesting observation when the sensor moved to the homing position, especially in the Y-axis, was that since the switch triggered on the plastic printed cover of the Y-motor with considerable force (with the contribution of momentum over the considerable length from the final measuring point) the cover acted as a spring, pushing the Y-axis back some small variable length into the direction it arrived from. As a solution, the homing function was called a second time so that the Y-axis approaches the home position from a shorter distance.

The control method implemented was discussed previously, and from first consideration of that method it is obvious that it would lack some accuracy against other more complicated control methods. Firstly, the method is open-loop, which in itself says that it receives no feedback and therefore the system cannot be monitored since it does not know what the output was. Then a second remark is required: the Raspberry Pi is not a dedicated processor and some questions remain regarding the timing accuracy - it could be interrupted or delayed by the processor accessing memory or several other events. Since the number of steps the motor is required to take is dictated through time, it can easily be seen why timing could contribute to error. Also, the required time is calculated but it might indicate that the motor should take for example 34.8 steps which is impossible since the motor cannot essentially step 0.8 without increasing the step mode - miss 0.8 ten times and this equates to 8 steps or 2.89 mm linear displacement.

Many control methods are available but most require an extremely accurate clock which is easily supplied by a dedicated processer - this would significant improvement to the control, accuracy and script streamlining.

6.6.3 Design Suggestions

Reviewing several important factors mentioned at the start of the project:

1. The system should be fully automated.
2. The measurements should mimic what is fundamentally ”seen” by a solar module; including the type and angle of light and how dust is accumulated on the glass.
3. The system should be able to withstand outdoor conditions, which include rain, substantial wind and dust, which may include light sandstorms.

On the first point, the requirement was basically met: the sensor moves to specific locations without human interference and a measurement is completed; additionally, the sensor is closed when a measurement is not being acquired. The data is also automatically stored - this supplies the options of storing data locally on the Pi, locally on an additional server or even on the web. Finally, the script automatically executes on start-up of the Pi, the measuring process automatically executing on every half-hour. The one issue with the automation is that since power is supplied by its own system, the power cannot remotely be turned on and off. This means when there is serious failure of the system, the script will turn off the motors but current will still be available that could cause the motor to continue to fail even though the script and Raspberry Pi is shutdown. Currently, the only way to turn off the power on the system is by removing the battery terminals or turning off the charge controller locally. A design suggestion which could remove this problem is the addition of circuitry

to the voltage regulators - an easy instruction to the Pi to switch that circuitry so that no current will be available to the motors for use.

The second point refers to the validity of the measurements in relation to what the solar module would see. Of course, the accuracy of the measurements and the location specifically is of great importance, as mentioned in the previous section but structurally imitating a solar module has its own complications. Irradiance measurements usually include environmental light, this includes environmental reflections, refractions and deflections of various planes. Starting local to the sensor, this requires that the frame containing all the plotter elements, as well as the frame containing the glass is required to be non-reflective. Since most metals are quite reflective, all the surfaces that could be coated was covered in a black "paint" that usually serves as an undercoat.

Back reflection is almost impossible in a solar module since the cells are mostly black or dark blue. Eliminating back reflection in the plotter, a temporary black coated hardboard surface was added to a section of the plotter where most measurements would have been acquired. Covering the whole back of the plotter frame would have been even better in reducing back reflection but since the glass does not cover the whole front of the plotter frame, the collection of water and dust would prevail within the frame.

Since the plotter is installed between previously installed solar modules, an interesting occurrence was observed: the plotter glass seems to hold moisture on its surface much longer than the solar modules - almost more than 2 hours longer. The condensation on the glass surface is expected to occur in the morning but it was not considered that condensation would form on the back-side of the plotter glass as well.

The condensation on the solar modules, naturally evaporated quicker since directly behind the glass surface is the dark cells which absorbs more radiation and therefore heats up the module, as well as the glass covering. Unfortunately, the black backing added to the plotter is not close enough to the glass to recreate this warming of the glass and therefore the plotter glass condensation takes longer to evaporate. It was observed that the cells of darker colour evaporates moisture first; also, as seen in figure 6.19 that the condensation is evaporated on the edges of the glass first - this off course can easily be explained by the heat transfer theory: the metal frame conducts heat faster than the glass so the edge closest to the metal frame would induce a higher evaporation rate. Similarly, the edge of the glass plane would conduct heat before the centre of the glass plane since, in effect, there is more air flow around these edges.

In most cases, the extended period of moisture would not specifically be an issue but the logic goes: the extended period of surface moisture would allow more dust particles to settle within the moisture and so attach to the glass when the moisture evaporates. The opposite might also be true - the plotter glass may remain cleaner since it harbours moisture longer. Only time will tell which is true, unfortunately this does not allow for direct correlation between the soiling on the plotter glass and the solar modules since no quantitative relation can be supplied for the soiling.

Perhaps the easiest solution would be to bring the dark back surface closer to the glass so stimulate a higher evaporation rate. With long-term comparison between the amount of soiling on solar modules versus the amount accumulating on the plotter glass, a relation could perhaps be determined.

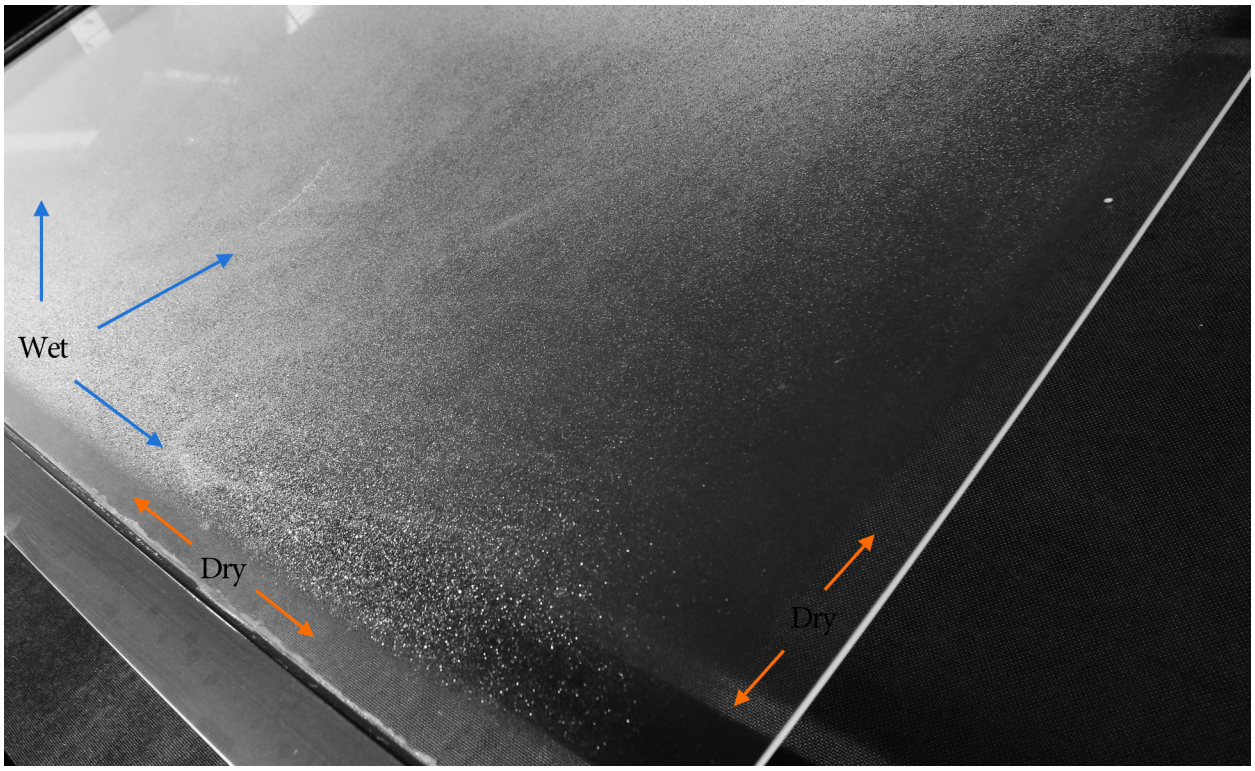

Figure 6.19: Condensation on the plotter glass at approximately 10:00.

The last factor is quite a substantial issue. Even in industry, manufacturing items that can last outdoor conditions are complicated and very expensive. Quite often, this need is removed by regular maintenance and the short lifetime specified on some items - the item is exchanged long before its due date to prevent failure of a system.

Some other preventive methods are coating items, usually in point or oil, to extend the lifetime and decrease the chances of corrosion and wear. Although the plotter frame and elements were covered with an undercoat to prevent local light reflections, it serves a second purpose: preventing rust and corrosion of metal parts. Since the undercoat usually does not singularly serve as a rust preventive, it was expected that the scratching of the material could allow for spot rusting of that element.

Naturally, the shafts could not be coated in a permanent paint or undercoat to prevent rust and therefore, originally it was decided to acquire shafts of a material that would not corrode in outdoor conditions. As mentioned previously, manufacturing such items are expensive - to have shafts treated for rust prevention and corrosion, costs three times what the shaft would originally cost. The shafts were simply manufactured therefore of untreated carbon steel, which is not corrosion resistant since it contains iron which forms iron oxide (rust) when combined with oxygen. In figure 6.20, rust spots can be seen on the shaft; this rust was observed after the first rain after installation, approximately three days of rain without cleaning or coating the shaft. All three shafts were similarly affected by the rust.

After the initial corrosion, the shafts were lightly sanded with sand paper to remove surface rust and prevent severe pitting of the material; the shafts were afterwards coated in a silicon spray that supplies an oil layer on the shaft. Although this would suffice for short term corrosion prevention, it would not last long - the oil layer would have to be reapplied quite often and this is therefore not a long-term solution. For a final prototype, it is suggested to either have the carbon steel shafts treated or more expensive stainless steel shafts should be acquired.

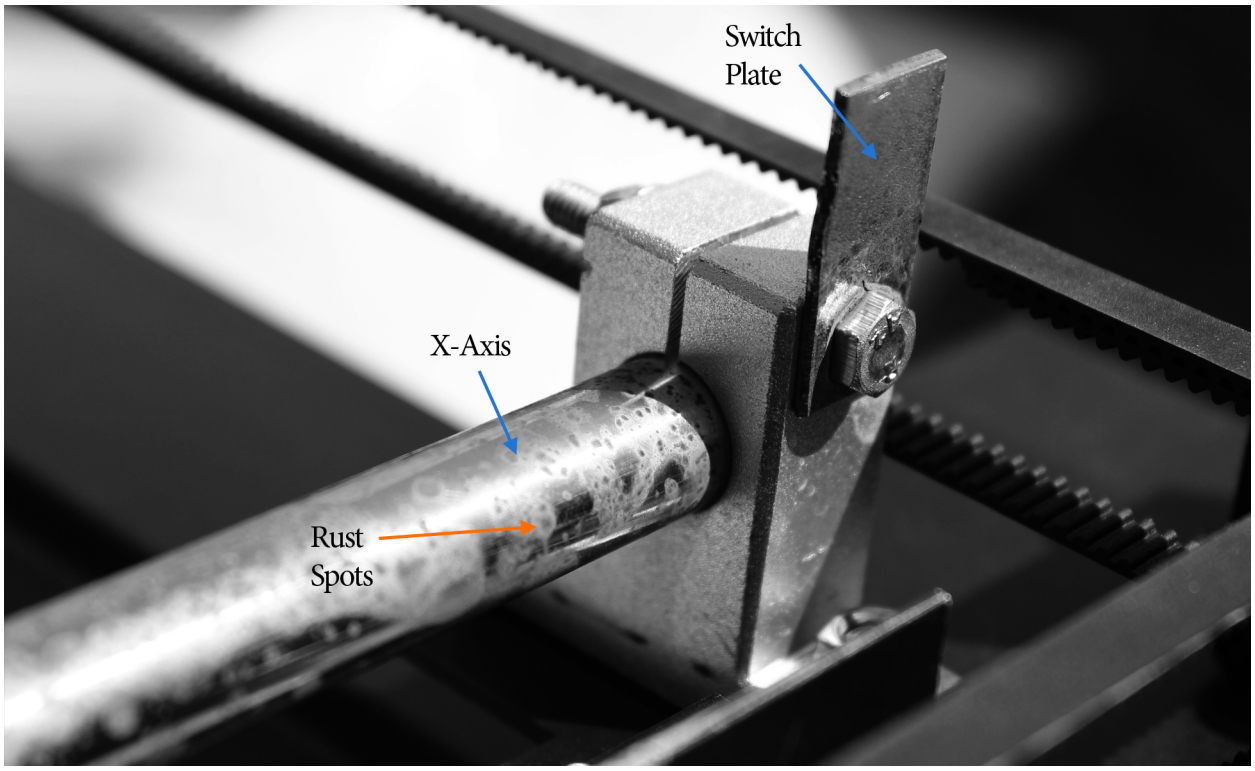

Figure 6.20: Iron oxide formation on the carbon steel shafts due to moisture exposure.

In short, the design requires an increase in robustness - this includes the upgrading of all protective covers (micro switches, motors and spectrometer) to at least IP 65 rating. The system will become increasingly important in extreme arid areas where dust quantity is significantly large. Off course, installing a plotter in such harsh conditions will increase the design cost exponentially since robustness in material and items are hard to come by.

A smaller plotter design would decrease the design cost since the largest expense (excluding the spectrometer) is the shafts, even though they did not even fully comply to the design requirements. The system could benefit from increased compactness as well, perhaps locating the motors and belts within the frame. Many design options are probable, but if keeping the initial design requirements in mind and combining it with compactness and a smaller measuring surface the design could be at its optimal state.

Despite the various issues pointed out in this section, the designed and built automated system is sufficient for the measuring period specified for this project.

Chapter 7

Results

7.1 Introduction

The automated system discussed in Chapter 6, was installed and collected measurements since 1 August 2017. The idea was that the system would be fully automated but with rainy days the script has to be stopped manually so that no measurements should be acquired. It was decided to not measure on rainy days since the period the shutter is open for the measurements, is enough to cause water to collect within the shutter around the receptor - this might cause water damage to the receptor. Otherwise, the system measures between 09:00 and 16:30 every 30 minutes. One other observation, the spectrometer shows interesting behaviour when the power is reconnected - the first measurement after this restart is a string of maximum count points (saturation). So, it can be observed that some days the first measurement is unavailable.

Python scripts were used to extract data from the database, to convert *count* values to irradiance, calculating total irradiance values, and for all other analysing methods. These scripts assist in supplying constant and correct analyses of data over all the measuring sets. Also another advantage of using an automated system is that measurements in a set can be acquired effectively and within a short period of time - the total period of one measurement set of 15 measurements is between $1\,min\,25\,s$ and $1\,min\,30\,s$.

Since the automated measurements consist of more measurements within a set and acquired over more days, than the previous measurements, the baseline measurement analysis procedure followed before is adapted to suite all the measurement points. Also, some adaption was required for the glass and soiling transmission loss analysis since the glass was only cleaned at the start of the measuring period and therefore no direct distinction is made between the clean and soiled glass sample at every measurement set.

7.2 Clear-Sky Baseline Measurements

This section will start with an in-depth clear-sky baseline measurement breakdown, this includes: confirming that the use of an approximate black spectrum is a worthy approximation, a comparison of the spectrometer measured irradiance and irradiance values from a pyranometer.

7.2.1 Measured Data Comparison to DNI, DHI and GHI Data

As mentioned previously, it was decided to implement an approximate black spectrum of 1500 *counts* to the automated system measurements. A first plot of every measurement set's baseline measurements indicated an interesting observation: from as early as 10:30 on some days, the subtraction of the black spectrum ensues in negative irradiance values in the wavelgength band of approximately $1000 - 1100\,nm$. Alternatively, morning measurements indicated an extreme increasing trend towards $1000\,nm$. This begged the question if it is suitable to include this black spectrum, or rather, is the measured irradiance a better approximation with (W) or without (W/O) the black spectrum.

Figure 7.1 is an example of the prevalent trend observed in morning measurements, and opposingly, the trend observed in the afternoon. Some comparison is still required between the distributions with and without the black spectrum, but this can only be accomplished by reducing the wavelength range analysed. While limiting the range to $300.26 - 999.65\,nm$ to exclude the wild trend at the last wavelength band, quite a large variance is still observed in this limited range. The difference in the two distributions at 14:30, in the limited range specified, does seem small but was calculated to be 27.023 %. This percentage difference was calculated by first transposing every data point into an irradiance value and calculating the area (with Simpson's rule), then simply calculating the difference between the two distributions. Off course, it is expected that there would be a difference since in effect the distribution with the black spectrum is essentially calculated by subtracting 1500 *counts* from every data point before it is converted to irradiance - the difference caused by this process within *count* measurements is simply 12.01 %, indicating an additional 15.01 % is cause by the superimposed calibration.

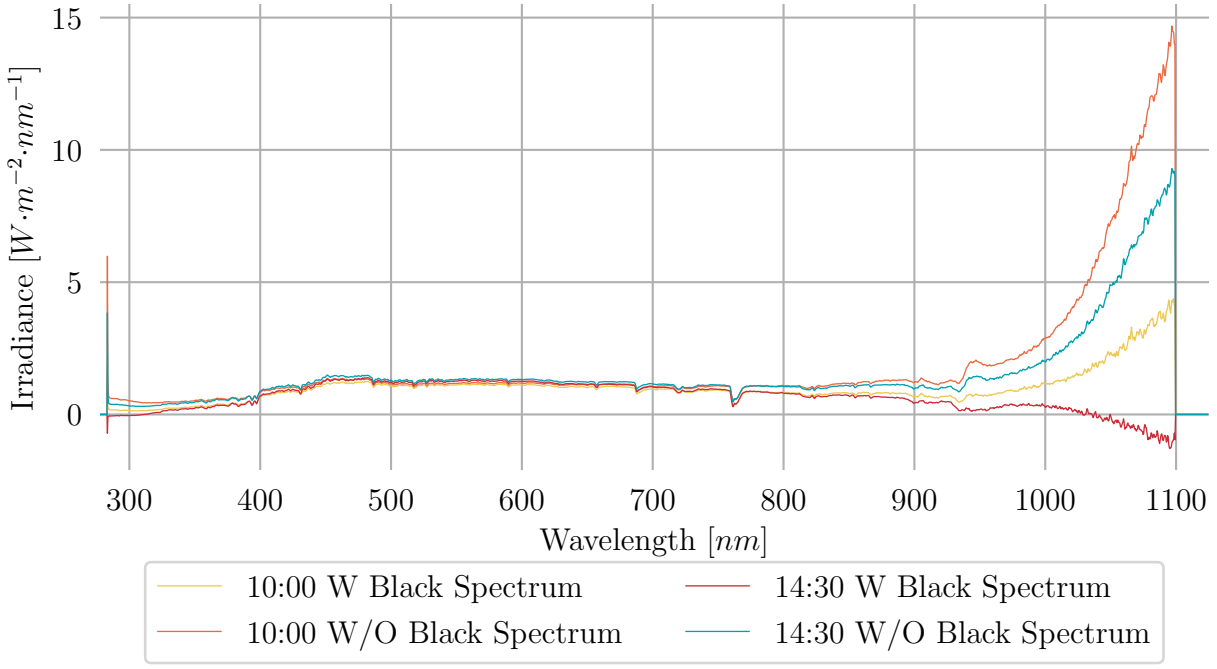

Figure 7.1: Two measurements on 14 August 2017 with (W) and without (W/O) taking into account the black spectrum of approximately 1500 *counts*.

From previous discussion in this thesis, these wild trends were attributed to the sensitivity of the spectrometer in these ranges, but unfortunately it now has a significant impact on the measured data. As before, a comparison between the measured distribution and acquired pyranometer data is analysed - this could also determine if the data with or without the black spectrum is a better approximation of the true irradiance.

Three days in August (18-20 August) were chosen for this analysis, their clear-sky baseline measurements are transposed into irradiance and the total is calculated for each baseline measurement. The SAURAN data is supplied minutely, therefore the first three baseline measurements are compared to the irradiance measured on the hour (e.g. 10:00) and the last three to a minute past the hour's data (e.g. 10:01). Figures 7.2 to 7.4 indicate the comparison with SAURAN data.

The SAURAN data is collected by a pyranometer from Kipp & Zonen, the instrument collects radiant fluxes impinging on a surface plane which is integrated, similar to the spectrometer measurements, but the range of the pyranometer is approximately $285 - 2800\,nm$ [74].This means that the spectrometer is only measuring a part of the range observed by the pyranometer, fortunately the band measured by the spectrometer is the band where the larger portion of irradiance is observed. Now it can be argued that the irradiance measured by the spectrometer will be lower than that measured by the pyranometer.

Still, some comparison between total measurements and the spectrometer measured data is required and for this reason three types of data from SAURAN is plotted: DHI, DNI and GHI. The diffuse (DHI) and direct (DNI) irradiance values are measured by the SAURAN measuring station and the global (GHI) irradiance values are calculated through a simplification of the research provided in section 2.2.1 [25]. The global horizontal irradiance,

$$GHI = DNI \times \cos\theta_z + DHI, \tag{7.1}$$

with θ_z the sun angle.

On 18 August, figure 7.2, the measurement with the black spectrum estimates the DNI measurement, the measured data being slightly higher in the morning with a turning point at 11:00, where the DNI is slightly higher. The measurement without the black spectrum does not as closely relate to a specific measurement but there is some similar data points between the measured and the diffuse, as well as the global irradiance.

The measurements on 19 August is quite variant but this is a good indication that the variances in the measured data is not caused by the system or incorrect measurements but are indeed caused by environmental conditions, as seen in figure 7.3 at 14:00 and 15:30, for example.

20 August (figure 7.4) supplies a more constant response overall, with slight variation in the morning. Again, the measurement without the black spectrum relate somewhat to the DHI values but the discrepancy between the two measurement types increase towards afternoon. Although the divergence between the DNI and measured spectrum (W) relate quite closely, a greater divergence is also prevalent towards late afternoon. The turning point where the DNI is increasingly larger of value than the measured (W), is observed is at 11:30, with a difference between the two sets of approximately $2 - 8\,\%$.

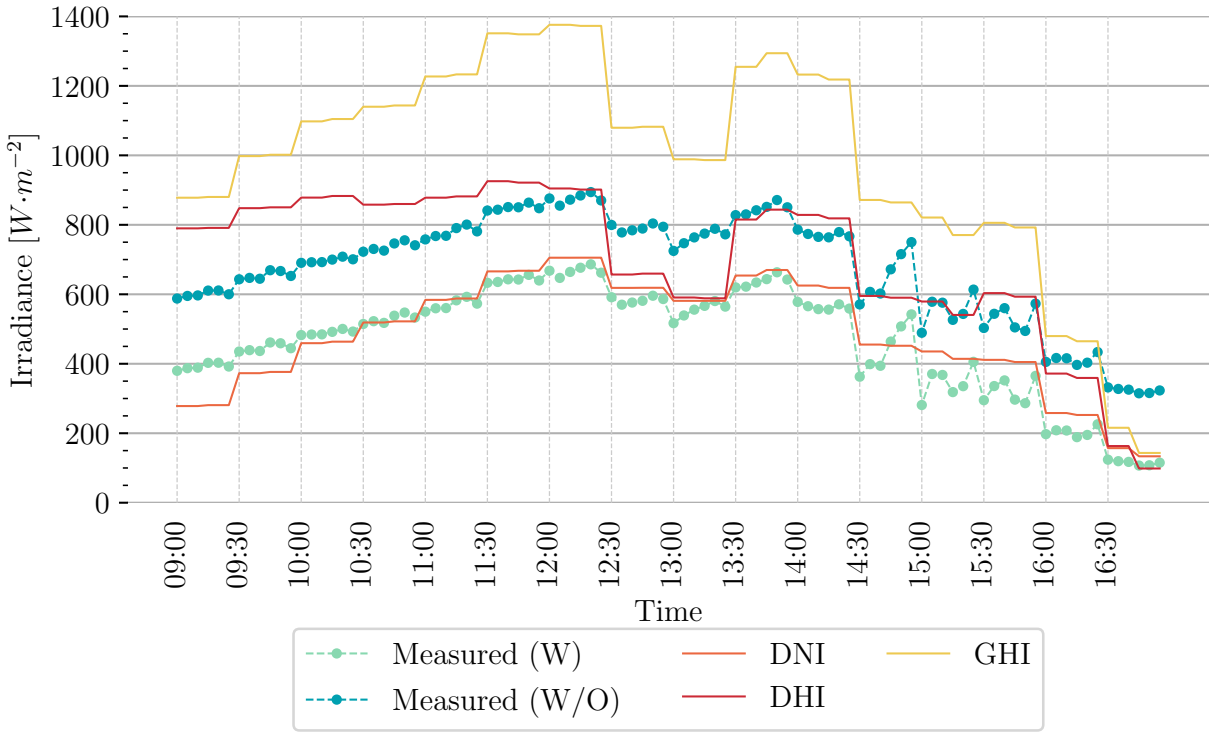

Figure 7.2: SAURAN measurement in comparison to the spectrometer measured totals with (W) and without (W/O) the approximate black spectrum (18 August 2017).

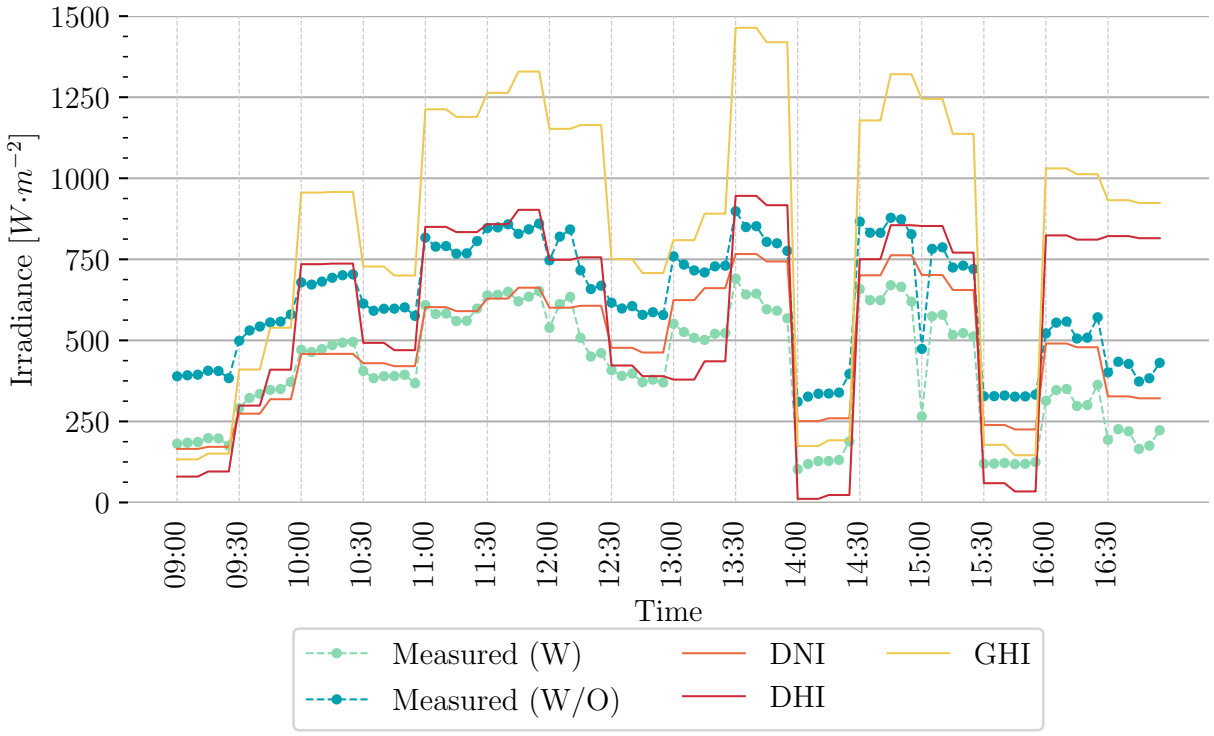

Figure 7.3: SAURAN measurement in comparison to the spectrometer measured totals (19 August 2017).

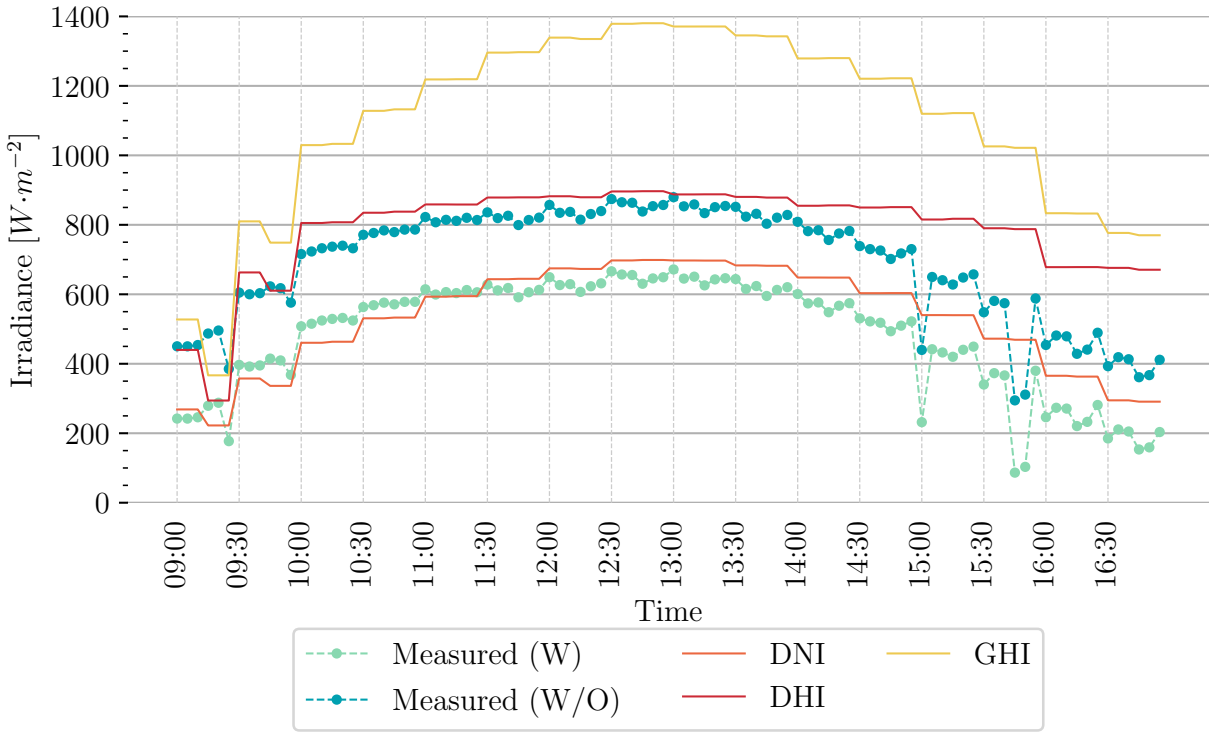

Figure 7.4: SAURAN measurement in comparison to the spectrometer measured 20 August 2017.

Observing the sun angles in figure 7.5, calculated from equations 2.13 to 2.19, solar noon can be approximated at 12:48 for these three days in August. The red dot indicates the effective measuring point of the spectrometer in the automated system, indicating that although the largest number of photons will be available at solar noon, a maximum number of photons will not necessarily be measured here since the sun actually sits "higher" in the sky than what the spectrometer is observing at its fixed angle of 30°.

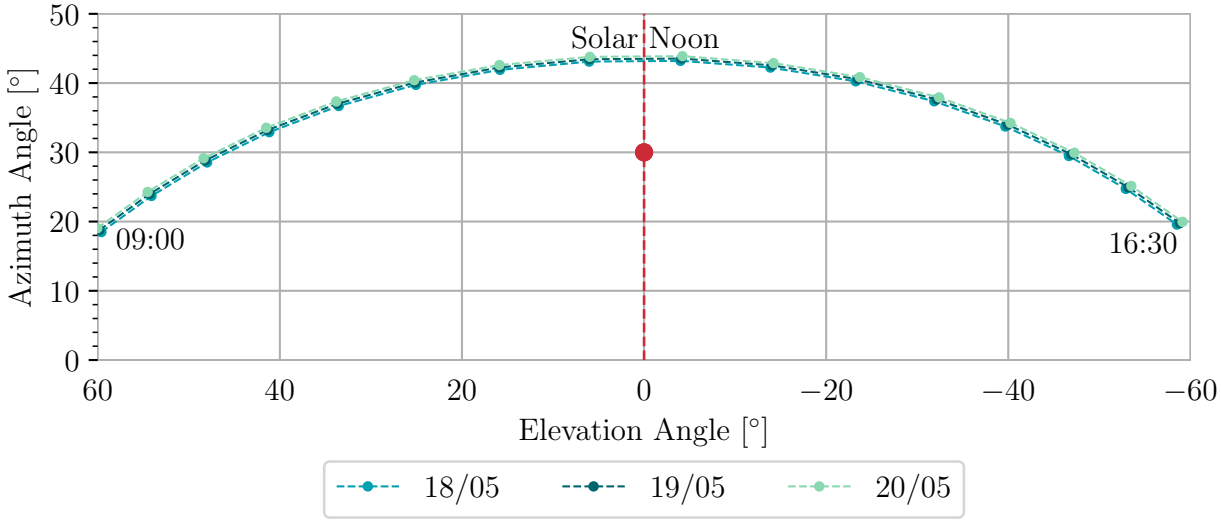

Figure 7.5: The sun azimuth and elevation angles on 18 - 20 August.

Further, the restriction on measuring direct irradiance is the field of view, or acceptance angle, of only 5° according to ISO 9060 [74]. Therefore, even though the spectrometer measured irradiance, seems to approximate DNI, it certainly is not. The following points of explanation is supplied:

1. From figure 7.5 it can in fact be seen that the receptor will never be directly in line with the sun position, it can only be in line in one of the directions.
2. The totals measured by the pyrano- and/or pyrheliometers are measured over an extended wavelength range - calculated from the $AM1.5$ data provided by NREL [67], is approximately 28.88 % larger than the limited used range of $300.26 - 999.65\,nm$.
3. Increasing the measured data (including the approximate black spectrum) with this difference calculated from the standard approximate the diffuse irradiance closer after the adaption, but still only around solar noon, as seen in figure 7.6.

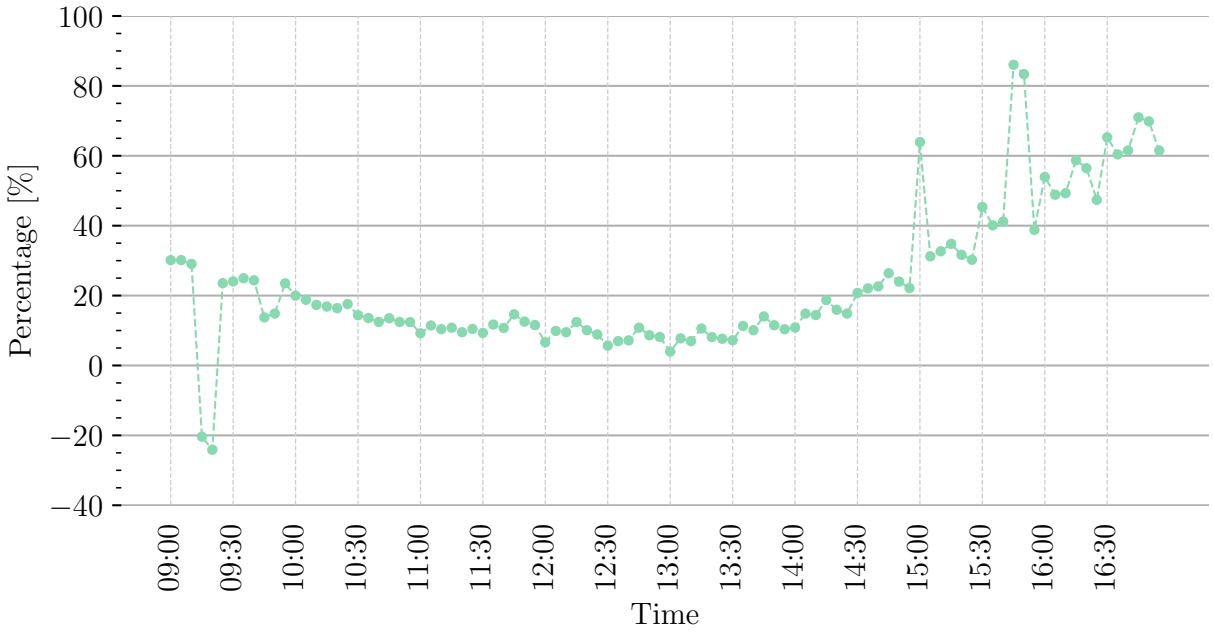

Figure 7.6: Percentage difference between the adapted spectrometer irradiance values and the DHI from SAURAN, from 20 August 2017.

In conclusion, although the adapted spectrometer data did approximate the diffuse irradiance better than before (rather than the incorrect approximation of direct irradiance), the approximation lacks accuracy earlier in the morning and late afternoon. Therefore, it could be said that the spectrometer, at a fixed angle, measures approximately diffuse irradiance around solar noon, but only partly measures diffuse irradiance - the diffuse irradiance is still $> 20\,\%$ - in the early morning and afternoons.

7.2.2 Measured Baseline Irradiance Values

Following the previous analysis, the data further includes the approximate black spectrum, as explained. Now, the total irradiance values over the measuring period is compared over various days and time periods, since full datasets between 09:00 and 16:30 exist. The extended and continuous measuring process (unlike the preliminary experiences) allows for

additional analysis of the baseline measurements and perhaps additional knowledge of the measuring environment. The distribution details are also required since it has not been analysed in depth before.

The total irradiance values, calculated at each baseline measurement between 09:00 and 16:30 over four days, are shown in figure 7.7. As expected, the two more constant measurement sets (20 and 28 August) are very similar around solar noon (12:30 to 13:30) in total, with an average difference in total baseline measurements of less than 3.5 %.

Even though percentage differences can be calculated for total irradiance values quite easily, it does not show what the distribution of the error is. As the angle of the receptor is fixed, similarly to the second preliminary experience, the error distribution throughout the day might be of interest. Figure 7.8 does show a very similar response to that observed previously in the preliminary experience - the percentage difference or error within the visible region is quite constant and decreases towards solar noon. This specific day was constant, but the first measurement at 09:00 did indicate more variance than experienced on other clear days - the average total percentage difference at this time is $4\,\% - 5\,\%$ but on 20 August the total difference was 26.84 %. This increased error could simply be ascribed to additional water vapour content in the air on that specific morning, perhaps even a stray cloud formation passing over.

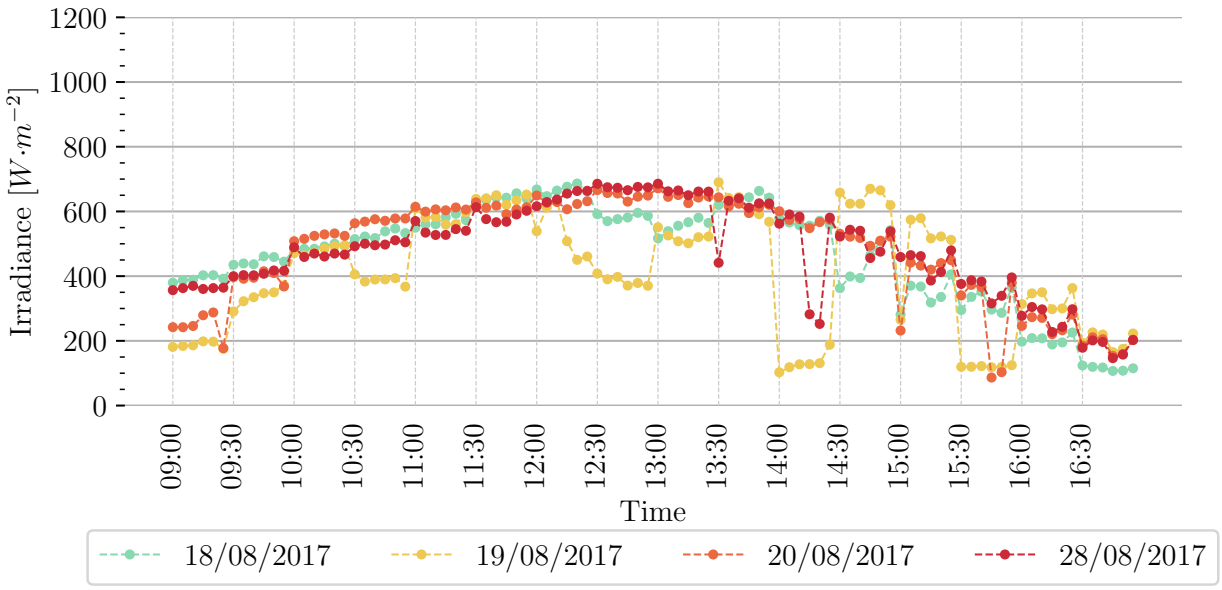

Figure 7.7: Total irradiance values over four days in August.

The noise observed at the start and end of the shown wavelength range, is expected and is a combination of the spectrometer sensitivity in these ranges as well as the influence of the calibration superimposed on the measurement. Still, it is determined that the percentage difference calculated from the total irradiance values is a good representation of the percentage range within the approximate visible range of $500 - 700\,nm$. For example, at 09:00 the total difference was calculated as 26.84 % and the error range within $500 - 700\,nm$ is approximately $26 - 33\,\%$; similarly at 10:00 the total was 3.18 % and the range $0.62 - 4\,\%$ and so forth for the other measurement sets. In the afternoon measurement an increase in error is observed from solar noon towards late afternoon - the total errors increase from 3.77 % at 13:00 to 12.50 % at 16:00.

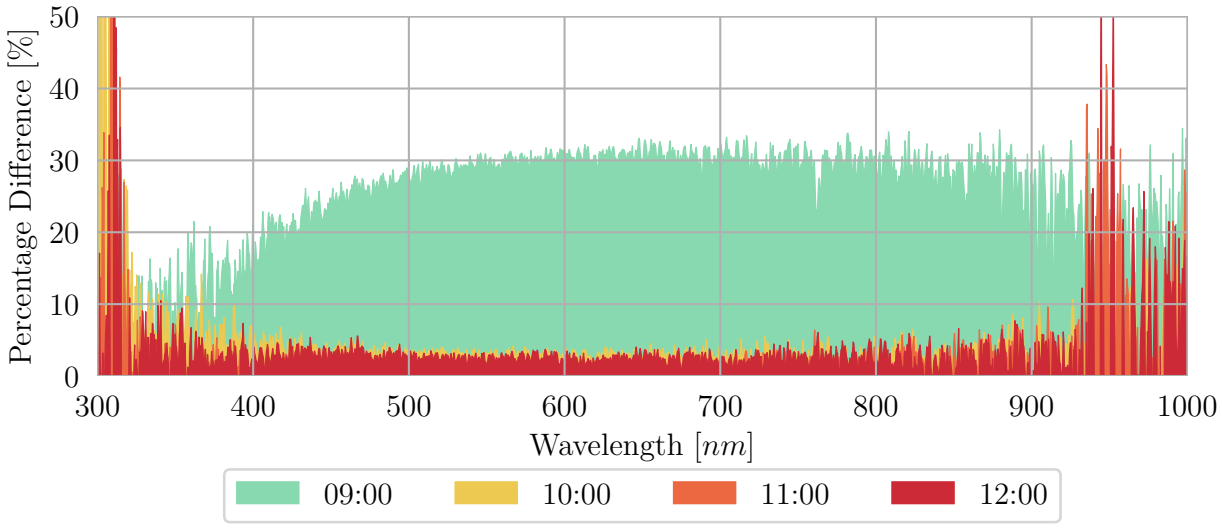

Figure 7.8: Calculated percentage difference distribution between the first and last baseline measurement within a set on the morning of 20 August 2017.

Although the previous analysis only determined the error between the first and the last measurement, it is of interest if all baseline measurements within a set differ with the same distribution. This requires detailed inspection of the distribution error of each measurement. Also, this analysis might later indicate whether the glass significantly changes the distribution of radiation beams transported through the glass

Observing the totals calculated in table 7.1, the first two baseline measurements (B1 an B2) only differ with 0.03 % in total and this difference is approximately equally divided between the various wavelength divisions. The differences between the first baseline measurement and the slightly larger B4 and B5 measurements, are slightly larger over all the divisions:,

$$\Delta Total(B1 - B4) = 15.80\,\%, \tag{7.2}$$

with the UV 10.58 % larger, Vis 17.30 % larger and NIR 14.33 % larger for B4. Similarly, the total difference between B1 and B5 is 13.20 %, with UV 9.02 % larger, Vis 14.49 % larger and NIR 11.90 % larger. These differences indicate that with an increasing total irradiance value, the visible light increases more significantly than the NIR and UV wavelength bands - this is mostly true since the total NIR band is not measured in its totality with the spectrometer measurements.

Table 7.1: The total baseline measurements on 09:00 (20 August) in the UV, visible and NIR wavelength bands.

	B1	**B2**	**B3**	**B4**	**B5**	**B6**
Total	242.24	242.17	245.94	279.07	287.70	177.23
UV	11.59	11.70	11.71	12.74	12.96	10.28
Vis	131.40	131.63	133.98	153.67	158.88	94.26
NIR	98.70	98.29	99.70	112.03	115.21	72.27

The following plots in figures 7.9 to 7.11 are specifically convenient for this error distribution analysis since an early morning measurement has a smaller difference between minimum and maximum measured values, making a detailed view accessible. Also, this specific set contains more varied total irradiance values - the error between the measurements range between 0.03 % and 38.40 %.

The distribution in the UV figure in 7.9 indicates that the instrument is not responsive enough below approximately 360 nm to indicate the true distribution difference between the measurements. Similarly, the amount of noise in the NIR (figure 7.11), longer than 900 nm, also does not provide clarity regarding the distribution difference within this range - only the measurement that differs significantly from the other, can be distinguished within this range. As previously determined, the difference between measurement are quite constant within the visible range and supplies a good approximation of the difference between the baseline measurements, figure 7.10.

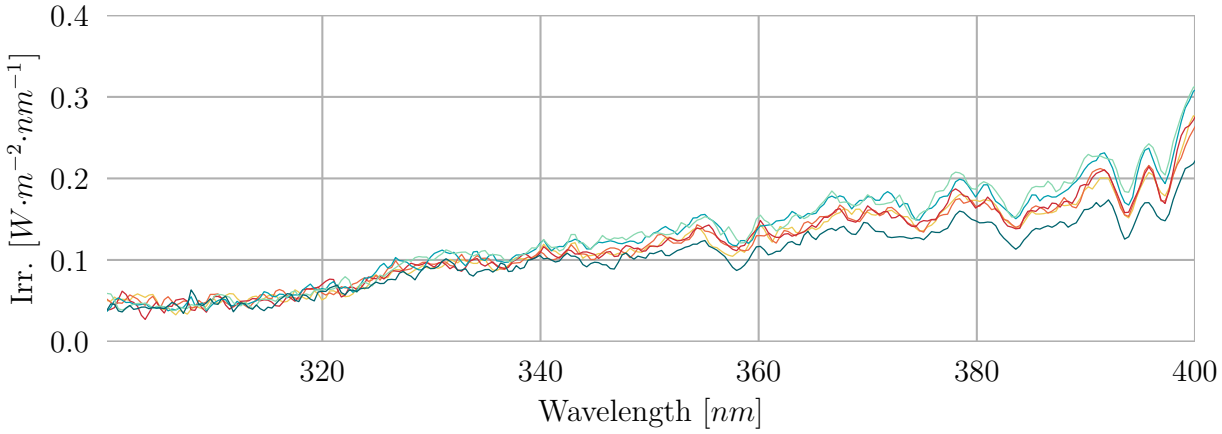

Figure 7.9: Detailed view of baseline measurements on 09:00 (20 August) in the UV wavelength band.

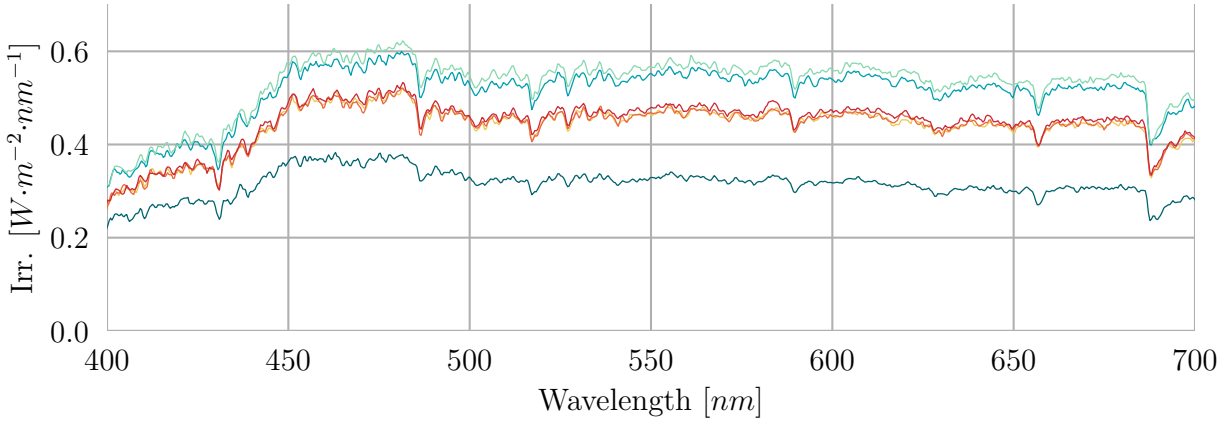

Figure 7.10: Detailed view of baseline measurements on 09:00 (20 August) in the visible-wavelength band.

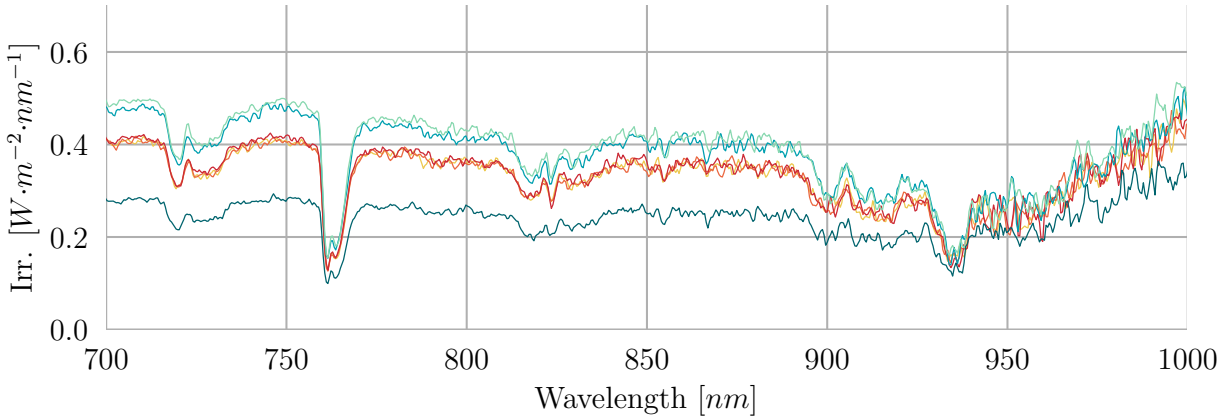

Figure 7.11: Detailed view of baseline measurements on 09:00 (20 August) in the NIR wavelength band.

Although this section supplied less quantifiable data than expected of a baseline measurement analysis, it supplied more observations regarding the distribution of irradiance and the distribution of error within a measurement set. Further, this section included seemingly inconsequential observations, such as these on the inclusion of a black spectrum. The use and measurement of black spectrums were unknown even after a significant amount of research but this insight was gained by many measurements and the in-depth analysis of it within this project. It should therefore perhaps be reiterated that this thesis attempts to supply a guide on spectral measurements that is all inclusive to irradiance measurement and analysis.

7.3 Glass/Soiled Measurements

With the previous experiences the stable condition requirement of 5 % were analytically discussed in the baseline measurement sections, but the automated glass or soiling measurements are more influenced by the baseline measurements and requires simultaneous analysis. This greater influence is simply because more measurements are included within one measurement set, and the fixed angle of the receptor increases the variance of the measurements, as observed in the previous section.

Further within this section, all table data will be supplied in the order of the original measuring scheme, as seen in table 7.2. Supplying the data within this format allows the reader to easily determine the location of the measurement within the automated system. As previously mentioned "B" indicates a baseline measurement, "G" a glass or soiling measurement and the consecutive number indicates its position within either the baseline or glass measurements independently.

Table 7.2: The automated measuring scheme and measuring locations.

X-Y	350	650	1050	1450	1650
200	B1	G1	G2	G3	B2
400	B4	G6	G5	G4	B3
600	B5	G7	G8	G9	B6

7.3.1 Total Measurement Sets

Firstly, observing a simple plot of all total irradiance values of a measurement set over multiple days within the measuring period, a definite decrease is observed in all the glass measurements, in comparison to the baseline measurements. Figure 7.12 indicates the loss of transmission even though it was a variant measuring period - this is a good example to indicate the importance of the stable condition requirement. The sets indicating tranmission loss with decisiveness, are all sets with errors smaller than 5 % between the total irradiance baseline measurements within the set.

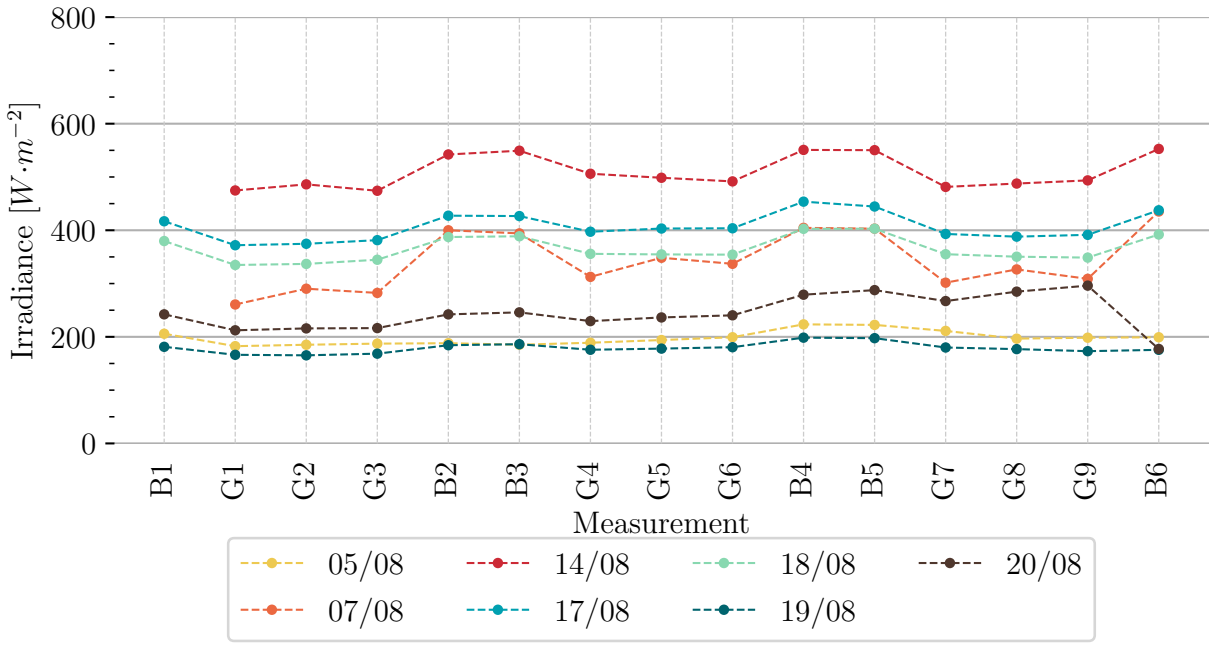

Figure 7.12: Total irradiance values over 7 days, with the glass/soiling measurements, at 09:00.

Now, observing the same measurement sets acquired closer to solar noon: all sets indicate the transmission loss, figure 7.13. Simply stated, minor cloud formation within the measuring view around solar noon will not cause as great an influence, as it would earlier in the morning and later in the afternoon, since the water vapour content within the atmosphere is significantly less around solar noon.

With these two comparative plots, it could already be said that measurements acquired with a fixed angle, especially relative transmission loss measurements, should occur as close to solar noon as possible. This decreases the possible inclusion of variability and error within the measurements. Since this thesis supplies a spectral guide, morning and late afternoon measurement will still be included in the analysis to determine if any other discrepancies occur within these time periods.

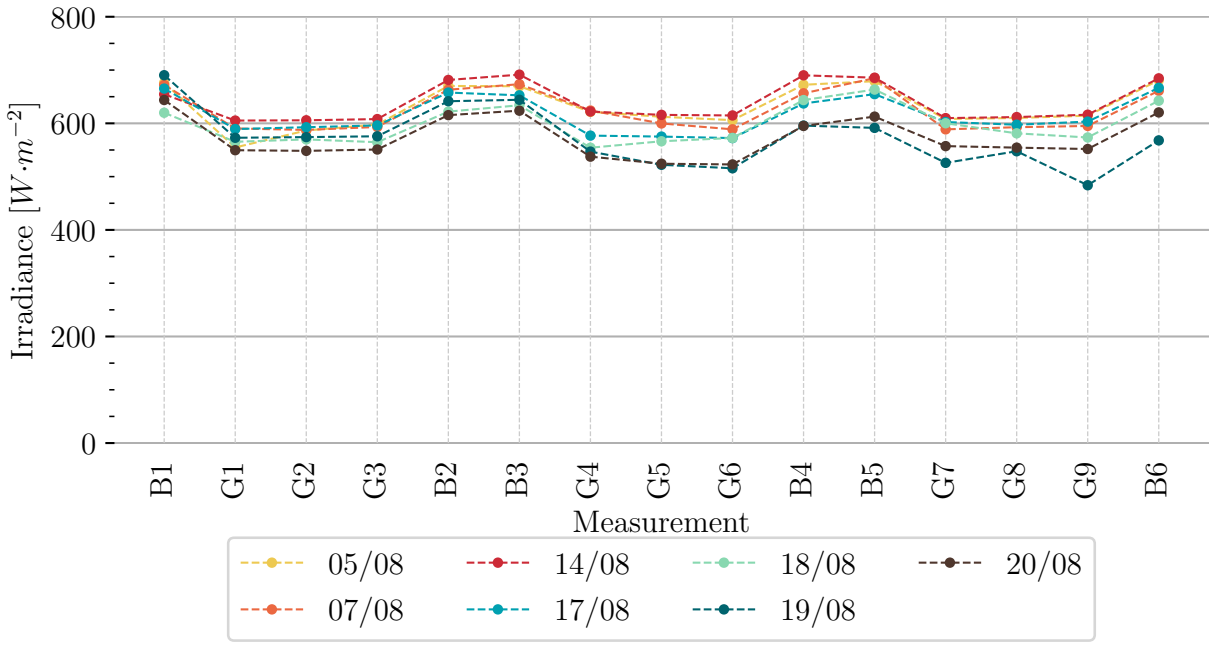

Figure 7.13: Total irradiance values over 7 days, with glass/soiling measurements at 13:30.

7.3.2 Transmission Loss (within a day)

The glass was cleaned on 4 August and an increase in soiling, and therefore an increase transmission loss, is expected over time. The glass and soiling analysis with the automated measurements are more laborious than within the preliminary experiences since multiple intermittent days of light rain was experienced in the measuring period, with prevalent extreme overcast sky-conditions. In fact, the longest period of measurement without rain or an overcast sky was four days. This means that if any soiling did gather on the glass surface, some of it would have been washed away by the light rain. Further, the water vapour collecting on the glass, as mentioned in the previous chapter, could either increase the soiling or remove some particles from the glass surface. Still, it is not unlikely that soiling could contribute to transmission loss and therefore it is never only assumed that clean glass is measured within this analysis.

To determine stable conditions, every measurement set is analysed according to table 7.3. As mentioned before, the measurement cell position indicates the actual measurement position in accordance to table 7.2. The top part of table 7.3 represents the total irradiance values measured at all points within the measuring scheme with B Avg. the average between the baselines within that row, therefore $avg(B1, B2)$, $avg(B4, B3)$ and $avg(B5, B6)$.

The bottom part of the table indicates the percentage difference between the total irradiance value of the cell and the baseline average of that specific row, which is shown within the specific cell. The last column indicates the total baseline difference between the two baseline measurements within that row - the usual calculation for stable conditions. Therefore, according to stable conditions, the last column in the table should be less than 5 %, to consider the row of data usable. The additional percentage difference analysis between the total and average is to ensure that the average value used is a viable approximation - this is limited to less than 1 %.

Table 7.3: Calculated total irradiance values and horizontal base averages, within the order of the measuring scheme, on 09:00 17 August 2017, followed by the calculated percentage differences between the cell total irradiance value and the base average of the row.

Total Irradiance $[W{\cdot}m^{-2}]$					**B Avg.**
416.90	371.93	374.63	381.44	427.37	422.13
453.70	403.75	403.27	397.28	426.66	440.18
444.56	393.08	388.05	391.43	437.51	441.04
Difference (Δ) [%]					**B Δ**
1.24	11.89	11.25	9.64	1.22	2.45
2.98	8.28	8.39	9.75	3.07	5.96
0.79	10.87	12.02	11.25	0.80	1.58

Following the tabular analysis, the data is first presented for daily values. Following the cleaning of the glass on 4 August, cloudy to extreme overcast conditions prevailed, with 7 August the first more stable measurement. Figure 7.14 indicates all the glass measurement points as a scatter plot for each half hour measured, the average of the measurements is also indicated for each half hour with a dash.

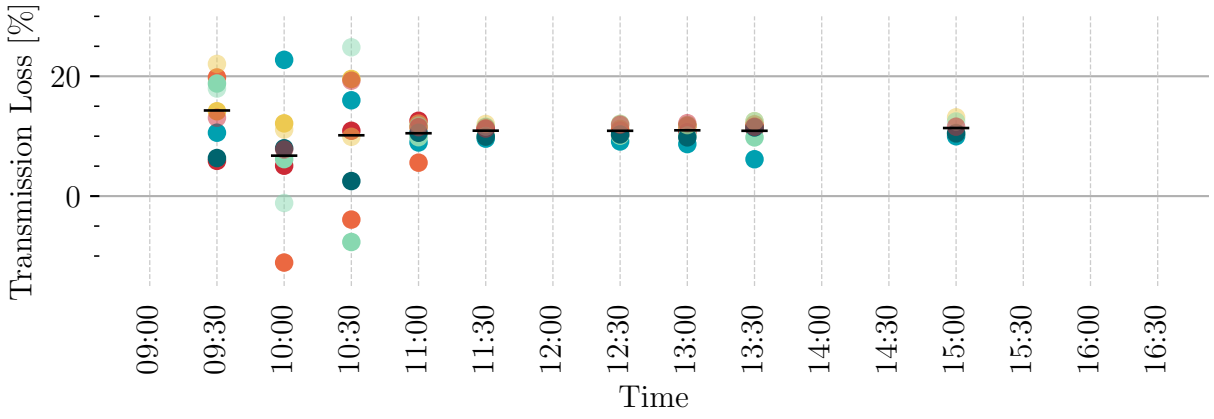

Figure 7.14: Calculated percentage differences for all glass measurements (with the method shown in table 7.3) on 7 August 2017.

This figure only indicates the differences according to the conditions explained for table 7.3 with the error smaller than 5 %. On this day, the morning indicates some variation as a result of some passing cloud formations; towards afternoon, the sky was clear but as a result of the fixed angle, measurement variation exceeded the set stable condition requirement. Interestingly on this day, some negative transmission loss values were calculated - the glass increased the transmission of irradiance. Also, the increase in transmission was only calculated within the centre column of glass measurements, G2, G5 and G8 with a baseline difference of only 0.136 % and an average error of 0.68 % at 10:00 with $\Delta G2 = -11.09\,\%$. Since the occurrence was only observed on this day within the measuring period, it can only be concluded that some variance was prominent within the measurements even though the baseline measurements do adhere to the stable conditions requirement. To draw any other conclusion, a second occurrence would be required.

Observing the less varying time periods on 7 August, a definite similarity in average can be observed: at 11:30 the average transmission loss for all points were calculated as 10.92 %, at 12:30 as 10.90 % and at 13:00 10.98 %.

Several days of no rain (but with condensation each morning) later, (14 August) more measurement sets indicated consistency, figure 7.15. The averages on this day are in the range of 9.04 − 11.35 %. It can also be observed that the calculated transmission loss increases towards late afternoon and is seemingly lower around solar noon. It is already known that lower light conditions (early morning and late afternoon) have increased variability and errors, therefore no conclusion regarding the increased transmission loss is supplied yet.

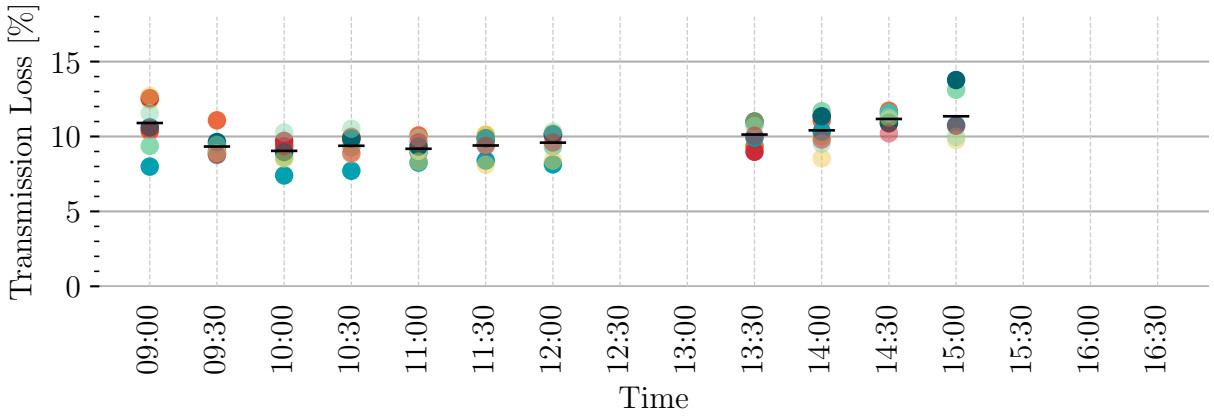

Figure 7.15: Calculated percentage differences for all glass measurements (with the method shown in table 7.3) on 14 August 2017.

On the previous discussed day (7 August), the transmission loss at the constant measurement set as 11:30 was supplied as 10.92 %, now on 14 August also at 11:30, the loss was calculated as 9.40 %, 1.52 % lower.

Then, three days later without any rain as well, 17 August supplies an extended range of measuring sets which are quite constant, as observed in figure 7.16. The calculated transmission loss range for this day is quite similar to 14 August - 9.32 − 11.44 % with 11:30 9.87 %, 0.47 % higher than on 14 August. Again, a higher transmission loss was calculated at 09:00, with an increasing trend from solar noon towards late afternoon.

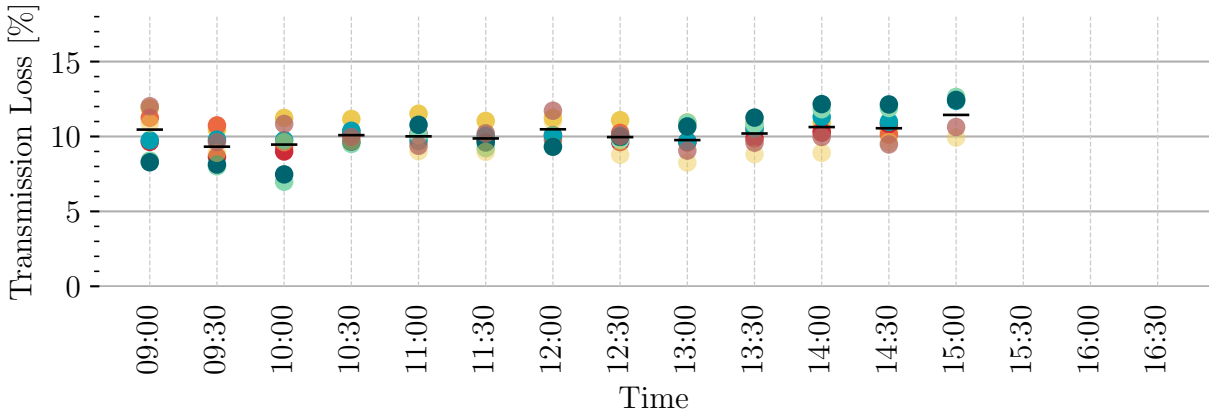

Figure 7.16: Calculated percentage differences for all glass measurements (with the method shown in table 7.3) on 17 August 2017.

Although days 18, 19 and 20 August were clear, an increase in variance is observed within a set, even around solar noon, figure 7.17. 19 August, was more variant than the other two days, where 18 and 20 August adhered to the stable condition requirements between 10:00 and 14:00 for all sets, and within every set.

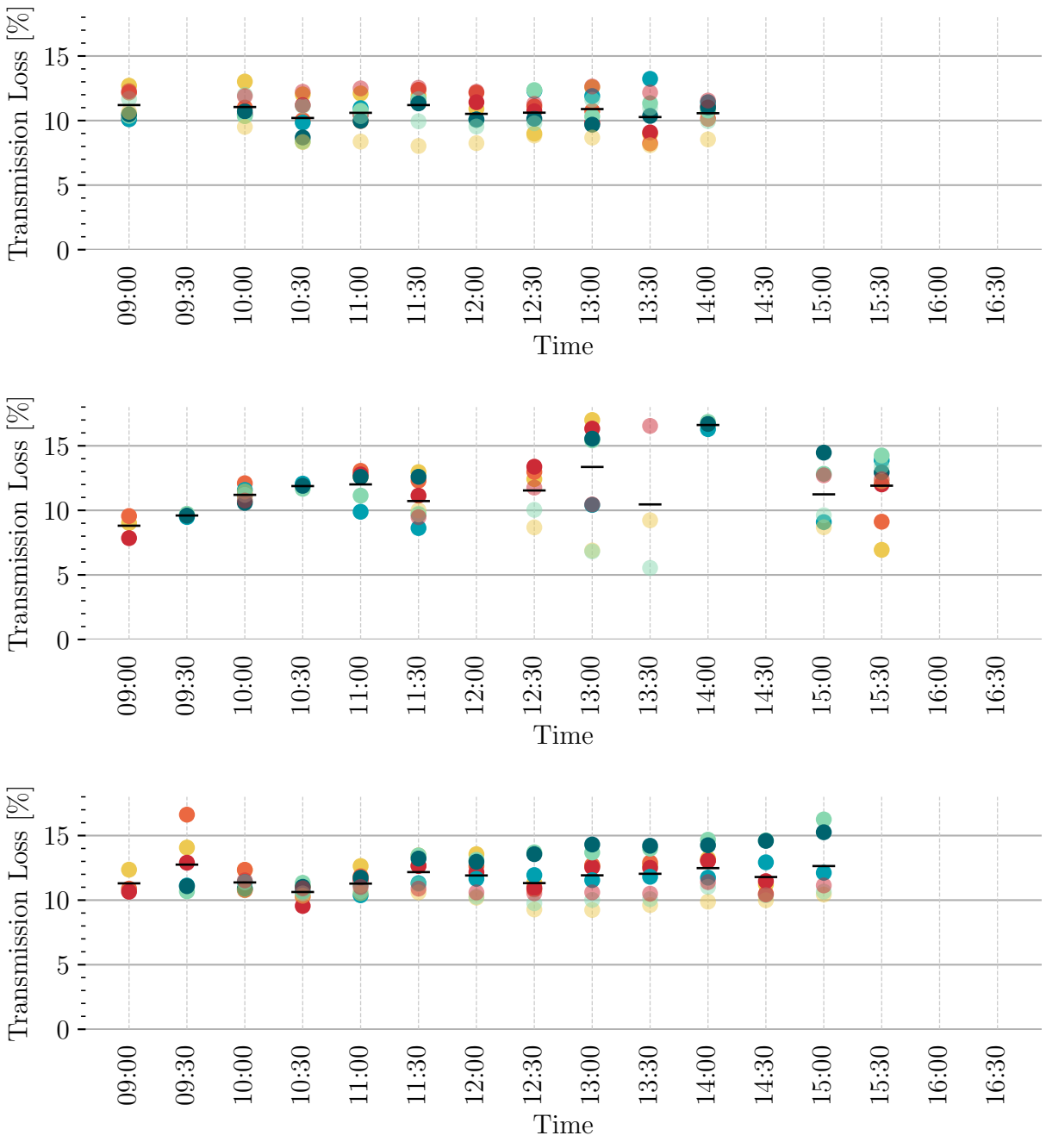

Figure 7.17: Calculated percentage differences for all glass measurements (with the method shown in table 7.3) on 18, 19 and 20 August 2017, independently.

Important to consider is that although the points within a set at a specific time might vary significantly, it does not indicate that the calculated transmission loss values within that set is inaccurate, only that an average value does not accurately indicate the amount of soiling on the surface. It is true though that there is a varying soiling distribution profile within every set since every glass measurement might not contain an equal number of particles, or particles of similar size - therefore the transport of radiation beams will not be affected

equally by these particles. Similarly, since the transmission through the soiled sample is not measured at a constant angle, the particles might absorb and reflect the radiation beams in various ways, with the varying sun angle.

The theory: if the soiling sample is measured at a constant angle, the average of transmission loss within a day for one specific measurement (e.g. G1, G2, etc.) is a more accurate transmission loss value for that specific point on the glass. According to this theory then, for constant measuring angle measurements, an average transmission loss value for a specific measurement can only be accurately determined around solar noon and this transmission loss value will still vary over the soiling period, increasing as additional particles adhere to the glass surface or decreasing when water and/or wind removes the particles from the surface.

7.3.3 Transmission Loss (over the measuring period)

Although solar noon was calculated being at 12:48 previously, only half hour measurements were acquired, therefore the particle distribution is supplied for 12:30 and 13:00 in figures 7.18 and 7.19. The measurement points with errors smaller than 5 % is still indicated in the 12:30 measurements; fortunately 13:00 had no errors larger than 5 %. At 12:30, figure 7.18, the transmission loss values are limited to the range $8.68 - 13.70$ % with one outlier, G1 on 5 August; the transmission loss of the points on 28 August are quite similar, $10.93 - 12.53$ %.

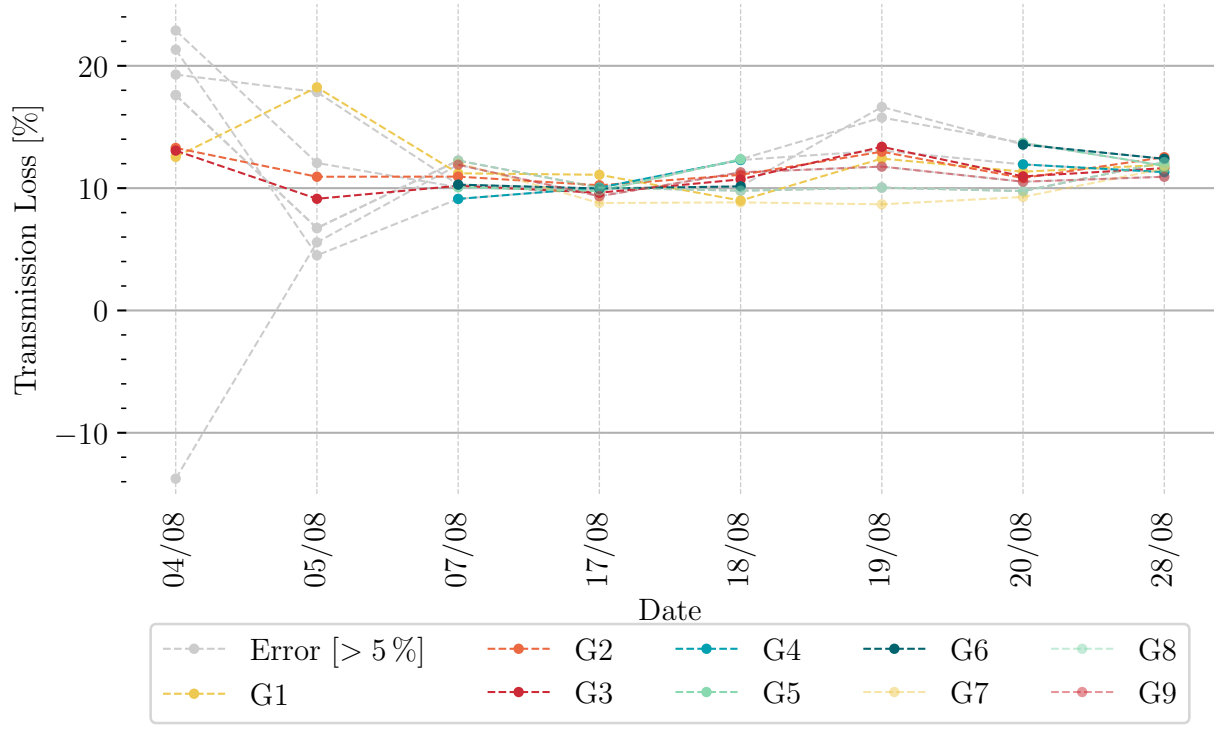

Figure 7.18: The particle distribution at 12:30 for all glass measuring points over the measuring period.

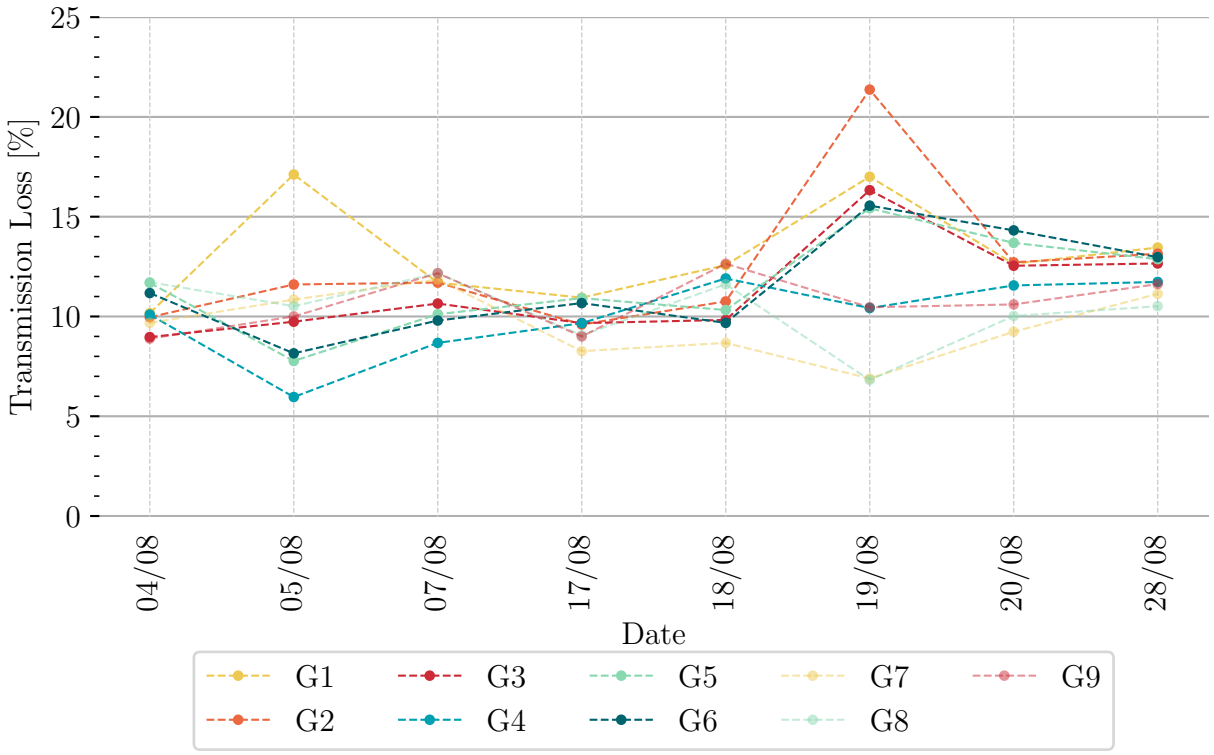

Figure 7.19: The particle distribution at 13:00 for all glass measuring points over the measuring period.

Comparing the 12:30 to 13:00 transmission loss values, some points which were found to have errors larger than 5 % at 12:00, are actually still calculated quite accurately - especially on 5 August, the bottom three points do represent the bottom three measurement at 13:00, within stable conditions. Further, observing an approximate 8 % difference between G2 on 19 August at 13:00 and at 12:30, it can still be said that a fixed measuring angle increases the variability within measurements but, it should also be said that their baseline measurement barely falls within stable conditions with errors $4.36 - 4.60\,\%$.

Further, comparing the dates of each time graph, where the measuring points are seemingly closest to each other are in fact the dates where the baseline condition total errors are the smallest: at 12:30, 17 August followed by 28 August and at 13:00, 4 August followed by 17 August.

7.3.4 Soiling Distribution

Essentially, figures 7.18 and 7.19 supplied a visualisation of the average soiling state of the glass surface, since all points on the glass are compared within the set at each date - comparing these sets over time supplies a visual method for the average increase or decrease of soiling overtime. Now, the glass measurement points can be divided so to only visually represent the vertical or horizontal relation.

Figure 7.20 is essentially the same graph as supplied in figure 7.19, the only difference is that the measurement within a horizontal line was grouped together (each colour represent a row). This figure indicates the distribution of soiling vertically over the glass. Now, some correlation can be observed regarding the soiling distribution at the fixed angle of 30°. Interestingly, the correlation seems to increase within a row as time passes. It is expected that some comparison within a row will be observed, rather than in a column (vertically)

since water (rain drops or condensation) will move towards the bottom of the glass vertically as a result of gravity.

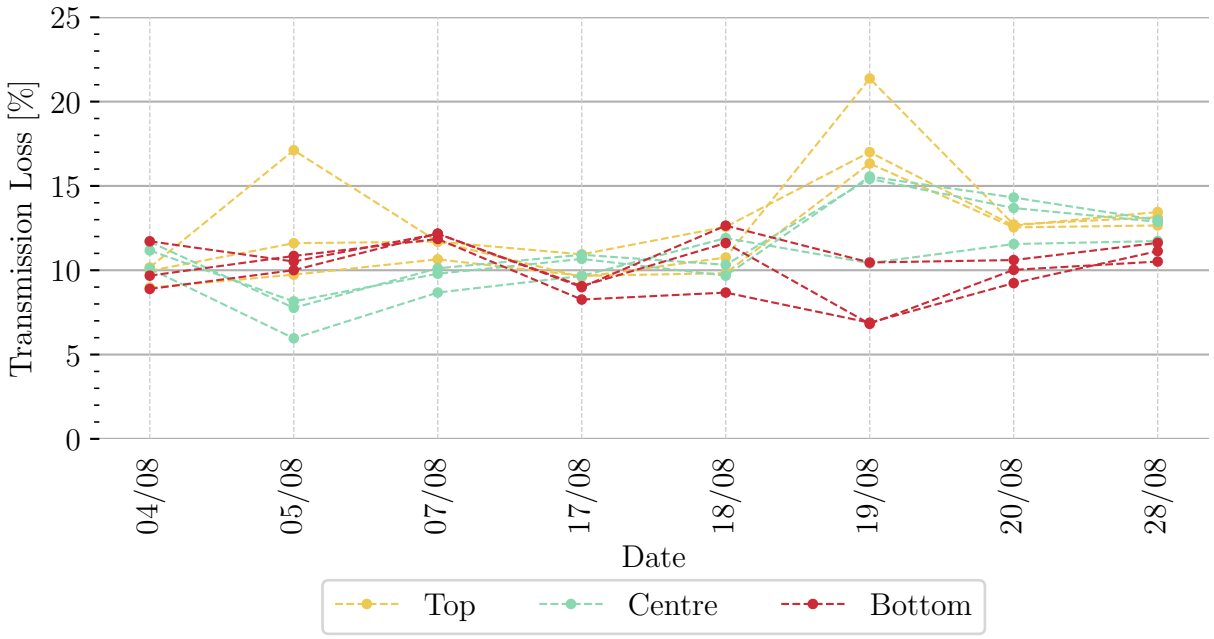

Figure 7.20: All measurements within a set at 13:00 over the measuring period, with horizontal measurement grouped together.

A similar comparison was tried with the vertical data grouped - no comparison was evident. This confirms the theory that horizontal measurements show some correlation within their row. The difference range in transmission loss in horizontal rows were calculated as $0.17 - 5.13\,\%$ (with an outlier of $7.38\,\%$) and the range for the vertical lines as $1.20 - 14.55\,\%$ - these ranges supply an indication of the relation observed within the horizontal lines.

7.3.5 Distribution Difference

Previously it was observed that the distribution within the visible range supplies the best approximation of the difference between baseline measurements, or transmission loss (the difference between a glass measurement and a baseline measurement). The question remains: does soiling change the spectral response of irradiance. Since the bottom row at 13:00 on 28 August had a baseline difference of only $0.033\,\%$, it was used for the content analysis of the distribution. Using this set of data is advantageous since the two baseline measurements approximates each other well, similarly, the three glass measurements are quite equal in transmission value.

As a first observation, the difference between the baseline and glass transmission seems to decrease towards $300\,nm$, in figure 7.21, with a constant difference from $320\,nm$ onwards towards $400\,nm$. This constant difference between the baseline and glass measurements is continued throughout the visible range. Although the noise increases towards $1000\,nm$, and the irradiance value moves past the horizontal zero line just before $950\,nm$, a decrease in difference between the baseline and glass measurement can again be observed from approximately $900\,nm$ and onwards. Intuitively, this decrease in difference seems like the glass pane has a smaller effect on the photons transported through the glass pane within these ranges, where the difference between baseline and glass decreases.

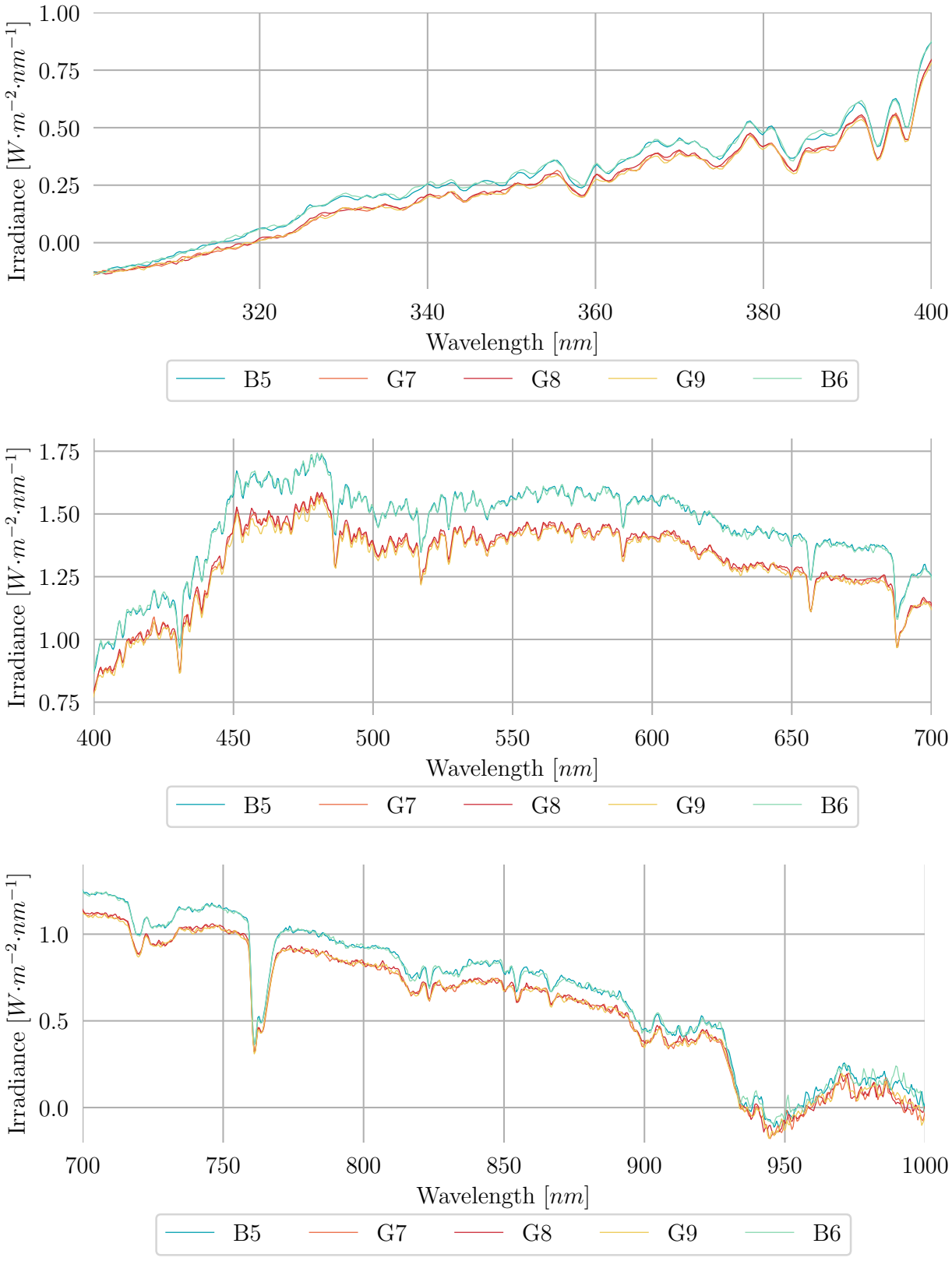

Figure 7.21: Detailed baseline and glass measurements on 13:00 (28 August) of the UV ($300 - 400\,nm$), Vis ($400 - 700\,nm$) and NIR ($700 - 1000\,nm$) band.

Rather than indicating the total irradiance values within the ranges of UV, Vis and NIR (as in table 7.1), the content percentage is indicated in table 7.4 to normalise the difference in total between the baseline and glass measurements. The most important observation

from this table: the glass pane increases the number of photons within the visible range transmitted but transmits less photons within the UV and NIR band, indicating that the glass and soiling does change the spectral response of irradiance, if only barely.

Now, considering table 7.4 in conjunction with the previous distribution graphs, one could observe that the number of photons transmitted within each range, are counterintuitive. With the graphs, it was shown that at the shortest and longest wavelengths, the glass and particles have almost no influence on the number of photons transported, but now in the table it indicates that the content of photons within the visible range has increased.

Table 7.4: The content percentage of the baseline and glass measurements on 13:00 (28 August) in the UV, visible and NIR wavelength bands.

	B5	**G7**	**G8**	**G9**	**B6**
UV	3.992 %	3.716 %	3.740 %	3.657 %	4.054 %
Vis	65.669 %	66.782 %	66.666 %	66.674 %	65.618 %
NIR	30.210 %	29.372 %	29.463 %	29.539 %	30.199 %

It is important to remember, that the difference in total irradiance indicates the number of photons that is reflected and absorbed by the glass and soil particles and therefore still, quantitively more photons within the visible range are observed in the baseline measurements than in the glass measurements.

According to the measured response of the glass in the laboratory experience, figure 5.3, it could have been expected that the glass will suppress more photons with wavelengths in the approximate range of $780 - 810\,nm$. The response indicates that the glass cannot increase the number of photons passing through the glass within the visible range, but merely allows a higher percentage of the photons to pass through, than in UV and NIR ranges.

Therefore, it is important to consider that the increase in visible light content percentage observed at 13:00 in table 7.4, between the glass and baseline measurement, only indicates that within the glass measurement itself, the change in the number of photons in the visible range, being transported from the sky through the glass, is greater than in the other ranges. In other words, in relation to the total number of photons per baseline or glass measurement independently, the number of photons within the visible range in a glass measurement are greater than the number of photons within the visible range in a baseline measurement.

Further, the content percentage was calculated at every time step within a day (28 August), where the stable condition requirement was met. This extended period of division analysis indicates a trend - all sets from 09:30 and onwards indicated an approximate 0.3 % decrease in UV content from the baseline to glass measurement, figure 7.22. This small difference was observed before at 13:00 but did not seem significant, since this occurrence is over all measurements it indicates that there is some photon suppression within the UV range as a result of the glass and surface particles.

Opposingly, the visible range indicates that a greater number of photons are transported within the visible range, with an increase in content between the baseline and glass measurement, in the range of $1 - 1.4$ %, with the exception of the measurements at 09:00, as seen in figure 7.23. Further, the content of visible light increases from 09:00 to approximately 11:00, and then decreases towards late afternoon - again opposingly, the UV light content is greater early morning, and even greater later in the afternoon - than calculated around solar noon.

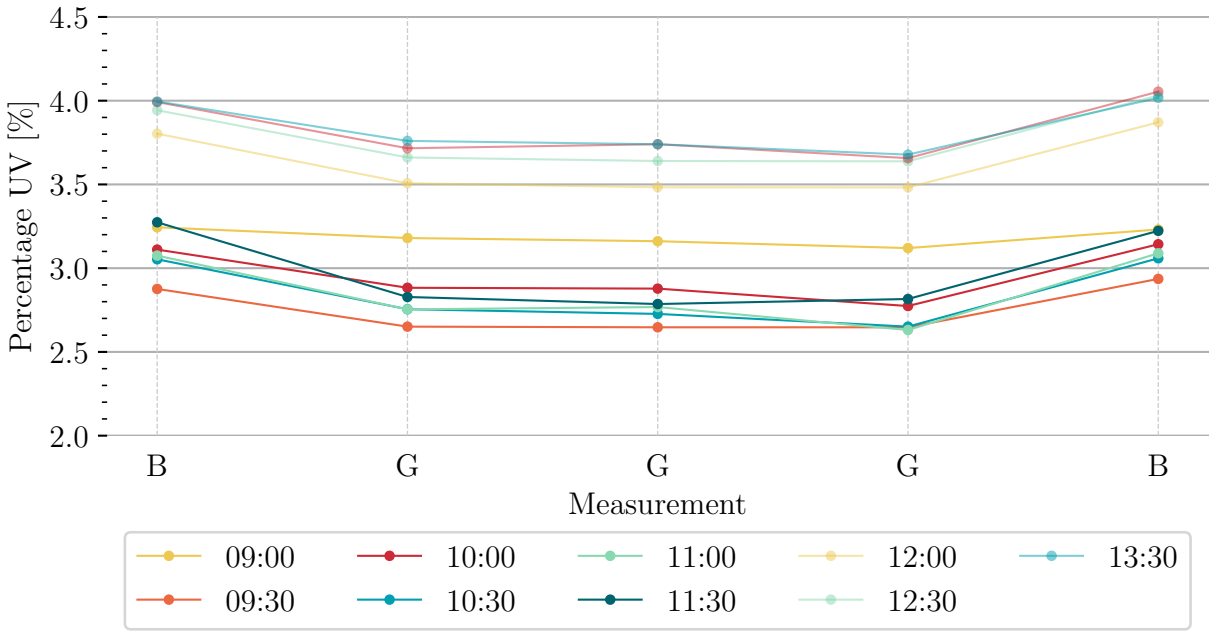

Figure 7.22: Content percentage of the UV band over several measurement sets on 28 August.

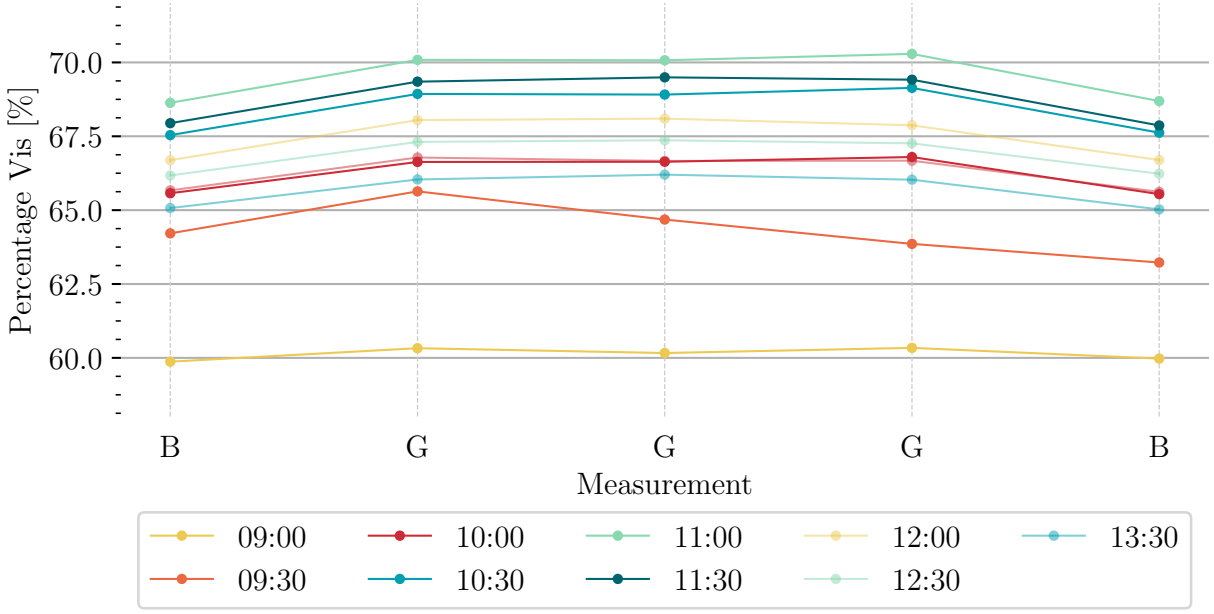

Figure 7.23: Content percentage of the visible band over several measurement sets on 28 August.

The NIR range difference in content percentage is more subtle but again it was observed that the highest content NIR is experienced at 09:00, decreasing towards noon and finally increasing again late afternoon.

Reiterating, it is important to understand what is meant by a difference in content between a baseline and glass measurement - the baseline measurement predominantly consists of a greater number of photons in its totality, also each range division consist of a greater number of photons than the glass measurement. The distinction lies in the distribution of particles

between the range divisions within a measurement. The baseline measurement indicates the light content as influenced by air particles, the glass measurement indicates the additional effect of the glass and surface soiling particles on the distribution of photons within the total number of photons received (as indicated by the baseline measurement).

7.4 Conclusion

For completion of the analysis, the APE was calculated for multiple days within the measuring period. Similar to the calculated APEs in the first preliminary experience, early morning and later afternoons indicated a lower APE value but in general the automated measurement APE values were calculated to be higher on average than that calculated previously. The APE value range calculated with the automated measurements is approximately $1.8-2.1\,eV$. Especially the morning APE values were higher than expected and with the increase in trend from $1000\,nm$ in the baseline measurement, a higher calculated APE is not unexpected. The maximum at $2.1\,eV$ could therefore also be ascribed to the higher uncertainty within the baseline measurements as a result of the count to irradiance conversion.

In conclusion to this chapter, an overview of analysis methods and conclusion is listed below:

1. A comparison of the use of an approximate black spectrum was supplied by first observing the distribution of the spectral response with and without the black spectrum, applied to a morning measurement and an afternoon measurement - this analysis indicated a difference but not necessarily what a better approximation would be.

2. The second analysis of the black spectrum was the comparison of total irradiance values with externally sourced DHI, DNI and GHI data - it was found that the measurements with the black spectrum should more closely approximate DHI but in fact approximated DNI towards noon.

3. The total baseline irradiance values calculated at every half hour measurement set, was supplied for multiple days within the measurement set and two more constant days were pointed out for further analysis.

4. Although total baseline irradiance values supply an overview of irradiance conditions it does not contribute much detail towards the distribution analysis - a second analysis indicates that, the variance is more constant within the visible range, also measurements closer to noon show lower errors between baseline measurements.

5. Further, a detailed view of baseline measurements were persuade, calculating the percentage contribution of the different wavelength bands, and the errors between baseline measurements - it was shown again that $360-900\,nm$ is actually the only part of the wavelength range of the spectrometer that has little noise.

6. As an initial indication of soiling, all measurements within a set was shown - from this simple plot, a clear increase in transmission loss was observed in the glass measurements and a stronger correlation between measurement were observed closer to noon.

7. Only the glass measurements were shown next, with all points shown at every half hour measurement - this indicated the average soiling distribution and if this is a suitable approximation.

8. Every point was further indicated over the measuring period at 12:30 and 13:00, since it was determined that at solar noon (12:48) the glass transmission is a better approximation to the true soiling on the glass, than what is measured early morning or later afternoon.

9. It was also shown that changing the visual analysis method of the nine glass measurement can supply a better approximation to the distribution of soiling on the glass surface.

10. The distribution of photons within a glass measurement was investigated and it was found that there is a shift within the distribution - the glass and soil particles suppress some photons in the UV and NIR ranges, allowing for an increase in content of the visible range.

This chapter supplied a more extensive analysis of spectrometer measurements but all the other measurement chapters contributed towards the process of determining this analysis and what is required of the measurements. This extensive analysis was made possible by the use of the automated system since an increased measurement period was possible, therefore an increased the number of measurements were collected. This increase in the number of measurements acquired, allowed for more conclusive statements regarding the soiling on the glass surface, when compared to the uncertainty observed within the preliminary experiences.

Chapter 8

Conclusion

8.1 Introductory Remarks

The development and incorporation of solar energy is indisputably important for society. This development includes the collection of knowledge on irradiance, meteorological conditions, as well as, the environmental factors of the solar module installation location. This thesis aims to contribute to this collection of knowledge by demonstrating a connection between the use of new technology, such as miniature field spectrometers, and the PV field. This collection includes acquiring knowledge specific to spectral irradiance and the effect of soiling on transmission losses.

Throughout the thesis, various elements of irradiance and soiling is discussed - some of these theoretical remarks are reiterated:

- The effect of soiling on solar modules through current measurements and output efficiency calculations has been investigated by many researches - this thesis extends the analysis method of determining the relative transmission loss as a result of soiling on PV modules, through spectroradiometric measurements.
- Soiling and its contribution to transmission loss is complex - four contributing factors: the amount of dust deposited on the surface, the size of the particles, their distribution on the surfaces, as well as the composition of these particles.
- The spectroradiometric measurements supply spectral information regarding the impinging radiation on the glass covering of the module, simplifying how transmission loss is determined even though soiling is complex.
- Few spectral radiation measurement methods are available within the PV field but one important method applied in this project is determining the content of the measured light through the APE.
- Selective absorption and reflection through air particles has a significant influence on the distribution expected from clear-sky irradiance measurements.

The theory contributed within this thesis determined the approach applied to spectral measurement and analysis. Accordingly, hand measurements were undertaken to acquire knowledge on the chosen measurement device.

8.2 Non-Automated Measurements

The non-automated measurements include the first and second preliminary experience. Even though there are some dissimilarities between the two experiences, the aim of the measurements is the same. Some conclusive remarks on the non-automated measurements:

- A calibrated spectrometer is required to measure irradiance in $W{\cdot}m^{-2}{\cdot}nm^{-1}$ - or rather the calibration is required to calculate irradiance values from the *count* measurements supplied by the spectrometer.
- The measurable wavelength range specified by the manufacturer, still includes wavelength bands with considerable noise and uncertainty, especially at shorter ($< 300\,nm$) and longer wavelengths ($> 1000\,nm$).
- The initial measurement of irradiance requires stable conditions, this includes the lack of cloud formations in the air, and the inclusion of very little water vapour.
- The response measured with the chosen spectrometer supplies a distribution profile very similar to the ASTM G173-03 reference spectrum at AM1.5, in the approximate wavelength range $300 - 1000\,nm$.
- The main absorption bands and Fraunhofer lines can be indicated within a spectral measurement, acquired by the chosen spectrometer.
- An analysis guide for baseline measurements is determined, this includes the critical stable condition requirement where two sky measurements should differ with less than $5\,\%$.
- Longer integration times decrease the amount of noise observed at wavelengths shorter than $300\,nm$ and longer than $1000\,nm$, but increases the chance of saturation of the measurement - only measurement with integration times shorter than $25\,ms$ was determined to be usable, although it contains considerable noise in the previously indicated wavelength ranges.
- Measurements acquired with the receptor in line with the sun position (with a 180° field of view) supplies data approximating GHI values but, if the measurements do not adhere to the stable condition requirement, this approximation is not guaranteed.
- Initially the method for calculating transmission loss through relativity, between a baseline and glass measurement, is shown - the clean solar glass approximation, low-iron float glass samples, cause a transmission loss of $9.125 - 9.236\,\%$, with baseline difference and average difference smaller than $1\,\%$.
- It is shown that the field of view of the spectrometer receptor influences the consistency and accuracy of measurements - a 180° FOV is determined to be most suitable for fixed angle measurements.
- Even with few measurements adhering to the stable condition requirement with a fixed angle, the solar glass transmission loss is calculated as approximately $9.31\,\%$ and an additional $1.97\,\%$ loss for minor particles adhering to the glass surface, from the measurement set with the smallest stable condition error.

From the comparison between the first and second experience, it is observed that the measuring angle of the spectrometer has a significant impact on the irradiance values measured, as well as, the accuracy of these measurements.

8.3 Automated Measurements

Finally, all of the previous experiences contributed to the final measurements and the setup thereof. The final data supplied a more comprehensive idea of the measurements that could be acquired with a spectrometer. In short, the following was concluded:

- It is shown why a black spectrum is indeed required, also that 1500 *counts* is a usable black spectrum approximation.
- The measured baseline irradiance is compared to GHI, DHI and DNI values, since the receptor was not directed towards the sun position, the measurements were expected to approximate the DHI values but even after a range adaption factor of 28.88 %, the measured values varies from the DHI values with an increase of 20 % early morning and late afternoon.
- A maximum total irradiance value is calculated of approximately $750\,W{\cdot}m^{-2}$, over the total measuring period - this value would have been higher if the receptor followed the sun position.
- It is discussed how the variance between baseline measurements decrease towards solar noon and that the percentage difference calculated form total irradiance values is a good approximation of the difference in the wavelength band of $500 - 700\,nm$.
- The average glass and soiling transmission losses is calculated as $9.32 - 12.53\,\%$ within the measuring period.
- Further, a relation between measurement position and the amount of soiling is determined - the horizontally located measuring points show a greater relation than the vertical measurements.
- Finally, the distribution of difference was investigated and it was found that there is a shift in division (UV, Vis and NIR) from the baseline to glass measurement - an increase of $1 - 1.4\,\%$ in content in the visible range was observed from the baseline to glass measurement.

The first two hypotheses set at the beginning of the thesis is already confirmed within the preliminary experiences: measurements at a fixed angle will estimate DHI, but is an even better approximation closer to solar noon. Through the increased number of measurement sets acquired through the automated system, the last three hypothesis is also confirmed: solar glass cause less transmission losses (versus other glass types), dust particles can either increase or decrease transmission loss and the automated system increase the repeatability of measurements.

8.4 Concluding Remarks

Even though all project tasks are completed and all hypotheses are confirmed, some question remains to what the true contribution of the automated system is. Perhaps the greatest advantage of the automated system is the consistency of the measurement angle and location - especially with the second experience completed within the field, great variability was observed as a result of the fixed measuring angle inconsistency. Measuring in variable conditions have many challenges and this showed when measurements are completed formultiple days, within harsh conditions. The automated system completely removes the human

element from the measurements and therefore an increase in accuracy and repeatability is indeed observed.

Many suggestions regarding the design of the automated system is discussed in chapter 6, but some improvement to measurements are also required. One consistent matter within the measurements were the range of good resolution - the shorter and longer wavelength bands are still important to PV research and only with the extension of good resolution within these bands can conclusive research be completed. A suggestion is to acquire a second spectrometer to specifically measure the NIR range to increase the resolution for wavelengths greater than $1000\,nm$. Another, perhaps easier solution, is to acquire a second filter so that an increased integration timeis possible with the current spectrometer - an increase in integration time would increase the resolution possible within the UV and NIR ranges.

The second measurement matter is observed when comparing the first preliminary measurements to all following measurements - measuring towards the sun location increase the stability of the measurements. Therefore, implementing the XY-plotter as is, with a double axis tracker, would supply measurements similar to those acquired within the first experience. This would supply GHI values, with less error between baseline measurements and therefore increasing the number of usable datasets measured within a day.

The advancement of spectrometers has made this research possible but the advancement of the implementation can increase the use of this technology. By increasing the consistency of measurements and the stability of the automated system, this technology could be implemented within remote locations to acquire data which was not possible before.

Appendix A

Technical Drawings

A.1 First Preliminary Experience Holder

As previously mentioned within Chapter 3, a holder for the spectrometer probe is required. The solution is a three-plate and bar holder that allows for the positioning of the probe (or receptor) within the middle plate, as well as, the inclusion of a low-iron float glass sample on the top plate. The parts list is supplied in table A.1.

Table A.1: First preliminary experience holder parts list.

PARTS LIST			
ITEM	**QUANTITY**	**PART NUMBER**	**DESCRIPTION**
1	1	Base Plate	Sheet 2/6
2	16	M8 x 1.25	Hex Nut
3	16	8 - 140 HV	Plain Washer
4	2	Bar	Sheet 5/6
5	2	Fitting	Sheet 6/6
6	2	M8 x 40	Hex-Head Bolt
7	2	M8	Wing Nut
8	2	M8 x 1.25 x 132	Threaded Bar
9	1	Middle Plate	Sheet 4/6
10	1	Top Plate	Sheet 3/6

Sheets $1-6$ indicated within the table, is illustrated on the following pages.

1:1

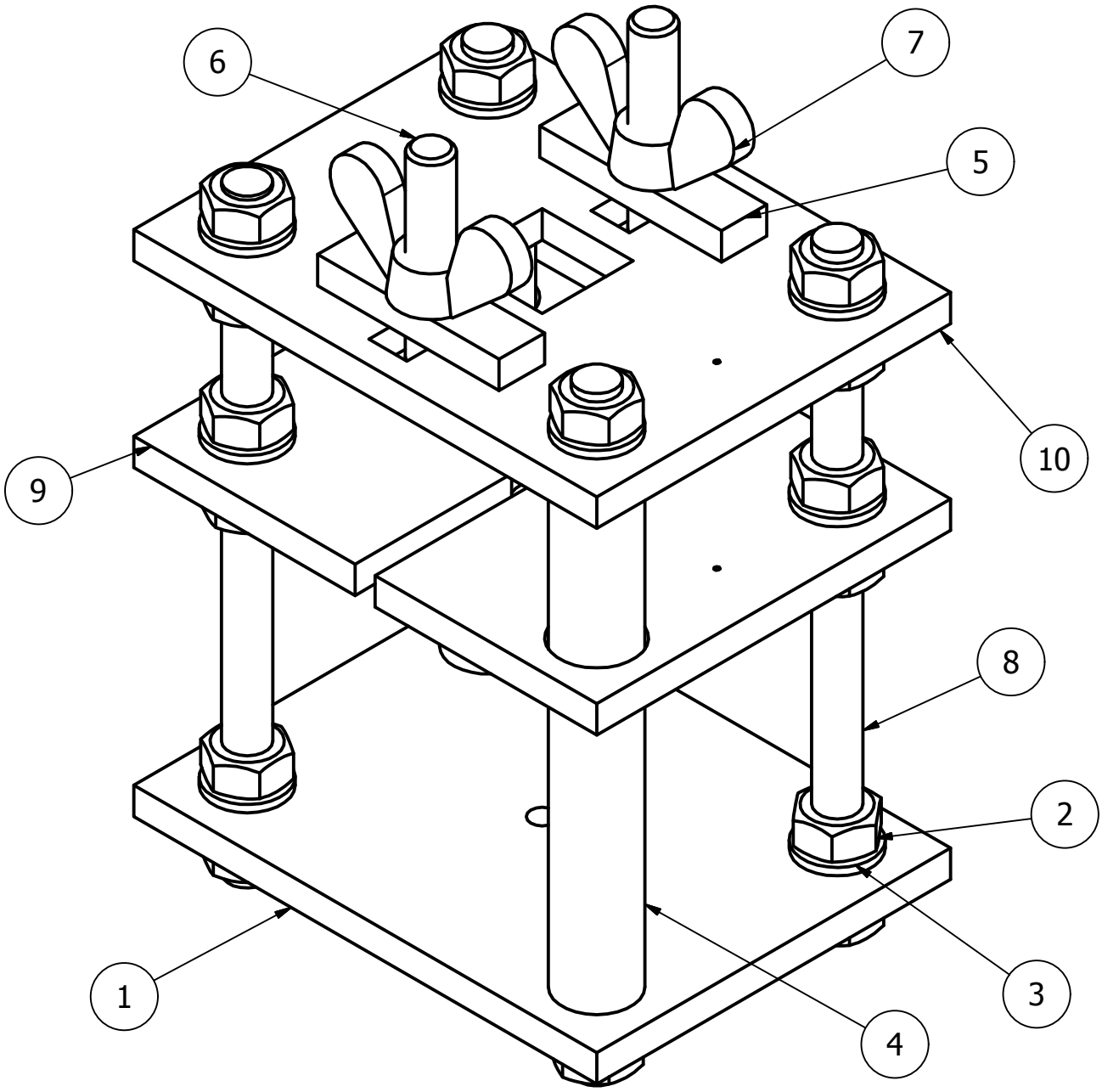

Designed by	Checked by	Approved by	Date		Date	
17006384					2016/05/09	

HOLDER ASSEMBLY

Assembly1	Edition	Sheet
		1 / 6

1:1
NOTES:
1. Material Thickness 6mm

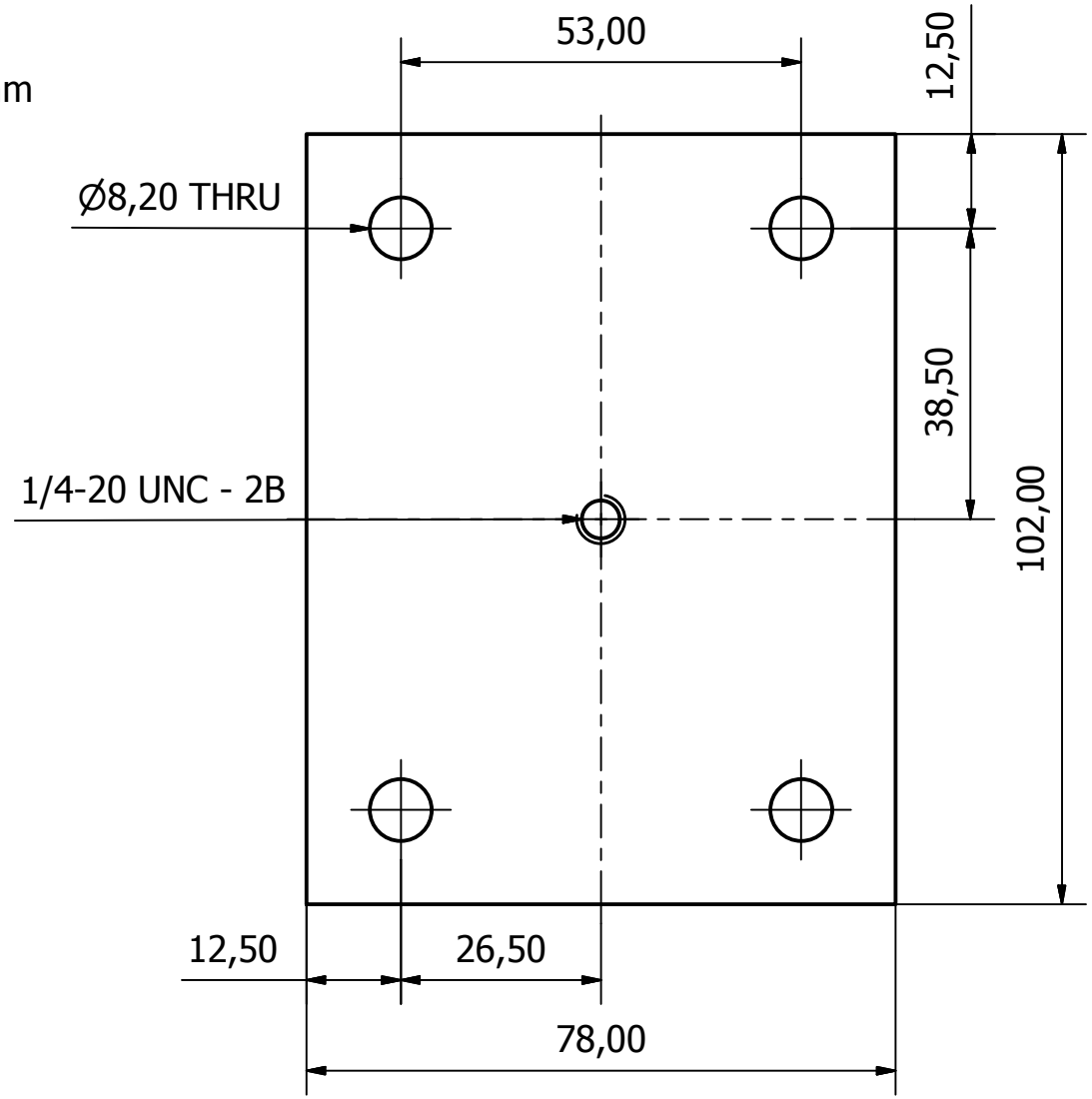

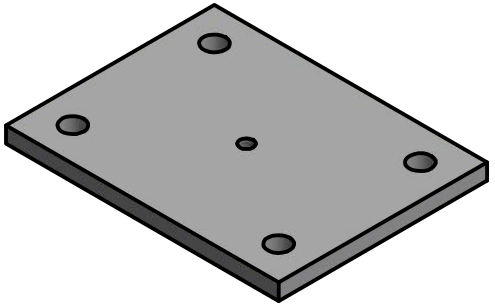

Designed by	Checked by	Approved by	Date		Date	
17006384					2016/05/09	

BASE PLATE

Assembly1		Edition	Sheet 2 / 6

1:1

NOTES:

1. Material Thickness 6mm

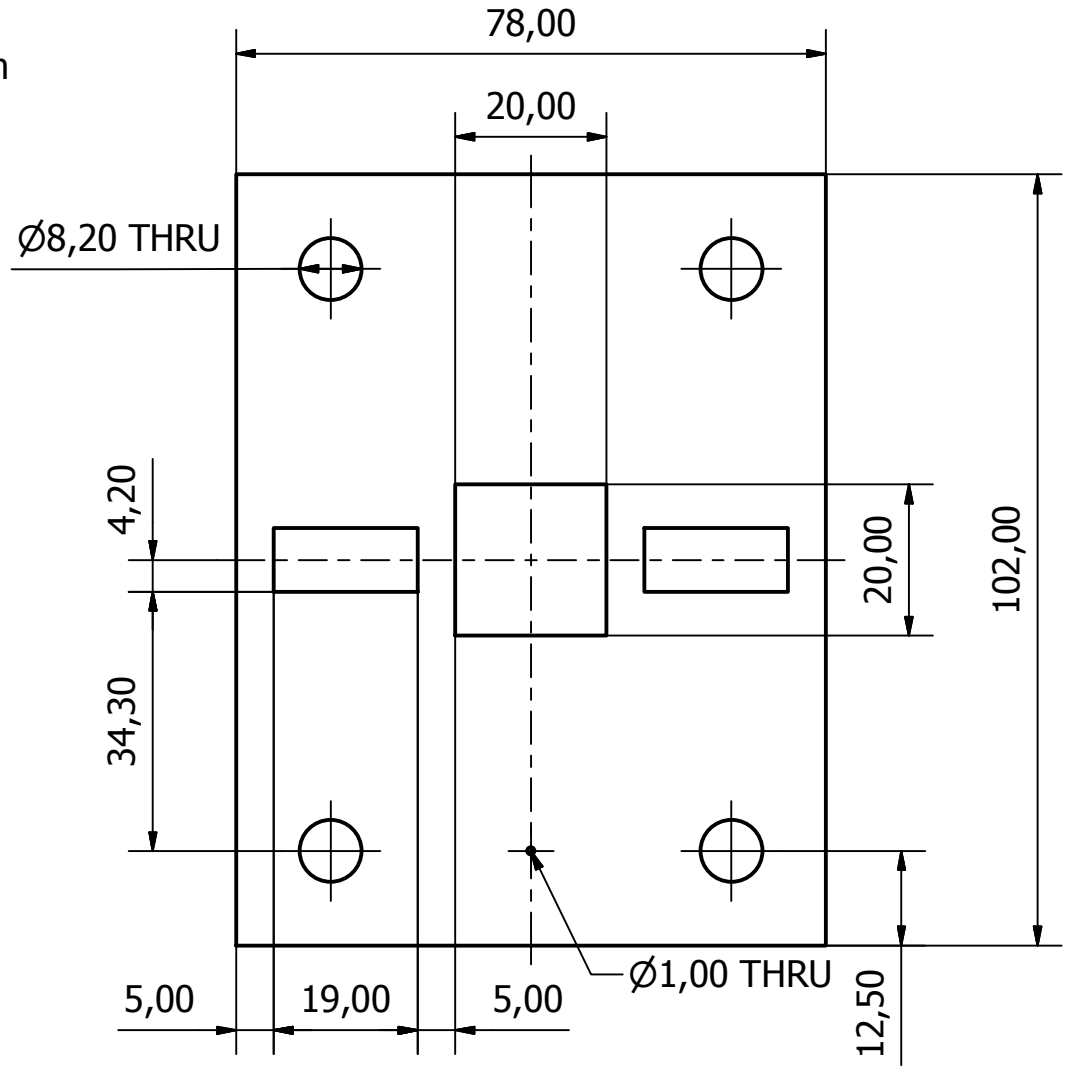

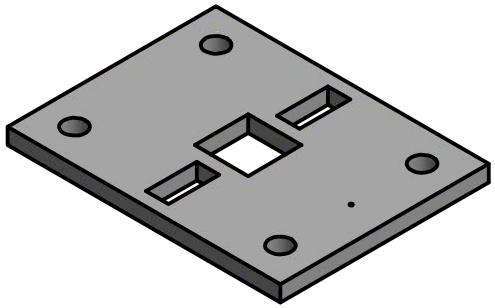

Designed by	Checked by	Approved by	Date		Date	
17006384					2016/05/09	

	TOP PLATE		
	Assembly1	Edition	Sheet 3 / 6

1:1
NOTES:
1. Material Thickness 6mm

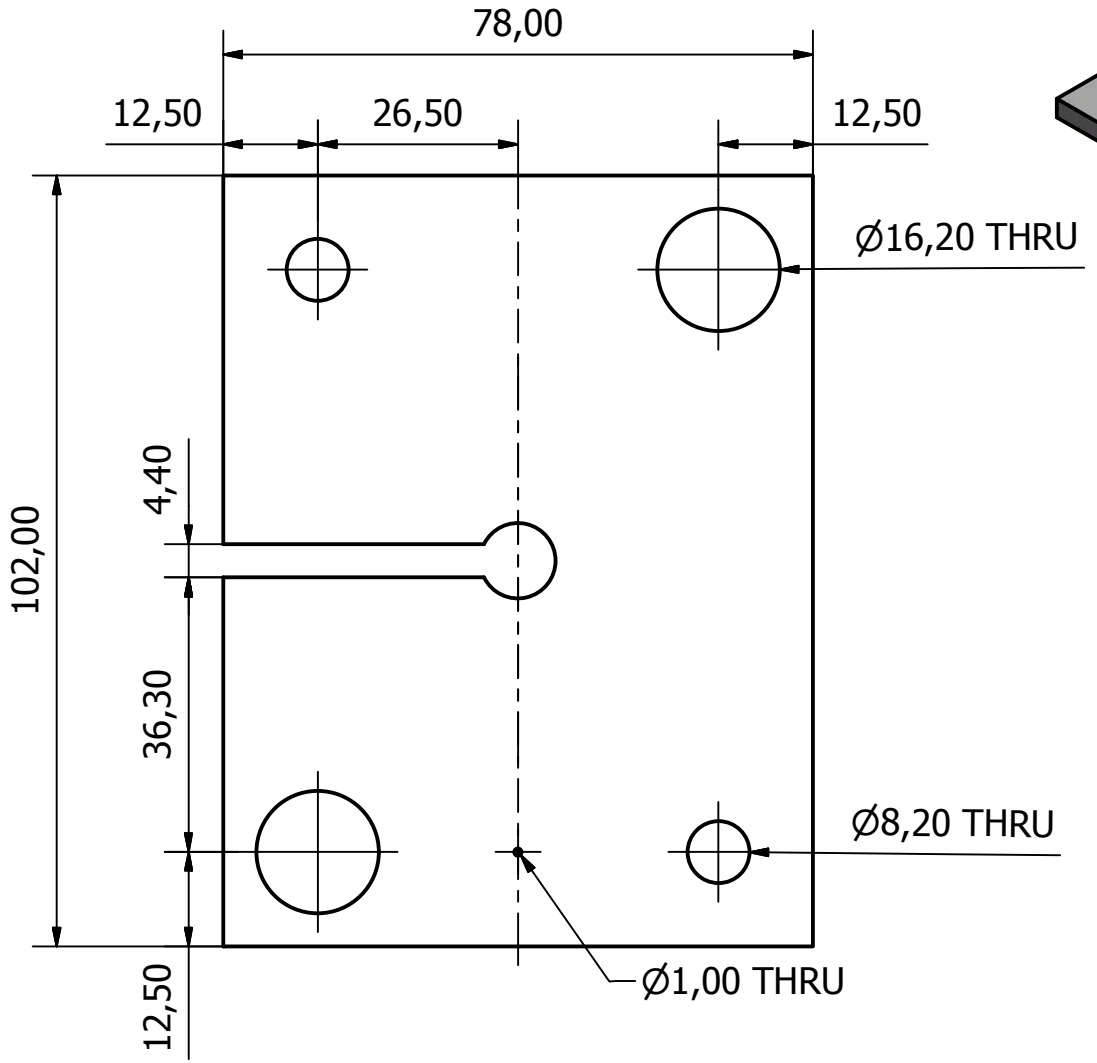

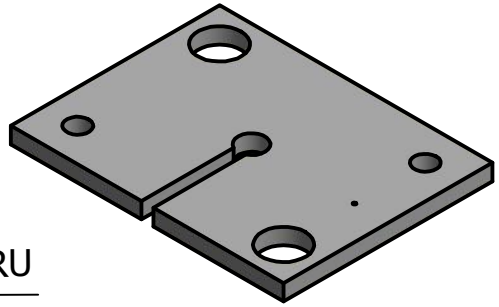

Designed by	Checked by	Approved by	Date		Date	
17006384					2016/05/09	

MIDDLE PLATE			
Assembly1		Edition	Sheet 4 / 6

1:1

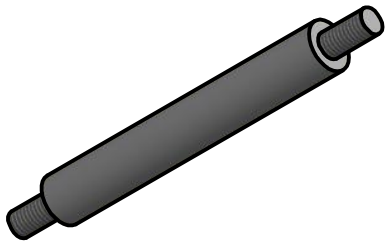

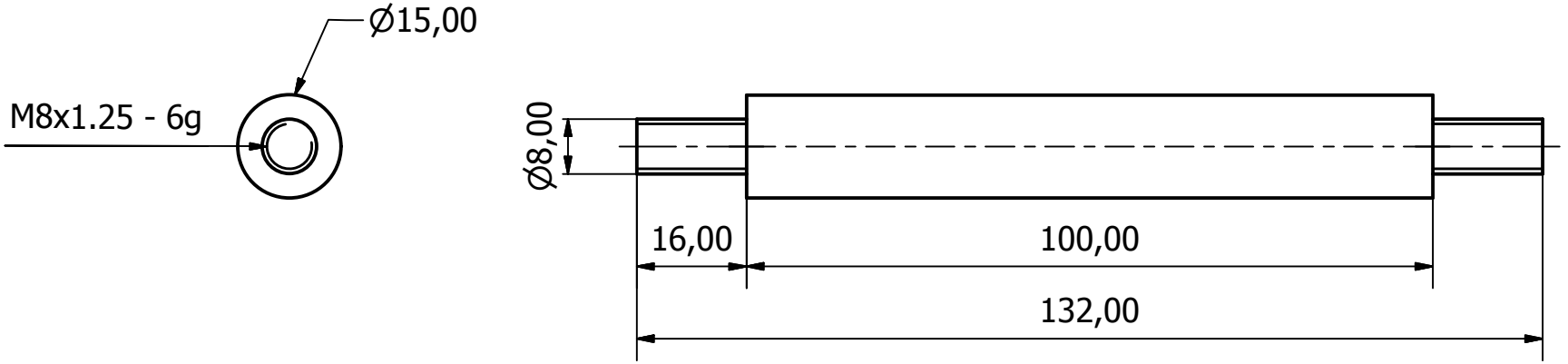

Designed by	Checked by	Approved by	Date		Date	
17006384					2016/05/09	

ROUND BAR

Assembly1 | Edition | Sheet 5 / 6

2:1
NOTES:
1. Material Thickness 6mm

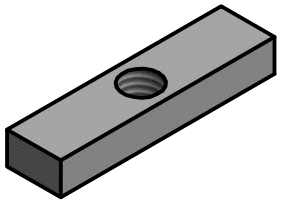

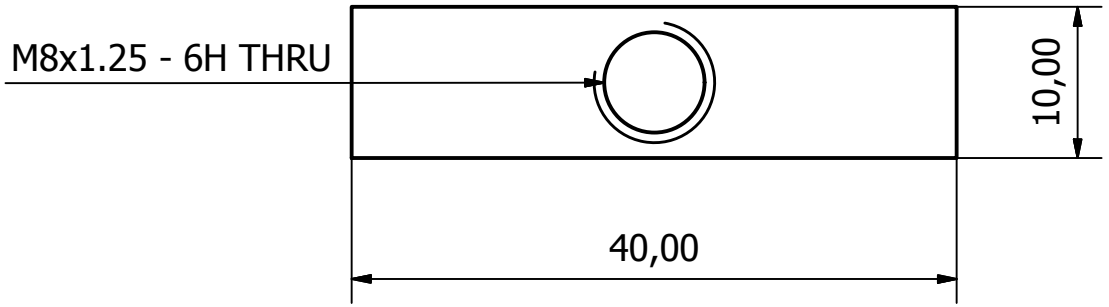

Designed by	Checked by	Approved by	Date		Date	
17006384					2016/05/09	

FITTING

Assembly1 | Edition | Sheet 6 / 6

A.2 Automated System

A.2.1 Technical Drawings

As an example of the assembly (and sub-assembly) process, the assembly list is supplied in table A.2. This assembly table communicates the required work on each part, as well as where each component is located within the drawing pack. In addition, an example assembly drawing of 16-01-04-00 is supplied, as well as, a detailed drawing of 16-01-06-01, below.

Table A.2: Automated system assembly list and process instruction.

pg.	ASSEMBLY	DETAIL	NAME	PROCESS
1	16-01-00-00 #1		Main Assembly	Assemble
2	16-01-00-00 #2		Main Assembly	Assemble
3	16-01-00-00 #3		Main Assembly	Assemble
4		16-01-00-01	Shaft Y	Buy Specific Length
5		16-01-00-02	Shaft X	Buy Specific Length
6		16-01-00-03 #1	Motor Holder	Holes, Treat
7		16-01-00-03 #2	Motor Holder	Cut, Bend, Pilot Holes
8	16-01-01-00		Frame Assembly	Weld, Treat
9		16-01-01-01	Frame X	Drill Holes
10		16-01-01-02	Frame Y	Drill Holes
11		16-01-01-03	Frame X	Drill Holes
12	16-01-02-00		Pulley Assembly	Assemble
13		16-01-02-01 #1	Pulley Holder	Holes, Treat
14		16-01-02-01 #2	Pulley Holder	Cut, Bend, Pilot Holes
15		16-01-02-02	Shaft	Manufacture
16		16-01-02-03	Bush	Manufacture
17	16-01-03-00		Motor Assembly	Assemble
18		16-01-03-01	Shaft	Manufacture
19	16-01-04-00		Pulley Bearing Assembly	Assemble
20		16-01-04-01	Base Plate	Cut, Pilot Holes, Treat
21		16-01-04-02 #1	Pulley Holder	Holes, Treat
22		16-01-04-02 #2	Pulley Holder	Cut, Bend, Pilot Holes
23		16-01-04-03 #1	Belt Clamp Bottom	Holes, Treat
24		16-01-04-03 #2	Belt Clamp Bottom	Cut, Bend, Pilot Holes
25		16-01-04-04	Belt Clamp Top	Cut, Holes, Treat
26		16-01-04-05	Shaft	Manufacture
27		16-01-04-06	Bush	Manufacture
28	16-01-05-00		Receptor Assembly	Assemble
29		16-01-05-01 #1	Belt Clamp Bottom	Holes, Treat
30		16-01-05-01 #2	Belt Clamp Bottom	Cut, Bend, Pilot Holes
31		16-01-05-02	Belt Clamp Top	Cut, Holes, Treat
32		16-01-05-03	Receptor Plate	Cut, Holes, Treat
33	16-01-06-00		Motor Bearing Assembly	Assemble
34		16-01-06-01	Base Plate	Cut, Holes, Treat
35		16-01-06-02 #1	Motor Holder	Holes, Treat
36		16-01-06-02 #2	Motor Holder	Cut, Bend, Pilot Holes

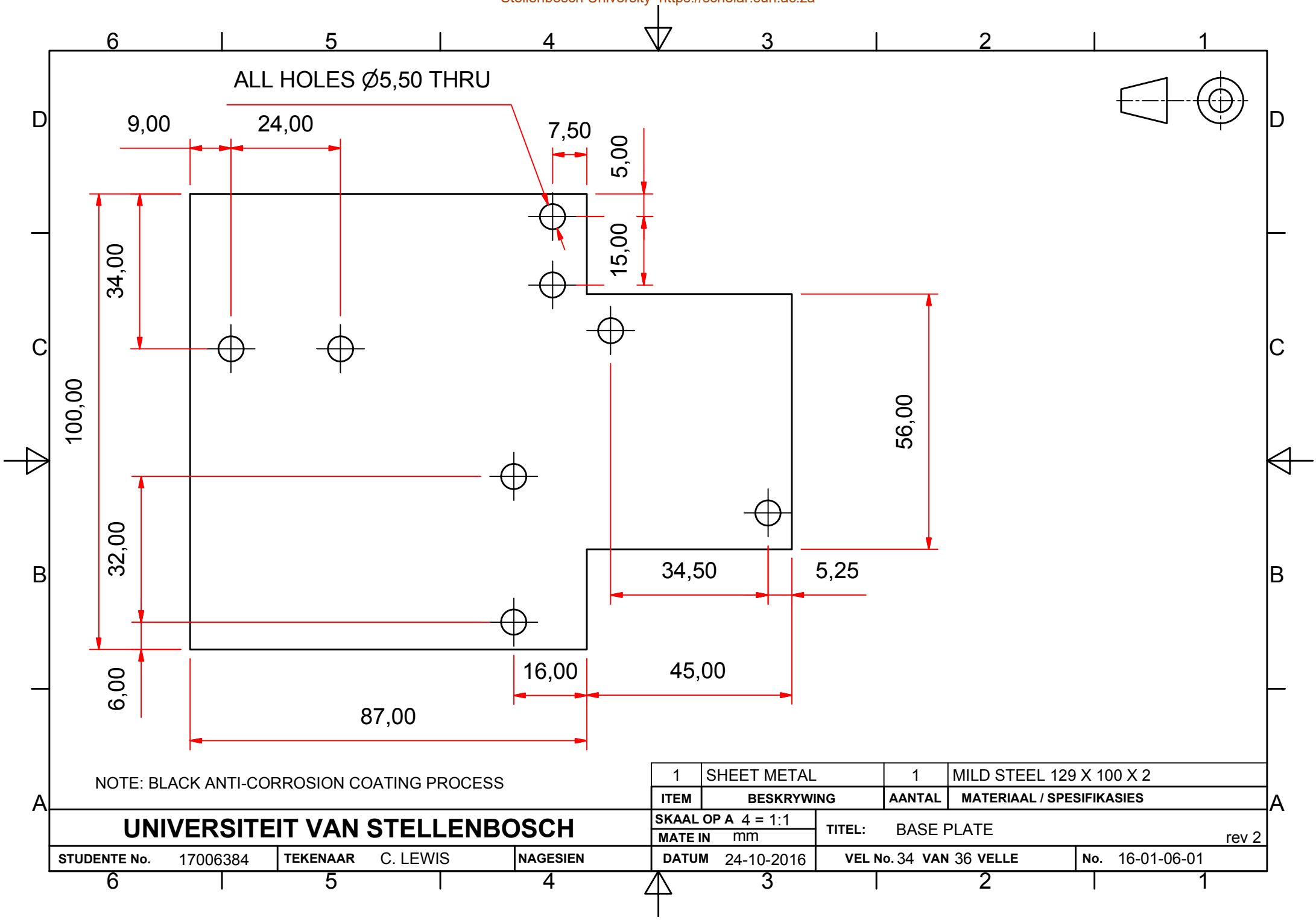

ITEM	BESKRYWING	AANTAL	MATERIAAL / SPESIFIKASIES
1	SHEET METAL	1	MILD STEEL 129 X 100 X 2

UNIVERSITEIT VAN STELLENBOSCH

SKAAL OP A 4 = 1:1		TITEL: BASE PLATE	rev 2
MATE IN mm			
STUDENTE No. 17006384	TEKENAAR C. LEWIS	NAGESIEN	DATUM 24-10-2016
VEL No. 34 VAN 36 VELLE		No. 16-01-06-01	

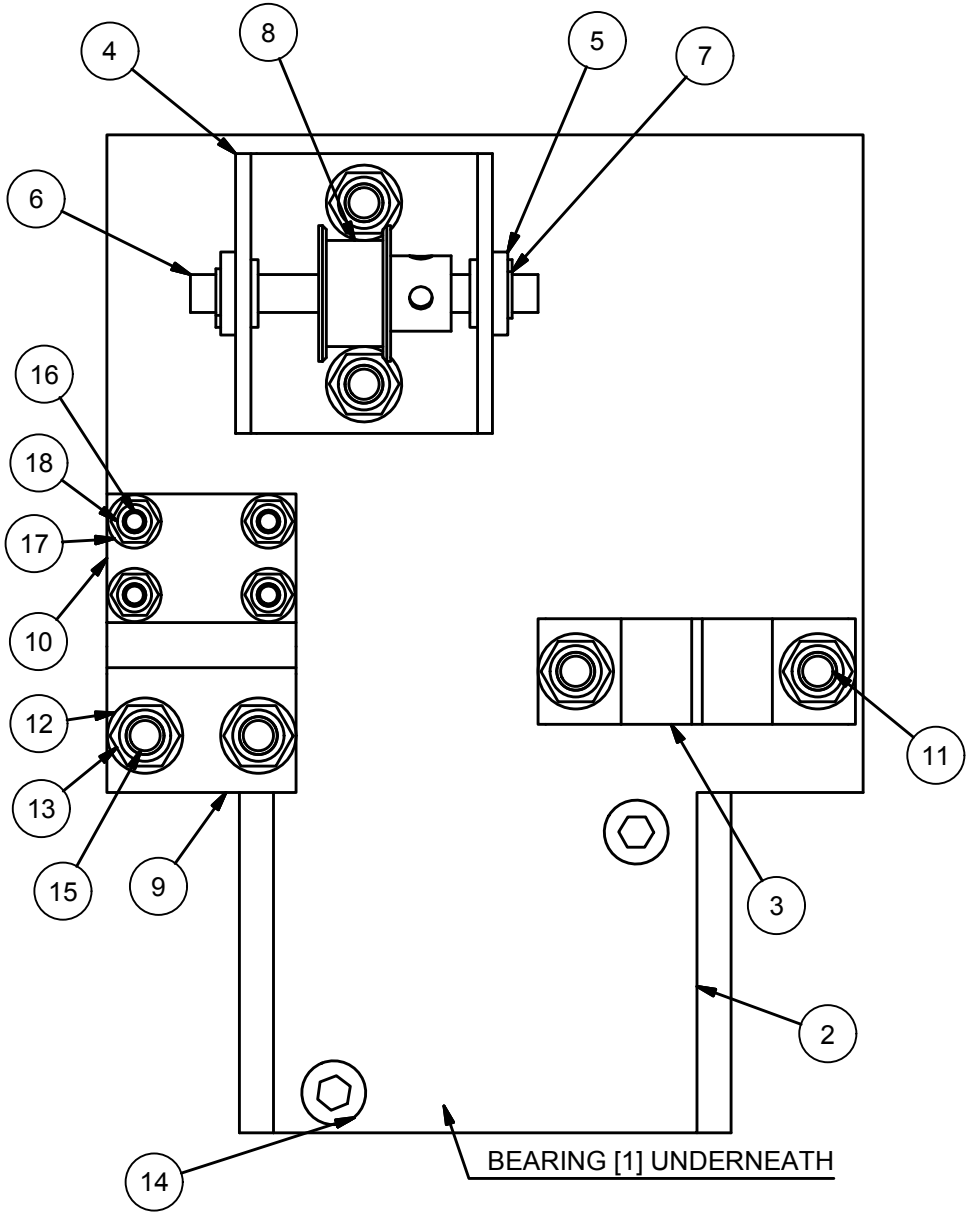

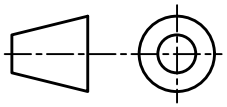

ITEM	BESKRYWING	AANTAL	MATERIAAL / SPESIFIKASIES
18	HEX NUT	4	DIN 934 - M3 STAINLESS STEEL 304
17	WASHER	4	DIN 125 - M3 STAINLESS STEEL 304
16	CYLINDER HEAD CAP SCREW	4	DIN 912 - M3 x 12 STAINLESS STEEL 304
15	CYLINDER HEAD CAP SCREW	4	DIN 912 - M5 x 10 STAINLESS STEEL 304
14	CYLINDER HEAD CAP SCREW	2	DIN 912 - M5 x 12 STAINLESS STEEL 304
13	HEX NUT	6	DIN 934 - M5 STAINLESS STEEL 304
12	WASHER	6	DIN 125 - M5 STAINLESS STEEL 304
11	CYLINDER HEAD CAP SCREW	2	DIN 912 - M5 x 16 STAINLESS STEEL 304
10	BELT CLAMP TOP	1	ref: 16-01-04-05
9	BELT CLAMP BOTTOM	1	ref: 16-01-04-02
8	PULLEY	1	GT2 36 TEETH 5MM
7	EXTERNAL CIRCLIP	2	DIN 471 - M5 STAINLESS STEEL 304
6	SHAFT	1	ref: 16-01-04-05
5	BUSH	2	ref: 16-01-04-06
4	PULLEY HOLDER	1	ref: 16-01-04-02
3	RAIL SHAFT SUPPORT	1	SK12
2	BASE PLATE	1	ref: 16-01-04-01

UNIVERSITEIT VAN STELLENBOSCH

STUDENTE No. 17006384	TEKENAAR C. LEWIS	NAGESIEN	
SKAAL OP A 4 = 1:1	MATE IN mm	DATUM 24-10-2016	
TITEL: PULLEY BEARING ASSEMBLY			rev 1
VEL No. 19 VAN 36 VELLE		No. 16-01-04-00	

List of References

[1] A. Sayyah, M. N. Horenstein, and M. K. Mazumder, "Energy yield loss caused by dust deposition on photovoltaic panels," *Solar Energy*, vol. 107, pp. 576–604, 2014.

[2] H. Qasem, T. R. Betts, H. Müllejans, H. AlBusairi, and R. Gottschalg, "Dust-induced shading on photovoltaic modules," *Progress in Photovoltaics: Research and Applications*, vol. 22, no. 2, pp. 218–226, 2014.

[3] A. O. Mohamed and A. Hasan, "Effect of dust accumulation on performance of photovoltaic solar modules in sahara environment," *Journal of Basic and applied scientific Research*, vol. 2, no. 11, pp. 11 030–11 036, 2012.

[4] M. J. Adinoyi and S. A. Said, "Effect of dust accumulation on the power outputs of solar photovoltaic modules," *Renewable energy*, vol. 60, pp. 633–636, 2013.

[5] M. S. El-Shobokshy and F. M. Hussein, "Effect of dust with different physical properties on the performance of photovoltaic cells," *Solar energy*, vol. 51, no. 6, pp. 505–511, 1993.

[6] H. Jiang, L. Lu, and K. Sun, "Experimental investigation of the impact of airborne dust deposition on the performance of solar photovoltaic (pv) modules," *Atmospheric Environment*, vol. 45, no. 25, pp. 4299–4304, 2011.

[7] J. Zorrilla-Casanova, M. Philiougine, J. Carretero, P. Bernaola, P. Carpena, L. Mora-López, and M. Sidrach-de Cardona, "Analysis of dust losses in photovoltaic modules," in *World Renewable Energy Congress-Sweden; 8-13 May; 2011; Sweden*, no. 057, 2011, pp. 2985–2992.

[8] A. Marouani, N. Bouaouadja, Y. Castro, and A. Duran, "Effect of the sandstorms on the solar panels," in *International Symposium on Innovative Technologies in Engineering and Science; 29-30 September; 2013; Turkey*, no. 01, 2013, pp. 318–325.

[9] M. R. Maghami, H. Hizam, C. Gomes, M. A. Radzi, M. I. Rezadad, and S. Hajighorbani, "Power loss due to soiling on solar panel: A review," *Renewable and Sustainable Energy Reviews*, vol. 59, pp. 1307–1316, 2016.

[10] C. Cornaro and A. Andreotti, "Influence of average photon energy index on solar irradiance characteristics and outdoor performance of photovoltaic modules," *Progress in Photovoltaics: Research and Applications*, vol. 21, no. 5, pp. 996–1003, 2013.

[11] G. A. Landis, "Dust obscuration of mars solar arrays," *Acta Astronautica*, vol. 38, no. 11, pp. 885–891, 1996.

[12] Nasa's sorce satellite marks a decade in the sun. [Online]. Available: https://nasa.gov/mission_pages/sunearth/news/sorce-10yrs.html

[13] Spectroscopy - science. [Online]. Available: https://global.britannica.com/science/spectroscopy

[14] Solar electric systems. [Online]. Available: http://www.solar.udel.edu/ELEG620/02_Solar_radiation09.pdf

[15] W. Widger Jr and M. Woodall, "Integration of the planck blackbody radiation function," *Bulletin of the American Meteorological Society*, vol. 57, no. 10, pp. 1217–1219, 1976.

[16] M. Campisi and D. H. Kobe, "Derivation of the boltzmann principle," *American Journal of Physics*, vol. 78, no. 6, pp. 608–615, 2010.

[17] Sunlight, department of physics and astronomy, oberlin college. [Online]. Available: http://www.oberlin.edu/physics/Scofield/p268/library/Ch-03\%20Sunlight.pdf

[18] W. G. Rees, *Physical Principles of Remote Sensing*, 3rd ed. Cambridge University Press, 2013.

[19] W. Vlasak, "Analyzing atoms using the spice computer program," *Computing in Science & Engineering*, vol. 14, no. 3, pp. 98–103, 2012.

[20] Oriel product training: Solar simulation. [Online]. Available: https://assets.newport.com/webDocuments-EN/images/12298.pdf

[21] S. Adachi, *Earth-Abundant Materials for Solar Cells: Cu2-II-IV-VI4 Semiconductors*. John Wiley & Sons, 2015.

[22] B. Leckner, "The spectral distribution of solar radiation at the earth's surface-elements of a model," *Solar energy*, vol. 20, no. 2, pp. 143–150, 1978.

[23] J. Spencer, "Fourier series representation of the position of the sun," *Search*, vol. 2, no. 5, pp. 172–172, 1971.

[24] V. Badescu, *Modeling solar radiation at the earth's surface*. Springer, 2014.

[25] G. M. Masters, *Renewable And Efficient Electric Power Systems*, 2nd ed. Hoboken, New Jersey: John Wiley & Sons, Inc., 2013.

[26] M. Jamil Ahmad and G. N Tiwari, "Optimization of tilt angle for solar collector to receive maximum radiation," *The Open Renewable Energy Journal*, vol. 2, no. 1, 2009.

[27] P. Cooper, "The absorption of radiation in solar stills," *Solar energy*, vol. 12, no. 3, pp. 333–346, 1969.

[28] W. B. Stine and M. Geyer, *Power from the Sun*. Power from the sun. net, 2001.

[29] Y. A. Eltbaakh, M. H. Ruslan, M. Alghoul, M. Y. Othman, K. Sopian, and M. Fadhel, "Measurement of total and spectral solar irradiance: Overview of existing research," *Renewable and Sustainable Energy Reviews*, vol. 15, no. 3, pp. 1403–1426, 2011.

[30] J. W. Salisbury, "Spectral measurements field guide," Earth Satellite Corp Chevy Chase MD, Tech. Rep., 1998.

[31] P. Shanmugam and Y. Ahn, "Reference solar irradiance spectra and consequences of their disparities in remote sensing of the ocean colour," in *Annales Geophysicae*, vol. 25, no. 6, 2007, pp. 1235–1252.

[32] A. F. Bais, "Absolute spectral measurements of direct solar ultraviolet irradiance with a brewer spectrophotometer," *Applied optics*, vol. 36, no. 21, pp. 5199–5204, 1997.

[33] H. McCartney and M. H. Unsworth, "Spectral distribution of solar radiation. i: direct radiation," *Quarterly Journal of the Royal Meteorological Society*, vol. 104, no. 441, pp. 699–718, 1978.

[34] T. R. Betts, "Investigation of photovoltaic device operation under varying spectral conditions," Ph.D. dissertation, Loughborough University, 2005.

[35] M. Norton, A. G. Amillo, and R. Galleano, "Comparison of solar spectral irradiance measurements using the average photon energy parameter," *Solar Energy*, vol. 120, pp. 337–344, 2015.

[36] R. Moreno-Sáez, M. Sidrach-de Cardona, and L. Mora-López, "Analysis and characterization of photovoltaic modules of three different thin-film technologies in outdoor conditions," *Applied Energy*, vol. 162, pp. 827–838, 2016.

[37] Is there a difference between the terms cloudy and overcast? [Online]. Available: http://blog.chron.com/sciguy/2011/03/is-there-a-difference-between-the-terms-cloudy-and-overcast/

[38] Chief meteorologist at wgn-tv, ask tom why. [Online]. Available: http://articles.chicagotribune.com/2000-12-06/news/0012060178_1_sky-overcast-dear-al

[39] S. Nann and C. Riordan, "Solar spectral irradiance under overcast skies (solar cell performance effects)," in *Photovoltaic Specialists Conference, 1990., Conference Record of the Twenty First IEEE*. IEEE, 1990, pp. 1110–1115.

[40] D. Watt, "On the nature and distribution of solar radiation," *Report for US DOE*, 1978.

[41] F. Kasten and A. T. Young, "Revised optical air mass tables and approximation formula," *Applied optics*, vol. 28, no. 22, pp. 4735–4738, 1989.

[42] M. Hankins, *Stand-alone solar electric systems: the earthscan expert handbook for planning, design and installation*. Routledge, 2010.

[43] D. G. F. Sonnenenergie, *Planning and installing photovoltaic systems: a guide for installers, architects and engineers*. Earthscan, 2007.

[44] Recording fraunhofer lines with a compact spectrometer. [Online]. Available: www.ld-didactic.de:https://www.ld-didactic.de/documents/en-US/EXP/P/P6/P6225sle.pdf

[45] A. Y. Al-Hasan and A. A. Ghoneim, "A new correlation between photovoltaic panel's efficiency and amount of sand dust accumulated on their surface," *International Journal of Sustainable Energy*, vol. 24, no. 4, pp. 187–197, 2005.

[46] T. Sarver, A. Al-Qaraghuli, and L. L. Kazmerski, "A comprehensive review of the impact of dust on the use of solar energy: History, investigations, results, literature, and mitigation approaches," *Renewable and Sustainable Energy Reviews*, vol. 22, pp. 698–733, 2013.

[47] W. C. Hinds, *Aerosol technology: properties, behavior, and measurement of airborne particles*. John Wiley & Sons, 2012.

[48] M. Piliougine, J. Carretero, M. Sidrach-de Cardona, D. Montiel, and P. Sánchez-Friera, "Comparative analysis of the dust losses in photovoltaic modules with different cover glasses," in *Proceedings of 23rd European Solar Energy Conference*, vol. 2008, 2008, pp. 2698–2700.

[49] R. E. Bird and C. Riordan, "Simple solar spectral model for direct and diffuse irradiance on horizontal and tilted planes at the earth's surface for cloudless atmospheres," *Journal of climate and applied meteorology*, vol. 25, no. 1, pp. 87–97, 1986.

[50] S. Chander, A. Purohit, A. Nehra, S. Nehra, and M. Dhaka, "A study on spectral response and external quantum efficiency of mono-crystalline silicon solar cell," *International Journal of Renewable Energy Research (IJRER)*, vol. 5, no. 1, pp. 41–44, 2015.

[51] I. D. Sara, T. R. Betts, and R. Gottschalg, "Determining spectral response of a photovoltaic device using polychromatic filters," *IET Renewable Power Generation*, vol. 8, no. 5, pp. 467–473, 2014.

[52] S. Thomsen, R. Hulme, L. Landa, and K. Landa, "Low iron transmission float glass for solar cell applications and method of making same," Sep. 3 2009, uS Patent App. 12/453,275. [Online]. Available: https://www.google.com/patents/US20090217978

[53] U. Blieske, T. Doege, M. Neander, A. Prat, and P. Gayout, "Textured transparent plate with high light transmission," May 6 2008, uS Patent 7,368,655. [Online]. Available: https://www.google.com/patents/US7368655

[54] M. Powalla, U. Lemmer, A. Colsmann, and G. Gomard, "Plant epidermal structures for enhanced sunlight harvesting in solar cells," *SPIE Newsroom, 10.1117/2.1201611.006701*, 2016.

[55] C. F. Bohren and D. R. Huffman, *Absorption and scattering of light by small particles*. John Wiley & Sons, 2008.

[56] E. Hecht, "Optics, 4th," *International edition, Addison-Wesley, San Francisco*, vol. 3, 2002.

[57] Meteorology glossary - opticall smooth. [Online]. Available: http://glossary.ametsoc.org/wiki/Optically_smooth

[58] R. Chimenti and R. Thomas. Spectrometers: Miniature spectrometer design opens new application potential. [Online]. Available: http://www.laserfocusworld.com/articles/print/volume-49/issue-05/features/spectrometers--miniature-spectrometer-designs-open-new-applicati.html

[59] An introduction to a spectrometer: Spectral resolution. [Online]. Available: https://www.azom.com/article.aspx?ArticleID=13369

[60] Part 2: Diffraction grating. [Online]. Available: http://bwtek.com/spectrometer-part-2-the-grating/

[61] Measurement techniques: Irradiance. [Online]. Available: https://oceanoptics.com/measurementtechnique/irradiance/

[62] A. K. Gaigalas, L. Wang, H.-J. He, and P. DeRose, "Procedures for wavelength calibration and spectral response correction of ccd array spectrometers," *Journal of research of the National Institute of Standards and Technology*, vol. 114, no. 4, p. 215, 2009.

[63] P. A. Gorry, "General least-squares smoothing and differentiation by the convolution (savitzky-golay) method," *Analytical Chemistry*, vol. 62, no. 6, pp. 570–573, 1990.

[64] D. Malacara, *Physical optics and light measurements*. Academic Press, 1989, vol. 26.

[65] K. Ohta and H. Ishida, "Comparison among several numerical integration methods for kramers-kronig transformation," *Applied Spectroscopy*, vol. 42, no. 6, pp. 952–957, 1988.

[66] C. Hill and R. L. Jones, "Absorption of solar radiation by water vapor in clear and cloudy skies: Implications for anomalous absorption," *Journal of Geophysical Research: Atmospheres*, vol. 105, no. D7, pp. 9421–9428, 2000.

[67] G. Committee *et al.*, "Tables for reference solar spectral irradiances: Direct normal and hemispherical on 37 tilted surface," *ASTM International*, 2012. [Online]. Available: http://rredc.nrel.gov/solar/spectra/am1.5/

[68] Southern african universities radiometric network, solar radiometric data for the public, sun - stellenbosch university station. [Online]. Available: http://www.sauran.net/ShowStation.aspx?station=4

[69] Geosun africa. [Online]. Available: http://geosun.co.za/

[70] Timing belt theory by gates mectrol co. [Online]. Available: http://www.gatesmectrol.com/mectrol/downloads/download_common.cfm?file=Belt_Theory06sm.pdf&folder=brochure

[71] R. Budynas and J. Nisbett, *Shigley's Mechanical Engineering Design*, 9th ed. Mc Graw Hill, 2011.

[72] Drv8711 stepper motor controller ic datasheet. [Online]. Available: http://www.ti.com/lit/ds/symlink/drv8711.pdf

[73] Spidev 3.2. [Online]. Available: https://pypi.python.org/pypi/spidev

[74] Pyranometers - kipp & zonen. [Online]. Available: www.kippzonen.com/Download/70/Brochure-Pyranometers